

Fluid driven and mechanically induced fracture propagation : theory and numerical simulations

Citation for published version (APA):

Remij, E. W. (2017). *Fluid driven and mechanically induced fracture propagation : theory and numerical simulations*. [Phd Thesis 1 (Research TU/e / Graduation TU/e), Mechanical Engineering]. Technische Universiteit Eindhoven.

Document status and date:

Published: 16/02/2017

Document Version:

Publisher's PDF, also known as Version of Record (includes final page, issue and volume numbers)

Please check the document version of this publication:

- A submitted manuscript is the version of the article upon submission and before peer-review. There can be important differences between the submitted version and the official published version of record. People interested in the research are advised to contact the author for the final version of the publication, or visit the DOI to the publisher's website.
- The final author version and the galley proof are versions of the publication after peer review.
- The final published version features the final layout of the paper including the volume, issue and page numbers.

[Link to publication](#)

General rights

Copyright and moral rights for the publications made accessible in the public portal are retained by the authors and/or other copyright owners and it is a condition of accessing publications that users recognise and abide by the legal requirements associated with these rights.

- Users may download and print one copy of any publication from the public portal for the purpose of private study or research.
- You may not further distribute the material or use it for any profit-making activity or commercial gain
- You may freely distribute the URL identifying the publication in the public portal.

If the publication is distributed under the terms of Article 25fa of the Dutch Copyright Act, indicated by the "Taverne" license above, please follow below link for the End User Agreement:

www.tue.nl/taverne

Take down policy

If you believe that this document breaches copyright please contact us at:

openaccess@tue.nl

providing details and we will investigate your claim.

Fluid driven and mechanically induced fracture propagation: theory and numerical simulations

PROEFSCHRIFT

ter verkrijging van de graad van doctor aan de
Technische Universiteit Eindhoven, op gezag van de
rector magnificus, prof.dr.ir. F.P.T. Baaijens, voor een
commissie aangewezen door het College voor
Promoties, in het openbaar te verdedigen
op donderdag 16 februari 2017 om 16.00 uur

door

Ernst Wilhelmus Remij

geboren te Nederweert-Eind

Dit proefschrift is goedgekeurd door de promotor en copromotoren.
De samenstelling van de promotiecommissie is als volgt:

voorzitter:	prof.dr.	L.P.H. de Goey
1e promotor:	prof.dr.ir.	D.M.J. Smeulders
2e promotor:	prof.dr.ir.	J.M.R.J. Huyghe
copromotor:	dr.ir.	J.J.C. Remmers
leden:	prof.dr.	J.G.M. Kuerten
	prof.dr.techn.	G. Meschke (Ruhr-Universität Bochum)
	prof.dr.	B.A. Schrefler (University of Padova)
adviseur:	dr.	C.J. de Pater (Fenix Consulting Delft)

Het onderzoek of ontwerp dat in dit proefschrift wordt beschreven is uitgevoerd in overeenstemming met de TU/e Gedragscode Wetenschapsbeoefening.

Voor Pap en Mam

*Zoelang dekke mer neet Mea Culpa hoeftj te zegge.
As long as you do not have to say Mea Culpa.*

Wiel Verheijen, 1928 - 2014
Beloved grandfather

This research project is part of the 2F2S consortium supported by Baker Hughes, EBN, ENGIE, the Dutch TKI Gas Foundation, Total and Wintershall.

Copyright © 2017 by E.W.Remij

Printed by Ipskamp Drukkers
Cover image: Shale rock, Whitby outcrops

ISBN: 978-90-386-4223-9
A catalogue record is available from the Eindhoven University of
Technology Library

Contents

Summary	ix
1 Introduction	1
1.1 Hydraulic fracturing	2
1.2 Fracture process	5
1.3 The eXtended Finite Element Method	6
1.4 Porous media	7
1.5 Objective and thesis outline	11
2 A Partition of unity based model for crack nucleation and propagation in porous media	13
2.1 Kinematic relations	15
2.2 Balance equations	17
2.3 Discretization and numerical implementation	20
2.3.1 Fracture propagation in an orthotropic material	23
2.4 Constitutive equations	24
2.4.1 Mechanical behaviour of the orthotropic bulk	24
2.4.2 Mechanical behaviour in the fracture	25
2.5 Examples	27
2.5.1 Unconfined compression	28
2.5.2 Fracture propagation in a transverse isotropic material	29
2.5.3 Mixed mode fracture	31
2.6 Conclusions	34
3 Investigation of step-wise propagation of a mode-II fracture in a poro-elastic medium	37
3.1 Model background	39
3.2 Numerical implementation	42
3.3 Example	43
3.4 Conclusions	50
4 The Enhanced Local Pressure model	53
4.1 Kinematic relations	56

4.2	Balance equations	58
4.2.1	Bulk behaviour	58
4.2.2	Microscopic model	60
4.3	Constitutive equations	60
4.3.1	Mechanical behaviour of the bulk	60
4.3.2	Mechanical behaviour in the discontinuity	61
4.3.3	Small scale pressure coupling	62
4.4	Weak form	63
4.5	Discretization	65
4.6	Numerical implemenation	69
4.7	Examples	69
4.7.1	Fluid leakage from an opened fracture	70
4.7.2	KGD fracture problem	72
4.7.3	Fracture from a circular hole	75
4.8	Conclusion	77
5	Simulation of crack interaction	79
5.1	Model background	82
5.1.1	Kinematic relations	82
5.1.2	Weak form	84
5.1.3	Discretization	87
5.1.4	Numerical implementation	89
5.1.5	Constitutive law at the fracture and the interface	91
5.2	Results	92
5.2.1	Performance of the crossing and diversion criterion	93
5.2.2	Influence of the shear stiffness	95
5.2.3	Influence of the interaction angle and the in situ stress	96
5.2.4	Interaction with a fracture network	101
5.3	Conclusions	102
6	An efficient parallel X-FEM computing method	105
6.1	Model background	108
6.1.1	A review of the extended finite element method	109
6.1.2	Solver and preconditioner	111
6.1.3	Domain decomposition	113
6.1.4	Tracking the fracture location	114
6.1.5	Numerical implementation of DD with X-FEM	115
6.2	Results	120
6.2.1	Mixed mode fracture propagation	121
6.2.2	KGD Hydraulic fracture problem	123

6.2.3	Two parallel hydraulic fractures	125
6.3	Conclusions	127
7	A 3D partition of unity based hydraulic fracture model	129
7.1	Model background	132
7.2	Numerical implementation	133
7.2.1	Tracking the discontinuity surface	135
7.2.2	2D level set propagation	136
7.2.3	3D level set propagation	136
7.3	Examples 3D X-FEM	140
7.4	The 3D ELP model	142
7.4.1	Example 3D hydraulic fracturing	146
7.5	Conclusions and future work	148
8	Conclusions and outlook	149
8.1	Conclusions	149
8.2	Outlook	151
	References	155
A	Leakage equation	169
B	System of equations in the ELP model	171
C	System of equations in the ELP model with multiple fractures	175
	Dankwoord	183
	Publications	185
	Curriculum Vitae	187

Summary

Understanding fractures in porous materials is important in a variety of fields, from medical treatment of intervertebral disc herniation and design optimization of diapers to applications in geo-mechanics. This thesis is focused on the last topic and specifically aims at the application of hydraulic fracturing. Hydraulic fracturing is the technique in which a fracture propagates due to hydraulic loading, i.e., by applying a fluid pressure inside the fracture. In geo-mechanics, the technique is applied to stimulate oil and gas reservoirs by injecting a viscous fluid into the underground formation. The induced fracture remains open under high confining stress after pressure release due to a proppant that is added to the fracturing fluid. The opened fractures enhance the permeability of the reservoir increasing oil and gas production rates. Optimizing a hydraulic fracture treatment will benefit from the ability to predict the rock failure process. In this thesis a numerical tool is developed for the simulation of the hydraulic fracture process.

The numerical tool is based on the eXtended Finite Element Method (X-FEM). A fracture is incorporated as a discontinuity in the finite element mesh by an additional discontinuous displacement field. This displacement field is only present at nodes surrounding the fracture. An advantage of this approach is the possibility to simulate crack propagation in arbitrary directions irrespective of the underlying mesh. Furthermore the implementation is computationally efficient since no topology changes are required in the mesh and the size of the stiffness matrix only increases proportional to the degrees of freedom that are added to nodes surrounding the fracture. The poro-elasticity is included in the model by using Biot's theory. Fluid through the porous material is governed by Darcy's law. The fracture process is described by the cohesive zone approach in which the growth and coalescence of small micro-separations in front of the crack tip are lumped into a single surface. The growth of the micro-separations into a complete

fracture is described by a traction-separation law. The direction of fracture propagation is based on an average stress criterion around the tip of the fracture.

Chapter 2 investigates fracture propagation and nucleation in a porous material using the extended finite element method. Isotropic and orthotropic material descriptions are considered. The average stress criterion is adapted to the orthotropic material by considering the directional stiffness of the material. A good consistency between the analytical Mandal-Cryer Benchmark and the numerical model is demonstrated for both isotropic and orthotropic materials. It is demonstrated that the fracture path is affected by the orthotropic material. Fracture propagation and nucleation are also found to depend on the intrinsic permeability. The same model is applied to study shear failure in Chapter 3. The limitation of fracture growth through only one element within one time increment is removed in order to investigate the effect of fracture propagation on different levels of mesh refinement. The fluid flow across the fracture shows alternating behavior corresponding to phases of fracture propagation and relaxation. The behavior becomes less prominent and vanishes in the refined meshes while the fracture path is identical for all levels of mesh refinement.

In Chapter 4 the model specifically designed for hydraulic fracturing in low permeable rocks is introduced. The model is referred to as the Enhanced Local Pressure (ELP) model since the pressure within the fracture is included as an additional degree of freedom. The pressure exhibits a jump from the formation to the fracture on the adjacent sides of the fracture surface. In low permeable rocks the discontinuous pressure is justified. By this approach the necessity to resolve steep pressure gradients near the fracture surface is avoided. Fluid injection goes exclusively into the fracture, unlike earlier approaches. The model is compared successfully with the KGD hydraulic fracture problem. The fracture path is observed to be consistent with experimental data from literature. The enhanced local pressure model proves to be an efficient tool for the simulation of hydraulic fracturing.

The ELP model is augmented to also analyze fracture interaction of a hydraulic fracture with an existing natural fracture network in Chapter 5. For each discontinuity an additional enrichment field is added. When two fractures are in the vicinity of each other, nodes may possess more than one enrichment field. Interaction behavior is characterized by two criteria describing whether a hydraulic fracture crosses a natural fracture and whether fluid will divert into the natural fracture or not. Simulated fracture behavior is found to agree with available experimental data from

literature.

In order to consider larger meshes with more degrees of freedom, a parallel implementation of the extended finite element model as well as the enhanced pressure model is introduced in Chapter 6. Parallel computing is carried out by subdividing the mesh in sub-domains and solving each domain on a single computational core. An efficient bookkeeping between sub-domains is necessary when the fracture propagates across sub-domain boundaries. On 192 computational cores a 100-fold speed-up is obtained. Beside the decrease in computational time there is also more memory available as the number of computational cores increase. The feature of parallel computing with the ELP model in combination with the interaction modeling contributes to the possibility to simulate more realistic hydraulic fracturing scenarios.

Finally the model is extended to 3D. Planar and non-planar fracture propagation are demonstrated in an elastic material. The 3D model is also applied to a planar hydraulic fracture.

1

Introduction

The Dutch industry benefited enormously by the availability of natural gas in the Netherlands and it has boosted the economy for decades (Correljé et al., 2003). The first natural gas resources in the Netherlands were discovered in Groningen in 1948. All Dutch municipalities were connected to the gas grid in 1968 which meant that Dutch households were able to enjoy gas related benefits such as cooking and central heating. Natural gas is a reliable, clean and relatively cheap source of energy (Correljé et al., 2003).

However, the production of natural gas from conventional resources is rapidly declining while the demand is still high. Statistics Netherlands (CBS) reported that since May 2015 gas import exceeds gas export as shown in Figure 1.1.

Apart from the conventional gas resources, the Netherlands, and many other EU countries, also possess unconventional resources located in shale formations and tight sandstones. The difference between these unconventional formations compared to the conventional fields is that the former have very low permeability. This makes unconventional resources unfit for production without additional stimulation.

With the recent advancement of a novel drilling technology (horizontal drilling) these resources have become accessible, as was demonstrated by the massive exploitation of shale gas the in United States (Howarth et al., 2011). Improving the exploitation of the unconventional resources would benefit from the ability to predict and optimize the creation of fracture networks in the subsurface and from further knowledge of fluid-rock interactions.

In this thesis a numerical tool is developed to simulate hydraulic fracturing in low permeable rocks. The ability to predict the failure process in permeable rocks is beneficial for optimizing the hydraulic fracture process.

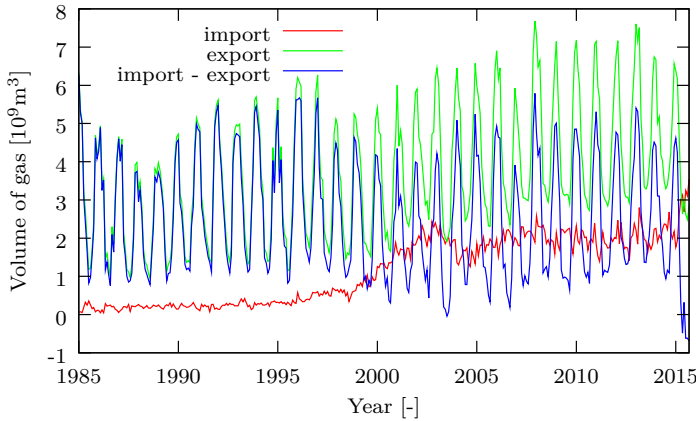


Figure 1.1: Import and export graph of natural gas in the Netherlands. Due to lower gas production, the export declines while the import amount grows. Data from Statistics Netherlands (CBS).

The model presented in this thesis is designed such that it can be applied to a fractured medium irrespective of if the material is elastic or poro-elastic (porous). Special attention is given to failure of low permeable rocks due to hydraulic fracturing. Many of the results in this thesis are therefore related to failure of porous materials but also applications in solid mechanics are presented.

In this first chapter a short introduction to porous media is given and the basic background of the mechanics of hydraulic fracturing is described. The failure process in relation to permeable materials is presented and numerical techniques are discussed. Finally the scope and the layout of the remainder of this thesis are given.

1.1 Hydraulic fracturing

The process of hydraulic fracturing became well known due to the massive extraction of shale gas in the United States. The increase in natural gas and crude oil production due to hydraulic fracturing in the United States is shown in Figure 1.2 indicating the importance of the technique. In 2015 hydraulic fracturing was used in two third of the natural gas production and in half of the produced crude oil. Remarkably the technique is not new. It has been applied already for decades since the introduction in 1947 by Stanolind Oil (Smith and Montgomery, 2015). Hydraulic fracturing is a technique to greatly improve the production rates of a well. This is mainly achieved by creating a conductivity channel near the well to further increase

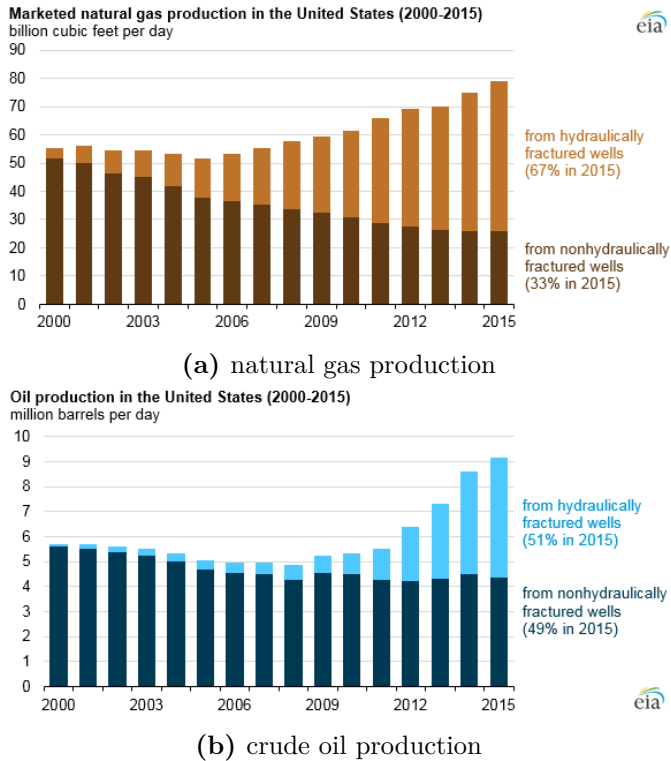


Figure 1.2: Overview for the natural gas and crude oil production in the United States from 2000 until 2015. Approximately two third of the gas production and half the oil production is accounted for due to hydraulic fracturing. Source: U.S. Energy Information Administration, IHS Global Insight and DrillingInfo Inc.

the productivity (Figure 1.3). The first hydraulic fracturing operations were performed on vertical wells. With horizontal drilling it became possible to drill parallel to an oil or gas bearing layer. The typical horizontal well is 600 to 900 meters long resulting in a large contact area. Compared to vertical wells the production rates of horizontal wells are thus sufficient to be applied at unconventional reservoirs due to the installation of multiple separate fracturing stages (King, 2010). In the hydraulic fracturing process fluid is being injected into the well at high flow rate. Typical injection rates are around $0.05 \text{ m}^3/\text{s}$ with fluid pressures of 30 MPa (Smith and Montgomery, 2015). When the flow rate exceeds the amount of fluid that can leak into the formation the pressure in the well increases. There is a pressure increase in the well if the flow rate is higher than the amount of fluid that can leak into the formation. This leads to the failure of the formation and the creation of hydraulic fractures. When the injection stops,

the injected fluid continues to leak into the formation and the pressure drops, leading to closure of the fracture. To prevent this from happening and to keep the fractured area available for production, a proppant agent is added to the fracturing fluid. The proppant is usually sand or a granular substitute for sand. After the injecting is halted the proppant stays in place leading to increased conductivity in the fractured area (Smith and Montgomery, 2015; Economides and Nolte, 2000).

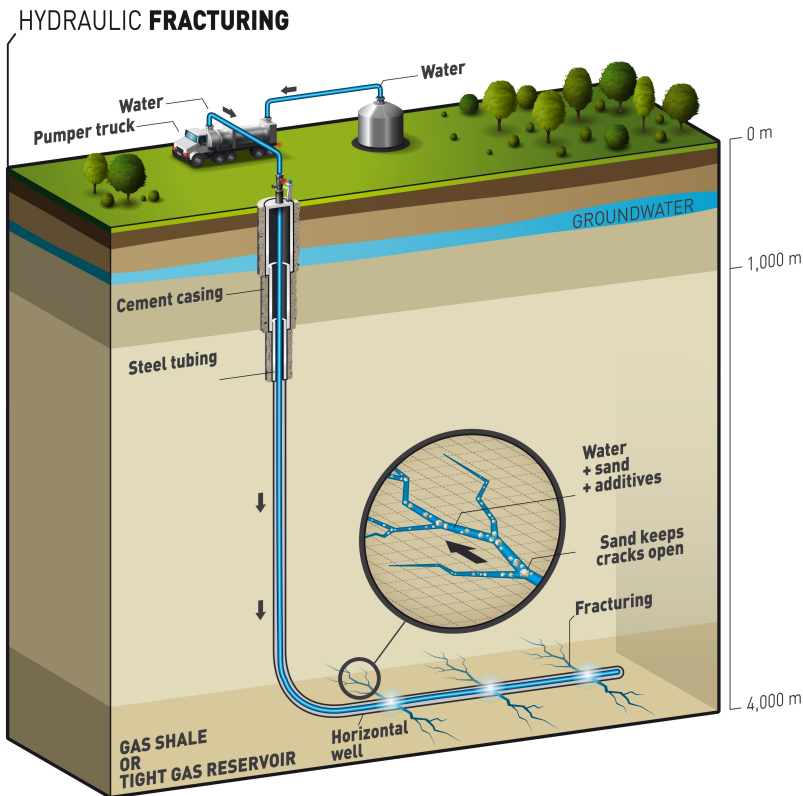


Figure 1.3: Schematic representation of the hydraulic fracturing process. Horizontal drilling along the gas rich layer followed by fluid injection creates the hydraulic fractures. The fractures remain open after fluid injection due to proppants creating a high conductivity path for the gas.¹

Apart from the extraction of the traditional fossil fuels hydraulic fracturing is also an important component in the development of Enhanced Geothermal Systems (EGS). With EGS heat is extracted from the subsurface by injecting a fluid or gas at an injection well. However, there is no or

¹Image from: <http://breakingenergy.com>

very limited conductivity in most rocks to obtain an efficient flow rate. Hydraulic fracturing is used to increase the conductivity, making EGS more efficient. Due to a pressure gradient between the injection well and the production well the cold fluid or gas will heat up by flowing through the warmer reservoir. (Pruess, 2006).

Predicting the hydraulic fracture process is important to optimize production rates. It is a challenging task since three different phenomena have to be taken into account: the fluid exchange between the fracture and the rock formation, the fluid flow in the fracture, and the changing in spatial configuration due to fracture propagation. Theoretical models were developed to predict single hydraulic fractures by Geertsma and De Klerk (1969); Khristianovic and Zheltov (1955) and Perkins and Kern (1961). These models were the starting point for more advanced models resulting in asymptotic solutions for various conditions. Adachi and Detournay (2008) present an overview of these solutions. Numerical models for complex geometries were developed for the cases in which theoretical models fall short. The first numerical model for hydraulic fracturing was introduced by Boone and Ingraffea (1990). Existing numerical methods for fracturing in poro-elastic materials are described later in this chapter.

1.2 Fracture process

The onset of a fracture² can be interpreted as the growth of small micro-separations in a process zone around an existing flaw or notch in a material (Figure 1.4a). Increasing damage leads to growing and merging of the micro-separations in the process zone until one dominant fracture arises. These micro-separations can be considered as cracks at the macro scale. The growth of micro-separations leads to energy dissipation in the form of friction and heat generation making the process irreversible and leading to reduction of strength and stiffness of the material (Remmers, 2006).

Without going into detail about the micro-structure of a material, the growth of a fracture can be summarized by the nucleation, growth and subsequent coalescence of the small micro-separations. The common approach in modelling this process is by lumping these effects into a single

²The naming of a fracture may give the reader of this thesis some confusion. In a numerical context a fracture is referred to as a discontinuity since it does not represent something physical but merely a step in the displacement field. A crack is another name of the same thing. In principle one may call a crack the result of a fracture process. In geomechanics it is common again to refer to fracture networks. Therefore, the three terms, a fracture, a crack and a discontinuity are used interchangeably where the latter is mainly used in the numerical context and the former two are physically oriented.

model. Griffith (1921) assumed that a fracture is allowed to grow if the surface energy required to create a new fracture surface is at least equal to the decrease in elastic energy due the fracture propagation. Linear Elastic Fracture Mechanics (LEFM) is a powerful theory to model fracture growth based on Griffith's work. Despite many successful applications it lacks accuracy if the process zone is not small compared to the size of the fracture. The theory is also based on the existence of a flaw which means that nucleation of fractures is not considered. Quasi brittle rocks such as shales and sandstones show a large area of softening and thus LEFM may not be the best candidate to describe the fracture process (de Pater, 2015; Yao et al., 2015). It may also be necessary to take the length of the process zone into account because the porosity may change when the micro-separations grow. The process zone can have much larger conductivity compared to intact material. The cohesive zone approach, developed independently by Dugdale (1960) and Barenblatt (1962), is an alternative approach where the process zone is explicitly modelled by lumping it along a plane (in 3D) or a line (in 2D as shown in Figure 1.4b) . The work needed to open and propagate the cohesive zone over a unit length is equal to the fracture energy. Constitutive relations describe the decay of energy thus it is not necessary to determine the length of the cohesive zone a priori.

A distinction is made between the tip of the crack and the tip of the cohesive zone in Figure 1.4b. The former represents the location along the crack where there is no bonding strength left and the latter the location where there still is perfect bonding. When referring to the fracture tip within this thesis the cohesive tip is meant and the cohesive zone length is included in the fracture length when given. This is the most convenient convention due to the numerical framework used. A distinction between the two tips or the fracture length and the cohesive zone length is explicitly made when required.

1.3 The eXtended Finite Element Method

The modelling of a fracture involves solving a discontinuity in the displacement field. Traditional polynomial approximation methods such as Finite Elements (FE) require that the mesh is conforming to the discontinuity and fine enough near the discontinuity. Modelling of evolving discontinuities often require remeshing techniques to maintain conformity between the mesh and the growing discontinuity. An alternative approach is to enrich the polynomial approximation by exploiting the partition of unity property of finite element shape functions (Melenk and Babuška, 1996). Here the dis-

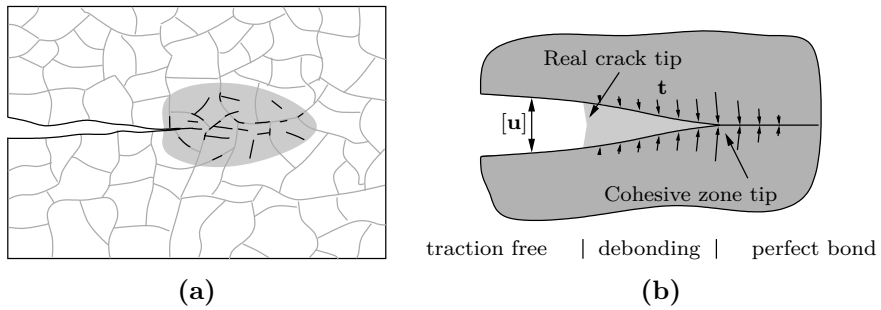


Figure 1.4: (a) Schematic representation of the process zone (shaded area) with micro-separations (thick solid lines in the process zone) in a granular material. (b) Representation of the cohesive zone. Interface tractions \mathbf{t} describe the perfect bonding and damaging process. The opening of the fracture is denoted as $[u]$. The location of the tip of the crack and the tip of the cohesive zone are shown (Remmers, 2006).

continuity is resolved independently of the underlying mesh. Belytschko and Black (1999) were the first to model a discontinuity by applying a local partition of unity based on tip enrichment functions. Small deviations from a straight discontinuity were solved by a mapping algorithm. The method was called eXtended Finite Element Method (X-FEM) by Moës et al. (1999) and Dolbow et al. (2000), who also introduced a combination of Heaviside enrichment and near-tip enrichment.

The X-FEM proved to be a very elegant way to incorporate a discontinuity in the displacement field irrespective of the location and structure of the underlying mesh. The method was further improved by Daux et al. (2000) by including multiple discontinuities. Wells and Sluys (2001) applied the technique to cohesive fracture growth. The extension to 3D was made by Sukumar et al. (2000). A good overview of the X-FEM can be found in Belytschko et al. (2009) and in Fries and Belytschko (2010).

1.4 Porous media

Hydrocarbon reservoirs consist of a solid matrix structure and pores in between. These pores can have huge variations of interconnectivity. In crystalline rocks, fluid inclusions may account for a large fraction of the total porosity, but in general disconnected porosity is small. The fact that most pores are interconnected opens the possibility to move fluids (liquids and gasses) out of the formation (hydrocarbon production). In shales hydraulic fracturing is always needed to obtain sufficient flow rates. The

easiness in which this transportation takes place is associated with the so-called permeability of the porous formation. Typical subsurface fluid velocities are small, say around a foot per day. A simplified representation of a porous medium is given in Figure 1.5 where both the matrix and the fluid are separate interconnected phases. Note that the reality is 3D which cannot truly be represented in this 2D plot. A Scanning Electron Microscope (SEM) image of shale rock is shown in Figure 1.6. The low permeable rock is characterized by a low porosity, 1-7% measured with a Helium porosimetry, and the majority of the pores show a diameter smaller than 300 nm (Houben et al., 2016).

The possibility of a fluid to freely move through the material represents a significant difference with elastic materials. A mechanically induced deformation is accompanied by movement of fluids and/or pore pressure changes. The velocity of fluid movement through the interconnected pores induces time dependent behaviour to the mechanical properties of rocks (Detournay and Cheng, 1993). The phenomenon of consolidation is caused by mechanically loading a porous material. The resulting compression rate is dependent on how fast the fluid can flow through the pores. Terzaghi (1923) introduced this theory describing the influence of the pore fluid on the deformation of soils in 1923. In a one-dimensional case Terzaghi described consolidation satisfying a diffusion type of equation and using the theory of effective stress, i.e. splitting the stress in a contribution depending directly on deformation of the solid skeleton (effective stress) and a contribution which does not directly depend on deformation (the pressure). Biot developed his theory of poroelasticity that coupled the solid deformation to changes in fluid content between 1935 and 1941 (Biot, 1935, 1941). Solutions to coupled problems, e.g. the Mandel-Cryer problem (Mandel, 1953; Cryer, 1963) and the Noordbergum problem (Verruijt, 1969), could only be solved based on Biot's theory.

Fractures in a porous material are different from those in solids because of fluid solid interactions. In solid materials fractures propagate because of external loads on the structure whereas in porous materials the fracture can also be induced by fluid injection in the pores. This is the quintessence of the hydraulic fracturing process.

Various methods exist for describing fractured porous media. Boone and Ingraffea (1990) were the first to simulate fracture propagation including coupled poro-elastic effects. The model was applied for hydraulic fracturing and was based on the finite element method (FEM) for the poro-elastic material with a cohesive zone description for the fracture process. The fluid flow in the fracture was solved using a finite difference method. In

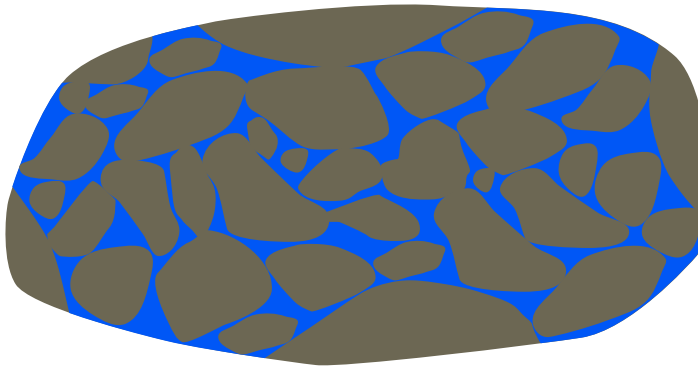


Figure 1.5: Schematic representation of a porous material saturated with a fluid. The solid grains are visualised in brown and the fluid in blue.

this context an adaptive remeshing scheme was developed by Schrefler et al. (2006) and Secchi et al. (2007). Extensions to 3D remeshing were made by Secchi and Schrefler (2012). Hydraulic fracturing was investigated in a permeable material by Sarris and Papanastasiou (2011) with a finite element analysis including cohesive zone elements. Segura and Carol (2004, 2008) introduced a hydro-mechanical coupling formulation using zero-thickness interface elements with double nodes based on FEM analysis. This approach was also applied in fracture in porous materials by Khoei et al. (2010) and Carrier and Granet (2012). Discrete methods such as the discrete element method (Nagel et al., 2013) and lattice models (Grassl et al., 2015; Milanese et al., 2016) were also used for fracture propagation in poro-elastic materials.

Significant advancements were recently made in fracture modelling using the phase-field approach (Bourdin et al., 2008; Miehe et al., 2010). The phase field approach is a fixed-mesh method purely based on energy minimization. The major advantage of this approach is that the main possibilities in fracture behaviour, such as propagation, nucleation, and multiple interacting and branching fractures, are automatically determined due to the energy minimisation requirement. The sharp interface of a fracture is regularized by a smeared damage parameter (the phase-field) avoiding the need to track the fracture surface. The phase-field method was recently applied to fluid-driven fracture propagation by Wheeler et al. (2014), Miehe et al. (2015) and Yoshioka and Bourdin (2016). However, the regularization of the fracture requires a fine mesh to be resolved on and thus causes a restriction on computational time. In situations with a single fracture or known fracture locations this presents no difficulties. However, the computational costs increase severely when considering larger domains with

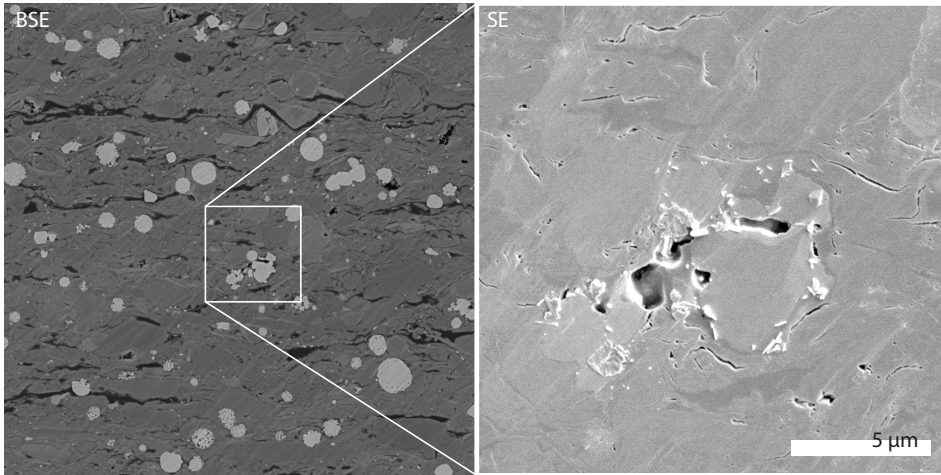


Figure 1.6: Scanning Electron Microscope (SEM) images of a shale rock, courtesy of M. Houben. On the left a Back Scattered Electron (BSE) image where different shades of grey represent different minerals. Organic matter is shown in black. On the right a Secondary Electron (SE) image. Pores that were almost invisible in the BSE image are visible here in black. Details about the mineralogy, porosity and the microstructure of this shale rock can be found in Houben et al. (2016).

many fractures. Extending to 3D is even more challenging. This is also acknowledged by Lee et al. (2016) where 3D hydraulic fracturing using the phase-field method is described. An adaptive remeshing scheme, based on the work by Heister et al. (2015) was proposed to limit the computational times.

The X-FEM approach was applied to fractures in porous media by de Borst et al. (2006) investigating shear banding. Both fluid and solid phases were described as being discontinuous across the fracture. Fluid flow was described by Darcy's law with a constant permeability. A continuous pressure description over the fracture was presented in Réthoré et al. (2007). In their work the fluid flow is related to crack opening and a viscous Couette flow profile is used in the crack. However, no crack propagation was considered. Kraaijeveld and Huyghe (2011) extended this work towards ionized porous materials and also considered propagating cracks. Pure mode-I and mode-II fractures were described with a continuous and discontinuous pressure across the fracture, respectively. Irzal et al. (2013) extended the concept into the finite deformation range. Mohammadnejad and Khoei (2012) developed an X-FEM model for cohesive crack growth in multiphase porous materials. They successfully applied their model for hydraulic fracturing simulations (Mohammadnejad and Khoei, 2013).

Meschke and Leonhart (2015) described the pressure across the fracture continuously by applying an enrichment scheme for the pressure based on a 1D analytical consolidation equation. Steep pressure gradients near the fracture surface were modelled successfully by this enrichment scheme. The phantom node method was applied by Sobhaniragh et al. (2016). Recent advancements in poro-elastic partition of unity based models are described in Mohammadnejad and Andrade (2016).

Note that there also exists abundant research on hydraulic fracturing into non-porous materials. X-FEM in combination with hydraulic fracturing was introduced by Lecampion (2009). 3D X-FEM models were introduced by Gupta et al. (Gupta and Duarte, 2014, 2015). Cohesive zone models were applied in Chen et al. (2009) and Chen (2012) and boundary element based methods in Dong and de Pater (2001) and Kresse et al. (2013).

In this thesis the extended finite element method is used for hydraulic fracturing simulations. The main reasons are, broad applicability, reasonable simulation times, and good interaction handling of propagating fractures with existing fracture networks. The method can also extend fractures through material interfaces and is applicable in 3D. However, the major advantage of X-FEM, compared to all methods with the exception of the boundary element method, is that the coarsening of the mesh and the absence of remeshing limits the computational time. Inhomogeneities such as material interfaces require additional measures in the boundary element method but can be incorporated more easily in the finite element based X-FEM.

1.5 Objective and thesis outline

The objective of this thesis is to bring the numerical model introduced by Kraaijeveld (2009) and Irzal et al. (2013) closer to realistic situations where we primarily focus on hydraulic fracturing. In Chapter 2, the standard X-FEM model for fracturing in poro-elastic materials is presented. The governing equations are derived based on momentum and mass balance. An orthotropic material is considered and the influence of the permeability on the fracture process is shown. The same model for isotropic materials is applied to shear failure in the third chapter. The coupling between fluid flow across the fracture is further investigated by using a very fine numerical discretization. The poro-elastic fracture model is extended specifically for the simulation of hydraulic fracturing in low permeable rocks in Chapter 4. In the fifth chapter the model is improved to exploit the X-FEM possi-

bility of having multiple interacting fractures. A fracture crossing criterion and fluid diversion criterion are introduced in order to study the interaction behaviour of a hydraulic fracture with a natural fracture network. In Chapter 6, a computational implementation of parallel computing applied to the fracture model is presented. Scalability analysis and the possibility to use large domains that are computationally expensive are shown. A 3D implementation of the model is presented in Chapter 7. Conclusions are given in Chapter 8.

2

A Partition of unity based model for crack nucleation and propagation in porous media

Abstract

In this chapter, we present a general partition of unity based cohesive zone model for fracture propagation and nucleation in saturated porous materials. We consider both two-dimensional isotropic and orthotropic media based on the general Biot theory. Fluid flow from the bulk formation into the fracture is accounted for. The fracture propagation is based on an average stress approach. This approach is adjusted to be directionally dependent for orthotropic materials. The accuracy of the continuous part of the model is addressed by performing Mandel's problem for isotropic and orthotropic materials. The performance of the model is investigated with a propagating fracture in an orthotropic material and by considering fracture nucleation and propagation in an isotropic mixed-mode fracture problem. In the latter example we also investigated the influence of the bulk permeability on the numerical results.

The necessity of a hydraulic fracturing model is evident based on the previous chapter. In this chapter we take one step back and will not consider hydraulic fracturing yet but focus on mechanically induced fractures in porous media. Additional attention is given to the response of an orthotropic material considering the special case of transverse isotropy. This is also relevant in hydraulic fracturing since layered rocks often possess this type of anisotropy but also to obtain insight in fracture in human tissues. Biological materials, such as cortical bone, with long parallel fibers and a random distribution in the cross section can be considered as transverse isotropic.

An isotropic poro-elastic numerical model, using the Finite Element Method (FEM), was developed by Boone and Ingraffea (1990) to simulate hydraulic fracturing. A cohesive zone description was used for the fracture process and the fluid flow in the fracture was solved using a finite difference method. In their work, the cohesive zone elements that model the crack were inserted in the finite element mesh beforehand, which requires an a priori knowledge of the fracture path. Secchi et al. (2007) used the finite element method to model a cohesive fracture as well, but included an adaptive remeshing method in order to accommodate for fracture propagation in arbitrary directions. This method was successfully applied to simulate a propagating crack in arbitrary directions and was even extended to three-dimensional situations (Secchi and Schrefler, 2012). Unfortunately, the remeshing algorithm is computationally inefficient and may give rise to incorrect results in the case of non-linear behaviour of the bulk material.

An alternative technique to model arbitrary crack growth, irrespective of the structure of the underlying finite element mesh is the use of the partition of unity property of finite element shape functions (Melenk and Babuška, 1996). Belytschko and co-workers (Belytschko and Black, 1999; Dolbow et al., 2000) used this property to model a propagating crack in a solid material following linear elastic fracture mechanics. The crack is modelled as a discontinuity which is incorporated in the finite element method by enhancing existing nodes by additional degrees of freedom and is commonly referred to as the eXtended Finite Element Method (X-FEM). Wells and Sluys (2001) incorporated a cohesive zone model in X-FEM to model fracture propagation in arbitrary directions in a solid. The strength of X-FEM is that a fracture can grow in any direction and at any time without the need of remeshing.

Recently, the partition of unity method has also been used to model fracture propagation in porous materials. De Borst et al. (2006) investigated shear banding in a porous material. A discontinuous description was

used for both solid and fluid phase. Fluid flow is described by Darcy's law with a constant permeability and a pressure gradient defined by the pressure difference on both sides of the crack. A continuous pressure description over the fracture was presented in (Réthoré et al., 2007). In this work the fluid flow is related to crack opening and a viscous Couette flow profile in the crack. However, no crack propagation was considered. Kraaijeveld and Huyghe (2011) extended this work towards ionized porous materials and considered propagating cracks. Pure mode-I and mode-II fractures were described with a continuous and discontinuous pressure, respectively.

In this chapter we enhance the aforementioned models to accommodate for crack nucleation similar to (Remmers et al., 2003), mixed-mode crack growth and propagation in an orthotropic material. We use the model to study the effect of the direction of crack growth in saturated porous media as a function of permeability. The porous material is described by the standard Biot equations and the fluid flow in the material is included by Darcy's law. The partition of unity method in combination with the cohesive zone approach is used to introduce a crack. The crack is described by a strong discontinuity in the displacement field while the pressure field is considered to be continuous across the fracture. Fluid flow from the crack into the formation is accounted for. The tangential fluid flow is described with lubrication theory.

In the next paragraph the kinematic relations are described. We then present the momentum and mass balance equations in Section 2.2 and describe the discretization and numerical implementation in Section 2.3. The constitutive equations are given in Section 2.4. Finally we show the performance of the numerical model in Section 2.5 and give some concluding remarks in Section 2.6.

2.1 Kinematic relations

Consider a body Ω that is crossed by a discontinuity Γ_d , as shown in Figure 2.1. The discontinuity divides the body in two domains, Ω^+ and Ω^- . The vector \mathbf{n}_d is defined as the normal of the discontinuity surface Γ_d pointing into domain Ω^+ . The total displacement field of the solid skeleton can, at any time t , be described by a regular displacement field $\hat{\mathbf{u}}(\mathbf{x}, t)$ and an additional displacement field $\tilde{\mathbf{u}}(\mathbf{x}, t)$ (Belytschko and Black, 1999; Moës et al., 1999; Remmers et al., 2008)

$$\mathbf{u}(\mathbf{x}, t) = \hat{\mathbf{u}}(\mathbf{x}, t) + \mathcal{H}_{\Gamma_d}(\mathbf{x})\tilde{\mathbf{u}}(\mathbf{x}, t), \quad (2.1)$$

where \mathbf{x} is the position of a material point in the domain Ω and \mathcal{H}_{Γ_d} is the

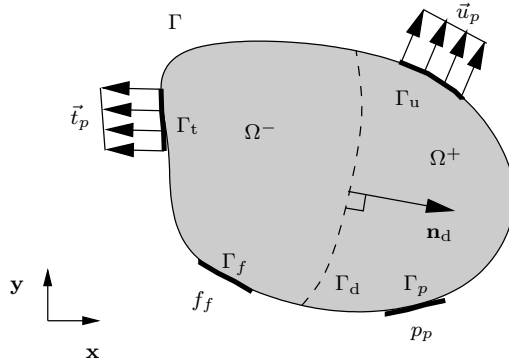


Figure 2.1: The body Ω crossed by discontinuity Γ_d . The body is completed with the boundary conditions.

Heaviside step function, which is defined as

$$\mathcal{H}_{\Gamma_d} = \begin{cases} 1 & \text{if } \mathbf{x} \in \Omega^+ \\ 0 & \text{if } \mathbf{x} \in \Omega^- \end{cases}. \quad (2.2)$$

The strain field ϵ results from differentiating the displacement field (2.1) with respect to material point \mathbf{x} with the assumption of small strain theory

$$\epsilon(\mathbf{x}, t) = \nabla^s \hat{\mathbf{u}}(\mathbf{x}, t) + \mathcal{H}_{\Gamma_d} \nabla^s \tilde{\mathbf{u}}(\mathbf{x}, t), \quad \mathbf{x} \notin \Gamma_d. \quad (2.3)$$

Here, ∇^s is the symmetric part of the differential operator

$$\nabla^s \mathbf{u} = \frac{1}{2} (\nabla \mathbf{u} + (\nabla \mathbf{u})^T). \quad (2.4)$$

The strain is undefined at the discontinuity surface Γ_d . Here, the opening of the discontinuity is the governing kinematic quantity, which is equal to the jump in the displacement field

$$[\mathbf{u}(\mathbf{x}, t)] = \tilde{\mathbf{u}}(\mathbf{x}, t), \quad \mathbf{x} \in \Gamma_d. \quad (2.5)$$

The pressure field contains a weak discontinuity over the fracture. The gradient of this pressure difference quantifies the interaction of fluid flow between the fracture and the formation. By enhancing the pressure field with a signed distance function, as was used by Réthoré et al. (2007), the gradient near a discontinuity is taken into account in a natural way

$$p(\mathbf{x}, t) = \hat{p}(\mathbf{x}, t) + \mathcal{D}_{\Gamma_d}(\mathbf{x}) \tilde{p}(\mathbf{x}, t), \quad (2.6)$$

where the distance function $\mathcal{D}_{\Gamma_d}(\mathbf{x})$ is defined as

$$\mathcal{D}_{\Gamma_d}(\mathbf{x}) = |(\mathbf{x} - \mathbf{x}_{\Gamma_d}) \cdot \mathbf{n}_d| \quad \mathbf{x} \in \Omega. \quad (2.7)$$

Here, \mathbf{x}_{Γ_d} is the coordinate of the nearest point on the discontinuity and \mathbf{n}_d is the corresponding normal vector. The pressure gradient follows from the spatial derivative of the pressure field (2.6)

$$\nabla p(\mathbf{x}) = \nabla \hat{p}(\mathbf{x}) + \mathcal{D}_{\Gamma_d}(\mathbf{x}) \nabla \tilde{p}(\mathbf{x}) + \nabla \mathcal{D}_{\Gamma_d}(\mathbf{x}) \tilde{p}(\mathbf{x}), \quad (2.8)$$

where the gradient of the distance function \mathcal{D}_{Γ_d}

$$\nabla \mathcal{D}_{\Gamma_d}(\mathbf{x}) = \begin{cases} \mathbf{n}_d & \text{if } \mathbf{x} \in \Omega^+ \\ -\mathbf{n}_d & \text{if } \mathbf{x} \in \Omega^-. \end{cases} \quad (2.9)$$

2.2 Balance equations

The system is described by two balance equations: the balance of linear momentum and the mass balance. In the following, the weak form of both balance equations will be derived for both the bulk material and the interface.

The porous solid skeleton is considered to be fully saturated with a fluid. We assume that there is no mass transfer between the two constituents. The process is isothermal and gravity, inertia and convection are neglected. With these assumptions the linear momentum balance reads

$$\nabla \cdot \boldsymbol{\sigma} = \mathbf{0}, \quad (2.10)$$

where $\boldsymbol{\sigma}$ is the total stress which is decomposed in Terzaghi's effective stress $\boldsymbol{\sigma}_e$ and the hydrostatic pressure p (Terzaghi, 1943)

$$\boldsymbol{\sigma} = \boldsymbol{\sigma}_e - p\mathbf{I}. \quad (2.11)$$

In this equation \mathbf{I} is the unit matrix. The effective stress $\boldsymbol{\sigma}_e$ is related to the strains $\boldsymbol{\epsilon}$ which have been defined in (2.3) by means of the constitutive law. In rate form, this reads

$$\dot{\boldsymbol{\sigma}}_e = \mathbf{C}\dot{\boldsymbol{\epsilon}}. \quad (2.12)$$

The momentum balance is completed with the following boundary conditions, see Figure 2.1.

$$\begin{aligned} \boldsymbol{\sigma} \cdot \mathbf{n}_\Gamma &= \mathbf{t}_p(\mathbf{x}, t), & \mathbf{x} \in \Gamma_t, \\ \mathbf{u}(\mathbf{x}, t) &= \mathbf{u}_p(\mathbf{x}, t), & \mathbf{x} \in \Gamma_u, \end{aligned} \quad (2.13)$$

with $\Gamma_t \cup \Gamma_u = \Gamma$, $\Gamma_t \cap \Gamma_u = \emptyset$.

Under equal assumptions as made for the momentum balance, and assuming the fluid to be incompressible, the mass balance is written as

$$\nabla \cdot \mathbf{v}_s + \nabla \cdot \mathbf{q} = 0, \quad (2.14)$$

where \mathbf{v}_s is the deformation velocity of the solid skeleton and \mathbf{q} is the seepage flux, which is related to the pressure gradient by means of Darcy's law: Darcy's relation is assumed to hold for the fluid flow in the bulk material (Biot, 1941)

$$\mathbf{q} = -\mathbf{k} \cdot \nabla p, \quad (2.15)$$

where \mathbf{k} is the permeability tensor, which is assumed to be constant in time and space (Kraaijeveld and Huyghe, 2011). In the case of an isotropic material, the permeability is equal to:

$$\mathbf{k} = k\mathbf{I} = \frac{k_{\text{int}}}{\mu}\mathbf{I}, \quad (2.16)$$

where k_{int} is the intrinsic permeability and μ is the dynamic viscosity (Detournay and Cheng, 1993). The mass balance is completed with the following boundary conditions, see Figure 2.1.

$$\begin{aligned} \mathbf{q}(\mathbf{x}, t) \cdot \mathbf{n}_\Gamma &= f_f, & \mathbf{x} \in \Gamma_f, \\ p(\mathbf{x}, t) &= p_p, & \mathbf{x} \in \Gamma_p, \end{aligned} \quad (2.17)$$

with $\Gamma_q \cup \Gamma_p = \Gamma$, $\Gamma_f \cap \Gamma_p = \emptyset$.

In accordance with the cohesive zone approach, the softening of the material is governed by a traction acting on the discontinuity surface. This traction is coupled to the hydrostatic pressure in the crack. Assuming continuity of stress from the formation to the fracture we can write the local momentum balance as

$$\boldsymbol{\sigma} \cdot \mathbf{n}_d = \mathbf{t}_d - p_d \mathbf{n}_d, \quad (2.18)$$

where p_d is the hydrostatic pressure in the discontinuity

$$p_d = p(\mathbf{x} \in \Gamma_d) \quad (2.19)$$

Mass balance is described by an equilibrium of fluid exchange between the formation and the fracture, the opening rate of the fracture, and the tangential fluid flow in the fracture. This is written as

$$\mathbf{q}_{\Gamma_d}^+ \cdot \mathbf{n}_d - \mathbf{q}_{\Gamma_d}^- \cdot \mathbf{n}_d = -\dot{u}_n + u_n \frac{\partial}{\partial s} \left(k_d \frac{\partial p_d}{\partial s} \right), \quad (2.20)$$

with $\mathbf{q}_{\Gamma_d}^+$ and $\mathbf{q}_{\Gamma_d}^-$ being the fluid flow from the fracture into formation for the fracture lip of the Ω^+ and the Ω^- domain, respectively, \dot{u}_n denotes the time derivative of the normal opening of the fracture and k_d being the permeability in the fracture. The latter is given by Witherspoon et al. (1980):

$$k_d = \frac{u_n^2}{12\mu}, \quad (2.21)$$

where μ is the viscosity of the fluid. For the derivation of this equilibrium equation, we refer to Irzal et al. (2013). In Equation (2.20) we used, under the assumption of small deformations, that the normal vector of the two fracture lips is in opposite direction.

The weak form of the balance equation is obtained by multiplying Eqs.(2.10) and (2.14) with an admissible displacement and pressure field, $\boldsymbol{\eta}$ and ζ , respectively. These admissible fields have the same form as the original fields

$$\boldsymbol{\eta} = \hat{\boldsymbol{\eta}} + \mathcal{H}_{\Gamma_d} \tilde{\boldsymbol{\eta}}, \quad \zeta = \hat{\zeta} + \mathcal{D}_{\Gamma_d} \tilde{\zeta}. \quad (2.22)$$

Substituting the variations into Eqs. (2.10) and (2.14), Applying Gauss's theorem, using the symmetry of the Cauchy stress tensor, introducing the internal boundary Γ_d and the corresponding admissible displacement jump and using the boundary conditions at the external boundaries Γ_t and Γ_f gives

$$\begin{aligned} \int_{\Omega} \nabla \hat{\boldsymbol{\eta}} : \boldsymbol{\sigma} d\Omega + \int_{\Omega} \mathcal{H}_{\Gamma_d} \nabla \tilde{\boldsymbol{\eta}} : \boldsymbol{\sigma} d\Omega = \\ \int_{\Gamma_t} \hat{\boldsymbol{\eta}} \cdot \mathbf{t}_p d\Gamma_t + \int_{\Gamma_t} \mathcal{H}_{\Gamma_d} \tilde{\boldsymbol{\eta}} \cdot \mathbf{t}_p d\Gamma_t - \int_{\Gamma_d} \tilde{\boldsymbol{\eta}} \cdot (\boldsymbol{\sigma} \cdot \mathbf{n}_d) d\Gamma_d \end{aligned} \quad (2.23)$$

$$\begin{aligned} - \int_{\Omega} \hat{\zeta} \nabla \cdot \mathbf{v}_s d\Omega - \int_{\Omega} \mathcal{D}_{\Gamma_d} \tilde{\zeta} \nabla \cdot \mathbf{v}_s d\Omega + \int_{\Omega} \nabla(\hat{\zeta}) \cdot \mathbf{q} d\Omega \\ + \int_{\Omega} \nabla(\mathcal{D}_{\Gamma_d} \tilde{\zeta}) \cdot \mathbf{q} d\Omega = \\ \int_{\Gamma_f} \hat{\zeta} f_f d\Gamma_f + \int_{\Gamma_f} \mathcal{D}_{\Gamma_d} \tilde{\zeta} f_f d\Gamma_f - \int_{\Gamma_d} \hat{\zeta} \mathbf{q}_{\Gamma_d}^+ \cdot \mathbf{n}_d d\Gamma + \int_{\Gamma_d} \hat{\zeta} \mathbf{q}_{\Gamma_d}^- \cdot \mathbf{n}_d d\Gamma. \end{aligned} \quad (2.24)$$

In these equations, \mathbf{t}_p and f_f are the prescribed traction and prescribed fluid outflow boundary conditions, respectively (Figure 2.1) and Γ_d represents the integral over the internal boundary of the discontinuity. The terms $\boldsymbol{\sigma} \cdot \mathbf{n}_d$, $\mathbf{q}_{\Gamma_d}^+ \cdot \mathbf{n}_d$ and $\mathbf{q}_{\Gamma_d}^- \cdot \mathbf{n}_d$ are given by the balance Equations at the discontinuity (2.18) and (2.20). By taking one of the admissible variations

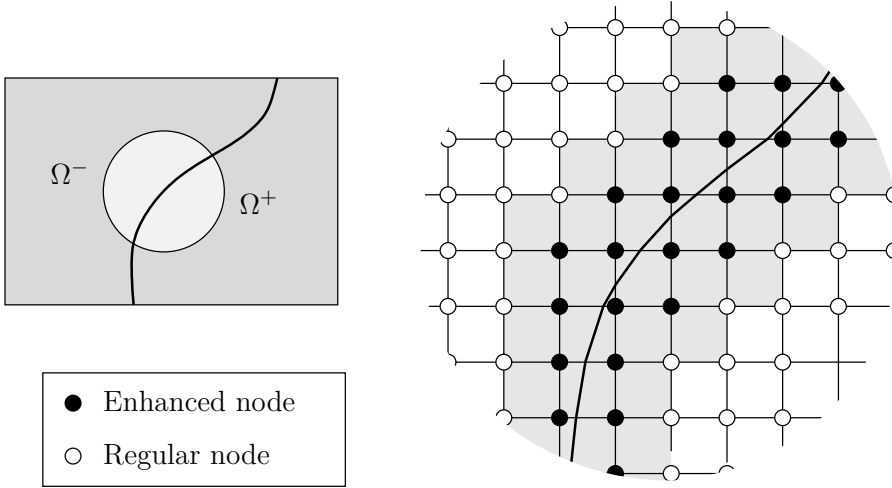


Figure 2.2: A two dimensional finite element mesh crossed by a discontinuity represented by the black line. The black nodes surrounding the discontinuity are enhanced with additional degrees of freedom. The grey elements therefore contain additional terms in the stiffness matrix and the force vector.

$\delta\hat{\eta}$, $\delta\tilde{\eta}$, $\delta\hat{\zeta}$ and $\delta\tilde{\zeta}$ at the time, the weak form of equilibrium can be separated into four sets of equations. A detailed description is given in (Réthoré et al., 2007; Wells and Sluys, 2001).

2.3 Discretization and numerical implementation

The spatial discretization of the system of equations is based on the partition of unity property of finite element shape functions (Melenk and Babuška, 1996). Using this property, the fracture is included in the FEM by adding a additional degrees of freedom to the finite element nodes surrounding the fracture (Figure 2.2). These additional degrees of freedom have the form of the additional terms in the field Equations (2.1) and (2.6) for the displacement and the pressure, respectively. The time discretization is performed using an implicit Euler time scheme. The resulting system is non-linear and is therefore solved with a Newton-Raphson iterative procedure. A detailed derivation and description is given in (Irzal et al., 2013; Kraaijeveld and Huyghe, 2011; Réthoré et al., 2007).

The numerical implementation is based on and described in detail in the work of (Remmers, 2006; Remmers et al., 2008). The most import aspects will be recaptured in this section. In addition, the new implementations of the nucleation of cracks and the propagation of cracks in transverse

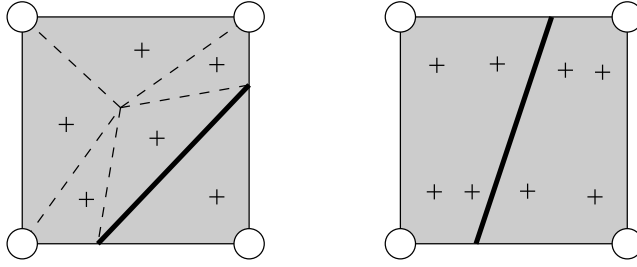


Figure 2.3: Numerical integration of a quadrilateral element crossed by a discontinuity.

isotropic materials are introduced.

Consider a finite element domain crossed by a discontinuity as shown in Figure 2.2. A structured mesh containing four nodal elements is used in this chapter. Additional degrees of freedom are added to the black nodes which are crossed by the discontinuity. It is assumed that the discontinuity within an element is a straight line, always ends at an element edge, and is referred to as a cohesive segment. The numerical integration is performed by the standard Gauss integration. However, only using the original integration points is not sufficient any more since the discontinuity can cross an element at an arbitrary location. To acquire sufficient integration points at each side of the discontinuity, an integration method (Figure 2.3) introduced by Wells and Sluys (2001), is used. Two integration points per element are located at the discontinuity to integrate the discretized local balance equations.

To govern the propagation of a fracture, a fracture criterion is needed to determine the moment and the direction of propagation. The stress state at the crack tip is estimated based on the average stress in the vicinity of the tip. The averaging is calculated with a Gaussian weighting function (Jirásek, 1998). The average stress σ_{av} at the crack tip is then the weighted sum of the stress in the integration points near the crack tip

$$\sigma_{av} = \sum_{i=1}^{n_{int}} \frac{w_i}{w_{tot}} \sigma_{e,i} \quad \text{with} \quad w_{tot} = \sum_{j=1}^{n_{int}} w_j. \quad (2.25)$$

Here n_{int} is the number of integration points in the domain, $\sigma_{e,i}$ is the current effective stress state in integration point i which has a weight factor w_i defined as

$$w_i = \frac{(2\pi)^{-\frac{3}{2}}}{l_a^3} e^{-\frac{r_i^2}{2l_a^2}}, \quad (2.26)$$

with r_i being the distance between the crack tip and the integration point

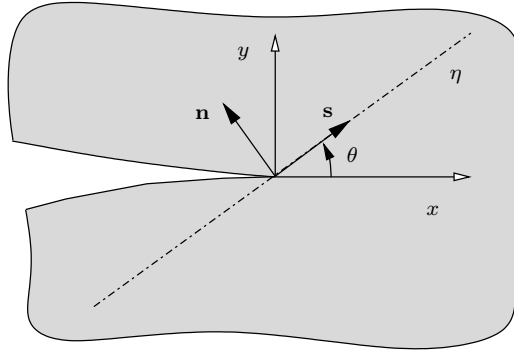


Figure 2.4: Schematic representation of a material with at the crack tip the global x-y coordinate system and the local coordinate system, described with a normal unit vector \mathbf{n} and a tangential unit vector \mathbf{s} .

n_i , and l_a being a length scale parameter defining how fast the weight factor decays as a function of the distance between the integration points and the crack tip. As was proposed by Remmers et al. (2008), the average stress surrounding the crack tip is used to determine both the moment and the direction of propagation. From this average stress, an equivalent traction t_{eq} at the crack tip is calculated (Camacho and Ortiz, 1996)

$$t_{\text{eq}}(\theta) = \sqrt{\langle t_n \rangle^2 + \frac{1}{\beta} t_s^2} \quad \text{with} \quad \langle t_n \rangle = \begin{cases} 0 & \text{if } t_n \leq 0 \\ t_n & \text{if } t_n > 0 \end{cases}, \quad (2.27)$$

where β is a scaling factor for the shear stress, t_n and t_s are the normal and shear traction, respectively

$$t_n = \mathbf{n}^T \boldsymbol{\sigma}_{\text{av}} \mathbf{n} \quad t_s = \mathbf{s}^T \boldsymbol{\sigma}_{\text{av}} \mathbf{n}. \quad (2.28)$$

Here \mathbf{n} is the normal vector and \mathbf{s} is the tangent vector to an axis η which is rotated by an angle θ with respect to the x-axis (Figure 2.4). If the maximum equivalent traction exceeds the ultimate strength τ_{ult} of the material the fracture is extended in the direction of angle θ through one element.

The disadvantage of using an average stress in the fracture criterion is that the crack propagation can be slightly delayed due to the averaging of the stress. The advantage is that the direction of propagation is more reliable since it is based on a global stress state. However, the initial traction in the discontinuity will also be underestimated (Remmers et al., 2008). To avoid this two different length scale parameters l_a are used,

see Equation (2.26). The moment and direction of fracture propagation are determined by a length scale parameter which is typically three times the element length (Wells and Sluys, 2001), while the initial tractions are calculated with one fourth of this length scale.

The average stress criterion based on the equivalent traction in Equation (2.27) is also used to determine the moment of fracture nucleation. Instead of calculating this criterion in each integration, which would be computationally inefficient, an additional checkpoint is added in the centre of each element (Figure 2.5). Once the equivalent traction in one of the checkpoints exceeds the nucleation criterion a discontinuity is added. The cohesive segment is assumed to be straight and crosses the checkpoint under the angle θ with respect to the x-axis. The cohesive zone of the nucleated crack must have a length of at least one element. The numerical implementation of this restriction is illustrated in Figure 2.5 with three examples. If the nucleation criterion is exceeded in multiple checkpoints at the same time, nucleations occurs in the checkpoint with the highest equivalent traction.

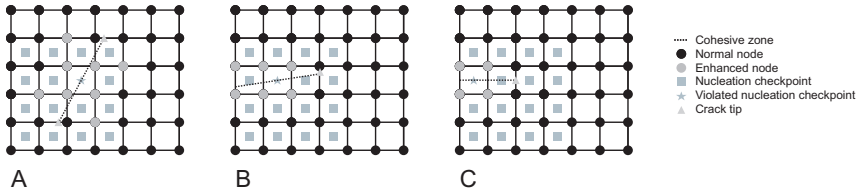


Figure 2.5: Three different locations of nucleation checkpoints with corresponding cohesive zones.

2.3.1 Fracture propagation in an orthotropic material

The structure of an orthotropic material induces anisotropic fracture properties. We assume the strongest direction of the orthotropic material as a fibre direction. Following Yu et al. (2002) we can define a directional depended ultimate strength as

$$\tau_{\text{ult}}(\alpha) = \tau_{\text{min}} + (\tau_{\text{max}} - \tau_{\text{min}}) \cos(\alpha)^2, \quad (2.29)$$

here α is the angle between the fibres and normal \mathbf{n} of the fracture, τ_{max} is the ultimate strength in the fibre direction, and τ_{min} is the ultimate strength perpendicular to the fibre direction (Figure 2.6). To determine if the equivalent traction (2.27) at angle θ exceeds the fracture criterion it is necessary to express Equation (2.29) in terms of θ

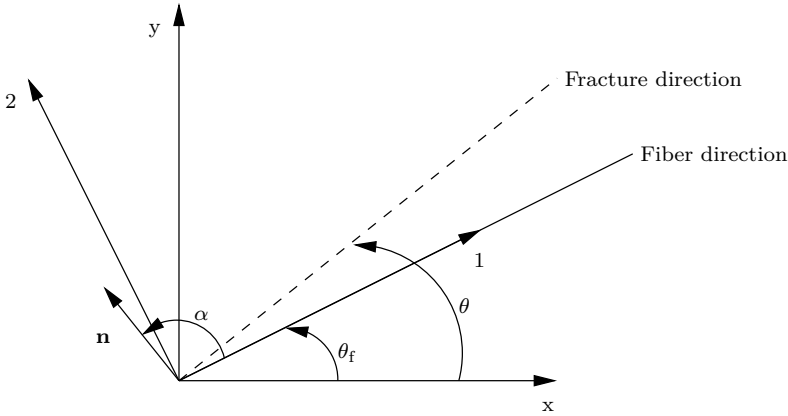


Figure 2.6: Schematic representation of a fracture under an angle θ in an orthotropic isotropic material. The strength of the material defined by a fibre direction θ_f . The angle α is the angle between the fibre direction and the normal \mathbf{n} of the fracture.

$$\tau_{\text{ult}}(\theta) = \tau_{\text{min}} + (\tau_{\text{max}} - \tau_{\text{min}}) \cos\left(\theta + \frac{1}{2}\pi - \theta_f\right)^2. \quad (2.30)$$

In the orthotropic material a fracture propagates or initiates if

$$\frac{t_{\text{eq}}(\theta)}{\tau_{\text{ult}}(\theta)} > 1. \quad (2.31)$$

2.4 Constitutive equations

The mathematical formulation of the balance equations are completed by constitutive behaviour for the bulk material and the fracture. The constitutive relation for an orthotropic bulk material is also given.

2.4.1 Mechanical behaviour of the orthotropic bulk

In this paragraph we describe the constitutive behaviour of a special orthotropic material; a transverse isotropic material. Transverse isotropy is a common form of anisotropy in rock formations but is also present in many biological materials (Abousleiman et al., 1996; Weiss et al., 1996). A transverse isotropic material is an orthotropic material with one axis of material rotational symmetry. We assume that the strength of the transverse isotropic material is highest in the direction of the axis of rotational

symmetry. Defining this direction again as the fibre direction, the isotropic relationships for the effective stress are replaced by

$$\begin{pmatrix} \sigma_{11} \\ \sigma_{22} \\ \sigma_{12} \end{pmatrix} = \mathbf{C} \begin{pmatrix} \epsilon_{11} \\ \epsilon_{22} \\ \gamma_{12} \end{pmatrix}, \quad (2.32)$$

where the stress components σ and the strain components ϵ are defined in a local coordinate system (1, 2), as shown in Figure 2.6. The [3x3] stiffness matrix \mathbf{C} is defined as

$$\mathbf{C} = \begin{pmatrix} \frac{E_{11}^2(1-\nu_{23})}{E_{11}(1-\nu_{23})-2E_{22}\nu_{12}^2} & \frac{E_{11}E_{22}\nu_{12}}{E_{11}(1-\nu_{23})-2E_{22}\nu_{12}^2} & 0 \\ \frac{E_{11}E_{22}\nu_{12}}{E_{11}(1-\nu_{23})-2E_{22}\nu_{12}^2} & \frac{E_{22}(E_{11}-E_{22}\nu_{12}^2)}{(1+\nu_{23})[E_{11}(1-\nu_{23})-2E_{22}\nu_{12}^2]} & 0 \\ 0 & 0 & G_{12} \end{pmatrix}. \quad (2.33)$$

In this equation, E_{11} and E_{22} are Young's moduli, ν_{12} and ν_{23} are the Poisson's ratios representing the compressive strain in the direction of the second subscript due to a tensile stress in the direction of the first subscript, and G_{12} is the shear modulus in the 1-2 plane. Here, based on symmetry, the following identity was used

$$\frac{\nu_{12}}{E_{11}} = \frac{\nu_{21}}{E_{22}}. \quad (2.34)$$

The permeability is also a parameter depending on direction in an orthotropic material (Abousleiman et al., 1996). We also describe the fluid flow in an orthotropic material by Darcy's law Eq. (2.15), with the permeability tensor \mathbf{k} being defined as

$$\mathbf{k} = \begin{pmatrix} k_1 & 0 \\ 0 & k_2 \end{pmatrix} \quad (2.35)$$

where k_1 and k_2 are the permeabilities in the direction of the subscript.

2.4.2 Mechanical behaviour in the fracture

The constitutive mechanical behaviour at the discontinuity is given by a relation between the traction at the interface and the displacement jump \mathbf{u}_d across the discontinuity (Irzal et al., 2013)

$$\mathbf{t}_d = \mathbf{t}_d(\mathbf{u}_d, \kappa). \quad (2.36)$$

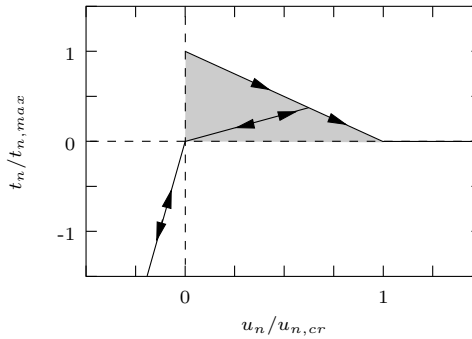
Here κ is a history parameter that is equal to the largest displacement jump reached. The relation between the traction \mathbf{t}_d and the displacement jump

\mathbf{u}_d can be any phenomenological relation, see e.g. (Shet and Chandra, 2002), and is referred to as a cohesive law.

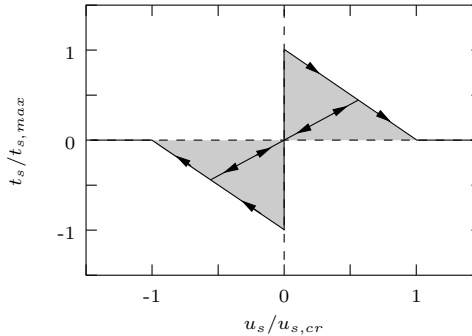
The initial normal and shear tractions, respectively written as t_{n0} and t_{s0} , are taken to be equal to the normal and shear traction at the moment of propagation (2.28) in order to avoid sudden jumps in the stress. Based on the work of Camacho and Ortiz (1996) a distinction is made between normal and shear softening behaviour. If the initial normal traction is positive the discontinuity is assumed to open as a cleavage crack. The normal and shear tractions then decay linearly to zero from their initial values as a function of the normal opening of the crack (Figure 2.7)

$$t_n = t_{n0} \left(1 - \frac{u_n}{u_{n,cr}}\right) \quad t_s = t_{s0} \left(1 - \frac{u_n}{u_{n,cr}}\right) \text{sgn}(u_s). \quad (2.37)$$

Here u_n and u_s are respectively the normal and sliding the displacement, $\text{sgn}(\cdot)$ is the signum function.



(a) Tensile crack.



(b) Shear crack.

Figure 2.7: The normalised tractions across the discontinuity as a function of the displacement jump in: (a) a cleavage crack and (b) a shear crack.

The parameter $u_{n_{cr}}$ is the length of the fully developed traction-free crack. This parameter depends on the fracture toughness \mathcal{G}_c , which is the area under the softening curve, and the initial normal traction t_{n_0}

$$u_{n_{cr}} = \frac{2\mathcal{G}_c}{t_{n_0}}. \quad (2.38)$$

The traction separation relations for unloading and shear opening are described in detail in (Camacho and Ortiz, 1996). Self-contact of the fracture is simulated by using a penalty stiffness method.

It is necessary to perform a linearisation on Eq.(2.36) in order to use the tangential stiffness matrix in an incremental iterative solution

$$\Delta \mathbf{t}_d = \mathbf{T} \Delta \mathbf{u}_d. \quad (2.39)$$

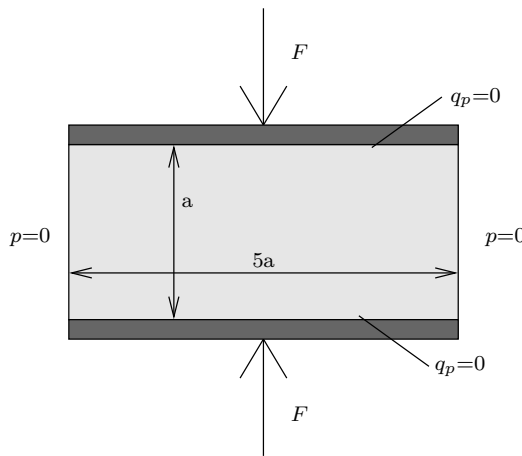


Figure 2.8: Scheme and result of the Mandel-Cryer benchmark

2.5 Examples

In the first two examples the accuracy of the model for an isotropic and a transverse isotropic material is analysed in an unconfined compression test. An analytical solution is available for both problems. In the last two examples the performance of the numerical model is investigated by simulating fracture propagation in a transverse isotropic material and by a mixed mode fracture problem. All examples are two dimensional in a plane strain setting. The mesh consists of quadrilateral elements with bilinear

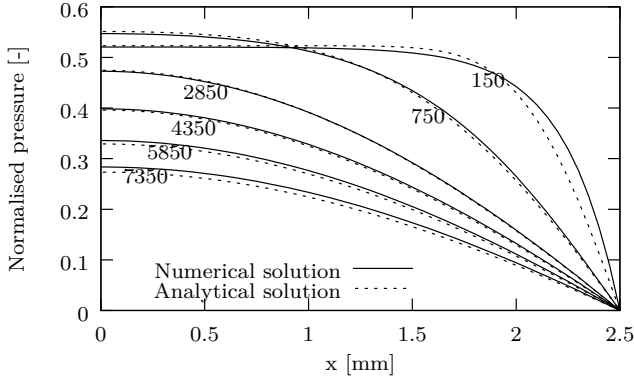


Figure 2.9: Normalised pressure $\frac{5a}{F}p$ over the sample in x-direction, where $x = 0$ is in the centre. The numbers drawn in the line indicate the time in seconds. Analytical solution from Mandel (1953).

shape functions for both the displacement and the pressure. This interpolation order means we violate the Babuška-Brezzi condition (Brezzi, 1974). However, no adverse effects of the violation have been observed in the numerical results.

2.5.1 Unconfined compression

The accuracy of the poro-elastic model is tested by considering the Mandel-Cryer benchmark (Cryer, 1963; Mandel, 1953). In the Mandel-Cryer problem an infinitesimal long plate, considered under plane strain conditions, is rigidly compressed by a force of $F = 0.1$ N. (Figure 2.8). The specimen dimension is taken as $a = 1$ mm. The material parameters are given in table 2.1. The squared elements have a size of 0.05 mm and the time step is 150 s. Free drainage is assumed at the lateral sides of the specimen. Due to the drainage a pore pressure decrease occurs, leading to a loss of stiffness at the sides. To compensate for this loss, the pore pressure rises in the undrained centre of the specimen. This non-monotonic pressure response characterizes the Mandel-Cryer problem. The normalised pore pressure across the specimen in the x-direction is shown in Figure 2.9. The numerical pore pressure is consistent with the analytical solution.

E	$=$	1.5	[Mpa]	ν	$=$	0.2	[-]
k	$=$	2.8e-4	[mm ⁴ /Ns]				

Table 2.1: Model Parameters used in the isotropic Mandel-Cryer benchmark

The isotropic solution for the Mandel-Cryer problem was extended to transverse isotropic materials by Abousleiman et al. (1996). This analytical solution is used to determine the accuracy of the numerical model for a transverse isotropic material. The benchmark problem is similar than that in the isotropic case (Figure 2.8). The transverse isotropic material has a higher stiffness in the vertical direction ($\theta_f = 90^\circ$). The material parameters are given in table 2.2. The anisotropic permeability has no influence on the analytical solution. Therefore, we consider the permeability also isotropic in this example. The numerical result for the anisotropic Mandel-Cryer problem is also consistent with the analytical solution (Figure 2.10).

E_{11}	=	15.0	[Mpa]	ν_{12}	=	0.30	[-]	θ_f	=	90°	[-]
E_{22}	=	1.5	[Mpa]	ν_{23}	=	0.18	[-]	k	=	$2.0e-5$	[mm ⁴ /Ns]

Table 2.2: Model Parameters used in the anisotropic Mandel-Cryer benchmark

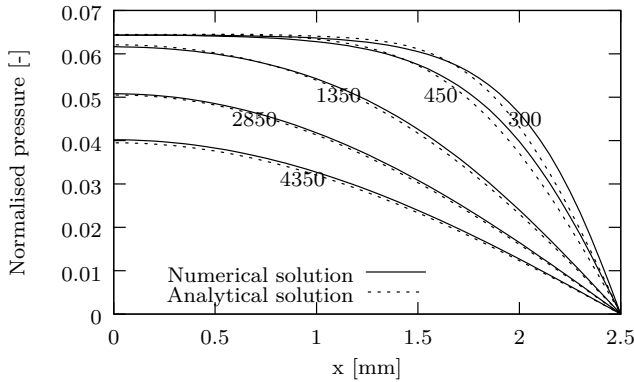


Figure 2.10: Normalised pressure $\frac{5a}{F}p$ over the sample in x-direction, where $x = 0$ is in the centre. The numbers drawn in the line indicate the time in seconds. Analytical solution from Abousleiman et al. (1996).

2.5.2 Fracture propagation in a transverse isotropic material

To illustrate the performance of the numerical model for a fracture propagating in a transverse isotropic material a mode I fracture is considered (Figure 2.11). Free drainage ($p = 0$) is assumed at the sides of the specimen. An initial fracture with a length of 5.0 mm is created in the centre and the anisotropic stiffness taken as $\theta_f = 70^\circ$. The top and bottom surface are pulled with a constant velocity $v = 5.0e^{-6}$ mm/s in vertical direction

while the displacement in horizontal direction is constrained. The element length is 0.20 mm and a time step of 50 s is used. The average stress is scaled by parameter $l_a = 0.6$ mm. An overview of the material parameters are given in table 2.3.

A small influence of the transversal permeability can be seen in the pressure distribution before propagation occurs (Figure 2.12a). The pressure gradient is aligned with the direction of the low permeability. Using the adapted propagation criterion (2.30) for anisotropic materials, the crack grows parallel to the anisotropic stiffness (Figure 2.12b). This is a result of the values for τ_{\max} and τ_{\min} but does represent the propagation of a fracture in a transverse isotropic material.

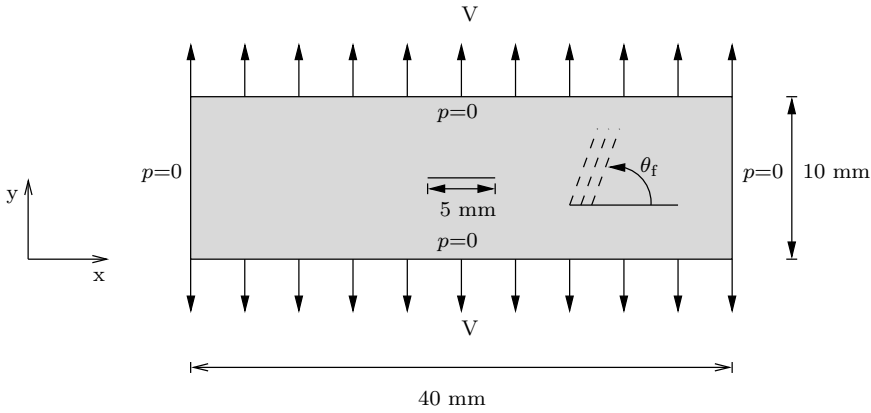


Figure 2.11: A rectangular plate of porous material with an initial crack. The material is transverse isotropic with $\theta_f = 70^\circ$.

E_{11}	=	90.0	[MPa]	θ_f	=	70	[°]	τ_{\min}	=	0.004	[MPa]
E_{22}	=	15.0	[MPa]	k_1	=	7.5e-3	[mm ⁴ /Ns]	\mathcal{G}_c	=	0.00001	[N/mm]
ν_{12}	=	0.30	[-]	k_2	=	7.5e-4	[mm ⁴ /Ns]	β	=	2.3	[-]
ν_{23}	=	0.18	[-]	τ_{\max}	=	0.40	[MPa]	μ	=	1.0e-4	[Pa · s]

Table 2.3: Model Parameters used in the anisotropic Mode 1 fracture simulation.

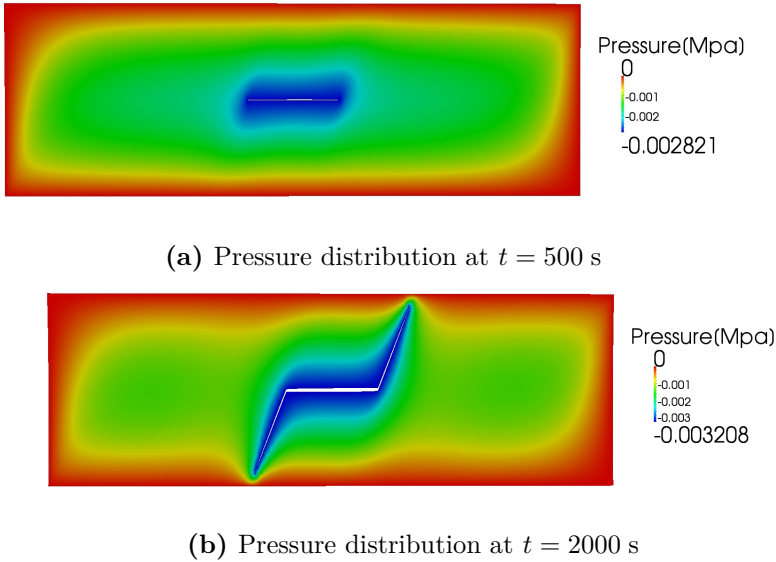


Figure 2.12: Visualization of the pressure distribution. The displacements are amplified by a factor 10.

2.5.3 Mixed mode fracture

The performance of the numerical model is analysed considering a mixed mode fracture in a L-shaped porous material (Figure 2.13). This type of problem has been investigated experimentally by Winkler (2001) in a concrete material and was successfully reproduced using solid mechanics X-FEM (Dumstorff and Meschke, 2007; Unger et al., 2007). In this example we consider a soft porous material with a Young's modulus of 90.0 MPa and a permeability of $7.5e^{-3}$ mm⁴/Ns. The time step is 300 s and the element length is 10.0 mm. The average stress parameter is taken as $l_a = 30.0$ mm. Further material parameters are given in table 2.4. The specimen is constrained in both directions at the bottom surface. At the right surface free drainage is prescribed while the other surfaces are impervious. There is no initial crack present in the material so the nucleation point will be determined numerically. A velocity $U = 2.5e^{-4}$ mm/s is prescribed at a distance of 30 mm of the boundary at the middle surface.

The early pressure distribution can be seen in Figure 2.14a. The prescribed displacement induces a positive pressure near the loading point. At the middle surface a negative pressure arises due to extension. This leads to fluid flow towards this region (Figure 2.15). Fracture nucleation takes place, as expected, at the central corner and results in a negative pressure

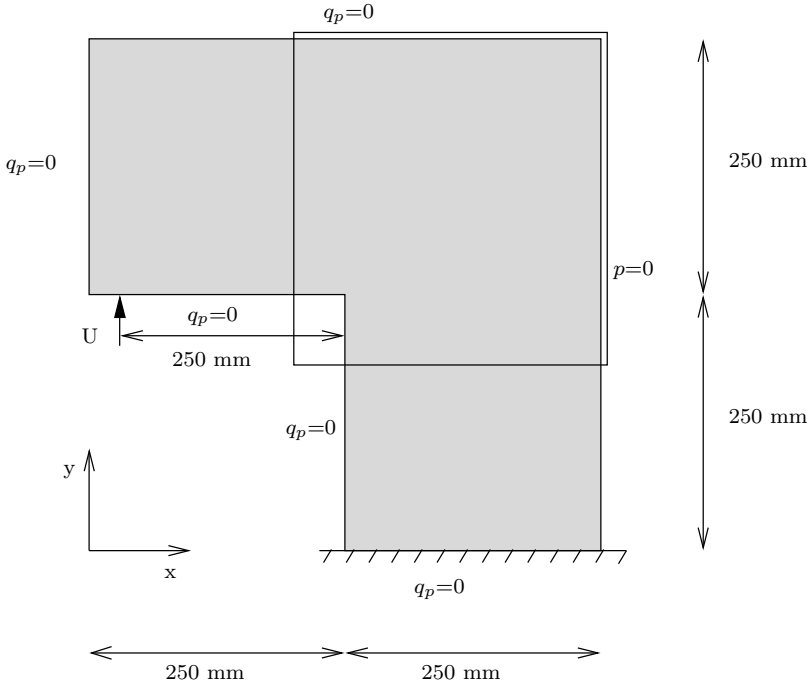


Figure 2.13: Schematic representation of the L-shaped fracture problem

E	$= 90$	[Mpa]	β	$= 2.3$	[-]
ν	$= 0.18$	[-]	τ_{ult}	$= 0.2$	[MPa]
k	$= 7.5e^{-3}$	[mm ⁴ /Ns]	\mathcal{G}_c	$= 0.15$	[N/mm]
μ	$= 1.0e^{-4}$	[Pa · s]			

Table 2.4: Material properties L-shaped mixed mode test.

surrounding the fracture (Figure 2.14b). The negative pressure is generated by the triaxial stress state near the fracture tip (Anderson, 2005). This stress is first taken up by the fluid resulting in negative pore pressure. The pressure profiles at two later time points can be seen in Figures 2.14c and 2.14d. The low pressure surrounding the fracture leads to fluid flow from the formation into the fracture (Figure 2.16). Immediately after fracture nucleation occurred, closing of the fracture took place. This is a result of the initial traction present in the nucleated fracture. To prevent this, the initial traction in the element at the mesh border is neglected.

To further investigate the performance of numerical model the same simulation is repeated with two different permeabilities. Permeability values of $7.5e^{-2}$ mm⁴/Ns and 7.5 mm⁴/Ns are used. The permeability has

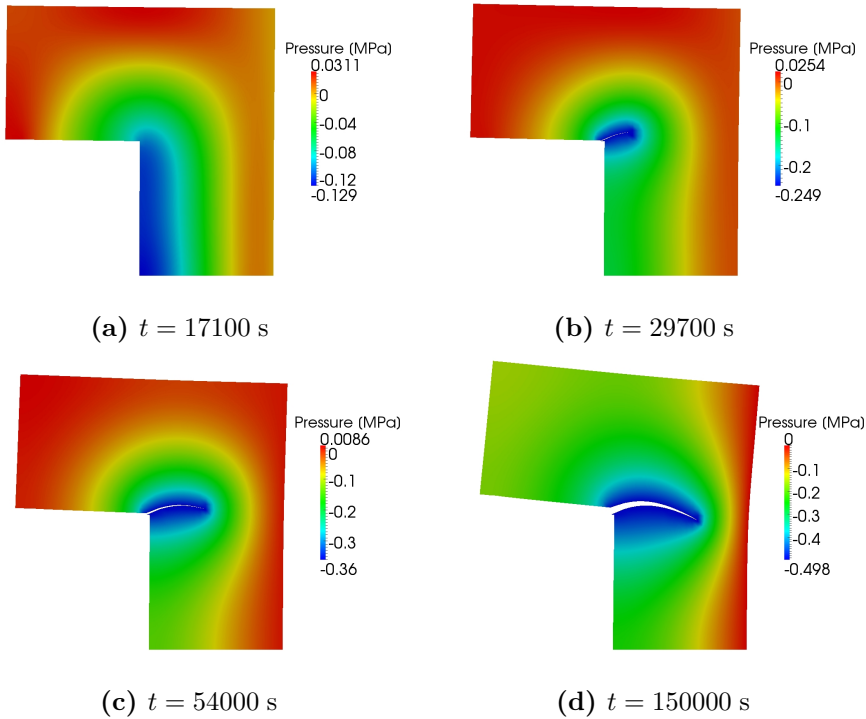


Figure 2.14: Pressure distribution of the L-shaped mixed mode fracture

an influence on the moment of fracture nucleation, on the fracture propagation velocity and on the fracture pattern (Figure 2.17). The higher the permeability, the earlier a fracture nucleates. This phenomenon is a consolidation effect. The tensile stress near the nucleation point is initially carried by the fluid pressure. This results in a negative pressure and a fluid flow towards this point (Figures 2.14a and 2.15). There is a stress transfer from the fluid towards the solid skeleton as fluid flow progresses. Since the fluid flow is linearly depended on the permeability there is a faster stress transfer in a more permeable material. The fracture criterion is therefore exceeded earlier. For the same reason the fracture propagates faster in a highly permeable material.

We hypothesize that the bending of the crack is also correlated with the consolidation theory. The right part of the sample is in compression and fluid is squeezed out of this area resulting a slower tensile stress transfer. This effect is strengthened in case of a lower permeability. Therefore the fracture propagates downwards because the right side of the material compressed.

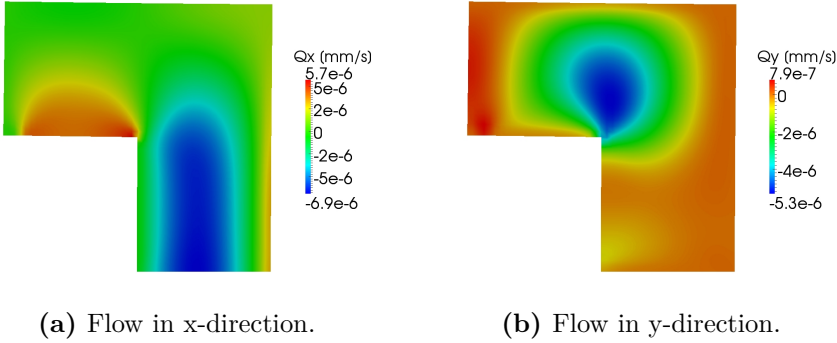


Figure 2.15: Flow (mm/s) distribution of the L-shaped mixed mode fracture at $t = 17100$ s

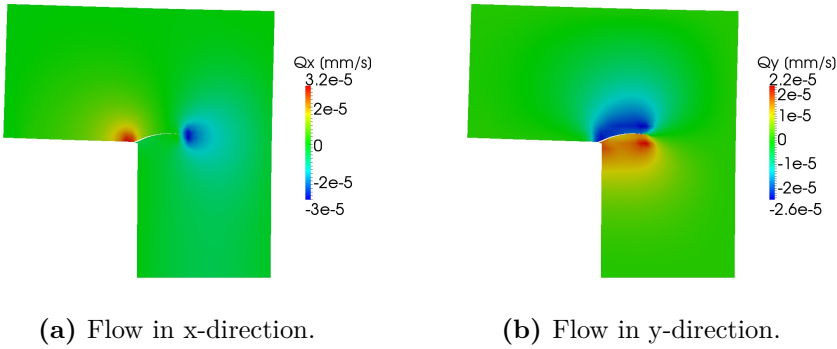


Figure 2.16: Flow (mm/s) distribution of the L-shaped mixed mode fracture at $t = 42300$ s.

2.6 Conclusions

We have extended two-dimensional numerical formulation for fracture propagation in porous materials to model nucleation in orthotropic materials. A fracture can grow in arbitrary directions by exploiting the partition of unity property of finite element shape functions. The direction of propagation is based on an average stress criterion surrounding the crack tip. This criterion is adapted for an orthotropic material by considering the directional stiffness of the material. The exchange of fluid between the formation and the fracture is accounted for. The tangential fluid flow in the fracture is included by the lubrication theory. The accuracy of the numerical model is investigated using the Mandel-Cryer Benchmark for both isotropic and transverse isotropic materials. The results show good consistency with the

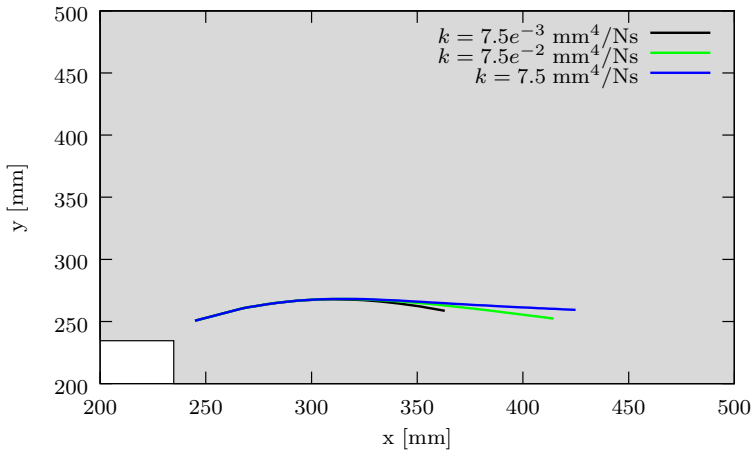


Figure 2.17: Crack path for 3 different permeability values at $t = 60000$ s. The graph is zoomed in at the grey box shown in Figure 2.13.

analytical solution.

In the transverse isotropic mode I fracture problem we successfully showed a propagating fracture in an anisotropic material. The pressure distribution is depending on the anisotropic permeability and the fracture direction is aligned with the highest strength direction of the material. The L-shaped problem demonstrates the possibility to use a poro-elastic partition of unity based cohesive zone model to simulate crack nucleation and subsequent mixed-mode growth in porous materials. The fracture path and propagation velocity are found to depend on the permeability of the bulk material. It shows the capability of our numerical model to respond to a change in a material parameter.

Simulations in this chapter are configured such that multiple time steps were necessary to propagate the crack through one element. This is required because the crack is restricted to grow through only one element within one time increment. In the next chapter the capability of the model to simulate fracture in a poro-elastic material is exploited again for shear failure but the crack growth is allowed to go through several elements in one time increment.

3

Investigation of step-wise propagation of a mode-II fracture in a poro-elastic medium

Abstract

In this chapter we use an extended finite element method based model for the simulation of shear fracture in fully saturated porous materials. The fracture is incorporated as a strong discontinuity in the displacement field by exploiting the partition of unity property of finite element shape functions. The pressure is assumed to be continuous across the fracture. However, the pressure gradient, i.e. the fluid flow, can be discontinuous. The failure process is described by the cohesive zone approach and a Tresca fracture condition without dilatancy. We investigate the propagation of a shear fracture under compression asking the question whether or not a Tresca criterion can result in stepwise propagation in a poro-elastic medium. In order to evaluate possible numerical artefacts, we also look at the influence of the element size and the magnitude of a time increment. The performance of the X-FEM model and the influence of the pore pressure on the fracture propagation are addressed. Our simulations do not show evidence for step wise progression in mode II failure.

In the previous chapter the basic framework for an eXtended Finite Element Method (X-FEM) based poro-elastic fracture model was derived. It was demonstrated that fracture path and propagation velocity are depended on the on the intrinsic permeability. In this chapter the model is applied to simulate shear failure which is the controlling mechanism in earthquakes. A major improvement to the model compared to the previous chapter lies in the numerical implementation where we now also have the possibility to cut multiple elements within one time increment. Due to this improvement the influence of mesh refinement near the fracture surface can be better addressed.

Earthquakes are generally attributed to stick-slip phenomena between sliding tectonic plates. As pointed out by Beroza and Ide (2009), the role of pore fluids in tremors and slow earthquakes observed e.g. in Cascadia (Rogers and Dragert, 2003) and Japan (Obara et al., 2004) is still to be worked out. Faulkner et al. (2006) suggest that fluid pressurisation may facilitate slipping of tectonic plates over each other. In the literature there is a vast body of research available on the experimental observation and numerical simulation of the initiation and propagation of cracks in solids (Xu and Needleman, 1994; Schlangen and van Mier, 1992; de Borst et al., 2004). The equations governing the coupling between fluid flow and deformation in fluid saturated media are also well known Lewis and Schrefler (1987). Nevertheless, literature on crack propagation through fluid saturated porous media is much scarcer.

In the past decades numerical models for fracture in porous materials, mainly developed for hydraulic fracturing, did arise. Most of these models are based on the Finite Element Method (FEM) either in combination with remeshing (Schrefler et al., 2006), with zero thickness interface elements (Carrier and Granet, 2012), or using partition of unity based approaches (Mohammadnejad and Khoei, 2013). Other type of models make use of the phase field approach (Wheeler et al., 2014) or are lattice based models (Grassl et al., 2015). These models differ in physics with earthquake models due to (i.) there is fluid being injected in the fracture and (ii.) the failure criterion is usually based on mode I failure while earthquakes are predominated by mode II failure.

In this chapter we will focus on shear failure in a poro-elastic material. The propagation of a shear band was shown by de Borst et al. (2006) using the eXtended Finite Element Method (X-FEM). A similar model, including osmotic effects, was used by Kraaijeveld and Huyghe (2011). It is shown in these papers that there exists an interaction between the propagation of a fracture and the pore pressure. In the latter work a serious deficiency arose

because the discontinuity could only propagate through one element per time increment. This has implications on the choice of the time increment and the mesh size. Compared to the numerical implementation of the previous chapter, the possibility to have the discontinuity propagate through multiple elements within one time increment is now included. We use this model to reconsider the work of Kraaijeveld et al. in this chapter.

In contrast to the work of Kraaijeveld et al. we assume a continuous pressure over the fracture. This means that we need finer meshes to correctly resolve pressure gradients near the fracture. The complete coupling between the solid and the fluid is described by Biot's theory. As an example we consider the same compression test as was performed by Kraaijeveld et al. We will investigate whether or not the step wise progression observed by Kraaijeveld et al. was physical or a numerical artefact.

3.1 Model background

We employ a partition of unity based model for the failure of fully saturated rocks (Kraaijeveld and Huyghe, 2011). The extended finite element method incorporates a discontinuity in a finite element mesh by exploiting the partition of unity property of finite element shape functions. Consider the domain as shown in Figure 3.1. The displacement field is enriched by a Heaviside step function giving rise to the discontinuous nature of a fracture

$$\mathbf{u}(\mathbf{x}, t) = \hat{\mathbf{u}}(\mathbf{x}, t) + \mathcal{H}_{\Gamma_d}(\mathbf{x})\tilde{\mathbf{u}}(\mathbf{x}, t). \quad (3.1)$$

The pressure field is not discontinuous but may have significant gradients near a fracture surface. Enriching the pressure with a signed distance functions, as was used by Réthoré et al. (2007), the gradient near a discontinuity is taken into account in a natural way

$$p(\mathbf{x}, t) = \hat{p}(\mathbf{x}, t) + \mathcal{D}_{\Gamma_d}(\mathbf{x})\tilde{p}(\mathbf{x}, t), \quad (3.2)$$

where the distance function $\mathcal{D}_{\Gamma_d}(\mathbf{x})$ is defined as

$$\mathcal{D}_{\Gamma_d}(\mathbf{x}) = |(\mathbf{x} - \mathbf{x}_{\Gamma_d}) \cdot \mathbf{n}_d| \quad \mathbf{x} \in \Omega. \quad (3.3)$$

Here, \mathbf{x}_{Γ_d} is the coordinate of the nearest point on the discontinuity and \mathbf{n}_d is the corresponding normal vector (Figure 3.1). It is noted here that the choice for the distance function as enrichment is not based on physical insights but is merely a practical decision. The pressure near a fracture will not be linear. However, by using a fine mesh we can approximate the

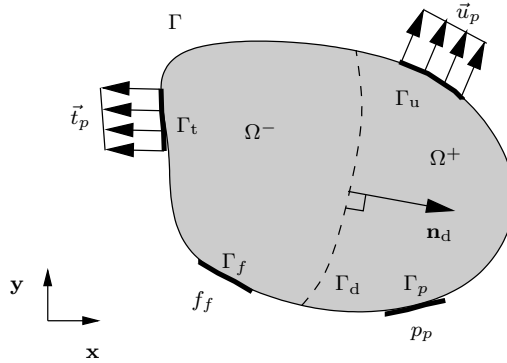


Figure 3.1: The body Ω crossed by discontinuity Γ_d . The body is completed with the boundary conditions.

pressure gradient based on the linear enrichment. The pressure gradient follows from the spatial derivative of the pressure field (3.2)

$$\nabla p(\mathbf{x}) = \nabla \hat{p}(\mathbf{x}) + \mathcal{D}_{\Gamma_d}(\mathbf{x}) \nabla \tilde{p}(\mathbf{x}) + \nabla \mathcal{D}_{\Gamma_d}(\mathbf{x}) \tilde{p}(\mathbf{x}), \quad (3.4)$$

where the gradient of the distance function \mathcal{D}_{Γ_d}

$$\nabla \mathcal{D}_{\Gamma_d}(\mathbf{x}) = \begin{cases} \mathbf{n}_d & \text{if } \mathbf{x} \in \Omega^+ \\ -\mathbf{n}_d & \text{if } \mathbf{x} \in \Omega^-. \end{cases} \quad (3.5)$$

Linear momentum balance and mass balance are prescribed to define a complete coupled system based on Biot's theory. We consider a porous solid skeleton that is completely saturated with fluid. Neglecting the contribution of gravity, inertia, and convection on the momentum balance, we can write the latter as

$$\nabla \cdot \boldsymbol{\sigma} = \mathbf{0}, \quad (3.6)$$

where $\boldsymbol{\sigma}$ is the total stress, which is decomposed in Terzaghi's effective stress $\boldsymbol{\sigma}_e$ and the hydrostatic pressure p (Terzaghi, 1943)

$$\boldsymbol{\sigma} = \boldsymbol{\sigma}_e - p\mathbf{I}, \quad (3.7)$$

with \mathbf{I} being the unit matrix. Here we assume that the fluid and solid constituents are incompressible. Neglecting mass transfer between both constituent, the mass balance equation can be written as (de Borst et al., 2006)

$$\nabla \cdot \mathbf{v}_s + \nabla \cdot \mathbf{q} = 0, \quad (3.8)$$

where \mathbf{q} is the seepage flux and \mathbf{v}_s is the deformation velocity of the solid skeleton. Constitutive behaviour for the momentum balance is described by a linear reversible stress-strain relation. Darcy's equation is used as constitutive relation in the mass balance equation.

The softening of the material is governed by a traction acting on the fracture surface based on the cohesive zone approach. Assuming continuity of stress across the discontinuity, we can write the local momentum balance as:

$$\boldsymbol{\sigma} \cdot \mathbf{n}_d = \mathbf{t}_d - p_d \mathbf{n}_d, \quad (3.9)$$

where \mathbf{t}_d is the traction and p_d is the pressure in the fracture that is also acting on the fracture surface. We use a pure mode II cohesive law (shown in Figure 3.2) based on the work of Kraaijeveld and Huyghe (2011). The shear traction is a function of the opening u_s as:

$$t_s = \frac{\tau_{\text{ult}}^2}{\mathcal{G}_c} u_s \exp\left(-\left(\frac{u_s \tau_{\text{ult}}}{\mathcal{G}_c}\right)^2\right), \quad (3.10)$$

where τ_{ult} is the ultimate strength of the material, \mathcal{G}_c is the fracture toughness and t_s and u_s are the shear traction and the shear displacement, respectively. In mode I we only apply a penalty condition to prevent penetration of the two fracture surfaces. The model has no dilatancy.

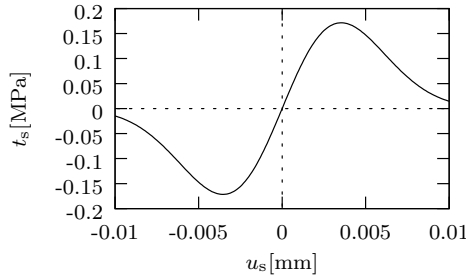


Figure 3.2: Traction separation law for the mode II fracture.

The local mass balance is based on conservation of mass between the bulk and volume of fluid in the fracture. This can be written as

$$\left(\mathbf{q}_{\Gamma_d}^+ - \mathbf{q}_{\Gamma_d}^-\right) \cdot \mathbf{n}_d + \dot{u}_n + u_n \left\langle \frac{\partial \dot{u}_s}{\partial s} \right\rangle - u_n \frac{\partial}{\partial s} \left(k_d \frac{\partial p_d}{\partial s} \right) + \frac{u_n}{K_f} \dot{p}_d = 0, \quad (3.11)$$

with $\mathbf{q}_{\Gamma_d}^+$ and $\mathbf{q}_{\Gamma_d}^-$ being the fluid flow from the discontinuity in the bulk for both sides for the fracture, \dot{u}_n denoting the time derivative of the normal

opening of the discontinuity, u_s being the shear opening of the discontinuity, $\langle \cdot \rangle = \frac{\cdot^+ + \cdot^-}{2}$ describing the average across the discontinuity, and k_d being the permeability in the discontinuity. The latter is given by (Witherspoon et al., 1980):

$$k_d = \frac{u_n^2}{12\mu}, \quad (3.12)$$

with μ being the dynamic viscosity of the fluid. For the derivation of these equilibrium equations, we refer to Irzal et al. (2013).

The spatial discretization of the balance equations is based on the partition of unity property of finite element shape functions as described in the work of Melenk and Babuška (1996). The variational forms of the displacement field and the pressure field are discretized similarly following the Bubnov-Galerkin approach. Time integration is performed with the implicit Euler scheme. The final system of equations is non linear and therefore solved using a Newton-Raphson iterative procedure. For a detailed description and derivation we refer to (Kraaijeveld and Huyghe, 2011; Réthoré et al., 2007; Irzal et al., 2013).

3.2 Numerical implementation

The propagation of the cohesive zone is based on an averaged stress at the crack tip. This stress is calculated based on a Gaussian weighting function that depends on a length scale parameter l_a (see Section 2.3). Within an element, the cohesive zone always propagates in a straight line and always ends on an element edge. It is possible to cut multiple elements within one time increment. Once a converged solution is obtained, the averaged stress at the crack tip is evaluated to determine whether or not the crack propagates. If a crack propagates, the discontinuity is extended into the next element by enhancing the corresponding nodes with new degrees of freedom. Instead of propagating to the next time increment, the current increment is recalculated with the extended discontinuity. Once a converged solution is obtained for which no propagation is observed, the analysis is continued with the next time increment.

By enriching the nodes with the additional degrees of freedom we incorporate the discontinuity in the original finite element mesh. We use an adopted integration scheme introduced by Wells and Sluys (2001) to numerically integrate elements that are crossed by a discontinuity. The discontinuity is prohibited to cut too close to a finite element node in order to prevent the integration of zero surface elements that may occur on one

side of the discontinuity. The balance equations over the discontinuity are integrated by two integration points per element (Remmers et al., 2003).

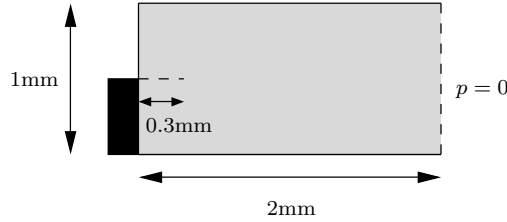


Figure 3.3: Scheme for the compression example.

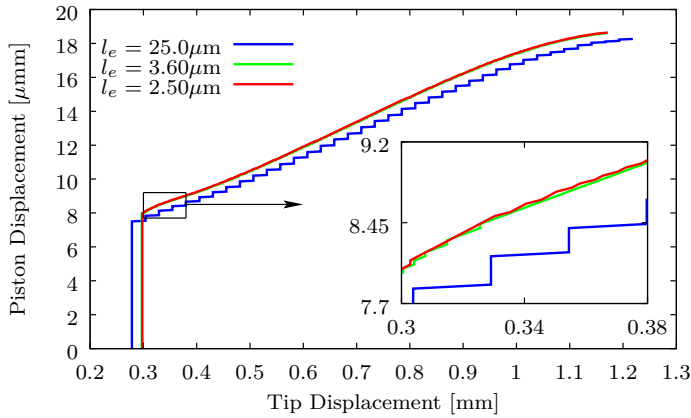


Figure 3.4: Piston displacement versus the tip displacement.

3.3 Example

We consider a sample made of a porous material with a fracture of length 0.30 mm (Figure 3.3). The sample is completely boxed and free drainage is assumed on the right hand side. A load is applied below the initial fracture, leading to shear stress around the tip of the fracture. The material has a Young's modulus of $E = 90$ MPa and a Poisson's ratio of $\nu = 0.20$. The propagation direction is based on Tresca's failure criterion. The ultimate strength of the sample is $\tau_{\text{ult}} = 0.4$ MPa and the fracture toughness is $\mathcal{G}_c = 0.2$ N/m. The intrinsic permeability of the material is $k_{\text{int}} = 0.28e^{-18}$ m² and the fluid has a dynamic viscosity of $\mu = 1.0e^{-3}$ Pa · s. The following condition has to be satisfied for stable time integration (Vermeer and Verruijt, 1981):

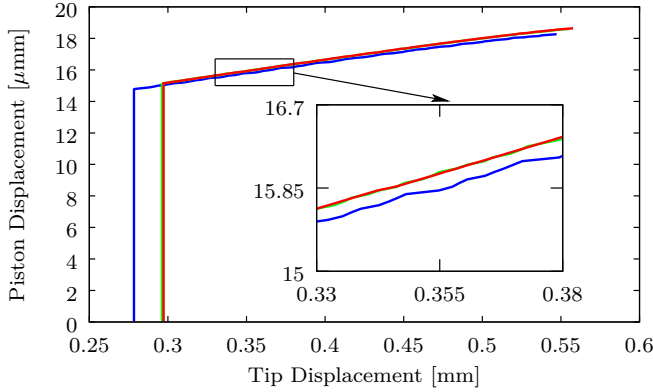


Figure 3.5: Piston displacement versus the location of the beginning of the cohesive zone. The colours in the graph are identical to those used in Figure 3.4.

$$\Delta t_{\text{crit}} > \frac{\Delta x^2 \mu}{EK_{\text{int}}} \quad (3.13)$$

Since we are interested in the fundamental behaviour of the pore pressure we satisfy this condition with all our meshes. In the work of Kraaijeveld et al. evidence was found of discontinuous behaviour of fracture propagation due to time effects in the pore pressure. By satisfying the condition on the time increment we ensure that we can accurately describe these time effects. An overview of the different meshes can be seen in Table 3.1. All the meshes are made of squared quadrilateral elements and with an element length l_e . The critical time increment with the material parameters for the coarsest mesh is $\Delta t_{\text{crit}} = 0.025$ s. We use this time increment in all the simulations.

l_e (μm)	Δt_{crit} (s)	Number of nodes
25.0	0.025	3200
3.60	0.00051	156800
2.50	0.00025	320000

Table 3.1: Mesh Overview

We first investigate the global response in the sample in Figures 3.4-3.7. In Figure 3.4 it can be seen that there is a slight difference in the tip displacement comparing the coarsest and finest meshes. In the coarsest mesh ($l_e = 25.0 \mu\text{m}$) the tip propagates in a step wise fashion. This effect becomes less prominent for finer meshes and therefore can be attributed

to the discretization since the fracture must propagate from element edge to element edge. The influence of this restriction to the numerical results is most significant in the coarser mesh. Instead of looking at the location of the fracture tip, we can also show the location of the beginning of the cohesive zone, i.e. the location where the traction of the cohesive law is less than 1% of τ_{ult} . We show this graph in Figure 3.5. In this case the location of the tip is not restricted to the element edge, leading to smoother fracture growth. Similar behaviour is observed for the load necessary to push the piston forward (Figure 3.6). The fracture path is shown in Figure 3.7. The beginning of the fracture path is directed along the x-axis. As the fracture propagates the direction slightly turns into the negative y-direction. This decreases the surface area below the fracture tip eventually leading to complete failure of the material. In the simulations we observe that the fracture completely breaks the material within one time increment as complete failure occurs. This is a significant difference with the work of Kraaijeveld and Huyghe (2011). There, the fracture was prohibited to grow through more than one element per time increment. The fracture was therefore delayed in propagation and complete failure of the material was not observed.

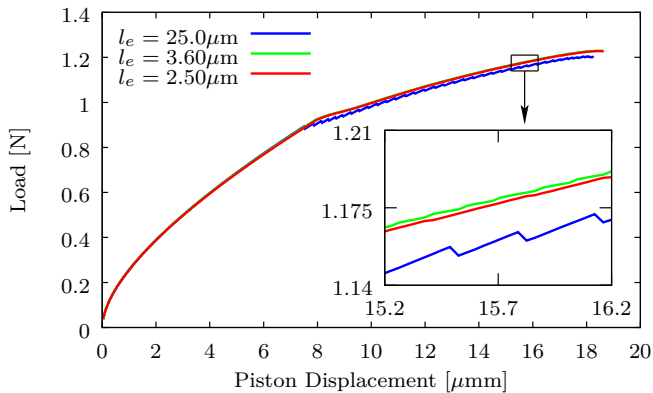


Figure 3.6: Piston displacement versus the applied load.

The fluid flow across the fracture, in the initial fracture at $x = 0.25$ mm, is shown in Figure 3.8. Before fracture propagation, fluid is being pushed out of the region below the initial fracture due to the increasing load of the piston. Consolidation effects are observed behind the fracture tip once propagation starts. The compressive stress behind the tip decreases immediately after fracture propagation. This leads to relaxation of the fluid phase, decreasing the normal flow across the fracture. In the coarse mesh

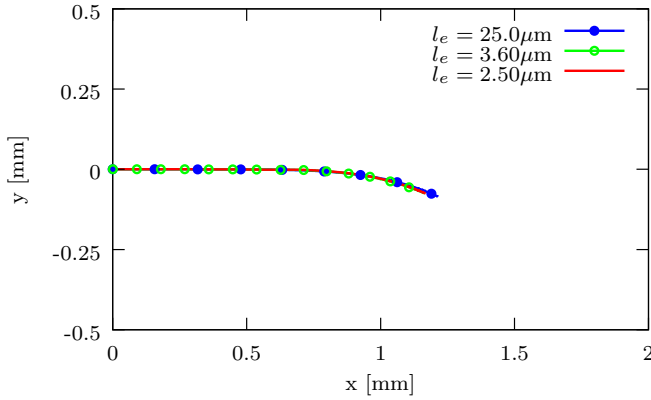


Figure 3.7: The final fracture path.

the region where relaxation occurs is so large that fluid is being retracted from the upper side of the fracture. A similar effect is observed for a point not in the initial fracture but at $x = 0.34$ mm.

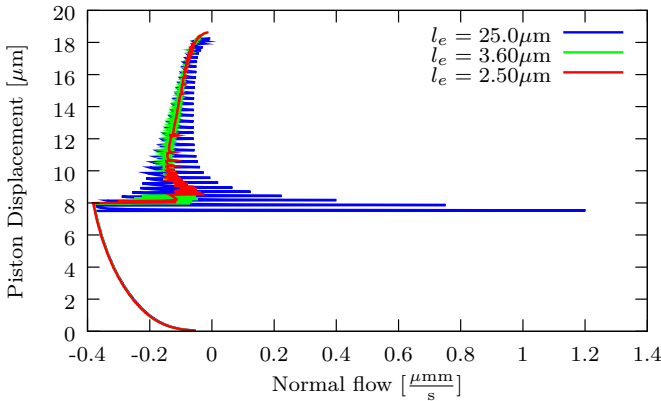


Figure 3.8: The normal flow across the fracture at point $x = 0.25$ mm is plotted against the piston displacement.

The difference in the normal flow between the various meshes can be distinguished more accurately in Figure 3.10. In the coarse mesh the fluid flow relaxes, and even changes sign again, after the fracture has propagated. This effect repeats itself once the fracture propagates through the next element. In the finer meshes this effect is less obvious (to observe). The mesh is finer, hence decreasing the area where relaxation of pore pressure occurs, leading to lower values for the normal fluid flow. In the finest mesh ($l_e = 2.50 \mu\text{m}$) we even observe a continuous fluid flow (between piston

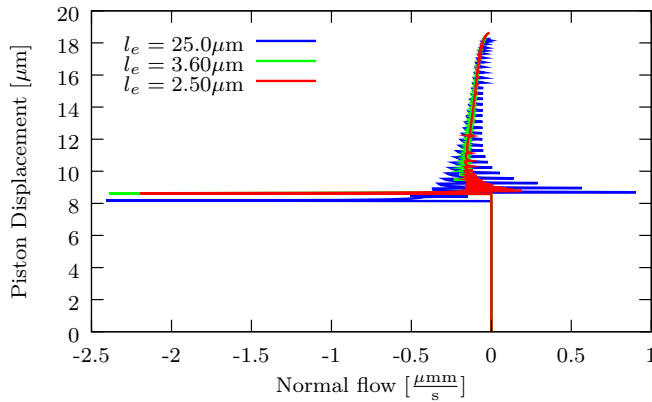


Figure 3.9: The normal flow across the fracture at point $x = 0.34$ mm is plotted against the piston displacement.

displacement $d = 0.0082 - 0.0085$ mm). This effect is caused by continuous fracture propagation.

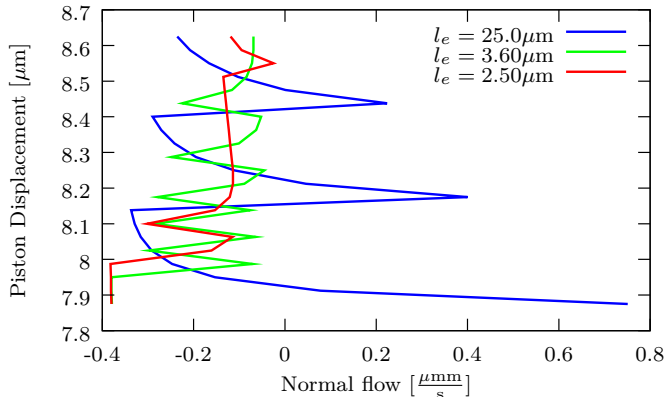


Figure 3.10: Zoom of the normal flow across the fracture at point $x = 0.25$ mm.

From these results we conclude that fracture propagation in a porous material in our model is affected by the element size. To obtain better understanding in the time effects we reproduce the same simulation, using the finest mesh, with two different time increments; $\Delta t = 0.0125$ s and $\Delta t = 0.00625$ s. Using a smaller time increment will lower the load increment per possible propagation step. The propagation of the fracture through multiple elements that we observed with a larger time increment may vanish using smaller time increments. We indeed see this effect in Figure 3.11: decreasing the increment size leads to crack arrest in one time step followed

by crack propagation in the next. This also has effect on the fluid flow across the fracture as we see in Figure 3.12.

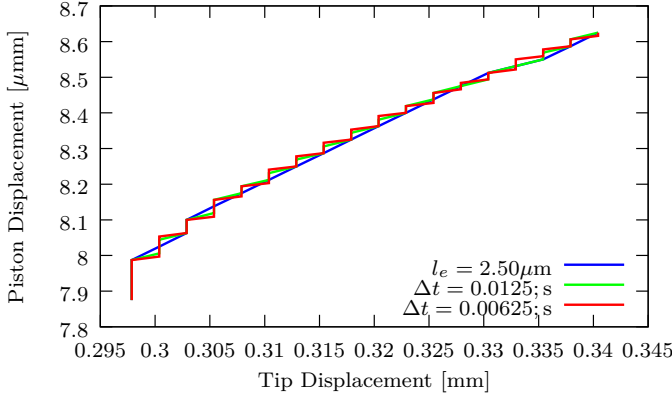


Figure 3.11: Zoom of the tip displacement versus the piston displacement for the same mesh ($l_e = 2.50 \mu\text{m}$) using 3 different time increments.

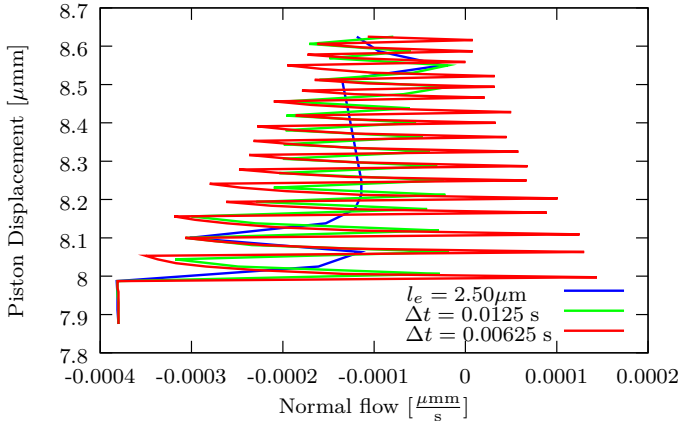


Figure 3.12: Zoom of the normal flow across the fracture at point $x = 0.25 \text{ mm}$ considering the same mesh ($l_e = 2.50 \mu\text{m}$) using 3 different time increments.

A final parameter that may influence fracture propagation in a porous material is the intrinsic permeability. In this last example we decrease the intrinsic permeability with two orders to $k_{\text{int}} = 0.28\text{e}^{-20} \text{ m}^2$. Using the finest mesh with the original time increment size of $\Delta t = 0.025 \text{ s}$ we still satisfy the critical time increment restriction. The effect of the permeability on the applied load is clear from Figure 3.13. The material behaves more stiff because consolidation effects are much slower. This leads to the increased load necessary to push the piston down. In Figure

3.14 we see that fracture propagation occurs earlier in the lower permeable material. This is counter intuitive since we expected the load transfer to be slower in the material with a lower permeability. However, the area where consolidation takes place is smaller, leading to a higher concentration of stress near the fracture tip. Furthermore, the pore pressure only effects the hydrostatic component of the stress. The increase of shear stress is thus unaffected by the stress transfer and leads to earlier fracture propagation in the materials with a lower permeability. The intrinsic permeability also influences the fracture path (Figure 3.15).

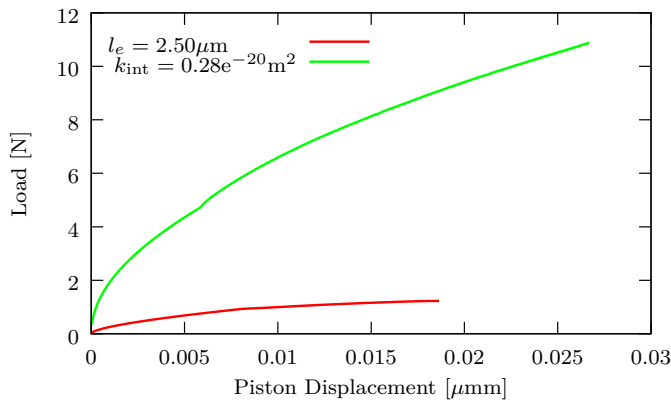


Figure 3.13: The influence of the intrinsic permeability on the piston displacement versus the applied load.

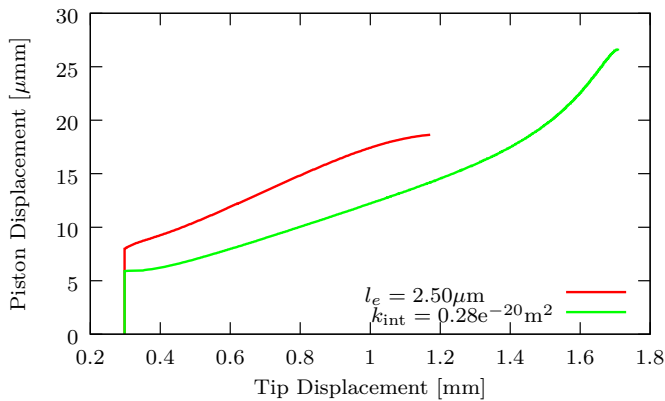


Figure 3.14: Tip displacement versus the piston displacement where we considered 2 different permeabilities.

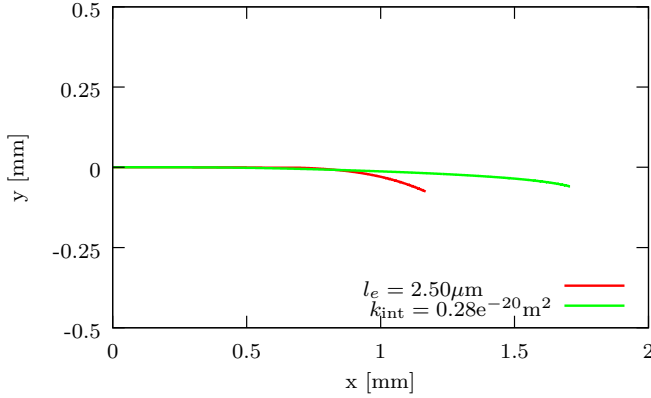


Figure 3.15: Final crack path in the simulation with 2 different permeabilities.

3.4 Conclusions

Stepwise progression was observed experimentally by Pizzocolo et al. (2013) in mode I. Evidence was also found in numerical results by Schrefler et al. (2006). The phenomenon of step wise propagation in mode I is also discussed in (Coa et al., 2016, in press). We do observe step wise fracture growth in our mode II simulations but we attribute it to a numerical artefact, generated by the element edge to element edge growth of the fracture. Step wise growth disappeared upon mesh refinement for mode II fractures but appeared again upon refinement of the magnitude of the time increment Δt . Step wise propagation of the beginning of the cohesive zone is less distinct since this location is not bound to the element edges. Thus, we can conclude that our simulations do not point at a physical origin of the step wise progression in mode II.

No dilatancy is included in our mode II model for reasons of simplicity. We are aware that dilatancy may be a major factor affecting mode II propagation. Mode II failure in fully saturated materials - and particularly the question whether or not step wise propagation takes place - may be strongly affected by this physical phenomenon.

We also investigated the effect of discretization on a propagating shear fracture in a poro-elastic material. The global response of the material is independent of the mesh size as long as the critical time increment, Eq. (3.13) is satisfied. Decreasing the material permeability has an effect on the material response due to slower stress transfer. Changes in fracture path and load necessary to push the piston down are observed. Whereas the global pattern of crack propagation is mesh independent, the local

interaction between pore pressure, local flow across the crack and crack propagation was highly dependent on the discretization in space and time. Compared to the work of Kraaijeveld and Huyghe (2011), we made a significant improvement by allowing to propagate the fracture through multiple elements within one time step. However, this improvement is insufficient to eliminate mesh dependence entirely.

In order to eliminate all mesh dependence of the XFEM model, the element edge to element edge growth should be abandoned and crack growth through part of an element should be made possible. This is, however, beyond the scope of this study.

Solving a problem with poro-elasticity in a finite element based model usually leads to assumptions on the time discretization. With our results we showed that the choice of the time increment and the mesh size should be carefully picked. If the interest is understanding the physics of the fracture propagation behaviour, a mesh satisfying the critical time criterion is not sufficient any more and results should be interpreted carefully. However, when the main goal is looking at the fracture behaviour on a larger scale the restriction on the mesh are less strict and the X-FEM model is very suitable.

The signed distance function to enrich the pressure field across the fracture is not physically based. It is demonstrated that the approximation of the pressure gradient near the fracture surface is dependent on the mesh size. In the next chapter an alternative method to model the pressure across the fracture is presented and compared to the signed distance based model used in this chapter and in Chapter 2.

4

The Enhanced Local Pressure model

Abstract

In this chapter, an extension to the extended finite element method based models as discussed in the previous chapters is presented. Using the partition of unity property of finite element shape functions, the displacement and pressure field across the fracture are described as a strong discontinuity. The pressure in the fracture is included by an additional degree of freedom. The pressure gradient due to fluid leakage near the fracture surface is reconstructed based on Terzaghi's consolidation solution. With this numerical formulation, it is ensured that all fluid flow goes exclusively into the fracture and that it is not necessary to use a dense mesh near the fracture to capture the pressure gradient. Fluid flow in the rock formation is described by Darcy's law. The fracture process is governed by a cohesive traction separation law. The performance of the numerical model for fluid-driven fractures is shown in three numerical examples.

In Chapter 2 an eXtended Finite Element Method (X-FEM) model is used to simulate fracture in poro-elastic materials. It is demonstrated that there is an influence of intrinsic permeability on the fracture behaviour. In Chapter 3 an assessment of the effect of mesh refinement on fluid leakage was given. Mesh refinement led to different responses in fluid leakage. The signed distance function, used in approximating the pressure gradient near the fracture surface, requires sufficient fine numerical discretization to resolve the gradient. In applications of hydraulic fracturing, applied in low permeable rocks such as shales, this effect is even more severe. In this chapter a different method is proposed where the pressure is included in the fracture as separate degree of freedom.

A model to predict the hydraulic fracturing process can be used to optimize the generation of a fracture network and eventually may increase production rates. However, the correct modelling of the hydraulic fracturing process is complex since three different phenomena have to be taken into account: (i) the fluid exchange between the fracture and the rock formation (ii) the fluid flow in the fracture and (iii) the changing spatial configuration due to fracture propagation (Adachi et al., 2007).

The first theoretical hydraulic fracture models that took these requirements in consideration were developed in the 1950s (Adachi and Detournay, 2008). Perkins and Kern (1961) developed a theoretical model based on the classic Sneddon plane strain crack propagation. Fluid loss was included in this model by Nordgren (1972) and is now referred to as the PKN model. Similar models with slightly different geometrical assumptions were independently developed by Geertsma and De Klerk (1969) and Khristianovic and Zheltov (1955). These models have been used for analysing several parameters that control hydraulic fracturing. This research has shown that hydraulic fracturing can be categorized in a parametric space based on hydraulic fractures that are dominated by fluid leak-off, toughness, or viscosity. Several asymptotic solutions are derived in this parametric space. An overview of these solutions is given by Adachi and Detournay (2008).

Various numerical models have been developed for complex geometries where the analytical solutions fail. Boone and Ingraffea (1990) developed a numerical model based on the Finite Element Method (FEM) for a poro-elastic material where a cohesive zone description was used for the fracture. The fluid flow in the crack was solved using a finite difference method. Schrefler and co-workers (Schrefler et al., 2006; Secchi et al., 2007; Secchi and Schrefler, 2012) modelled a cohesive fracture using the FEM but included a mesh adaptation scheme so that propagating fractures in arbitrary directions can be modelled in two- and three-dimensional situations. Hy-

draulic fracturing was investigated in a permeable material by Sarris and Papanastasiou (2011) with a finite element analysis including cohesive zone elements. Segura and Carol (2004, 2008) introduced a hydro-mechanical coupling formulation using zero-thickness interface elements with double nodes based on the finite element method. Carrier and Granet (2012) also used interface elements but included an additional degree of freedom for the pressure in the fracture. Recently, also advancements were made in continuum based hydraulic fracturing simulations using a phase-field approach (Wheeler et al., 2014).

The extended finite element method is a proven technology in solid mechanics and has as an important advantage compared to the previously mentioned fracture models; a fracture can grow in arbitrary directions without the need to remesh (Remmers et al., 2003). In X-FEM a fracture is modelled as a discontinuity in the displacement field by exploiting the partition of unity property of finite element shape functions (Melenk and Babuška, 1996). Belytschko and Black (1999) and Moës et al. (1999) were the first to implement this in the FEM by adding additional degrees of freedom to the existing nodes in the finite element mesh. A cohesive zone description for the fracture process was included by Wells and Sluys (2001). The X-FEM was successfully applied to fracturing in porous materials, see e.g. (Irzal et al., 2013; de Borst et al., 2006; Kraaijeveld et al., 2013). Recently, Mohammadnejad and Khoei (2012) developed an extended finite element method model for cohesive crack growth in multiphase porous materials. They successfully applied their model for hydraulic fracturing simulations (Mohammadnejad and Khoei, 2013). In these works, similar as to the model presented in Chapter 2 and Chapter 3, the pressure field across the fracture is enriched with a linear distance function. This leads to a continuous pressure description across the fracture while the fluid flow is discontinuous. The model described in the previous two chapters is used for benchmarking purposes in this chapter and is referred to as the continuous pressure X-FEM model.

A drawback of a continuous pressure description is that an inflow, as present in hydraulic fracturing, must be prescribed as a boundary condition of the continuous external fluid flow. Therefore, a mesh dependent part of the fluid flow goes directly in the formation instead of into the fracture. This effect decreases in an opened fracture due to the high permeability in the fracture compared with the rock formation. However, the effect may be significant in an initial closed fracture, particularly when the mesh is coarse. A second drawback, the necessity to use a fine mesh near the fracture to capture the pressure gradient, is demonstrated in Chapter 3.

To quantify these effects, we develop a model with an additional, separate, degree of freedom for the fluid pressure in the fracture. By doing this, we ensure that the inflow goes exclusively into the fracture. The fluid leaks off into the formation only from the fracture itself. We enrich the pressure, as we do for the displacement field, with a Heaviside function, making the pressure discontinuous over the fracture. Hence, the pressure exhibits a jump for the fracture to the formation on the left and another jump for the fracture to the formation on the right as in Figure 4.1. The steep pressure gradients along the boundaries of the fracture are therefore not resolved. The steep gradients along the boundaries of the fracture are reconstructed assuming a scale separation between on the one hand the consolidation phenomenon around the fracture, and on the other hand the macroscopic fluid flow in the formation. The consolidation phenomenon itself is reconstructed from an one-dimensional analytical solution based on Terzaghi's consolidation equation (Terzaghi, 1943). The numerical model is only valid when the characteristic distance of consolidation around the fracture is small relative to the mesh-size of the formation. We will refer to this model as the Enhanced Local Pressure (ELP) model. The pressure near the fracture can be compared to an one-dimensional analytical solution. By comparing the ELP model and the continuous X-FEM formulation with the analytical solution we investigate if indeed the ELP better approximates the pressure in the fracture at small distance-scales.

In the remainder of this chapter we first describe the kinematic relations. In Section 4.2 we present the balance equations and in Section 4.3 the governing equations are introduced. The weak form is given in Section 4.4 and the discretization and numerical implementation are given in Section 4.5. In Section 4.7 we illustrate the performance of the model with three examples. Finally, conclusions are drawn in Section 4.8.

4.1 Kinematic relations

Consider a body Ω crossed by a discontinuity Γ_d , as shown in Figure 4.2a. The discontinuity divides the body in two domains, Ω^+ and Ω^- . The vector \mathbf{n}_d is defined as the normal of the discontinuity surface Γ_d pointing into domain Ω^+ . The total displacement field of the solid skeleton can, at any time t , be described by a regular displacement field $\hat{\mathbf{u}}(\mathbf{x}, t)$ and an additional displacement field $\tilde{\mathbf{u}}(\mathbf{x}, t)$ (Belytschko and Black, 1999; Moës et al., 1999; Remmers et al., 2008)

$$\mathbf{u}(\mathbf{x}, t) = \hat{\mathbf{u}}(\mathbf{x}, t) + \mathcal{H}_{\Gamma_d}(\mathbf{x})\tilde{\mathbf{u}}(\mathbf{x}, t), \quad (4.1)$$

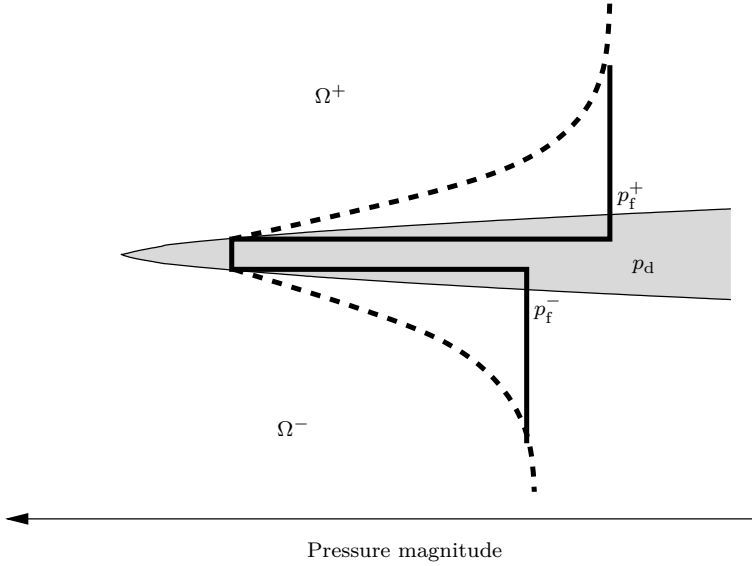


Figure 4.1: Schematic representation of the pressure magnitude over an open discontinuity in grey. The discontinuity separates the formation into two bodies, Ω^+ and Ω^- , with a pressure p_f^+ and p_f^- , respectively. The pressure in the discontinuity is given by p_d . The striped line indicates the physical pressure gradient over the discontinuity. The solid line represents the discontinuous pressure profile.

where \mathbf{x} is the position of a material point and \mathcal{H}_{Γ_d} is the Heaviside step function. Across the discontinuity, this is defined as

$$\mathcal{H}_{\Gamma_d} = \begin{cases} 1 & \text{if } \mathbf{x} \in \Omega^+ \\ 0 & \text{if } \mathbf{x} \in \Omega^- \end{cases} \quad (4.2)$$

The strain field results from differentiating the displacement field (4.1) with respect to material point \mathbf{x} with the assumption of small strain theory

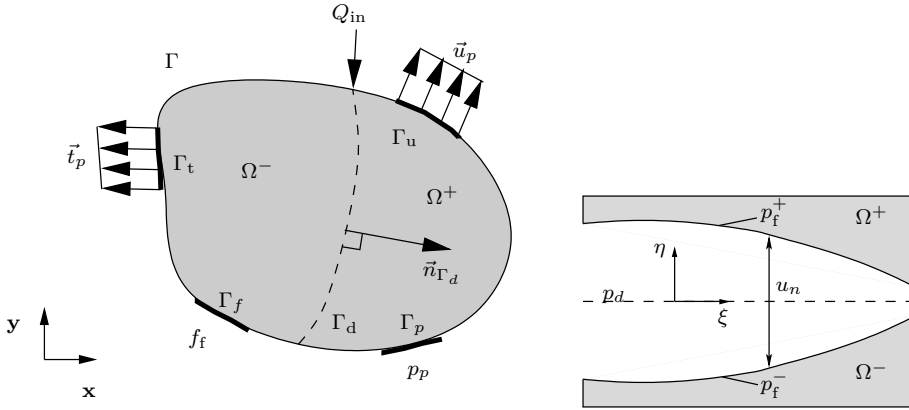
$$\boldsymbol{\epsilon}(\mathbf{x}, t) = \nabla^s \hat{\mathbf{u}}(\mathbf{x}, t) + \mathcal{H}_{\Gamma_d} \nabla^s \tilde{\mathbf{u}}(\mathbf{x}, t), \quad \mathbf{x} \notin \Gamma_d. \quad (4.3)$$

Here ∇^s is the symmetric part of the differential operator

$$\nabla^s \mathbf{u} = \frac{1}{2} (\nabla \mathbf{u} + (\nabla \mathbf{u})^T). \quad (4.4)$$

At the discontinuity Γ_d , the strain field is undefined and the kinematic quantity is defined by a jump in the displacement field

$$[\mathbf{u}(\mathbf{x}, t)] = \tilde{\mathbf{u}}(\mathbf{x}, t), \quad \mathbf{x} \in \Gamma_d. \quad (4.5)$$



(a) The body Ω crossed by discontinuity Γ_d . The body is completed with the boundary conditions. (b) Schematic representation of a discontinuity.

Figure 4.2: Schematic representation of body Ω and of a discontinuity.

The pressure inside an opening fracture is different from the pressure inside the surrounding formation. The gradient of this pressure difference quantifies the interaction of fluid flow between the fracture and the formation. We assume the pressure to be discontinuous across the fracture:

$$p(\mathbf{x}, t) = \hat{p}(\mathbf{x}, t) + \mathcal{H}_{\Gamma_d}(\mathbf{x})\tilde{p}(\mathbf{x}, t). \quad (4.6)$$

In the discontinuity, the pressure is equal to an independent variable p_d (Figure 4.2b).

$$p_d = p \quad \mathbf{x} \in \Gamma_d. \quad (4.7)$$

4.2 Balance equations

The balance equations consist of two parts, namely balance equations in the bulk material and on a more local scale inside the fracture. These two types are identified separately in this section.

4.2.1 Bulk behaviour

The porous solid skeleton is considered to be fully saturated with a fluid. The process is isothermal and gravity, inertia, body forces, and convection are neglected. With these assumptions the momentum balance reads

$$\nabla \cdot \boldsymbol{\sigma} = \mathbf{0}, \quad (4.8)$$

where $\boldsymbol{\sigma}$ is the total stress which is decomposed in Terzaghi's effective stress $\boldsymbol{\sigma}_e$ and the hydrostatic pressure p (Terzaghi, 1943)

$$\boldsymbol{\sigma} = \boldsymbol{\sigma}_e - \alpha p \mathbf{I}, \quad (4.9)$$

with \mathbf{I} being the unit matrix and α being the Biot coefficient

$$\alpha = 1 - \frac{K}{K_s}. \quad (4.10)$$

Here, K and K_s are the bulk moduli of the porous material and the solid constituent, respectively. The momentum balance is completed with the following boundary conditions (Figure 4.2a)

$$\begin{aligned} \boldsymbol{\sigma} \cdot \mathbf{n}_\Gamma &= \mathbf{t}_p(\mathbf{x}, t) & \mathbf{x} \in \Gamma_t, \\ \mathbf{u}(\mathbf{x}, t) &= \mathbf{u}_p(\mathbf{x}, t) & \mathbf{x} \in \Gamma_u, \end{aligned} \quad (4.11)$$

with $\Gamma_t \cup \Gamma_u = \Gamma$, $\Gamma_t \cap \Gamma_u = \emptyset$.

We neglect mass transfer between the two constituents. The mass balance is written as (de Borst et al., 2006)

$$\alpha \nabla \cdot \mathbf{v}_s + \nabla \cdot \mathbf{q} + \frac{1}{M} \dot{p} = 0, \quad (4.12)$$

where \mathbf{v}_s is the deformation velocity of the solid skeleton, \mathbf{q} is the seepage flux, and M is the compressibility modulus defined as

$$\frac{1}{M} = \frac{\phi}{K_f} + \frac{1 - \phi}{K_s}. \quad (4.13)$$

Here ϕ is the porosity of the porous material and K_f is the bulk modulus of the fluid. The mass balance is completed with the following boundary conditions (Figure 4.2a)

$$\begin{aligned} \mathbf{q}(\mathbf{x}, t) \cdot \mathbf{n}_\Gamma &= f_f & \mathbf{x} \in \Gamma_f, \\ p(\mathbf{x}, t) &= p_p & \mathbf{x} \in \Gamma_p, \end{aligned} \quad (4.14)$$

with $\Gamma_f \cup \Gamma_p = \Gamma$, $\Gamma_f \cap \Gamma_p = \emptyset$.

4.2.2 Microscopic model

Following a cohesive zone approach, the softening of the material is governed by a traction acting on the discontinuity surface. This traction is coupled to the hydrostatic pressure in the discontinuity. Assuming continuity of stress from the continuum into the discontinuity, we can write the local momentum balance as

$$\boldsymbol{\sigma} \cdot \mathbf{n}_d = \mathbf{t}_d - p_d \mathbf{n}_d. \quad (4.15)$$

The local mass balance in the discontinuity can be found by integrating the continuous mass balance across the discontinuity.

$$\left(\mathbf{q}_{\Gamma_d}^+ - \mathbf{q}_{\Gamma_d}^- \right) \cdot \mathbf{n}_d + \dot{u}_n + u_n \left\langle \frac{\partial \dot{u}_s}{\partial s} \right\rangle - u_n \frac{\partial}{\partial s} \left(k_d \frac{\partial p_d}{\partial s} \right) + \frac{u_n}{K_f} \dot{p}_d = 0, \quad (4.16)$$

with $\mathbf{q}_{\Gamma_d}^+$ and $\mathbf{q}_{\Gamma_d}^-$ being the fluid flow from the discontinuity into formation for the discontinuity lip of the Ω^+ and the Ω^- domain, respectively, \dot{u}_n denoting the time derivative of the normal opening of the discontinuity, u_s being the shear opening of the discontinuity, $\langle \cdot \rangle = \frac{\cdot^+ + \cdot^-}{2}$ describing the average across the discontinuity, and k_d being the permeability in the discontinuity. The latter is given by (Witherspoon et al., 1980):

$$k_d = \frac{u_n^2}{12\mu}, \quad (4.17)$$

where μ is the viscosity of the fluid. For the derivation of this equilibrium equation, we refer to Irzal et al. (2013).

4.3 Constitutive equations

The mathematical formulation of the balance equations are completed by constitutive behaviour for the bulk material and the discontinuity.

4.3.1 Mechanical behaviour of the bulk

The effective stress in the bulk material is related to the strain with a linear reversible stress-strain relation:

$$\boldsymbol{\sigma}_e = 2\mu\boldsymbol{\epsilon} + \lambda \text{tr}(\boldsymbol{\epsilon})\mathbf{I}, \quad (4.18)$$

where μ and λ are respectively the first and second Lamé constants given in an isotropic material by

$$\mu = \frac{E}{2(1 + \nu)} \quad \lambda = \frac{\nu E}{(1 + \nu)(1 - 2\nu)}, \quad (4.19)$$

with E and ν being the Young's modulus and the Poisson's ratio, respectively.

The fluid flow in the bulk material can be described by Darcy's relation (Biot, 1941)

$$\mathbf{q} = -k\nabla p, \quad (4.20)$$

where k is the permeability, which is assumed to be isotropic and constant in time and space, and is defined as

$$k = \frac{k_{\text{int}}}{\mu}. \quad (4.21)$$

Here k_{int} is the intrinsic permeability and μ is the dynamic viscosity (Detournay and Cheng, 1993).

4.3.2 Mechanical behaviour in the discontinuity

The constitutive mechanical behaviour at the discontinuity is given by a relationship between the traction at the interface and the displacement jump \mathbf{u}_d across the discontinuity (Irzal et al., 2013):

$$\mathbf{t}_d = \mathbf{t}_d(\mathbf{u}_d, \kappa). \quad (4.22)$$

Here κ is a history parameter that is equal to the largest displacement jump reached. It is necessary to perform a linearisation on Eq.(4.22) in order to use the tangential stiffness matrix in an incremental iterative solution:

$$\Delta \mathbf{t}_d = \mathbf{T} \Delta \mathbf{u}_d. \quad (4.23)$$

The relation between the traction \mathbf{t}_d and the displacement jump \mathbf{u}_d can be any traction-separation relation and is referred to as the cohesive law. We assume that the fluid pressure inside the hydraulic fractures only causes fracture opening in normal direction. Therefore, shear tractions are neglected and we use an exponential cohesive law that is only a function of normal opening u_n (Figure 4.3)

$$t_n = \tau_{\text{ult}} \exp\left(-\frac{u_n \tau_{\text{ult}}}{\mathcal{G}_c}\right). \quad (4.24)$$

Here is τ_{ult} the ultimate strength of the material and \mathcal{G}_c the fracture toughness.

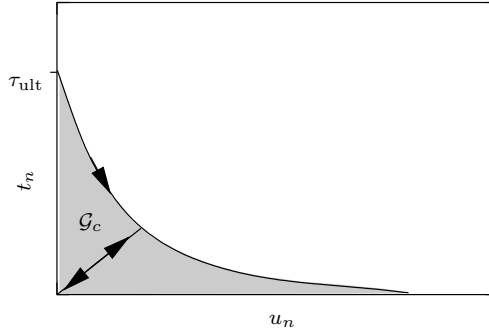


Figure 4.3: Exponential traction-separation law.

4.3.3 Small scale pressure coupling

Due to the discontinuous pressure formulation, the pressure gradient between the discontinuity and the formation is undetermined. If the consolidation distance is small compared to the dimensions of the finite elements near the discontinuity, we approximate the pressure gradient using the 1D analytical solution for a semi-infinite formation, given by Eq. (A.7) in Appendix A. In this analytical solution, the value p represents the pressure difference between the boundary surface and the initial pressure due to the loading of the formation. In the case of a discontinuity, there is a pressure gradient between the discontinuity and the formation, see Figure 4.2b. We therefore substitute p with this pressure difference. The fluid leakage is then taken from the analytical solution and thus given by

$$\mathbf{q} \cdot \mathbf{n} = Q_{\text{in}} = \frac{k}{2} \frac{p_d - p_f}{\sqrt{\frac{c_v t}{\pi}} \exp \frac{-\eta^2}{4c_v t} - \frac{\eta}{2} \operatorname{erfc} \left(\frac{\eta}{2\sqrt{c_v t}} \right)}. \quad (4.25)$$

At the boundary of discontinuity, defined by $\eta = 0$, the fluid flow simplifies into

$$\mathbf{q} \cdot \mathbf{n} = \frac{k}{2} \frac{p_d - p_f}{\sqrt{\frac{c_v t}{\pi}}}. \quad (4.26)$$

Here p_f is the pressure in the formation at the edge of the fracture (Figure 4.2b) and t is the time that expired after the discontinuity was inserted. The diffusion coefficient c_v is given by

$$c_v = kM \frac{K + \frac{4}{3}\mu}{K_u + \frac{4}{3}\mu}, \quad (4.27)$$

with K_u being the undrained bulk modulus

$$K_u = K + \alpha^2 M. \quad (4.28)$$

Taking the side of the discontinuity into consideration, we can write this equation as

$$\left(\mathbf{q}_{\Gamma_d^+} - \mathbf{q}_{\Gamma_d^-}\right) \cdot \mathbf{n}_d = C_a \left(2p_d - p_f^+ - p_f^-\right), \quad (4.29)$$

where the C_a is an analytical constant define by

$$C_a = \frac{k}{2\sqrt{\frac{c_v t}{\pi}}}. \quad (4.30)$$

4.4 Weak form

The weak form of the previously derived equilibrium equations can be expressed by multiplying them with admissible test functions for each field variable. The test functions for the momentum balance and the mass balance have the same form as the displacement field u and the pressure field p , respectively:

$$\boldsymbol{\eta} = \hat{\boldsymbol{\eta}} + \mathcal{H}_{\Gamma_d} \tilde{\boldsymbol{\eta}} \quad \zeta = \hat{\zeta} + \mathcal{H}_{\Gamma_d} \tilde{\zeta}. \quad (4.31)$$

The pressure in the fracture p_d is continuous along the discontinuity and therefore multiplied by the test function ψ .

Multiplying the momentum balance (4.8) with the test function $\boldsymbol{\eta}$, using Gauss's theorem and incorporating the boundary conditions, the weak momentum balance can be written as

$$\begin{aligned} \int_{\Omega} \nabla(\hat{\boldsymbol{\eta}} + \mathcal{H}_{\Gamma_d} \tilde{\boldsymbol{\eta}}) : \boldsymbol{\sigma} d\Omega &= \int_{\Gamma_t} \nabla(\hat{\boldsymbol{\eta}} + \mathcal{H}_{\Gamma_d} \tilde{\boldsymbol{\eta}}) \mathbf{t}_p d\Gamma_t \\ &- \int_{\Gamma_d^+} \nabla(\hat{\boldsymbol{\eta}} + \mathcal{H}_{\Gamma_d} \tilde{\boldsymbol{\eta}}) \cdot (\boldsymbol{\sigma} \cdot \mathbf{n}_d) d\Gamma_d^+ + \int_{\Gamma_d^-} \nabla(\hat{\boldsymbol{\eta}} + \mathcal{H}_{\Gamma_d} \tilde{\boldsymbol{\eta}}) \cdot (\boldsymbol{\sigma} \cdot \mathbf{n}_d) d\Gamma_d^-. \end{aligned} \quad (4.32)$$

Multiplying the mass balance (4.12) with the test function ζ results in:

$$\begin{aligned} &- \alpha \int_{\Omega} (\hat{\zeta} + \mathcal{H}_{\Gamma_d} \tilde{\zeta}) \nabla \cdot \mathbf{v}_s d\Omega + \int_{\Omega} \nabla(\hat{\zeta} + \mathcal{H}_{\Gamma_d} \tilde{\zeta}) \cdot \mathbf{q} d\Omega \\ &- \int_{\Omega} (\hat{\zeta} + \mathcal{H}_{\Gamma_d} \tilde{\zeta}) \frac{1}{M} \frac{\partial p}{\partial t} d\Omega = \int_{\Gamma_f} (\hat{\zeta} + \mathcal{H}_{\Gamma_d} \tilde{\zeta}) f_f d\Gamma. \end{aligned} \quad (4.33)$$

Here we do not consider the fluid leakage. This term is included in the microscopic pressure coupling. The mass balance for the fluid flow in the fracture (4.16) is multiplied by test function ψ :

$$\begin{aligned} & \int_{\Gamma_d^+} \psi \mathbf{q}_{\Gamma_d^+} \cdot \mathbf{n}_d d\Gamma - \int_{\Gamma_d^-} \psi \mathbf{q}_{\Gamma_d^-} \cdot \mathbf{n}_d d\Gamma + \int_{\Gamma_d} \psi \dot{u}_n d\Gamma + \int_{\Gamma_d} \psi u_n \left\langle \frac{\partial \dot{u}_s}{\partial s} \right\rangle d\Gamma \\ & + \int_{\Gamma_d} \psi \frac{u_n}{K_f} \dot{p}_d d\Gamma - \int_{\Gamma_d} \psi u_n \frac{\partial}{\partial s} k_d \frac{\partial p_d}{\partial s} d\Gamma = 0. \end{aligned} \quad (4.34)$$

These two weak equations must hold for all variations of test functions and can therefore be solved separately for $(\hat{\boldsymbol{\eta}} = 0, \tilde{\zeta} = 0)$ and for $(\hat{\boldsymbol{\eta}} = 0, \hat{\zeta} = 0)$. This results in the following four equations

$$\int_{\Omega} (\nabla \hat{\boldsymbol{\eta}}) : \boldsymbol{\sigma} d\Omega = \int_{\Gamma_t} \hat{\boldsymbol{\eta}} \cdot \mathbf{t}_p d\Gamma, \quad (4.35)$$

$$\int_{\Omega} \mathcal{H}_{\Gamma_d} \nabla \tilde{\boldsymbol{\eta}} : \boldsymbol{\sigma} d\Omega + \int_{\Gamma_d} \tilde{\boldsymbol{\eta}} \cdot (\mathbf{t}_d - p_d \mathbf{n}_d) d\Gamma = \int_{\Gamma_t} (\mathcal{H}_{\Gamma_d} \tilde{\boldsymbol{\eta}}) \cdot \mathbf{t}_p d\Gamma, \quad (4.36)$$

$$- \alpha \int_{\Omega} \hat{\zeta} \nabla \cdot \mathbf{v}_s d\Omega + \int_{\Omega} \nabla \hat{\zeta} \cdot \mathbf{q} d\Omega - \int_{\Omega} \hat{\zeta} \frac{1}{M} \frac{\partial p}{\partial t} d\Omega = \int_{\Gamma_f} \hat{\zeta} f_f d\Gamma, \quad (4.37)$$

$$- \alpha \int_{\Omega} \mathcal{H}_{\Gamma_d} \tilde{\zeta} \nabla \cdot \mathbf{v}_s d\Omega + \int_{\Omega} \mathcal{H}_{\Gamma_d} \nabla \tilde{\zeta} \cdot \mathbf{q} d\Omega - \int_{\Omega} \mathcal{H}_{\Gamma_d} \tilde{\zeta} \frac{1}{M} \frac{\partial p}{\partial t} d\Omega = \quad (4.38)$$

$$\int_{\Gamma_f} \mathcal{H}_{\Gamma_d} \tilde{\zeta} f_f d\Gamma.$$

Here we assumed stress continuity over the discontinuity ($\boldsymbol{\sigma} \cdot \mathbf{n}_d = \mathbf{t}_d - p_d \mathbf{n}_d$) and used the definition of the Heaviside function Eq. (4.2).

The fifth equilibrium equation, the mass balance for the fluid flow in the fracture (4.34), can be rewritten by using the divergence theorem in:

$$\int_{\Gamma_d} \psi u_n \frac{\partial}{\partial s} k_d \frac{\partial p_d}{\partial s} d\Gamma = \psi \frac{1}{12\mu} u_n^3 \frac{\partial p_d}{\partial s} \Big|_{S_d} - \int_{\Gamma_d} \frac{1}{12\mu} u_n^3 \frac{\partial \psi}{\partial s} \cdot \frac{\partial p_d}{\partial s} d\Gamma. \quad (4.39)$$

The term $\frac{1}{12\mu} u_n^3 \frac{\partial p_d}{\partial s} \Big|_{S_d}$ represents the fluid inflow at the end of the fracture and is rewritten as

$$\frac{1}{12\mu} u_n^3 \frac{\partial p_d}{\partial s} \Big|_{S_d} = Q_{\text{in}} \Big|_{S_d}. \quad (4.40)$$

This gives the following relation for the mass balance in the discontinuity

$$\begin{aligned}
& \int_{\Gamma_d} \psi \mathbf{q}_{\Gamma_d}^+ \cdot \mathbf{n}_d d\Gamma - \int_{\Gamma_d} \psi \mathbf{q}_{\Gamma_d}^- \cdot \mathbf{n}_d d\Gamma + \int_{\Gamma_d} \psi \dot{u}_n d\Gamma + \int_{\Gamma_d} \psi u_n \left\langle \frac{\partial \dot{u}_s}{\partial s} \right\rangle d\Gamma \\
& + \int_{\Gamma_d} \psi \frac{u_n}{K_f} \dot{p}_d d\Gamma + \int_{\Gamma_d} \frac{1}{12\mu} u_n^3 \frac{\partial \psi}{\partial s} \cdot \frac{\partial p_d}{\partial s} d\Gamma = \psi Q_{\text{in}}|_{S_d}.
\end{aligned} \tag{4.41}$$

4.5 Discretization

The spatial discretization of the balance equations is based on the partition of unity property of finite element shape functions as described in the work of Melenk and Babuška (1996). The variational forms, the displacement field, the pressure field, and the pressure in the fracture are discretized similarly following the Bubnov-Galerkin approach for a single element by:

$$\begin{aligned}
\boldsymbol{\eta} &= \mathbf{N}\hat{\boldsymbol{\eta}} + \mathcal{H}_{\Gamma_d}\mathbf{N}\tilde{\boldsymbol{\eta}}, & \mathbf{u} &= \mathbf{N}\hat{\mathbf{u}} + \mathcal{H}_{\Gamma_d}\mathbf{N}\tilde{\mathbf{u}}, \\
\boldsymbol{\zeta} &= \mathbf{H}\hat{\boldsymbol{\zeta}} + \mathcal{H}_{\Gamma_d}\mathbf{H}\tilde{\boldsymbol{\zeta}}, & p &= \mathbf{H}\hat{\mathbf{p}} + \mathcal{H}_{\Gamma_d}\mathbf{H}\tilde{\mathbf{p}}, \\
\psi &= \mathbf{V}\underline{\boldsymbol{\psi}}, & p_d &= \mathbf{V}\underline{\mathbf{p}}_d,
\end{aligned} \tag{4.42}$$

where \mathbf{N} , \mathbf{H} , and \mathbf{V} are matrices containing the standard shape functions for respectively, the nodal displacement, the pressure, and the pressure in the fracture for all nodes that support the element. Note that the shape functions for the nodal displacement and the pressure are two-dimensional functions while the pressure in fracture is described in an one-dimensional domain (Figure 4.4). The columns $\hat{\mathbf{u}}$ and $\hat{\mathbf{p}}$ contain the continuous nodal values of respectively, the displacement and the pressure while $\tilde{\mathbf{u}}$ and $\tilde{\mathbf{p}}$ contain the values of the enhanced nodes. The column $\underline{\mathbf{p}}_d$ contains the nodal values of the pressure in the fracture. The discretized strain in the bulk can be derived by differentiation as

$$\boldsymbol{\epsilon} = \mathbf{B}\hat{\mathbf{u}} + \mathcal{H}_{\Gamma_d}\mathbf{B}\tilde{\mathbf{u}}, \tag{4.43}$$

where $\mathbf{B} = \mathbf{L}\mathbf{N}^T$ contains the spatial derivative of the standard shape functions. The differential matrix operator \mathbf{L} is in the two-dimensional case defined as

$$\mathbf{L} = \begin{bmatrix} \frac{\partial}{\partial x} & 0 \\ 0 & \frac{\partial}{\partial y} \\ \frac{\partial}{\partial y} & \frac{\partial}{\partial x} \end{bmatrix}. \tag{4.44}$$

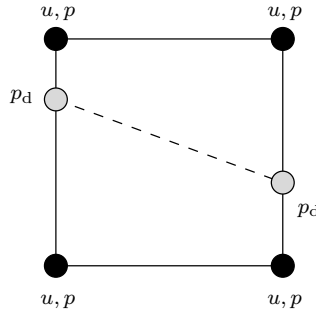


Figure 4.4: Four nodal element with crossed by a discontinuity (dashed line).

The discretized gradient of the pressure is defined as follows:

$$\nabla p = \nabla \mathbf{H} \hat{\mathbf{p}} + \mathcal{H}_{\Gamma_d} \nabla \mathbf{H} \tilde{\mathbf{p}} \quad (4.45)$$

Inserting Equation (4.42) into the weak form of the momentum balance and the mass balance yields in the following relations

$$\int_{\Omega_e} \mathbf{B}^T \boldsymbol{\sigma} d\Omega_e = \int_{\Gamma_t} \mathbf{N}^T \mathbf{t}_p d\Gamma, \quad (4.46)$$

$$\int_{\Omega_e} \mathcal{H}_{\Gamma_d} \mathbf{B}^T \boldsymbol{\sigma} d\Omega_e + \int_{\Gamma_d} \mathbf{N}^T (\mathbf{t}_d - p_d \mathbf{n}_d) d\Gamma = \int_{\Gamma_t} \mathcal{H}_{\Gamma_d} \mathbf{N}^T \mathbf{t}_p d\Gamma, \quad (4.47)$$

$$- \int_{\Omega} \alpha \mathbf{H}^T \mathbf{m}^T \nabla \dot{\mathbf{u}} d\Omega + \int_{\Omega} \nabla \mathbf{H}^T \mathbf{q} d\Omega - \int_{\Omega} \mathbf{H}^T \frac{1}{M} \dot{p} d\Omega = \int_{\Gamma_f} \mathbf{H}^T f_f d\Gamma, \quad (4.48)$$

$$- \int_{\Omega} \alpha \mathcal{H}_{\Gamma_d} \mathbf{H}^T \mathbf{m}^T \nabla \dot{\mathbf{u}} d\Omega + \int_{\Omega} \nabla \mathcal{H}_{\Gamma_d} \mathbf{H}^T \cdot \mathbf{q} d\Omega - \int_{\Omega} \frac{1}{M} \mathcal{H}_{\Gamma_d} \mathbf{H}^T \frac{\partial p}{\partial t} d\Omega = \quad (4.49)$$

$$\int_{\Gamma_f} \mathcal{H}_{\Gamma_d} \mathbf{H}^T f_f d\Gamma,$$

and for the mass balance in the fracture (4.41):

$$\begin{aligned} & \int_{\Gamma_d^+} \mathbf{V}^T (\mathbf{q}_{\Gamma_d}^+ - \mathbf{q}_{\Gamma_d}^-) \cdot \mathbf{n}_d d\Gamma + \int_{\Gamma_d} \mathbf{V}^T \dot{u}_n d\Gamma + \int_{\Gamma_d} \mathbf{V}^T u_n \left\langle \frac{\partial \dot{u}_s}{\partial s} \right\rangle d\Gamma \quad (4.50) \\ & + \int_{\Gamma_d} \mathbf{V}^T \frac{u_n}{K_f} \dot{p}_d d\Gamma + \int_{\Gamma_d} \frac{1}{12\mu} u_n^3 \frac{\partial \mathbf{V}^T}{\partial s} \cdot \frac{\partial p_d}{\partial s} d\Gamma = \mathbf{V}^T Q_{\text{in}}|_{S_d}, \end{aligned}$$

with the vector \mathbf{m} in the two-dimensional situations being defined as $\mathbf{m} = (1, 1, 0)^T$.

To solve these equations the time depended terms are approximated linearly as the difference between the current time step and the previous time step

$$\frac{\partial(\cdot)}{\partial t} = \frac{(\cdot)^{t+\Delta t} - (\cdot)^t}{\Delta t}, \quad (4.51)$$

where $(\cdot)^{t+\Delta t}$ is the unknown solution at the next time step, $(\cdot)^t$ is the known solution from the previous time step, and Δt is the length of the time step. The time independent terms are approximated by the weighted result of the current time step and the new time step:

$$(\cdot) = \bar{\theta}(\cdot)^{t+\Delta t} + (1 - \bar{\theta})(\cdot)^t, \quad \bar{\theta} \in [0, 1]. \quad (4.52)$$

Stabilization is reached if $\bar{\theta} \geq \frac{1}{2}$. The Euler implicit time scheme is retrieved when $\bar{\theta} = 1$, while for $\bar{\theta} = 0$ the explicit Euler scheme is retrieved. Taking a short time step leads to initial oscillations. To have a stable time integration, the following criterion needs to be satisfied (Kraaijeveld, 2009)

$$\Delta t > \frac{\Delta x^2}{cK}. \quad (4.53)$$

Here Δx is the element length and c is defined as $c = 2u + \lambda$.

The resulting system of equations is solved using a Newton-Raphson iterative method. Linearising the aforementioned balance equations (Eqs. 4.46 - 4.50), filling in the the constitutive laws of Terzaghi effective stress (4.18), Darcy's law (4.20), and the leakage law (4.29), and including the spatial discretization (Eq. 4.42) and time discretization (Eqs. 4.51 and 4.52) we can write the final system

$$\begin{bmatrix} \mathbf{K}_{\hat{u}\hat{u}} & \mathbf{K}_{\hat{u}\hat{u}} & \mathbf{C}_{\hat{u}\hat{p}} & \mathbf{C}_{\hat{u}\hat{p}} & \mathbf{0} \\ \mathbf{K}_{\hat{u}\hat{u}} & \mathbf{K}_{\hat{u}\hat{u}} & \mathbf{C}_{\hat{u}\hat{p}} & \mathbf{C}_{\hat{u}\hat{p}} & \mathbf{Q}_{\hat{u}p_d} \\ \mathbf{C}_{\hat{p}\hat{u}} & \mathbf{C}_{\hat{p}\hat{u}} & \mathbf{D}_{\hat{p}\hat{p}} & \mathbf{D}_{\hat{p}\hat{p}} & \mathbf{0} \\ \mathbf{C}_{\hat{p}\hat{u}} & \mathbf{C}_{\hat{p}\hat{u}} & \mathbf{D}_{\hat{p}\hat{p}} & \mathbf{D}_{\hat{p}\hat{p}} & \mathbf{0} \\ \mathbf{Q}_{p_d\hat{u}} & \mathbf{F}_{p_d\hat{u}} & \bar{\theta}\Delta t\mathbf{Q}_{p_d\hat{p}} & \bar{\theta}\Delta t\mathbf{Q}_{p_d\hat{p}} & \mathbf{F}_{p_dp_d} \end{bmatrix} \begin{bmatrix} \partial\hat{\underline{\mathbf{u}}} \\ \partial\hat{\underline{\mathbf{u}}} \\ \partial\hat{\underline{\mathbf{p}}} \\ \partial\hat{\underline{\mathbf{p}}} \\ \partial\hat{\underline{\mathbf{p}}}_d \end{bmatrix} = \begin{bmatrix} \mathbf{f}_{\hat{u}}^{\text{ext}} \\ \mathbf{f}_{\hat{u}}^{\text{ext}} \\ \Delta t\mathbf{f}_{\hat{p}}^{\text{ext}} \\ \Delta t\mathbf{f}_{\hat{p}}^{\text{ext}} \\ \Delta t\mathbf{f}_{p_d}^{\text{ext}} \end{bmatrix} - \begin{bmatrix} \mathbf{f}_{\hat{u}}^{\text{int}} \\ \mathbf{f}_{\hat{u}}^{\text{int}} \\ \mathbf{f}_{\hat{p}}^{\text{int}} \\ \mathbf{f}_{\hat{p}}^{\text{int}} \\ \mathbf{f}_{p_d}^{\text{int}} \end{bmatrix} \quad (4.54)$$

The separate terms of the stiffness matrix are given in Appendix B. The external and internal force are defined as

$$\mathbf{f}_{\hat{u}}^{\text{ext}} = \int_{\Gamma_t} \mathbf{N}^T \mathbf{t}_p^{t+\Delta t} d\Gamma$$

$$\mathbf{f}_{\hat{u}}^{\text{int}} = \int_{\Omega_e} \mathbf{B}^T \boldsymbol{\sigma}_{j-1} d\Omega_e$$

$$\mathbf{f}_{\hat{u}}^{\text{ext}} = \int_{\Gamma_t} \mathcal{H}_{\Gamma_d} \mathbf{N}^T \mathbf{t}_p^{t+\Delta t} d\Gamma$$

$$\mathbf{f}_{\hat{u}}^{\text{int}} = \int_{\Omega_e} \mathcal{H}_{\Gamma_d} \mathbf{B}^T \boldsymbol{\sigma}_{j-1} d\Omega_e + \int_{\Gamma_d^+} h \mathbf{N}^T \{h \mathbf{t}_{d_{j-1}} - p_{d_{j-1}} \mathbf{n}_d\} d\Gamma$$

$$\mathbf{f}_{\hat{p}}^{\text{ext}} = \int_{\Gamma_f} \Delta t \mathbf{H}^T (\bar{\theta} f_f^{t+\Delta t} + (1 - \bar{\theta}) f_f^t) d\Gamma$$

$$\begin{aligned} \mathbf{f}_{\hat{p}}^{\text{int}} = & \mathbf{C}_{\hat{p}\hat{u}} \cdot (\hat{\mathbf{u}}_{j-1}^{t+\Delta t} - \hat{\mathbf{u}}^t) + \mathbf{C}_{\hat{p}\tilde{u}} \cdot (\tilde{\mathbf{u}}_{j-1}^{t+\Delta t} - \tilde{\mathbf{u}}^t) + \Delta t \mathbf{K}_{\hat{p}\hat{p}} \cdot (\bar{\theta} \hat{\mathbf{p}}_{j-1}^{t+\Delta t} + (1 - \bar{\theta}) \hat{\mathbf{p}}^t) \\ & + \Delta t \mathbf{K}_{\hat{p}\tilde{p}} \cdot (\bar{\theta} \tilde{\mathbf{p}}_{j-1}^{t+\Delta t} + (1 - \bar{\theta}) \tilde{\mathbf{p}}^t) + \mathbf{M}_{\hat{p}\hat{p}} \cdot (\hat{\mathbf{p}}_{j-1}^{t+\Delta t} - \hat{\mathbf{p}}^t) + \mathbf{M}_{\tilde{p}\tilde{p}} \cdot (\tilde{\mathbf{p}}_{j-1}^{t+\Delta t} - \tilde{\mathbf{p}}^t) \end{aligned}$$

$$\mathbf{f}_{\hat{p}}^{\text{ext}} = \int_{\Gamma_f} \Delta t \mathcal{H}_{\Gamma_d} \mathbf{H}^T (\bar{\theta} f_f^{t+\Delta t} + (1 - \bar{\theta}) f_f^t) d\Gamma$$

$$\begin{aligned} \mathbf{f}_{\hat{p}}^{\text{int}} = & \mathbf{C}_{\hat{p}\hat{u}} \cdot (\hat{\mathbf{u}}_{j-1}^{t+\Delta t} - \hat{\mathbf{u}}^t) + \mathbf{C}_{\hat{p}\tilde{u}} \cdot (\tilde{\mathbf{u}}_{j-1}^{t+\Delta t} - \tilde{\mathbf{u}}^t) \\ & + \Delta t \mathbf{K}_{\hat{p}\hat{p}} \cdot (\bar{\theta} \hat{\mathbf{p}}_{j-1}^{t+\Delta t} + (1 - \bar{\theta}) \hat{\mathbf{p}}^t) + \Delta t (\mathbf{K}_{\tilde{p}\tilde{p}} + \mathbf{Q}_{\tilde{p}\tilde{p}}) \cdot (\bar{\theta} \tilde{\mathbf{p}}_{j-1}^{t+\Delta t} + (1 - \bar{\theta}) \tilde{\mathbf{p}}^t) \\ & + \mathbf{M}_{\hat{p}\hat{p}} \cdot (\hat{\mathbf{p}}_{j-1}^{t+\Delta t} - \hat{\mathbf{p}}^t) + \mathbf{M}_{\tilde{p}\tilde{p}} \cdot (\tilde{\mathbf{p}}_{j-1}^{t+\Delta t} - \tilde{\mathbf{p}}^t) \end{aligned}$$

$$\mathbf{f}_{p_d}^{\text{ext}} = \mathbf{H} \mathbf{Q}_{\text{in}} |_{S_d}$$

$$\begin{aligned} \mathbf{f}_{p_d}^{\text{int}} = & \mathbf{Q}_{p_d \hat{u}} \cdot (\hat{\mathbf{u}}_{j-1}^{t+\Delta t} - \hat{\mathbf{u}}^t) + (\mathbf{Q}_{p_d \tilde{u}}^{(1)} + \mathbf{Q}_{p_d \tilde{u}}^{(3)}) \cdot (\tilde{\mathbf{u}}_{j-1}^{t+\Delta t} - \tilde{\mathbf{u}}^t) \\ & + \Delta t \mathbf{Q}_{p_d \hat{p}} \cdot (\bar{\theta} \hat{\mathbf{p}}_{j-1}^{t+\Delta t} + (1 - \bar{\theta}) \hat{\mathbf{p}}^t) + \Delta t \mathbf{Q}_{p_d \tilde{p}} \cdot (\bar{\theta} \tilde{\mathbf{p}}_{j-1}^{t+\Delta t} + (1 - \bar{\theta}) \tilde{\mathbf{p}}^t) \\ & + \mathbf{Q}_{p_d p_d}^{(2)} \cdot (\mathbf{p}_{d_{j-1}}^{t+\Delta t} - \mathbf{p}_d^t) + \Delta t \mathbf{Q}_{p_d p_d}^{(3)} \cdot (\bar{\theta} \mathbf{p}_{d_{j-1}}^{t+\Delta t} + (1 - \bar{\theta}) \mathbf{p}_d^t) \\ & + \Delta t \bar{\theta} \frac{\delta \mathbf{H}}{\delta s} q_{t_{j-1}}^{t+\Delta t} + \Delta t (1 - \bar{\theta}) \frac{\delta \mathbf{H}}{\delta s} q_t^t \end{aligned}$$

with q_t being the tangential fluid flow:

$$q_t = \frac{1}{12\mu} u_n^3 \frac{\partial \mathbf{H}^T}{\partial s} \mathbf{p}_d. \quad (4.55)$$

4.6 Numerical implementation

The most important aspects of the numerical implementation and the ELP implementation are summarized in this section. The numerical implementation and description is similar to the work of Remmers et al. (Remmers et al., 2008; Remmers, 2006) and is also summarized in more detail in Paragraph 2.3.

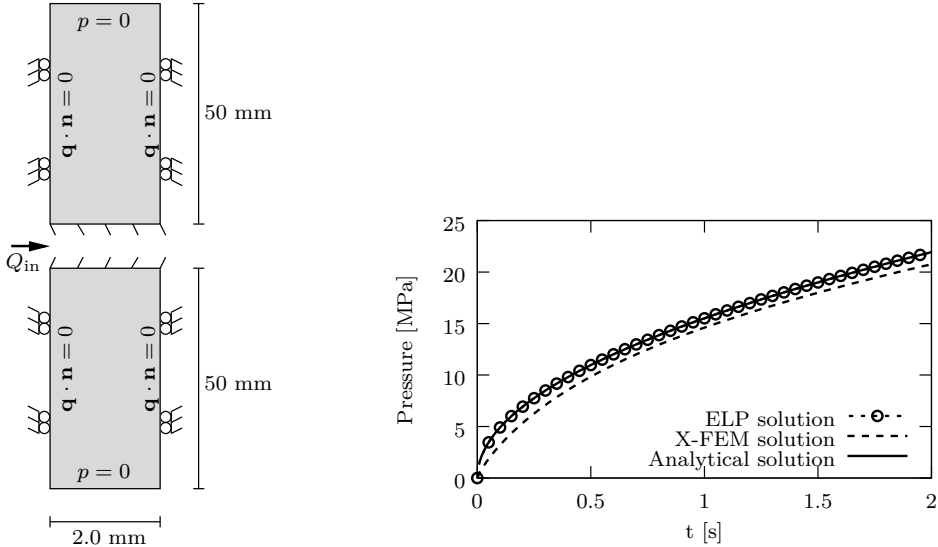
Nucleation and propagation of cohesive zones are based on the Camacho-Ortiz average stress criterion (Camacho and Ortiz, 1996). The average stress is calculated by a Gaussian weighting function that is depended on a length scale parameter l_a . The nodes surrounding a discontinuity are enhanced the additional degrees of freedom. It is assumed that the discontinuity through an element is a straight line and always ends at the edge of the element. The fracture can grow through multiple elements in one time step. Numerical integration is performed with the standard Gaussian integration. Due to the arbitrary locations of the discontinuity the original integration points are not sufficient any more to. Therefore, the adopted integration scheme introduced by Wells and Sluys (2001) is used for elements that are crossed by a discontinuity. The balance equation over the discontinuity are integrated by two integration points per element. The additional degree of freedom for the ELP model is carried by new nodes placed on the cross-points of the discontinuity and the element edge. These nodes only contribute to the one-dimensional pressure field in the discontinuity, see Figure 4.4.

4.7 Examples

In this section three examples are considered. In the first two examples the enhanced local pressure model is used but also an extended finite element method based model with a continuous pressure profile across the fracture. In the third example we only use the ELP model. The X-FEM model is similar to the model used in Chapters 2 and 3 but does include the possibility to simulate hydraulic fracturing. More details about the model can thus be found in those two chapters but also in the work of Kraaijeveld et al. (2013).

In the first example, we inject a constant volume in an opened fracture. With this example we illustrate the differences between the ELP and X-FEM model for the pressure in the fracture and the pressure profile at either sides of the fracture. In the second example, both models are compared with an analytical solution for hydraulic fracture propagation. In the third

example we consider fracture nucleation and propagation from a circular hole. An implicit time scheme ($\theta = 1$) is used in both examples under two dimensional plane strain settings.



(a) Flow through a discontinuity. (b) Pressure in the discontinuity for the ELP model and the X-FEM model.

Figure 4.5: Schematic representation of the consolidation of a soil column due to flow through a discontinuity (a) and the result for the pressure in the discontinuity over the time (b).

4.7.1 Fluid leakage from an opened fracture

In this example we benchmark the analytical leakage approximation (Eq. 4.29) with the numerical models. Consider a column of rock formation with a horizontal traction free initial fracture in the middle of the column (Figure 4.5a). The top and bottom surfaces of the column are both moved 0.01 mm away from the fracture creating a highly permeable fracture. The top and bottom fracture surfaces are then fixed in displacement and fluid is being injected with a constant rate $Q_{in} = 2.0e^{-5} \text{ m}^2/\text{s}$ at the left fracture entrance and the time step is taken as $\Delta t = 0.01 \text{ s}$. We assume that the opened fracture is filled with fluid so that all injected fluid must leak into the rock formation. The rock formation has an intrinsic permeability $k_{int} = 1.0e^{-20} \text{ m}^2$ and a fluid viscosity $\mu = 1.0e^{-4} \text{ Pa} \cdot \text{s}$. The Young's modulus equals $E = 17.0 \text{ GPa}$ with a Poisson's ratio of $\nu = 0.2$. Both solid

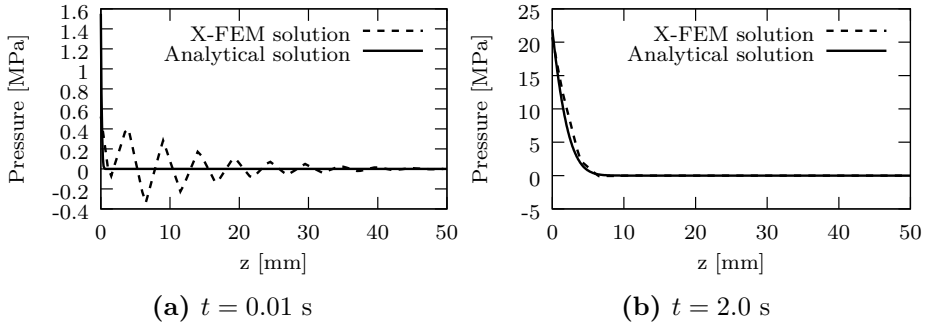


Figure 4.6: Pressure for various times for the X-FEM model due to a constant fluid flow in the discontinuity.

and fluid constituents are considered to be compressible with $K_s = 36.0$ GPa and $K_f = 3.0$ GPa.

The consolidation distance of one time step can be approximated by $\Delta x_{\text{crit}} = \sqrt{(\Delta t E k)} = 0.13$ mm (Vermeer and Verruijt, 1981). To resolve the pressure gradient it is necessary to use elements with an height smaller than this consolidation distance. We violate this criterion deliberately by using elements with a height of 3.5 mm. In Figure 4.5b we show that we can still predict the pressure in the fracture with the ELP model while the X-FEM model underestimates that fluid pressure. The pressure profile across the fracture for the X-FEM model at various times is shown in Figure 4.6. It is clear that the pressure profile is not resolved in the X-FEM model, at early times (Figure 4.6a), due to the large mesh size. This may lead to inaccurate results or numerical instabilities. At $t = 2.0$ s the consolidation distance is $\Delta x_{\text{crit}} = 1.8$ mm. Since the element at the fracture surface is divided in half, the consolidation distance is larger than the length over which the numerical integration takes place. In Figure 4.6b it can be seen that indeed the X-FEM model can now resolve the pressure gradient on both sides of the fracture.

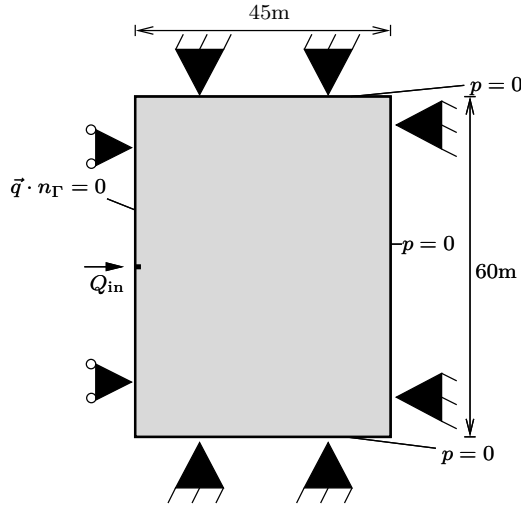


Figure 4.7: Scheme of the KGD fracture problem

4.7.2 KGD fracture problem

In this example, we analyse the KGD fracture problem as shown in Figure 4.7 (Geertsma and De Klerk, 1969). We consider a material with intrinsic permeability $k_{\text{int}} = 1.0e^{-18} \text{ m}^2$ and a fluid viscosity of $\mu = 1.0e^{-5} \text{ Pa} \cdot \text{s}$. The fracture toughness of the solid skeleton is taken as $\mathcal{G}_c = 120.0 \text{ N/m}$ with an ultimate strength of $\tau_{\text{ult}} = 3.75 \text{ Mpa}$. The fluid injection rate $Q_{\text{in}} = 0.0005 \text{ m}^2/\text{s}$ is assumed to be constant. The remainder of material properties and time discretization properties are equal to the previous example. The mesh near the fracture path is made of squared, $50.0 \times 50.0 \text{ mm}$, elements.

Figure 4.8 shows the pressure across the fracture with a single point indicating the pressure in fracture for the ELP model. It is not needed to resolve the pressure gradient caused by fluid leakage in the ELP model due to the analytical approximation of the pressure gradient. There are pressure oscillations near the fracture surface for the X-FEM model. Also, the pressure in the fracture simulated by X-FEM, is lower than in the rock formation. This leads to fluid being attacked into the fracture instead of fluid leakage to rock formation.

Bunger et al. (2005) derived an analytical solution for this type of fracture problem including fluid leak-off but neglecting any poroelastic effects in the bulk material. With the material properties the hydraulic fracture propagates in the storage dominated regime. The analytical solution approximates the fluid leak-off based with Carter's law (Howard and Fast,

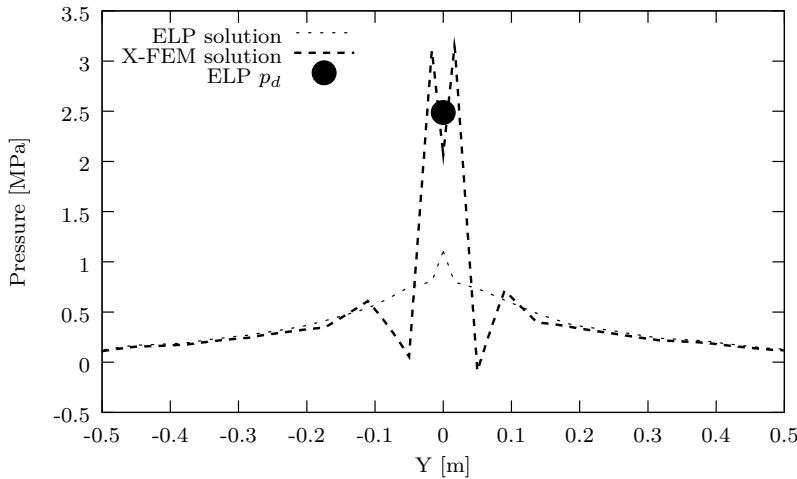


Figure 4.8: Pressure distribution across the fracture for the ELP model and the X-FEM model. The black dot indicates pressure in the fracture for the ELP model.

1957):

$$Q_{leakage} = \frac{2C_L}{\sqrt{t - t_0(x)}}, \quad (4.56)$$

where C_L is the leak-off coefficient, t is the current time, and t_0 is the time when the fracture arrived at position x . The leakage coefficient is an input parameter for the analytical solution and is therefore calculated by fitting equation (4.56) to the numerical leakage using the least squares method. The analytical solution is calculated with a leakage coefficient of $C_l = 5.6e^{-6} \text{ m}/\sqrt{\text{s}}$ obtained by fitting with the ELP results. The leakage in the X-FEM model could not be fitted by Carter's law. The comparison between the analytical solution and the numerical models is shown in Figure 4.9. There is some discrepancy between the numerical models and the analytical solution. We attribute this to the differences between the numerical formation and the analytical solution. Namely, we describe the fracture process with a cohesive zone while the analytical solution is based on linear elastic fracture mechanics. Another significant difference is that the rock is linear elastic in the analytical solution but we include poro-elastic effects in the rock formation.

To illustrate the difference between the ELP and the X-FEM model we repeat the KGD fracture example with 4 different meshes. These meshes have a constant element size of $\ell_x = 20.0 \text{ mm}$ in the fracture direction.

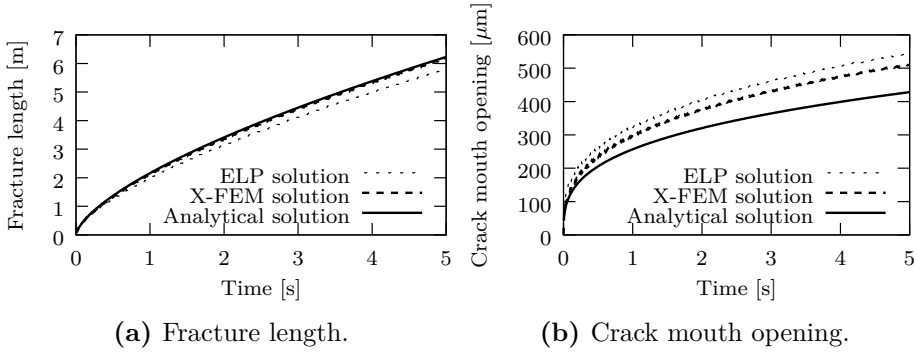


Figure 4.9: The results of the numerical models and the analytical solution plotted against the time.

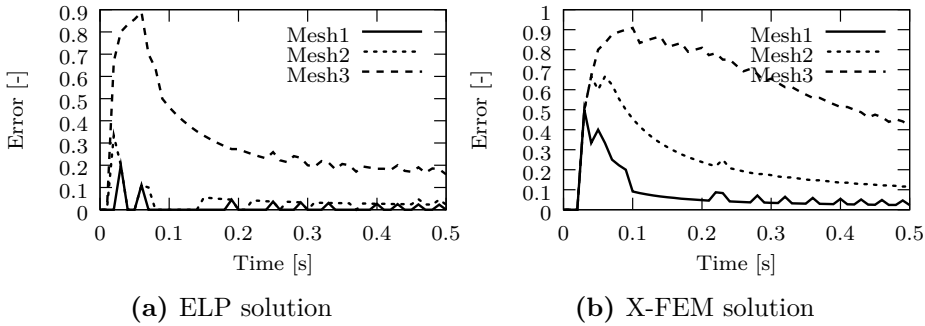


Figure 4.10: Absolute error in the fracture length for the ELP and X-FEM models.

The mesh is refined in the y -direction, with a smallest element size of $\ell_y = 78.94$ mm. We validated that the numerical solution did not converge further using smaller elements. Therefore, we use this mesh as a reference solution. The reference solution is compared with 3 different meshes, having element sizes of $\ell_y = 100.0$ mm, $\ell_y = 166.6$ mm and $\ell_y = 300.0$ mm referred to as respectively, mesh 1, mesh 2 and mesh 3. The absolute error in the fracture length with respect to the reference solution for these 3 meshes is shown for the ELP model and the X-FEM model in respectively, Figure 4.10a and Figure 4.10b. It is clear from these graphs that the error in the X-FEM models is larger and does not converge as fast to the reference solution as the ELP model.

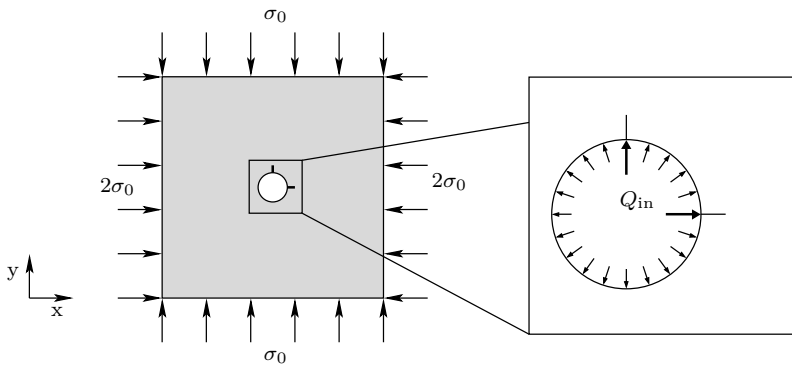


Figure 4.11: Scheme of the borehole fracture problem.

4.7.3 Fracture from a circular hole

In the final example the ELP model is used to model a propagating fracture growing from a two-dimensional circular hole (Figure 4.11). It assume that the confining stress $\sigma_0 = 1.25$ MPa in the y-direction is the half of the stress in the x-direction. We create two initial fractures, one perpendicular and one parallel to the highest confining stress. The fluid inflow $Q_{\text{in}} = 10.0$ mm²/s is constant and is distributed between the two fractures. Therefore, we assume that the fluid pressure is constant and equal in both fractures. The pressure at the fracture inlet is applied as a load on the circular wall to allow for deformations. The rock formation has an intrinsic permeability of $k_{\text{int}} = 1.0e^{-18}$ m² and a fluid viscosity of $\mu = 1.0e^{-4}$ Pa · s. The fracture toughness is taken as $\mathcal{G}_c = 120.0$ N/m and the ultimate strength as $\tau_{\text{ult}} = 1.25$ Mpa. A time step of $\Delta t = 6.0$ s is used. The remainder of material properties are again the same as the first example.

The initial stress concentration has been validated with Kirsch's analytical solution (Kirsch, 1898). From experimental measurements it is known that the preferred propagation direction of a hydraulic fracture is perpendicular to the minimum confining stress (Rahman et al., 2002). To illustrate this we also perform the simulation with only the initial fracture in the y-direction. The results of these two simulations can be seen Figure 4.12. In the left column it is shown that the fracture indeed turns in the direction of minimum confining stress. In the situation of two fractures (right column), only the fracture that is initially already perpendicular to the minimum confining stress propagates. This is expected as it costs less energy to grow the fracture in this direction. At the left side of the circular hole stress is being generated due to the loading of the circular wall.

In the next simulation we do consider the possibility of fracture nucleation. We start the simulation with only the initial fracture perpendicular to the highest confining stress (Figure 4.13a). The stress generated at both sides of the circular hole leads to the nucleation of two new fractures (Figure 4.13b).

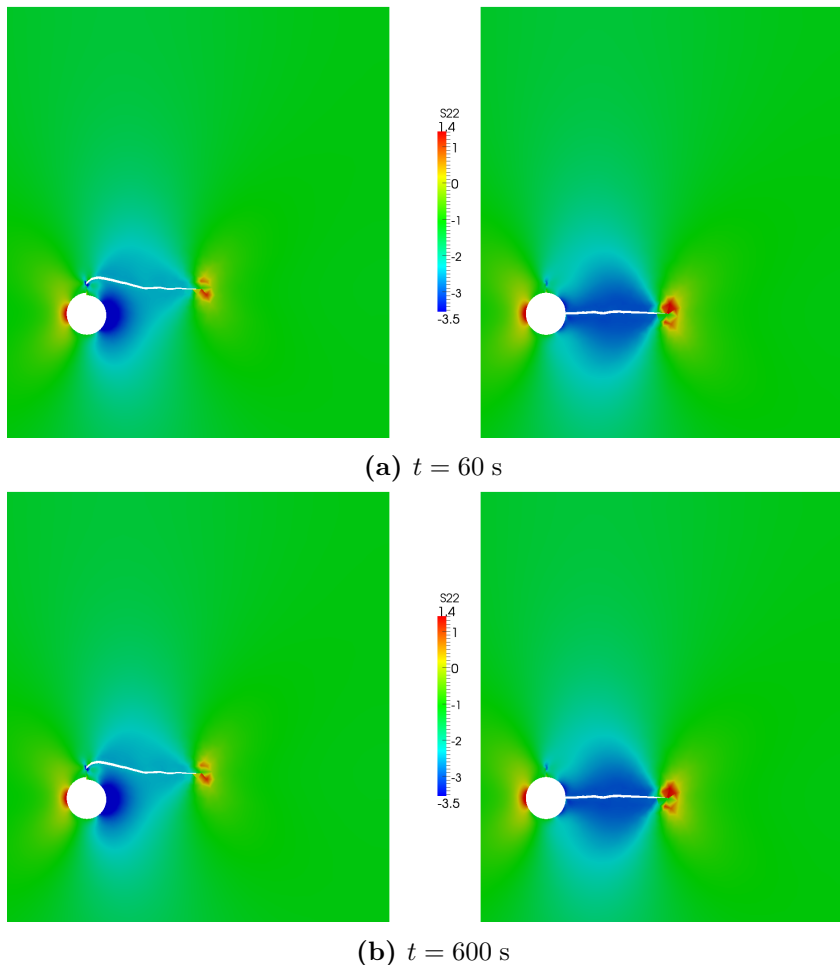


Figure 4.12: Contour plots effective stress for the circular hole fracture problem. The deformed configuration is magnified 100 times. The results of the simulation with only one fracture in the y-direction are shown in the left column. The right column contains the results of the simulation with two fractures.

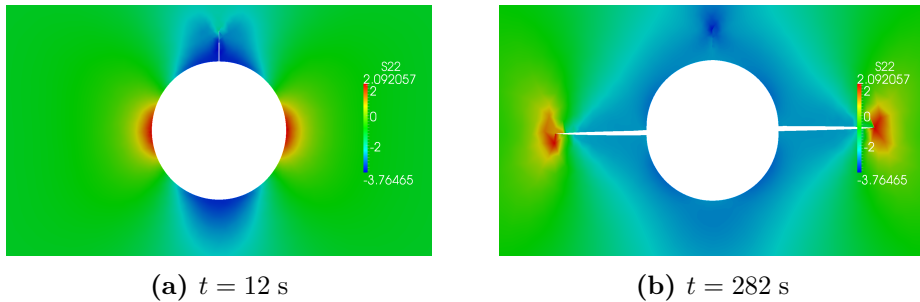


Figure 4.13: Contour plots of the effective stress for the circular hole. The deformed configuration is magnified 100 times. In the left figure, the situation before fracture nucleation is shown. In the right figure, the two nucleated fractures in preferential fracture direction are shown.

4.8 Conclusion

In this chapter, the enhanced local pressure model is presented. By exploiting the partition of unity property of finite element shape functions the method captures the discontinuous fracture. The fracture process is modelled by means of a cohesive zone description. The local, additional, degree of freedom for the pressure ensures that fluid flow goes exclusively in the fracture. The steep pressure gradient that may occur locally near the fracture surface is reconstructed based on Terzaghi's analytical solution.

We have illustrated this effect with an example where fluid is being injected in an opened fracture. Using an X-FEM model with a continuous pressure approach the pressure gradient can not be resolved at low time scales. The pressure in the fracture calculated with the ELP model is consistent with the analytical solution. We also have shown that at higher time scales the continuous X-FEM does describe the pressure gradient near the fracture surface. This indicates that the ELP model is better capable to model hydraulic fracturing at early stages while at later stages a switch to the continuous X-FEM should be considered.

In the second example we have compared the propagation of an hydraulic fracture under an constant fluid injection with an analytical solution in the storage dominated regime. The trend of the ELP model is comparable to the analytical solution. We attribute this due to the fact that the analytical solution is based on different assumptions such as linear elastic fracture mechanics and that poro-elastic effect in the rock formation are neglected. We also have demonstrated with a mesh refinement study that ELP model converges the reference solution faster than the X-FEM model.

In the last example we have considered fracture propagation from a circular hole that can deform depending on the pressure in fracture. Here we have shown that the fracture can grow in arbitrary propagation angles. The fracture propagates in the direction parallel to the highest confining stress. This behaviour is energetically favourable and is also in agreement with experimental data. In this example we have also included fracture nucleation. As expected the fractures nucleates in the plane of lowest confining stress.

Based on our results we conclude that the ELP model has significant advantages compared to the continuous X-FEM model in hydraulic fracturing of low permeable rock formations such as shales. Fluid can be injected exclusively in the fractures and it is not necessary to have a dense mesh to resolve the pressure gradient near the fracture.

Natural fracture networks exist in reservoirs and may interact with hydraulic fractures. The natural fracture may open upon the encounter with a hydraulic fracture providing a connected network to the well (Gale et al., 2007). Determining whether or not natural fractures open is important to optimize the fracture treatment. In the following chapter the enhanced local pressure model is improved to also include fracture interaction. With this model interaction behaviour between a hydraulic fracture and an existing fracture network can be studied.

5

Simulation of crack interaction

Abstract

In this chapter, the Enhanced Local Pressure (ELP) model is used to study crack interaction in hydraulic fracturing. The method is based on the eXtended Finite Element Method (X-FEM) where the pressure and the displacement fields are assumed to be discontinuous over the fracture exploiting the partition of unity property of finite element shape functions. The material is fully saturated and Darcy's law describes the fluid flow in the material. The fracture process is described by a cohesive traction-separation law, whereas the pressure in the fracture is included by an additional degree of freedom. Interaction of a hydraulic fracture with a natural fracture is considered by assuming multiple discontinuities in the domain. The model is able to capture several processes, such as fracture arrest on the natural fracture, or hydraulic fractures that cross the natural fracture. Fluid is able to flow from the hydraulic fracture into the natural fracture is taken into account as well. Two numerical criteria are implemented to determine whether or not the fracture is crossing or if fluid diversion occurs. Computational results showing the performance of the model and the effectiveness of the two criteria are presented. The influence of the angle between a hydraulic fracture and a natural fracture on the interaction behaviour is compared with experimental results and theoretical data.

The Enhanced Local Pressure (ELP) model was introduced in Chapter 4 for the simulation of hydraulic fracturing. The model is consistent with an analytical solution and fracture path dependency on the in situ stress conditions was observed. The simulations were limited to one or two hydraulic fractures and no fracture interaction was considered. However, interaction of a hydraulic fracture with a pre-existing fracture network is an important aspect in correctly predicting a hydraulic fracture network. Tectonic stress rotations tilt the natural fracture network at the time of the fracture formation which may result in tilt fractures that are not aligned with the maximum horizontal stress. Natural fractures may therefore intersect with hydraulic fractures, altering the propagation path leading to complex fracture geometries (Maxwell et al., 2002).

Lee et al. (2015) demonstrated experimentally the influence of calcite filled natural fractures on the propagation path of a mechanically induced fracture in shale rocks. Blanton (1982) showed by means of experiments that an induced hydraulic fracture may either cross a natural fracture, arrest onto the fracture, divert into the natural fracture or cross the natural fracture. These different hydraulic pathways interacting with a natural fracture are shown in Figure 5.1. The experiments show that the inclination angle between the natural fracture and the hydraulic fracture in relation to the in situ stress differences is important in determining which of the phenomena occurs. Zhou et al. (2008) performed similar experiments and investigated and demonstrated the influence the friction in the natural fracture.

In a theoretical study, Renshaw and Pollard (1995) studied a propagating fracture across an orthogonal interface and derived an analytical criterion, which was validated by experiments. The criterion is based on Linear Elastic Fracture Mechanics (LEFM) under the assumption that no slip occurs along the interface before the two fractures merge. The possibility of the fracture to divert into the natural fracture is not considered in this study. The criterion has been validated and extended by means of experiments for non-orthogonal angles by Gu et al. (2012) by solving the criterion numerically.

Another mechanism that causes crack tip branching occurs when the fracture propagation speed exceeds the Rayleigh wave speed of the material Freund (1998); Xu and Needleman (1994). Valko and Economides (1995) showed that hydraulic fractures propagate more slowly than the Rayleigh wave speed criterion. Therefore, branching of a single hydraulic fracture does not appear and does not have to be considered.

The eXtended Finite Element Method (X-FEM) is a proven concept

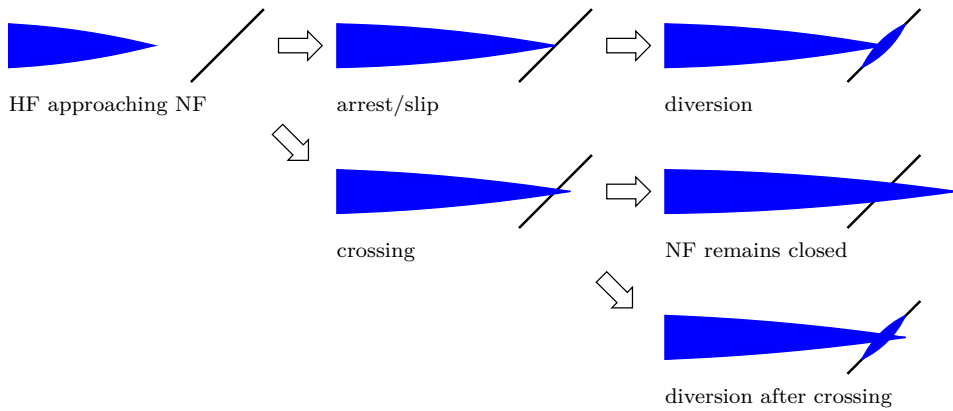


Figure 5.1: Possible pathways due to a hydraulic fracture (HF) interacting with a natural fracture (NF).

in numerical modelling of crack propagation and has the advantage that there is no need to remesh the domain (Belytschko and Black, 1999), i.e. the topology of the original mesh does not need to be modified as the crack evolves. By exploiting the partition of unity property of finite element shape functions, a crack is represented as a discontinuity in the displacement field (Melenk and Babuška, 1996). The discontinuity can simply be placed in arbitrary locations in the finite element mesh by adding additional degrees of freedom to existing nodes (Moës et al., 1999). Daux et al. (2000) showed that multiple discontinuities can be included in a similar manner by stacking up one additional set of degrees of freedom per discontinuity.

Dahi-Taleghani and Olson (2011) developed an X-FEM based model for the interaction between hydraulic and natural fractures. The influence of a diverted hydraulic fracture was compared to the fracture wing that did not interact. Khoei et al. (2016) used a similar approach but included frictional contact based on plasticity theory of friction using a penalty method. Similar to Dahi-Taleghani and Olson (2011), fracture crossing was not considered yet in their work. In addition, these X-FEM models did not consider the porosity of the bulk material. Nevertheless, the method was applied successfully for fracturing in porous materials, see e.g. (de Borst et al., 2006; Mohammadnejad and Khoei, 2012), also in combination with a single hydraulic fracture (Mohammadnejad and Khoei, 2013). Other methods that considered hydraulic fracturing in porous media are e.g. based on interface elements with a cohesive zone Carrier and Granet (2012), remeshing techniques (Secchi and Schrefler, 2012) and phase field approaches (Mikelić et al., 2015).

The ELP model, described in Chapter 4, was specifically developed for hydraulic fracturing in very low permeable rocks. The pressure is assumed to be discontinuous over the fracture to prevent the necessity to resolve the very steep pressure gradient near the fracture surface. By including an additional degree of freedom to account for the pressure in the fracture it is ensured that all the injected fluid goes into the fracture. Fluid leakage is included by an analytical solution based on Terzaghi's 1D consolidation equation.

In this chapter we extend the ELP model to account for multiple, interacting fractures. These fractures are included by adding a set of additional degrees of freedom for each fracture. Upon interaction of a hydraulic fracture with a natural fracture, the hydraulic fracture can either cross the natural fracture or fluid can divert into the natural fracture. The former is based on an average stress criterion and the latter on the opening displacement of the natural fracture. Both can happen simultaneously and are based on the numerical results so no additional theoretical criterion is needed. Compared to previously mentioned methods we include fracture crossing and fluid diversion simultaneously. The advantage of X-FEM, i.e. fracture growth irrespective of the underlying finite element mesh, is exploited with the ELP model. With the proposed model it is possible to predict the interaction mechanics between a hydraulic fracture and a natural fracture network in a poro-elastic material. We demonstrate the performance of the model by investigating four numerical examples.

5.1 Model background

5.1.1 Kinematic relations

The kinematic relations as described in Section 4.1 are followed in this section. Consider the body Ω , which contains m discontinuities, see Figure 5.2a. Each discontinuity Γ_i separates the domain in a two parts, Ω_i^+ and Ω_i^- . We can write the total displacement field at any time t , following the traditional X-FEM approach (Belytschko and Black, 1999; Moës et al., 1999; Remmers et al., 2008), as a continuous displacement field $\hat{\mathbf{u}}(\mathbf{x}, t)$ and m additional displacement fields $\tilde{\mathbf{u}}_i(\mathbf{x}, t)$. The total displacement field can be written as (Daux et al., 2000)

$$\mathbf{u}(\mathbf{x}, t) = \hat{\mathbf{u}}(\mathbf{x}, t) + \sum_{i=1}^m \mathcal{H}_{\Gamma_{d_i}}(\mathbf{x}) \tilde{\mathbf{u}}_i(\mathbf{x}, t), \quad (5.1)$$

where \mathbf{x} is the position of a material point and $\mathcal{H}_{\Gamma_{d_i}}$ is the Heaviside step

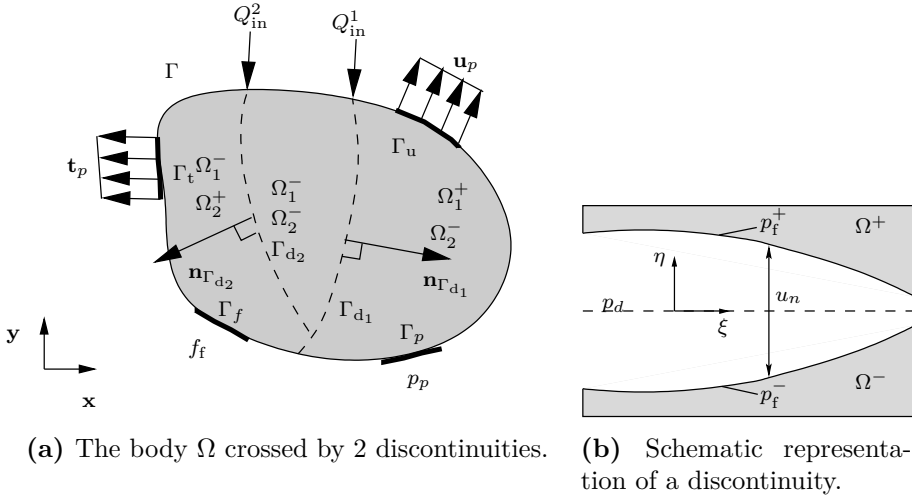


Figure 5.2: (a) Schematic representation of body Ω crossed by two discontinuities (dashed lines). The discontinuities, represented by a normal vector, divide the body in a positive and a negative part. (b) Schematic representation of a discontinuity including the local coordinate system.

function defined across discontinuity i as

$$\mathcal{H}_{\Gamma_{d_i}} = \begin{cases} 1 & \text{if } \mathbf{x} \in \Omega_i^+ \\ 0 & \text{if } \mathbf{x} \in \Omega_i^- \end{cases} \quad (5.2)$$

The pressure field is decomposed in a similar fashion in a continuous field $\hat{p}(\mathbf{x}, t)$ and m discontinuous pressure fields $\tilde{p}_i(\mathbf{x}, t)$

$$p(\mathbf{x}, t) = \hat{p}(\mathbf{x}, t) + \sum_{i=1}^m \mathcal{H}_{\Gamma_{d_i}}(\mathbf{x}) \tilde{p}_i(\mathbf{x}, t). \quad (5.3)$$

At the discontinuity, inside the crack, the pressure is equal to an independent variable p_d (Figure 5.2b).

$$p_d = p \quad \mathbf{x} \in \Gamma_d. \quad (5.4)$$

The displacement jump across discontinuity i is written as

$$[\mathbf{u}]_i = [\mathbf{u}]_i^+ - [\mathbf{u}]_i^- = \sum_{j=1}^m \left[\mathcal{H}_{\Gamma_{d_j}}(\mathbf{x}_i^+) - \mathcal{H}_{\Gamma_{d_j}}(\mathbf{x}_i^-) \right] \tilde{\mathbf{u}}_j(\mathbf{x}_i, t), \quad (5.5)$$

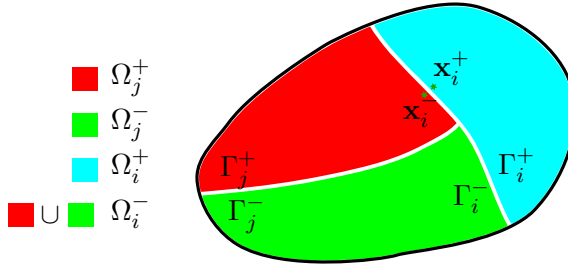


Figure 5.3: Representation of the opening of body Ω due to two discontinuities. The colours indicate the positive and negative domains used in the definition of the Heaviside function, Eq. (5.2). The points \mathbf{x}_i^+ and \mathbf{x}_i^- indicate the locations at the positive and negative side of discontinuity i , respectively.

where the notations $^+$ and $^-$ are used for the same location but located compared to the positive and the negative side of discontinuity, respectively, see Figure 5.3. This can be rewritten as

$$[\mathbf{u}]_i = \tilde{\mathbf{u}}_i(\mathbf{x}_i, t) + \sum_{j=1, j \neq i}^m \left[\mathcal{H}_{\Gamma_{d_j}}(\mathbf{x}_i^+) - \mathcal{H}_{\Gamma_{d_j}}(\mathbf{x}_i^-) \right] \tilde{\mathbf{u}}_j(\mathbf{x}_i, t). \quad (5.6)$$

The first term in this equation is the jump caused by discontinuity i The second term the jump caused by other discontinuities in the domain.

5.1.2 Weak form

The weak form for multiple discontinuities can be derived by multiplying the balance equation in Section 4.2 with admissible test functions in the same form as the displacement field and the pressure field as

$$\boldsymbol{\eta} = \hat{\boldsymbol{\eta}} + \sum_{k=1}^m \mathcal{H}_{\Gamma_{d_k}} \tilde{\boldsymbol{\eta}}_k \quad \zeta = \hat{\zeta} + \sum_{k=1}^m \mathcal{H}_{\Gamma_{d_k}} \tilde{\zeta}_k. \quad (5.7)$$

where $\boldsymbol{\eta}$ and ζ are the admissible displacement and pressure fields, respectively.

Multiplying the momentum balance with test function $\boldsymbol{\eta}$, including boundary conditions and using Gauss's theorem, gives the weak form of the momentum balance:

$$\begin{aligned}
& \int_{\Omega} \nabla \hat{\boldsymbol{\eta}} : \boldsymbol{\sigma} d\Omega + \sum_{k=1}^m \int_{\Omega} \mathcal{H}_{\Gamma_{d_k}} \nabla \tilde{\boldsymbol{\eta}}_k : \boldsymbol{\sigma} d\Omega = \\
& \int_{\Gamma_t} (\hat{\boldsymbol{\eta}} + \sum_{k=1}^m \mathcal{H}_{\Gamma_{d_k}} \tilde{\boldsymbol{\eta}}_k) \cdot \mathbf{t}_p d\Gamma_t \\
& - \sum_{j=1}^m \int_{\Gamma_{d_j}} \hat{\boldsymbol{\eta}} \cdot [\boldsymbol{\sigma}_j^+ \mathbf{n}_j^+] d\Gamma_{d_j} - \sum_{k=1}^m \sum_{j=1}^m \int_{\Gamma_{d_j}} \tilde{\boldsymbol{\eta}}_k \cdot [\mathcal{H}_{\Gamma_{d_k}}(\Gamma_{d_j}^+) \boldsymbol{\sigma}_j^+ \mathbf{n}_j^+] d\Gamma_{d_j} \\
& - \sum_{j=1}^m \int_{\Gamma_{d_j}} \hat{\boldsymbol{\eta}} \cdot [\boldsymbol{\sigma}_j^- \mathbf{n}_j^-] d\Gamma_{d_j} - \sum_{k=1}^m \sum_{j=1}^m \int_{\Gamma_{d_j}} \tilde{\boldsymbol{\eta}}_k \cdot [\mathcal{H}_{\Gamma_{d_k}}(\Gamma_{d_j}) \boldsymbol{\sigma}_j^- \mathbf{n}_j^-] d\Gamma_{d_j}.
\end{aligned} \tag{5.8}$$

Here, we use the notations $\mathcal{H}_{\Gamma_{d_k}}(\Gamma_{d_j}^+)$ and $\mathcal{H}_{\Gamma_{d_k}}(\Gamma_{d_j}^-)$ for the Heaviside function of variational field k integrated over discontinuity j for the positive and negative side, respectively. The traction at the interface is equal to $\mathbf{t}_j = \boldsymbol{\sigma}_j^+ \mathbf{n}_j^+ = -\boldsymbol{\sigma}_j^- \mathbf{n}_j^-$ where we used $\mathbf{n}_j^d = \mathbf{n}_j^+ = -\mathbf{n}_j^-$. Separation of the tractions into one part where the variational displacement $\tilde{\boldsymbol{\eta}}_k$ is acting on discontinuity $d\Gamma_{d_k}$ and into one part for the remainder of discontinuities, i.e. $j \neq k$ gives

$$\begin{aligned}
& \int_{\Omega} \nabla \hat{\boldsymbol{\eta}} : \boldsymbol{\sigma} d\Omega + \sum_{k=1}^m \int_{\Omega} \mathcal{H}_{\Gamma_{d_k}} \nabla \tilde{\boldsymbol{\eta}}_k : \boldsymbol{\sigma} d\Omega = \\
& \int_{\Gamma_t} \hat{\boldsymbol{\eta}} \cdot \mathbf{t}_p d\Gamma_t + \sum_{k=1}^m \int_{\Gamma_t} \mathcal{H}_{\Gamma_{d_k}} \tilde{\boldsymbol{\eta}}_k \cdot \mathbf{t}_p d\Gamma_t - \sum_{k=1}^m \int_{\Gamma_{d_k}} \tilde{\boldsymbol{\eta}}_k \cdot \mathbf{t}_k d\Gamma_{d_k} \\
& - \sum_{k=1}^m \tilde{\boldsymbol{\eta}}_k \cdot \left(\sum_{j=1, j \neq k}^m \int_{\Gamma_{d_j}} [\mathcal{H}_{\Gamma_{d_k}}(\Gamma_{d_j}^+) - \mathcal{H}_{\Gamma_{d_k}}(\Gamma_{d_j}^-)] \mathbf{t}_j d\Gamma_{d_j} \right).
\end{aligned} \tag{5.9}$$

Multiplying the mass balance with test function ζ gives

$$\begin{aligned}
& - \int_{\Omega} \alpha (\hat{\zeta} + \sum_{k=1}^m \mathcal{H}_{\Gamma_{d_k}} \tilde{\zeta}_k) \nabla \cdot \mathbf{v}_s d\Omega \\
& + \int_{\Omega} \nabla (\hat{\zeta} + \sum_{k=1}^m \mathcal{H}_{\Gamma_{d_k}} \tilde{\zeta}_k) \cdot \mathbf{q} d\Omega - \int_{\Omega} \frac{1}{M} (\hat{\zeta} + \sum_{k=1}^m \mathcal{H}_{\Gamma_{d_k}} \tilde{\zeta}_k) \frac{\partial p}{\partial t} d\Omega = \\
& \int_{\Gamma_f} (\hat{\zeta} + \sum_{k=1}^m \mathcal{H}_{\Gamma_{d_k}} \tilde{\zeta}_k) f_f d\Gamma_f.
\end{aligned} \tag{5.10}$$

These equation must be satisfied for all the variations of $\boldsymbol{\eta}$ and ζ . Separating the balance equations in a continuous part ($\tilde{\boldsymbol{\eta}}_k = 0 \forall k = 1..m$ and $\tilde{\zeta}_k = 0 \forall k = 1..m$):

$$\int_{\Omega} (\nabla \hat{\boldsymbol{\eta}}) : \boldsymbol{\sigma} d\Omega = \int_{\Gamma_t} \hat{\boldsymbol{\eta}} \cdot \mathbf{t}_p d\Gamma_t, \quad (5.11)$$

$$- \int_{\Omega} \alpha \hat{\zeta} \nabla \cdot \mathbf{v}_s d\Omega + \int_{\Omega} \nabla \hat{\zeta} \cdot \mathbf{q} d\Omega - \int_{\Omega} \frac{1}{M} \hat{\zeta} \frac{\partial p}{\partial t} d\Omega = \int_{\Gamma_f} \hat{\zeta} f_f d\Gamma_f. \quad (5.12)$$

The same can be done for the m discontinuous equations, with $(\hat{\boldsymbol{\eta}} = 0$ and $\hat{\zeta} = 0)$, gives

$$\begin{aligned} \int_{\Omega} \mathcal{H}_{\Gamma_{d_k}} \nabla \tilde{\boldsymbol{\eta}}_k : \boldsymbol{\sigma} d\Omega = & \\ & \int_{\Gamma_t} \mathcal{H}_{\Gamma_{d_k}} \tilde{\boldsymbol{\eta}}_k \cdot \mathbf{t}_p d\Gamma_t - \int_{\Gamma_{d_k}} \tilde{\boldsymbol{\eta}}_k \cdot \mathbf{t}_k d\Gamma_{d_k} \\ & - \tilde{\boldsymbol{\eta}}_k \cdot \left(\sum_{j=1, j \neq k}^m \int_{\Gamma_{d_j}} \left[\mathcal{H}_{\Gamma_{d_k}}(\Gamma_{d_j}^+) - \mathcal{H}_{\Gamma_{d_k}}(\Gamma_{d_j}^-) \right] \mathbf{t}_j d\Gamma_{d_j} \right), \end{aligned} \quad (5.13)$$

$$\begin{aligned} - \int_{\Omega} \alpha \mathcal{H}_{\Gamma_{d_k}} \tilde{\zeta} \nabla \cdot \mathbf{v}_s d\Omega + \int_{\Omega} \mathcal{H}_{\Gamma_{d_k}} \nabla \tilde{\zeta} \cdot \mathbf{q} d\Omega - \int_{\Omega} \frac{1}{M} \mathcal{H}_{\Gamma_{d_k}} \tilde{\zeta} \frac{\partial p}{\partial t} d\Omega = & \\ \int_{\Gamma_f} \mathcal{H}_{\Gamma_{d_k}} \tilde{\zeta} f_f d\Gamma. \end{aligned} \quad (5.14)$$

which must hold for $k = 1 \dots m$. The last balance equation is conservation of mass for the fluid flow in the discontinuity. In a weak form this is written as

$$\begin{aligned} & \sum_{j=1}^m \int_{\Gamma_{d_j}} \psi \mathbf{q}_{\Gamma_d}^+ \cdot \mathbf{n}_j^d d\Gamma_{d_j} - \sum_{j=1}^m \int_{\Gamma_{d_j}} \psi \mathbf{q}_{\Gamma_d}^- \cdot \mathbf{n}_j^d d\Gamma \\ & + \sum_{j=1}^m \int_{\Gamma_{d_j}} \frac{1}{12\mu} ([\mathbf{u}]_j \cdot \mathbf{n}_j^d)^3 \frac{\partial \psi}{\partial s} \cdot \frac{\partial p_d}{\partial s} d\Gamma_{d_j} + \sum_{j=1}^m \int_{\Gamma_{d_j}} \psi [\dot{\mathbf{u}}]_j \cdot \mathbf{n}_j^d d\Gamma_{d_j} \\ & + \sum_{j=1}^m \int_{\Gamma_{d_j}} \psi [\mathbf{u}]_j \cdot \mathbf{n}_j^d \left\langle \frac{\partial [\dot{\mathbf{u}}]_j \cdot \mathbf{s}_j^d}{\partial s} \right\rangle d\Gamma_{d_j} + \sum_{j=1}^m \int_{\Gamma_{d_j}} \psi \frac{[\mathbf{u}]_j \cdot \mathbf{n}_j^d}{K_f} \dot{p}_d d\Gamma_{d_j} = \\ & \sum_{j=1}^m \psi Q_{\text{in}}^j |_{S_d}. \end{aligned} \quad (5.15)$$

The first two terms represents the analytical calculated fluid leakage. The third term is the tangential fluid flow based on lubrication theory. Term

four and five are representing the opening rate terms in normal and shear direction, respectively, the sixth term is the compressibility of the fluid within the fracture, and the last term is the fluid injection within the fracture. The vector \mathbf{s}_j^d represents the tangential vector at discontinuity surface j . In the remainder of this chapter we neglect the fifth term representing the volume change due to elongation of the discontinuity surface in tangential direction. We assume that this contribution is small compared to the volume of the opening of the fracture in mode I.

5.1.3 Discretization

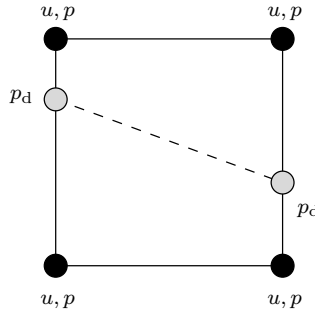


Figure 5.4: Four nodal element with crossed by a discontinuity (dashed line).

The spatial discretization of the balance equations is based on the partition of unity property of finite element shape functions as described in the work of Melenk and Babuška (1996). The displacement field, the pressure field, the pressure in the fracture and the variational forms are discretized similarly following the Bubnov-Galerkin approach for a single element by:

$$\begin{aligned}
 \boldsymbol{\eta} &= \mathbf{N}\hat{\boldsymbol{\eta}} + \sum_{k=1}^m \mathcal{H}_{\Gamma_{d_k}} \mathbf{N}\tilde{\boldsymbol{\eta}}_k, & \mathbf{u} &= \mathbf{N}\hat{\mathbf{u}} + \sum_{k=1}^m \mathcal{H}_{\Gamma_{d_k}} \mathbf{N}\tilde{\mathbf{u}}_k, \\
 \zeta &= \mathbf{H}\hat{\zeta} + \sum_{k=1}^m \mathcal{H}_{\Gamma_{d_k}} \mathbf{H}\tilde{\zeta}_k, & p &= \mathbf{H}\hat{p} + \sum_{k=1}^m \mathcal{H}_{\Gamma_{d_k}} \mathbf{H}\tilde{p}_k, \\
 \psi &= \mathbf{V}\hat{\psi}, & p_d &= \mathbf{V}\hat{p}_d,
 \end{aligned} \tag{5.16}$$

where \mathbf{N} , \mathbf{H} , and \mathbf{V} are matrices containing the standard shape functions for respectively, the nodal displacement, the pressure, and the pressure in the fracture for all nodes that support the element. Note that the shape functions for the nodal displacement and the pressure are two-dimensional

functions while the pressure in the fracture is described in a one-dimensional domain (Figure 5.4). The terms $\hat{\mathbf{u}}$ and $\hat{\mathbf{p}}$ contain the degrees of freedom of the continuous displacement and pressure fields, respectively. While $\tilde{\mathbf{u}}$ and $\tilde{\mathbf{p}}$ contain the values of the enhanced nodes. The term \mathbf{p}_d contains the nodal values of the pressure in the discontinuity. The discretized strain in the bulk can be derived by differentiation

$$\boldsymbol{\epsilon} = \mathbf{B}\hat{\mathbf{u}} + \sum_{i=1}^m \mathcal{H}_{\Gamma_{d_i}} \mathbf{B}\tilde{\mathbf{u}}, \quad (5.17)$$

where \mathbf{B} contains the spatial derivative of the standard shape functions. Filling in the discretized form in the balance Equations (5.11)-(5.14) give the continuous equations as

$$\int_{\Omega} \mathbf{B}^T \boldsymbol{\sigma} d\Omega = \int_{\Gamma_t} \mathbf{N}^T \mathbf{t}_p d\Gamma, \quad (5.18)$$

$$- \int_{\Omega} \alpha \mathbf{H}^T \mathbf{m}^T \nabla \dot{\mathbf{u}} d\Omega + \int_{\Omega} \nabla \mathbf{H}^T \mathbf{q} d\Omega - \int_{\Omega} \frac{1}{M} \mathbf{H}^T \dot{p} d\Omega = \int_{\Gamma_f} \mathbf{H}^T f_f d\Gamma, \quad (5.19)$$

and $k = 1 \dots m$ discontinuous equations

$$\begin{aligned} \int_{\Omega} \mathcal{H}_{\Gamma_{d_k}} \mathbf{B}^T \boldsymbol{\sigma} d\Omega = & \int_{\Gamma_t} \mathcal{H}_{\Gamma_{d_k}} \mathbf{N}^T \mathbf{t}_p d\Gamma_t - \int_{\Gamma_{d_k}} \mathbf{N}^T \mathbf{t}_k d\Gamma_{d_k} \\ & - \mathbf{N}^T \left(\sum_{j=1, j \neq k}^m \int_{\Gamma_{d_j}} \left[\mathcal{H}_{\Gamma_{d_k}}(\Gamma_{d_j}^+) - \mathcal{H}_{\Gamma_{d_k}}(\Gamma_{d_j}^-) \right] \mathbf{t}_j d\Gamma_{d_j} \right) \\ & - \int_{\Omega} \alpha \mathcal{H}_{\Gamma_{d_k}} \mathbf{H}^T \mathbf{m}^T \nabla \dot{\mathbf{u}} d\Omega + \int_{\Omega} \mathcal{H}_{\Gamma_{d_k}} \nabla \mathbf{H}^T \cdot \mathbf{q} d\Omega - \int_{\Omega} \frac{1}{M} \mathcal{H}_{\Gamma_{d_k}} \mathbf{H}^T \frac{\partial p}{\partial t} d\Omega = \\ & \int_{\Gamma_f} \mathcal{H}_{\Gamma_{d_k}} \mathbf{H}^T f_f d\Gamma, \end{aligned} \quad (5.20)$$

with the vector \mathbf{m} in the two-dimensional situations being defined as $\mathbf{m} = (1, 1, 0)^T$. Finally the discretized form of the mass balance in the discontinuity is given as

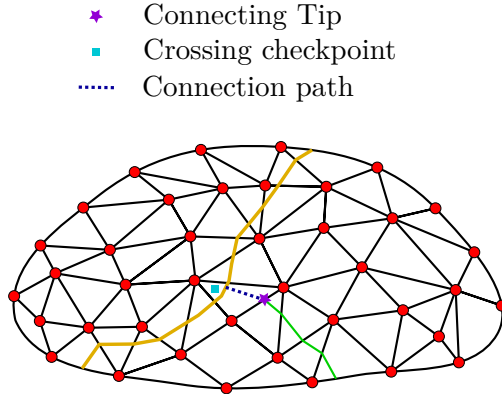


Figure 5.5: Situation when two discontinuities are in the vicinity of each other. The connecting tip is stopped from propagating after connecting. The average stress in the crossing checkpoint determines if the discontinuity crosses.

$$\begin{aligned}
 & \sum_{j=1}^m \int_{\Gamma_{d_j}} \mathbf{v}^T (\mathbf{q}_{\Gamma_d}^+ + \mathbf{q}_{\Gamma_d}^-) \cdot \mathbf{n}_j^d d\Gamma_{d_j} + \sum_{j=1}^m \int_{\Gamma_{d_j}} \mathbf{v}^T \frac{[\mathbf{u}]_j \cdot \mathbf{n}_j^d}{K_f} \mathbf{v} \mathbf{p}_d d\Gamma_{d_j} \\
 & + \sum_{j=1}^m \int_{\Gamma_{d_j}} \mathbf{v}^T [\dot{\mathbf{u}}]_j \cdot \mathbf{n}_j^d d\Gamma_{d_j} + \sum_{j=1}^m \int_{\Gamma_{d_j}} \frac{1}{12\mu} ([\mathbf{u}]_j \cdot \mathbf{n}_j^d)^3 \frac{\partial \mathbf{V}^T}{\partial s} \cdot \frac{\partial \mathbf{V}}{\partial s} \mathbf{p}_d d\Gamma_{d_j} = \\
 & \sum_{j=1}^m \psi Q_{in}^j |_{s_d}. \tag{5.22}
 \end{aligned}$$

These final equations can be linearized in a standard way and solved using a Newton-Raphson iterative method. More details about the constitutive equations, linearization and time integration can be found in Section 4.5.

5.1.4 Numerical implementation

Each discontinuity is able to propagate. The position and the direction of propagation are governed by two unique level sets (Stolarska et al., 2001). The propagation is based on the Camacho-Ortiz average stress criterion (Camacho and Ortiz, 1996). Depending on a length scale parameter l_a an average stress is calculated by a Gaussian weighting function (see also Section 2.3). A discontinuity is assumed to propagate in a straight line through an element and always ends on the element boundary at another discontinuity. The discontinuity can propagate through multiple elements within one single time step. Upon the interaction of two discontinuities there are two requirements on the numerical implementation i.e. i) two

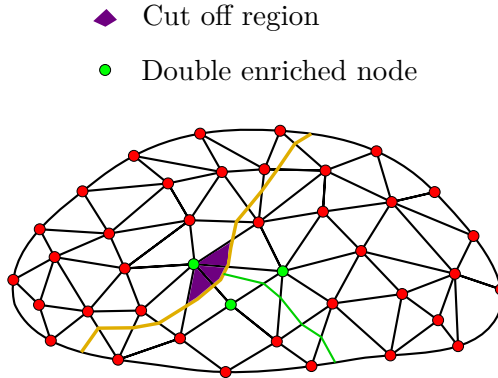


Figure 5.6: A finite element mesh containing two discontinuities. Integration points lying in the cut off region have a Heaviside value of zero for the green discontinuity. Nodes with a double enrichment, due to the two discontinuities, are shown in green.

discontinuities must be connected once a tip is in the vicinity of another discontinuity and ii) the connecting tip must be stopped from further propagating. We determine the event of connecting the two discontinuities by counting the number of elements between a tip and the nearest discontinuity. The number of elements is an input parameter of the simulation in which zero means that two discontinuities connect when the tip propagates into an element that already contains a discontinuity. This is often an undesirable situation since a small distance between a tip and a discontinuity may lead to numerical instabilities. In our simulations we therefore chose to connect two discontinuities if there is one element in between (Figure 5.5).

An additional crossing checkpoint is added at the opposite side of the interacting discontinuity. An average stress is calculated in the checkpoint and is used to determine whether the discontinuity crosses the existing crack (Figure 5.5). Note that the stress is only averaged at the side of the checkpoint. A new discontinuity nucleates, and thus crosses, when the average stress violates the same criterion as was used for the determination of crack propagation. The new discontinuity is given an initial length of three elements to prevent instantaneous interaction with the neighbouring discontinuity.

In the case of interacting fractures, the Heaviside enrichment given in Eq. (5.2) is no longer valid when there are two or more enrichments present in one element (Daux et al., 2000). The common way to solve this problem is by introducing a special junction enrichment function present in the

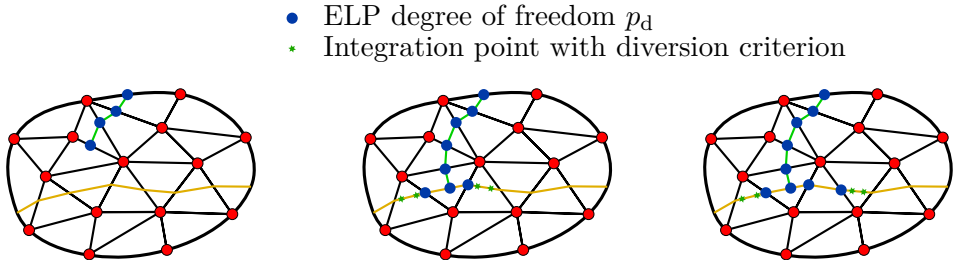


Figure 5.7: Schematic representation of a hydraulic fracture interacting with a natural fracture. From left to right, the hydraulic fracture interacts with the natural fracture and the ELP degree of freedom p_d is added to the interacting elements. The diversion criterion is evaluated in the integration points. In the right image the criterion is violated in the right element. Therefore the ELP degree of freedom is extended to the right.

multiple enriched elements. This would lead to additional terms in the kinematic relations in Eq. (5.1), (5.3) and (5.6). To avoid this we implement a modified Heaviside enrichment by evaluating whether an integration point belonging to multiple discontinuities is cut-off by one of the discontinuities (Figure 5.6). Integration points that lie in the shaded purple region do not have a contribution to the displacement field of green discontinuity. In these integration points the values for the Heaviside of this discontinuity are therefore set to zero. Hence, the kinematic relations do not have to be modified.

In the model we distinguish between two types of discontinuities. Discontinuities that possess the ELP degree of freedom are hydraulic fractures. The second type are discontinuities that do not possess this degree of freedom and can therefore be considered as a closed natural fracture. When two hydraulic fractures interact the mass balance in Eq. (5.22) is combined. The possibility of fluid diversion occurs when a hydraulic fracture interacts with a natural fracture. The ELP degree of freedom p_d is added to the interacting element but not in the remainder of the natural fracture (Figure 5.7). Fluid can divert into the natural fractures if a diversion criterion is violated. We propose that the criterion is violated if the opening displacement in all integration points in an element is positive, as shown in Figure 5.7.

5.1.5 Constitutive law at the fracture and the interface

The constitutive mechanical behaviour at a fracture is described by a relationship between the traction at the interface and the displacement jump

\mathbf{u}_d across the fracture (Irzal et al., 2013):

$$\mathbf{t}_d = \mathbf{t}_d(\mathbf{u}_d, \kappa). \quad (5.23)$$

where κ is a history parameter that is equal to the largest displacement jump reached. It is necessary to perform a linearisation on Eq.(5.23) in order to use the tangential stiffness matrix in an incremental iterative solution:

$$\Delta \mathbf{t}_d = \mathbf{T} \Delta \mathbf{u}_d. \quad (5.24)$$

The relation between the traction \mathbf{t}_d and the displacement jump \mathbf{u}_d can be any traction-separation relation and is referred to as the cohesive law. We assume that hydraulic fractures open in mode-I due to the internal pressurization. The shear tractions are therefore neglected and an exponential cohesive law is used that is only a function of the normal opening u_n (Wells and Sluys, 2001)

$$t_n = \tau_{\text{ult}} \exp\left(-\frac{u_n \tau_{\text{ult}}}{\mathcal{G}_c}\right). \quad (5.25)$$

Here is τ_{ult} the ultimate strength of the material and \mathcal{G}_c the fracture toughness.

In contact we assume a penalty constraint in both normal and shear direction. The linear relation between the traction and the opening displacement is defined by a stiffness parameter D_n and D_s for the normal and shear direction, respectively. In contact this gives the following penalty relations

$$t_n = -D_n u_n \quad \text{if } u_n < 0 \quad (5.26)$$

$$t_s = D_s u_s \quad \text{if } u_n < 0 \quad (5.27)$$

In the remainder of this study natural fractures are described by these contact relations. We do not consider additional cohesion in the natural fractures due to filling materials. However, the framework allows this to be added later.

5.2 Results

The performance of the model is demonstrated in four examples. Pore pressure is not considered in the first three examples in order to focus on

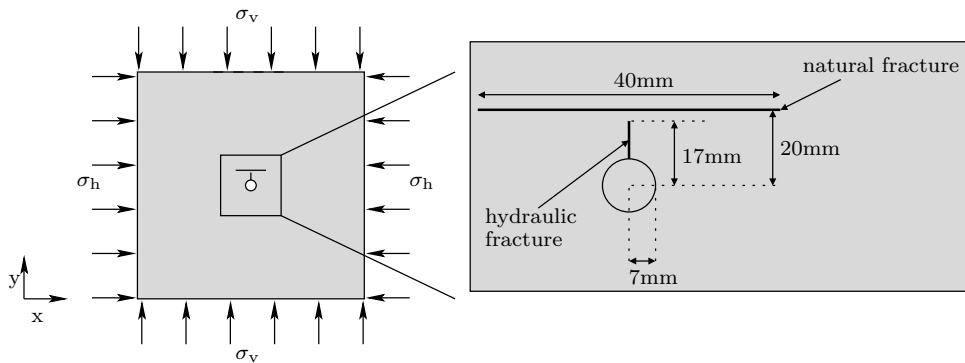


Figure 5.8: Scheme of a hydraulic fracture, indicated with the solid line, propagating from a circular hole into the direction of a natural fracture.

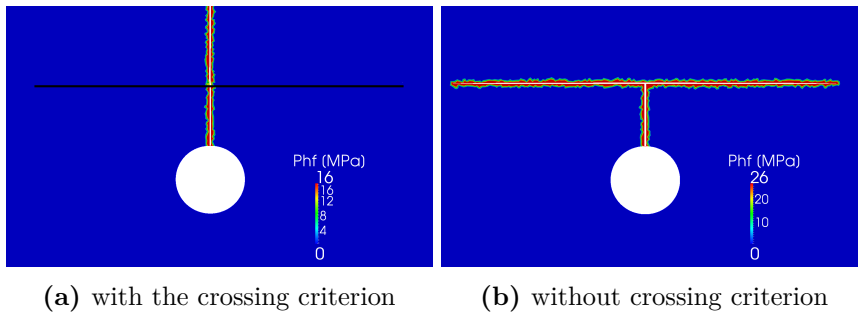


Figure 5.9: Contour plots of the pressure in the fracture after 300 seconds of fluid injection. The deformed mesh is magnified 10 times. The black line in Figure (a) indicates the location of the closed natural fracture. Note that the hydraulic fracture with crossing propagated further than shown in the image.

the interaction behaviour and the performance of the crossing and diversion criterion. In the first example we illustrate the performance of the criterion and we investigate the influence of the shear stiffness parameter in the second example. The third example consists of a comparison with an experiment and a theoretical crossing criterion. In the fourth example we do include pore pressure and show a propagating hydraulic fracture coming in contact with a small fracture network.

5.2.1 Performance of the crossing and diversion criterion

To illustrate the performance of the crossing and diversion criterion we consider a hydraulic fracture growing perpendicular into a natural fracture (Figure 5.8). The hydraulic fracture is propagating from a circular hole

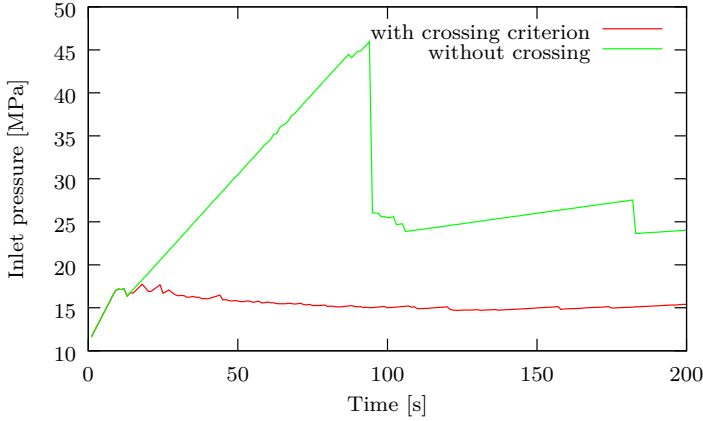


Figure 5.10: Injection pressure over time shown for the simulations with and without the fracture crossing criterion. The fluid is forced to divert into the natural fracture leading to higher injection pressures.

with a radius of 7 mm. The squared specimen has a width and height of 300 mm, Young's modulus of 30 GPa and a Poisson's ratio of 0.25. The in situ stresses are $\sigma_v = -20$ MPa and $\sigma_h = -12$ MPa. The hydraulic fracture is characterized by $\tau_{ult} = 5$ MPa and a fracture toughness $\mathcal{G}_c = 0.01125$ Pa m. The behaviour of the natural fracture is described by the penalty relation with stiffness parameters $D_n = 10^3$ Mpa and $D_s = 5 \cdot 10^3$ Mpa. Fluid is injected in the natural fracture with constant inflow rate of $Q_{in} = 0.0075$ mm²/s and the fluid has a dynamic viscosity of 0.001 Pa s. An implicit time stepping scheme is used with a time step of one second.

We demonstrate the effect of the crossing and diversion implementation by comparing two simulations. In the first simulation we include both criteria. In the second, we prohibit crossing and fracture growth after the hydraulic fracture merged with the natural fracture. Thus, the only path for fluid to distribute is to divert into the natural fracture. In Figure 5.9 the deformed mesh after 300 seconds of fluid injection is shown with the pressure in the fracture as contour. It is evident that with the crossing criterion the fracture propagated through the natural fracture as expected (Fig. 5.9a). Without the crossing criterion the fluid diverted into the natural fracture (Fig. 5.9b). The pressure in the fracture with crossing included is lower than the pressure when the fluid is forced to go into the natural fracture. This is a consequence of the natural fracture being perpendicular to σ_v .

Injection pressure over time shows similar behaviour, as shown in Figure 5.10. In the case without the crossing mechanism, this leads to improbable

magnitudes of injection pressure since fracture crossing would be energetically more favourable. The first drop in pressure (after ± 90 seconds) in the case without crossing is caused by fluid diverting mainly in the left wing of the natural fracture. Once the left wing is filled with fluid the pressure has to slightly build up again, after which the right wing is also completely filled with fluid (after ± 180 seconds). The preference of which wing will fill first is in this case a numerical artefact. Even though the problem is symmetric, the FE mesh is unstructured. As a result, one of the two sides opens first.

5.2.2 Influence of the shear stiffness

The magnitude of the shear stiffness is one of the key parameters in transferring stress from the hydraulic fracture across the natural fracture which can lead to fracture crossing. The magnitude of stress that is transferred is finite when described by the Coulomb friction law. We use a simplified penalty stiffness law to describe the friction, as explained in Section 5.1.5. The penalty law leads to an infinite friction which increases linearly with the shear displacement according to stiffness parameter D_s . In this example we show the effect of this shear stiffness on the fracture propagation. We consider the same specimen and material properties as in Example 5.2.1. The only parameters that are varied are stiffness values of the natural fracture. Also the natural fracture is placed further away from the hydraulic fracture at distance of five centimetre in y-direction measured from the centre of the circle.

To determine the effect of the shear stress transfer the shear stiffness is varied between 0.0 GPa and 20.0 GPa. A penalty stiffness of 10.0 GPa is used. The length of the hydraulic fracture, including the cohesive zone, is plotted against the time in Figure 5.11a. We observe almost identical fracture growth during the first stage of hydraulic fracturing. The natural fracture is too far away to influence the propagation. In the vicinity of the natural fracture, approximately 10.0 mm, there is a minor influence (Figure 5.11b). There is some strength loss due to the imperfect natural fracture, leading to accelerated fracture propagation with lower shear stiffness.

There are two possibilities for the fracture to grow further after the merging with the natural fracture. The fluid can divert into the natural fracture and eventually grow the natural fracture or the hydraulic fracture must cross the natural fracture. We did not observe fluid diverting into the natural fracture. Fluid diversion is unfavourable since the maximum confining stress must be overcome to open the natural fracture. In Figure 5.11c it is shown that after merging, the pressure is building up in the

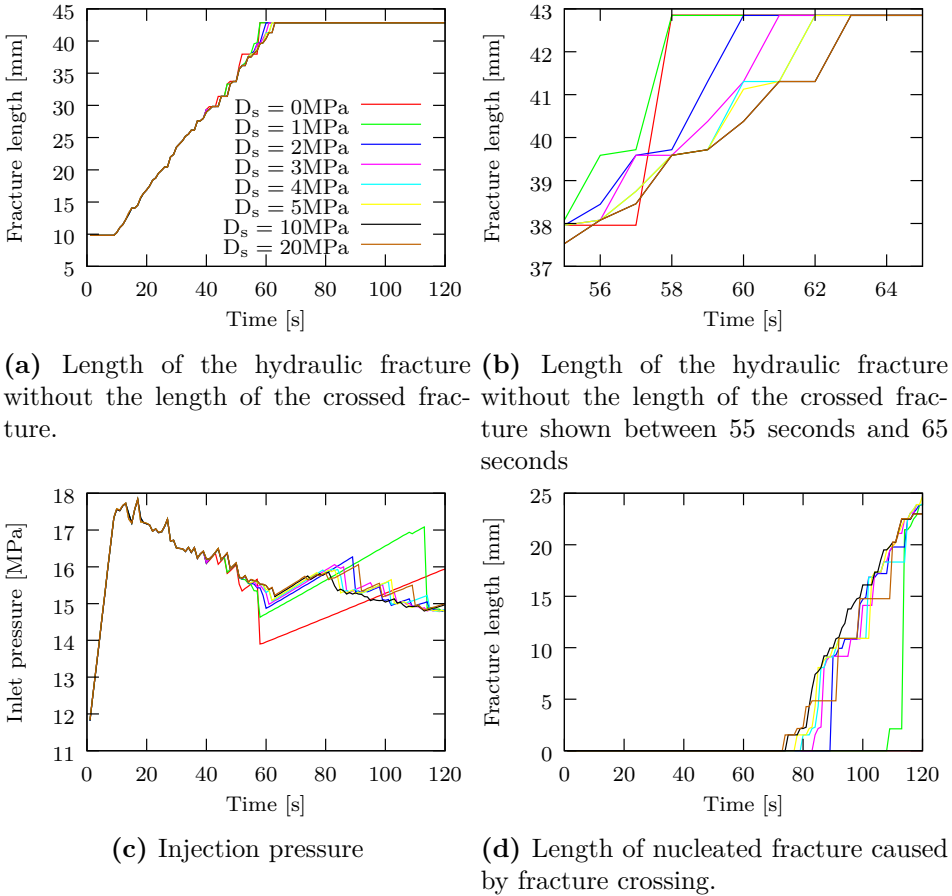


Figure 5.11: Various numerical results for different stiffness parameter D_s . The influence of the stiffness parameter is demonstrated and crossing is observed at an earlier time requiring less injection pressure.

hydraulic fracture. This leads to stress transfer across the natural fracture and eventually to fracture nucleation. The speed of stress transfer depends on the magnitude of the shear stiffness (Figure 5.11d). Only with zero shear stiffness we did not observe fracture crossing.

5.2.3 Influence of the interaction angle and the in situ stress

It is known that the ratio between in situ stresses and the angle between a hydraulic fracture and a natural fracture are important to predict whether the hydraulic fracture crosses, diverts or arrests on the natural fracture. This relation is shown in experimental results (Blanton, 1982; Zhou et al.,

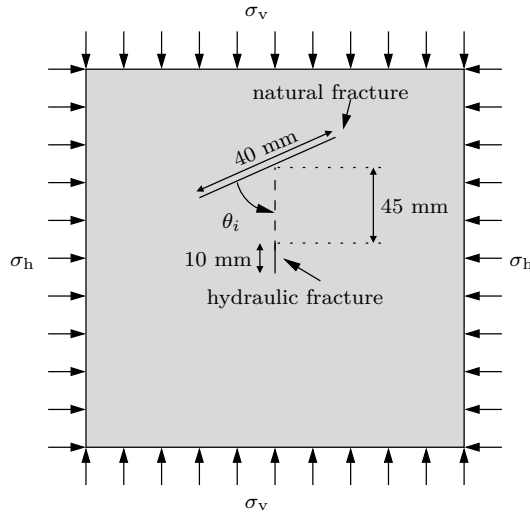


Figure 5.12: Scheme for the interaction example. Fluid is injected in the centre of the hydraulic fracture. The centre of the natural fracture is, independent of the interaction angle, located 45 mm above the hydraulic fracture.

2008) and is described with a crossing criterion by Gu et al. (2012). In this example we compare our numerical results with the crossing criterion. We vary the in situ stress by varying σ_h while keeping σ_v equal to -20 MPa. The orientation of the natural fracture is also varied between $\theta_i = 90^\circ$ and $\theta_i = 15^\circ$ (see Figure 5.12). The remainder of the material properties are identical to those used in example 5.2.1.

To interpret the results we distinguish between 4 different length measurements, i.e. the length of the hydraulic fracture, the length the natural fracture, the part of the hydraulic fracture that has crossed the natural fracture, and the part of the natural fracture that is filled with fluid. These results are shown for each interaction angle measured in Figure 5.14. It can be seen that high interaction angles show mainly crossing of the hydraulic fracture. In some cases the length of the crossed hydraulic fracture (shown in the blue bar) is small. We attribute this to the loss of friction due to the crossed fracture, which leads to relaxation of strain tangential to the natural fracture. Since a penalty friction law is used there is a lower stress transfer across the natural fracture. The bottom part of the hydraulic fracture then becomes the favourable growth direction. The results of the low interaction angles show diversion of fluid in the natural fracture. Only the right wing of the natural fracture, which is not feeling pressure exerted by the hydraulic fracture, is filled with fluid (Figure 5.13). In none of our

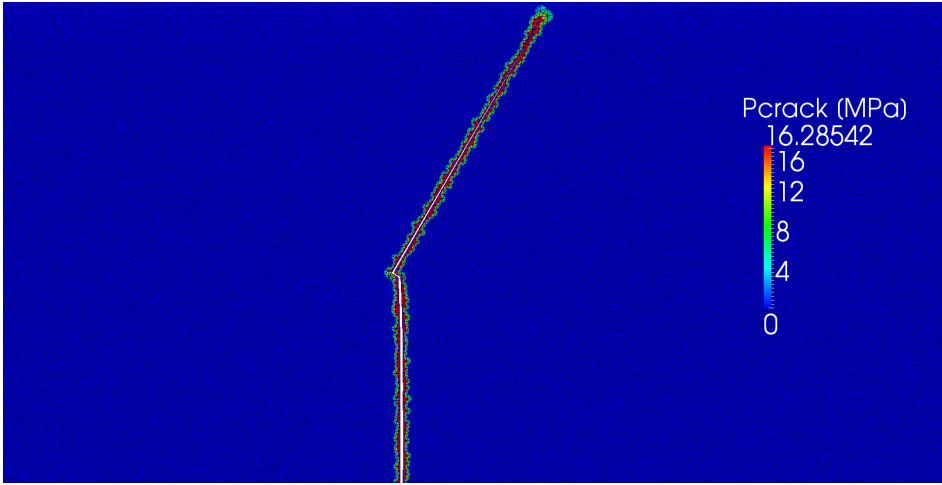


Figure 5.13: Contour plot for fracture diversion with $\Delta\sigma = 6$ MPa and $\theta_i = 30^\circ$.

results the natural fracture propagated. The bottom part of the hydraulic fracture propagates as soon as the right wing is filled with fluid. Interaction angles varying between $\theta_i = 50^\circ$ and $\theta_i = 60^\circ$ show crack arrest.

In Figure 5.15 we have extracted from Figure 5.14 whether fracture crossing, arrest or diversion occurred for the various interaction angles and stress differences simulated. Apart from one outlier we see a trend from fracture crossing to arrest and finally diversion with decreasing interaction angle. This tendency is also observed in the experiments. The influence of the stress difference is less pronounced. This is attributed to the friction law which does not possess the same properties as a Coulomb friction, which would better represent friction in rocks. There is no explicit relation between the magnitude of the friction and the normal stress to the natural fracture in our penalty friction law.

The tendency of crossing or diversion for various friction coefficients based on the crossing criterion from Gu et al. (2012) is also shown in Figure 5.15. The region right to the curve represents crossing. The left region indicated diversion except close to the line, where crack arrest is expected. The criterion does not distinguish between diversion or arrest. Our results are in the proximity of $\mu = 2.0$ and $\mu = 1.5$. Rocks typically do not possess such a high friction coefficient (Gu et al., 2012). It is likely that we overestimate the magnitude of the friction due to our penalty friction law. However, the trend from diversion to crack arrest and finally crossing as the interaction increases is visible in our numerical results.

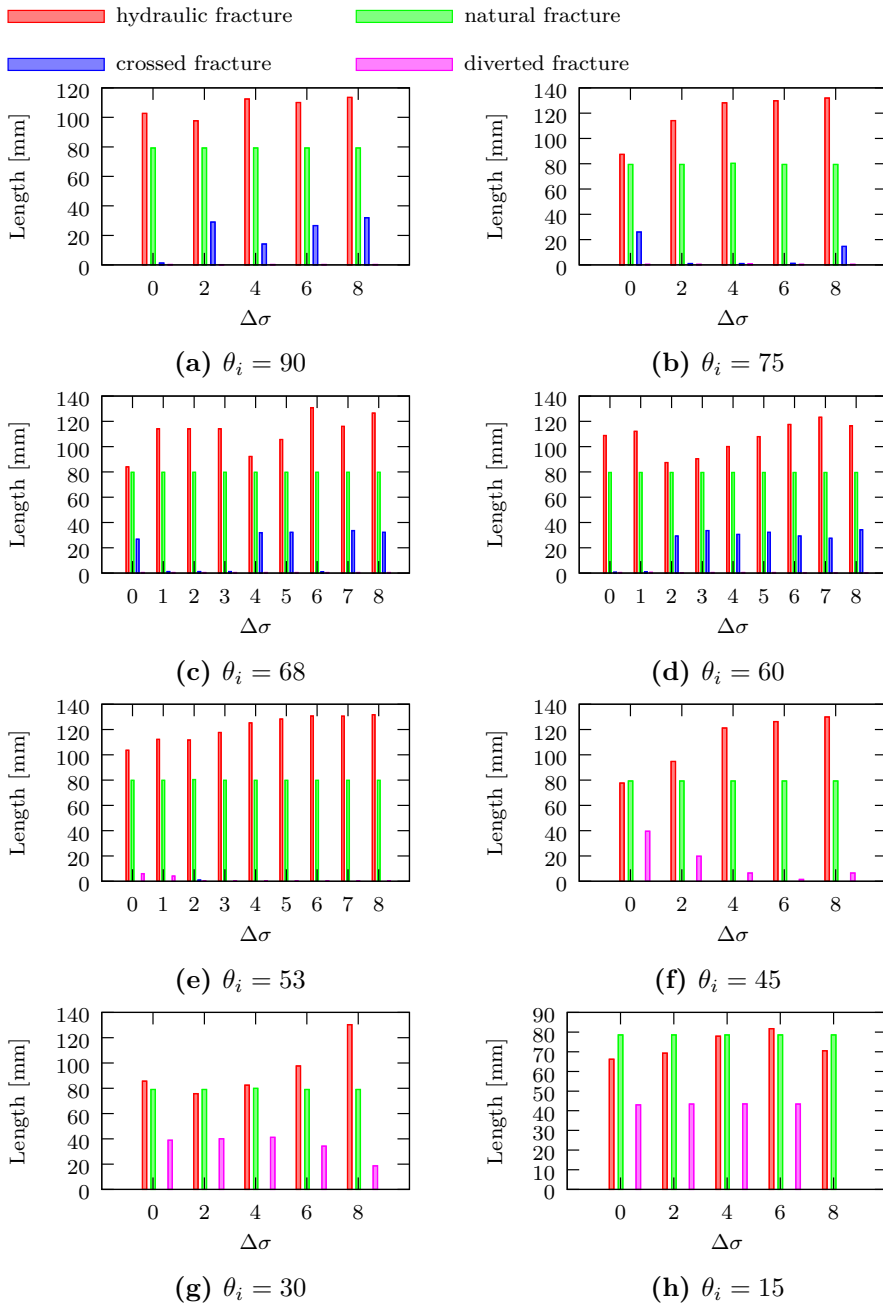


Figure 5.14: Overview of the different simulation results. The height of the bars indicate the length of respectively the hydraulic fracture, the natural fracture, the crossed fracture and the length of the natural fracture filled with diverted fluid.

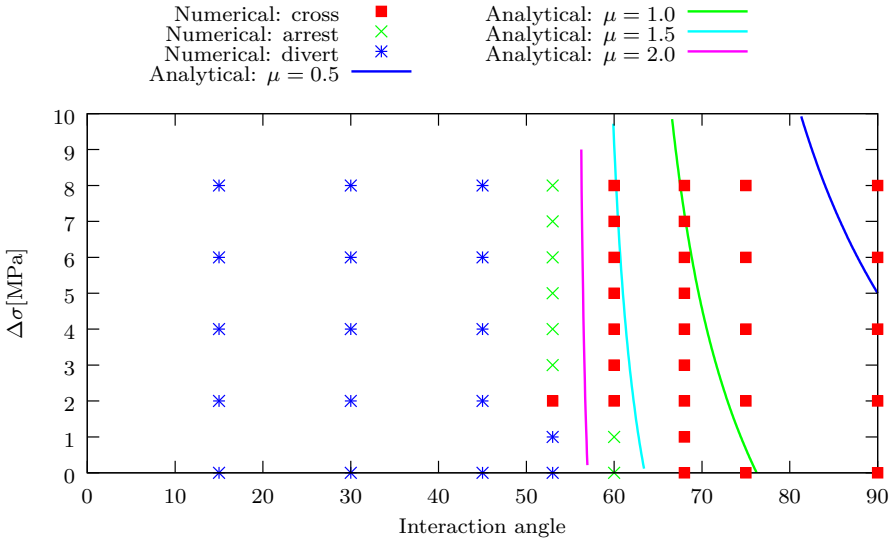


Figure 5.15: The numerical results whether fluid diversion, crack arrest or fracture crossing occurs due to varying interaction angles and stress differences are shown with the point markers. The crossing criterion from Gu et al. (2012) for various friction coefficients is shown with the lines. The region right of a line indicates crossing.

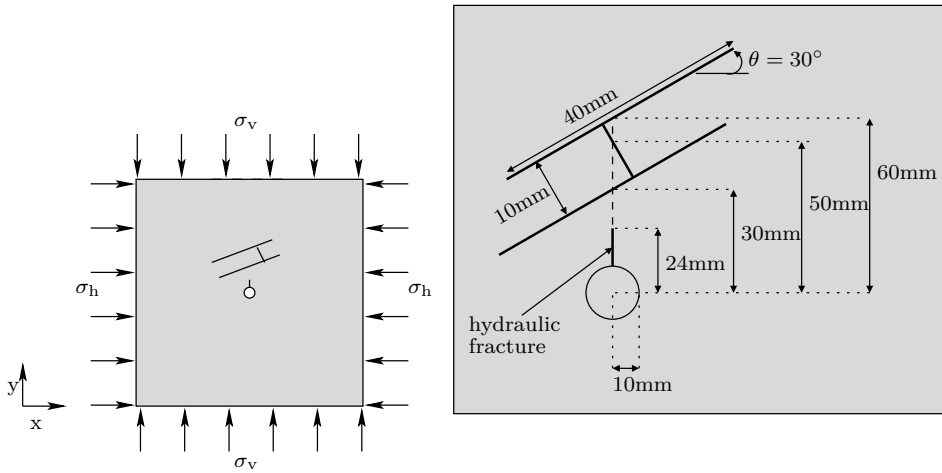


Figure 5.16: Scheme for the interaction with a small fracture network.

5.2.4 Interaction with a fracture network

In this final example we consider a hydraulic fracture propagating towards a small network consisting of three natural fractures that are in contact (Figure 5.16). The two larger natural fractures have a length of 40 mm and make an angle of 30° with the x-axis. The smaller natural fracture is perpendicular to both of the larger fractures. The specimen is now considered to be a low permeable rock with an intrinsic permeability of $k_{\text{int}} = 10^{-21} \text{ m}^2$. The solid grains have a compressibility of $K_s = 30 \text{ GPa}$ and the fluid compressibility is taken as $K_f = 3.6 \text{ GPa}$. The remainder of the material properties and boundary conditions are identical to those used in example 5.2.1. The initial pore pressure is set as zero.

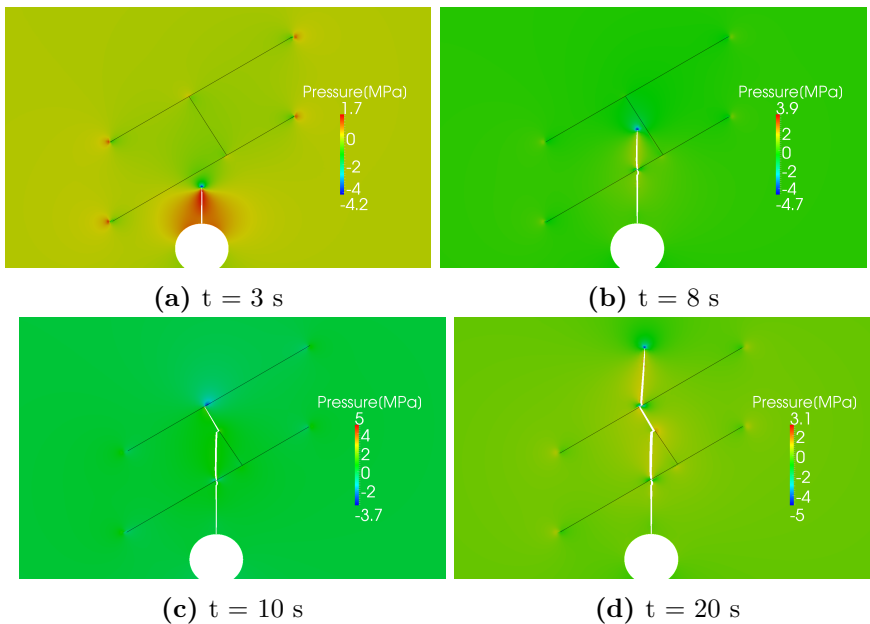


Figure 5.17: Contour plot of the pore pressure in the bulk at four different time instances. The solid black lines indicate the locations of the natural fractures. The deformed mesh is magnified 50 times.

The contour plot of the pore pressure in the bulk for four different time steps is shown in Figure 5.17. In Figure 5.17a the hydraulic fracture propagated and a low pressure in front of the cohesive zone can be seen. This is a result of tension due the pressurization of the hydraulic fracture and leads to fluid being attracted towards the region under tension. After 8 seconds of fluid injection the hydraulic fracture crossed the bottom natural fracture (Figure 5.17b). The angle between the middle natural fracture and

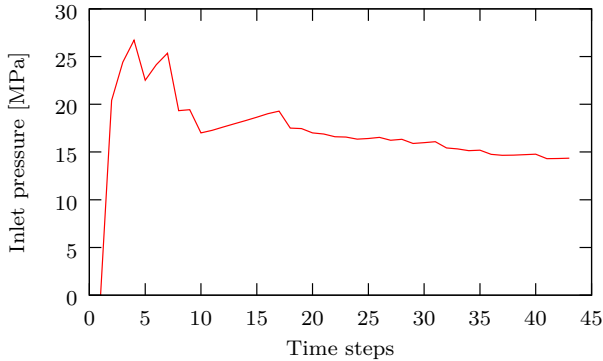


Figure 5.18: Injection pressure for various times in the simulation of a hydraulic fracture interacting with a natural fracture network.

the direction of σ_v is such that crossing is not likely to occur. This is also observed in Figure 5.17c. Fluid diverted from the hydraulic fracture into the natural fracture network. Fluid diversion stops when the fluid front reaches the top natural fracture. Tension is being generated at the top surface due to the friction law. This can also be seen at the low pressure in Figure 5.17c. Finally a new cohesive zone nucleates and the hydraulic fracture propagates away from the natural fracture network (Figure 5.17d).

A discontinuous injection pressure development over time is shown in Figure 5.18. On the one hand this is caused by numerical aspects such as the size of the time step and mesh resolution. On the other hand, the pressure decrease at 8 seconds and at 18 seconds is caused by the fracture propagating away from the natural fractures and after 10 seconds a decrease is observed due to fluid having the possibility to divert into the middle natural fracture.

5.3 Conclusions

In this chapter the ELP model is used to investigate the interaction of multiple cracks in hydraulic fracturing. There is no limit to the amount of fractures. Interaction and propagation can take place in arbitrary locations and directions. The criterion whether or not a fracture crosses a natural fracture is determined by an average stress criterion. Fluid is also given the possibility to divert into a natural fracture based on a criterion that examines whether the natural fracture opens. These two criteria are checked simultaneously and the competition between them determines the interaction behaviour. The fracture process is modelled by a cohesive zone

model. With the ELP model the injected fluid flow goes exclusively into the fracture and steep pressure gradients near the fracture surface are reconstructed based on Terzaghi's consolidation solution.

Four examples are presented to illustrate the implementation of the criteria and to show the performance of the numerical model. The first example was chosen to show the effect of the crossing and diversion implementation. A hydraulic fracture propagated perpendicular onto the natural fracture with the in situ stress taken such that crossing of the natural fracture is preferred. As expected the hydraulic fracture indeed crosses the natural fracture. The simulation was repeated but now the crossing criterion is not included in the model. This leads to fluid diversion into the natural fracture and has as a consequence that the required injection pressure is much higher. In the second example the effect of the implemented friction law is shown. The penalty friction leads to an imperfect natural fracture. With a higher stiffness the interaction took place earlier and also the fracture crosses the natural fracture at an earlier time requiring less injection pressure. The behaviour observed in these two examples is consistent with what would be expected from the chosen geometry and the boundary conditions. The influence of the interaction angle and the in situ stress conditions is studied in the third example. These results are compared with experimental data and with a theoretical crossing criterion. A trend from fracture crossing to arrest and fluid diversion is observed with a decreasing interaction angle. This is in line with the experiments and the theoretical criterion. In the last example poro-elasticity is included and a hydraulic fracture interacting with a small natural fracture network is studied. Due to tension a low pore pressure is observed in front of the cohesive zone. Fracture crossing and fluid diversion are both shown depending which natural fracture was interacting with the hydraulic fracture.

The proposed model is suitable to simulate complex hydraulic fracture patterns in fully saturated porous media. The simplified friction law leads to some discrepancy but the global fracture behaviour satisfies expectations and experimental results. Slip behaviour is not considered but could be included by replacing the friction law.

The domains of the specimens used in the simulations within this chapter are based on an experiment and therefore have a small size. To consider hydraulic fracture networks on a larger scale, with the element size used in this chapter, would result in high computational costs. Parallel computing is a technique where many calculations are performed simultaneously. In the next chapter this technique is applied to the ELP model to simulate larger size meshes with low computational costs.

6

An efficient parallel X-FEM computing method

Abstract

This chapter describes how to apply the domain decomposition approach to obtain a parallel implementation of an eXtended Finite Element Method (X-FEM) model involving hydraulic fracturing. In particular, it explains how to handle X-FEM-specific operations that span multiple sub-domains, including the addition of degrees of freedom and the calculation of enrichment functions. It shows, by means of examples, that a consistent model can be constructed by clever data management between sub-domains in a specific way. The resulting sequence of linear systems of equations are solved in parallel by means of the GMRES algorithm in combination with a two-level preconditioner. The chapter ends by describing the performance results that have been obtained for three different models including the enhanced local pressure model.

Scientific computing and numerical modelling have provided a major contribution in the fields of research and development. As problems get more complex the computational demands increase until the point that simulations become so large that their solution simply costs too much time or the memory resources are too limited to store the model. Parallel computing, where many computations are performed simultaneously is therefore a necessity (Asanovic et al., 2009). In this chapter we investigate the possibility to apply parallel computing power for the simulation of hydraulic fracturing based on the Enhanced Local Pressure (ELP) model. Typical hydraulic fracturing simulations cover various length scales. On the one hand, the fracture pattern is a complex network of fractures that exists on a relatively small length scale (see Chapter 5). On the other hand, a complete fracture network may span multiple meters up to hundreds of meters (King, 2010). Spanning this scale using a fixed discretization technique results in large meshes with many degrees of freedom (DOFS). Parallel computing may greatly decrease computation times and memory requirements per computational core in these simulations.

A finite element simulation can be divided into three different stages i.e. (1) assembly of the matrices and of the force vectors, (2) solving the system of equations, and (3) IO operations such as reading the mesh and post-processing results. First efforts in parallelizing the finite element method were purely focussed on parallelization of the solver step. Direct solutions techniques such as Gaussian elimination have been parallelized but may require large amounts of memory to solve large scale systems. Iterative methods have less severe storage requirements and can be faster when combined with a suitable preconditioner. Moreover, they can be implemented efficiently on parallel computers. An important drawback of only parallelizing the solver is that the efficiency is limited to the relative time needed for the solver step. If the solver step covers 80 % of the entire analysis time, the simulations can only be reduced by a factor 5, since the remaining 20 % is not parallelized (Graham et al., 2005; Heroux et al., 2006).

Domain decomposition (DD) methods refer to a collection of techniques based on the principle of divide and conquer (Smith et al., 2004). The method originated with the purpose to solve partial differential equations over regions in two or three dimensions. The domain decomposition method attempts to solve a problem in an entire domain by using solutions obtained in sub-domains. The motivation to apply this method in parallel computing, occurs when the entire global domain is too large to fit in the available memory of a single computing core. Partitioning in sub-domains that fit into the memory is a solution to this problem (Saad, 2003). The

structure of domain decomposition aligns very naturally with the concept of parallel computing since each sub-domain can be processed by one computer core leading to minimal communication between the sub-domains. In this chapter we seek to effectively apply iterative solvers combined with the DD method to the eXtended Finite Element Method (X-FEM).

The enhanced local pressure model for the simulation of hydraulic fracturing was introduced in Chapter 4. The ELP model applies the concept of the extended finite element method to simulate fracture propagation. The X-FEM is an advanced numerical technique to model boundaries, such as inclusions, propagating cracks and holes, irrespectively of the underlying mesh. The method is based on the partition of unity property of finite element shape functions (Melenk and Babuška, 1996). Belytschko and Black were the first to exploit this property to model crack growth (Belytschko and Black, 1999). The method was improved by Dolbow et al. (2000) and Moës et al. (1999) by using two enrichment functions for the discontinuous crack and for the singular tip, respectively. Wells and Sluys (2001) incorporated a cohesive process zone within the extended finite element framework. Branched and merged cracks were included by Daux et al. (2000) by superimposing multiple enrichment functions. The X-FEM has many successful modelling applications see e.g. for, inclusions (Sukumar et al., 2001), hydraulic fracturing (Lecampion, 2009; Mohammadnejad and Khoei, 2013), porous media (de Borst et al., 2006; Kraaijeveld et al., 2013), large deformations (Legrain et al., 2005) and 3D cracks (Sukumar et al., 2000).

The X-FEM is an elegant tool to model cracks but solving the system of equations can be complex. Conditioning of the matrix can become problematic if elements are cut into a large area and a small area (Loehnert, 2014). To use iterative solution methods robust preconditioners are necessary to obtain solutions within an acceptable time frame. Obtaining such preconditioners is challenging. Rannou et al. (2007) investigated the efficiency of the multigrid method applied to an X-FEM problem. Multigrid methods make use of the fact that iterative solvers are efficient in solving the high frequency part of a solution but less to calculate the low frequency part. By considering grids with different spatial dimensions an iterative solver can be used much more effectively (Saad, 2003). The multigrid method was applied by Rannou et al. in localized regions of cracks to achieve fast and accurate convergence.

Berger-Vergiat et al. (2012) pursued a different approach using the algebraic multigrid method (AMG). AMG is a more general multigrid method that does not rely on geometrical information but just constructs coarse

grids directly from the system matrix. Berger-Veriat et al. applied the domain decomposition approach to split the the mesh in such a way that fractures are isolated in separate domains. The algebraic multigrid method could then be applied to approximate a solution on the large non-fractured domain while not being influenced by the discretization of the fracture. The fractured domains were solved concurrently on direct solvers followed by a complete solve in a GMRES solver. The possibility to include multiple propagating fractures is described in Waisman and Berger-Vergiat (2013). Related to this approach, Gerstenberger and Tuminaro (2012) transformed the X-FEM formulation into a phantom node description and applied AMG directly to this system.

The aforementioned publications involving X-FEM have in common that they seek to obtain optimal convergence rates with iterative solvers. Good results were presented but none of them truly addresses the implications of using multiple, concurrent processors. This work, in contrast, does not exclusively focus on the positive effect of a preconditioner on the convergence rate, but aims to improve computation times and decrease memory requirements by using parallel processors. We investigate the possibility to use the DD approach in combination with X-FEM and also apply it to our ELP model. Viguera et al. (2015) used a similar approach to investigate composite fractures using cohesive zones in combination with X-FEM. They discuss mainly the X-FEM and cohesive zone implementation while the implementation on the parallel processors is only discussed briefly. By using a shifted Heaviside enrichment in their work, there is no necessity to inform neighbouring elements about the enrichment (Fries, 2008). Crack propagation is governed by a principal stress criterion where the element stress is extrapolated to the nodes. If nodes are shared by more than one sub-process this data is exchanged. However, more information must be exchanged between sub-domains if e.g. the shifted enrichment is not used or if the fracture propagation is based on an average stress or on stress intensity factors that involve a region around a fracture tip.

6.1 Model background

In this section the background of the model is discussed. The concept the extended finite element method is first explained followed by a description of the used solver and preconditioner. In the remainder of the section the domain decomposition method is introduced and consequences of including X-FEM within the DD framework are discussed.

6.1.1 A review of the extended finite element method

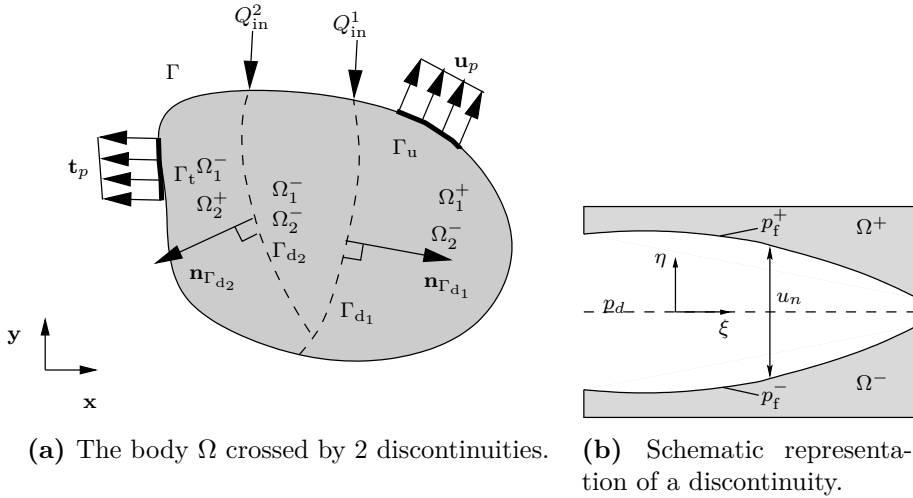


Figure 6.1: (a) Schematic representation of body Ω crossed by two discontinuities (dashed lines). The discontinuities, represented by a normal vector, divide the body in a positive and a negative part. (b) Schematic representation of a discontinuity including the local coordinate system.

The general framework of the kinematic relations for the hydraulic fracturing model is explained in Section 4.1. Suppose that a body Ω is crossed by m discontinuities (Figure 6.1a). At any time t and at location \mathbf{x} , an arbitrary displacement field in body Ω can be computed as the the sum of a continuous displacement field $\hat{\mathbf{u}}(\mathbf{x}, t)$ and m additional displacement fields $\tilde{\mathbf{u}}_i(\mathbf{x}, t)$ as in (Belytschko and Black, 1999; Moës et al., 1999; Remmers et al., 2008)

$$\mathbf{u}(\mathbf{x}, t) = \hat{\mathbf{u}}(\mathbf{x}, t) + \sum_{i=1}^m \mathcal{H}_{\Gamma_{d_i}}(\mathbf{x}) \tilde{\mathbf{u}}_i(\mathbf{x}, t), \quad (6.1)$$

where $\mathcal{H}_{\Gamma_{d_i}}$ is the Heaviside function that gives rise to a discontinuous displacement field due to discontinuity Γ_i given by

$$\mathcal{H}_{\Gamma_{d_i}} = \begin{cases} 1 & \text{if } \mathbf{x} \in \Omega_i^+ \\ 0 & \text{if } \mathbf{x} \in \Omega_i^- \end{cases} \quad (6.2)$$

The pressure in the discontinuity is defined by an independent variable p_d (Figure 6.1b(Section 4.1))

$$p_d = p \quad \mathbf{x} \in \Gamma_d. \quad (6.3)$$

The spatial discretization of the kinematic relations is based on the partition of unity property of finite element shape functions as described in the work of Melenk and Babuška (1996). The variational forms, the displacement field and the pressure in the fracture are discretized similarly following the Bubnov-Galerkin approach as

$$\mathbf{u} = \mathbf{N}\hat{\mathbf{u}} + \sum_{i=1}^m \mathcal{H}_{\Gamma_{d_i}} \mathbf{N}\tilde{\mathbf{u}}_i \quad (6.4)$$

and

$$p_d = \mathbf{V}\mathbf{p}_d \quad (6.5)$$

where \mathbf{N} and \mathbf{V} are the matrices containing the standard shape functions for the nodal displacements and the pressure in the discontinuity, respectively. The term $\hat{\mathbf{u}}$ contains the continuous nodal values of the displacement fields and the term $\tilde{\mathbf{u}}$ contains the displacement field associated with the enhanced nodes. The enhanced displacement is only present in nodes bordering a discontinuity and is given by \mathbf{p}_d (Figure 6.2). In this chapter poro-elasticity in the bulk is not considered. Details about the constitutive relations and the derivation of the momentum and mass balance equations are given in Sections 4.2-4.5.

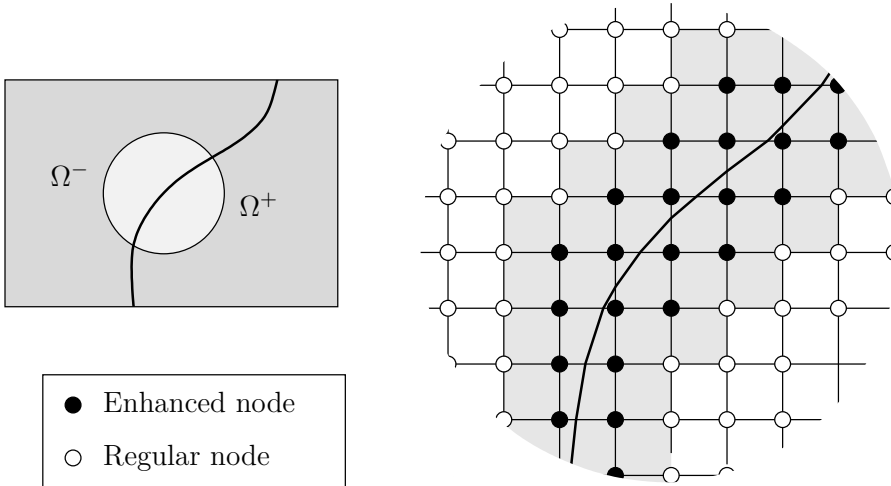


Figure 6.2: Domain crossed by one discontinuity.

6.1.2 Solver and preconditioner

Including the kinematic relations given in Equations (6.1) and (6.3) into balance equations and into constitutive relations (see Section 5.1.3), results in a non-linear system of equations. This system is solved using a Newton-Raphson scheme after applying linearization (see Section 4.5). Each Newton iteration requires the solution of a system of equations that is in the form of

$$\mathbf{K}\delta\mathbf{a} = \mathbf{f}_{\text{ext}} - \mathbf{f}_{\text{int}}. \quad (6.6)$$

The matrix \mathbf{K} is the stiffness matrix, $\delta\mathbf{a}$ is a vector containing the incremental degrees of freedom (DOF) of the displacement field and of the pressure in the discontinuity, and \mathbf{f}_{ext} and \mathbf{f}_{int} are the vectors containing the external and internal terms of the momentum and the mass balance, respectively. \mathbf{K} is a $n \times n$ non-singular matrix where n is equal to the total degrees of freedom in the system. Direct solution methods for this system exist based on the factorization of matrix \mathbf{K} in an upper and lower triangular matrix. However, the factorization is expensive process in computations with many degrees of freedom (Saad, 2003). Iterative methods generate a solution based on a sequence of approximate solutions and only involve matrix-vector multiplications. As a result, they require less computational power and are more straightforward to implement on parallel computers. In this work we use a GMRES iterative solver to find the solution of Eq. (6.6). The effectiveness of the GMRES solver can be improved by transforming Equation (6.6) into a system that has more favourable properties for the iterative solver. This can be achieved by finding a suitable preconditioner \mathbf{M} that transforms the equation in

$$\mathbf{M}^{-1}\mathbf{K}\mathbf{a} = \mathbf{M}^{-1}\mathbf{f}. \quad (6.7)$$

In this chapter we use a two-level preconditioner consisting of a restricted additive Schwarz (RAS) preconditioner that acts on the subdomain level, and a coarse grid preconditioner that acts on the global level. The RAS preconditioner is based on an incomplete Cholesky decomposition. The coarse grid preconditioner is based on the rigid body modes of the subdomains. A brief description of the preconditioner follows; more details about the preconditioners and the GMRES solver can be found in (Lingen et al., 2014).

The RAS preconditioner and the coarse grid preconditioner are combined in a multiplicative way. This means that:

$$\mathbf{M}^{-1} = \mathbf{P}_0^{-1} \left(\mathbf{I} - \mathbf{K} \mathbf{P}^{-1} \right) \quad (6.8)$$

where \mathbf{P}_0^{-1} denotes the coarse grid preconditioner and \mathbf{P}^{-1} denotes the RAS preconditioner. The latter can be written as a sum of sub-domain preconditioners:

$$\mathbf{P}^{-1} = \sum_{i=1}^{n_s} \mathbf{P}_i^{-1} \quad (6.9)$$

in which n_s denotes the number of sub-domains.

The coarse preconditioner \mathbf{P}_0^{-1} is obtained by projecting the stiffness matrix onto a vector space that forms the algebraic coarse grid. If this vector space is spanned by the columns of the matrix \mathbf{V} , then

$$\mathbf{P}_0^{-1} = \mathbf{V} \mathbf{A}^{-1} \mathbf{V}^T = \mathbf{V} \left(\mathbf{V}^T \mathbf{K} \mathbf{V} \right)^{-1} \mathbf{V}^T \quad (6.10)$$

with \mathbf{A} the projected stiffness matrix, also called the coarse matrix. The effectiveness of the coarse preconditioner is determined by the construction of the matrix \mathbf{V} . A good choice has proven to be:

$$\mathbf{V} = \left[\mathbf{N}_1 \quad \cdots \quad \mathbf{N}_n \right] \quad (6.11)$$

in which the rectangular matrices \mathbf{N}_i represent the coarse grid modes per sub-domain. That is, each matrix \mathbf{N}_i only contains non-zero values on the rows associated with sub-domain i . It has as many rows as the total number of degrees of freedom and as many columns as the number of coarse grid modes associated with sub-domain i .

The coarse preconditioner is most effective when it removes problematic eigenvalues from the stiffness matrix that can not be removed by the RAS preconditioner. In the context of this chapter these eigenvalues are related to the rigid body modes of the sub-domains. This implies that each matrix \mathbf{N}_i contains three columns representing two rigid translations and one (linearized) rotation of the i -th sub-domain. The three column vectors can be viewed as a series of pairs, one for each node in the sub-domain, representing the two displacements along the global coordinate axes. These pairs are given by:

$$\begin{aligned} \text{translation along the x-axis} & : [1, 0] \\ \text{translation along the y-axis} & : [0, 1] \\ \text{rotation about the z-axis} & : [-y, x] \end{aligned}$$

where x and y are the coordinates of the node with which the pair is associated.

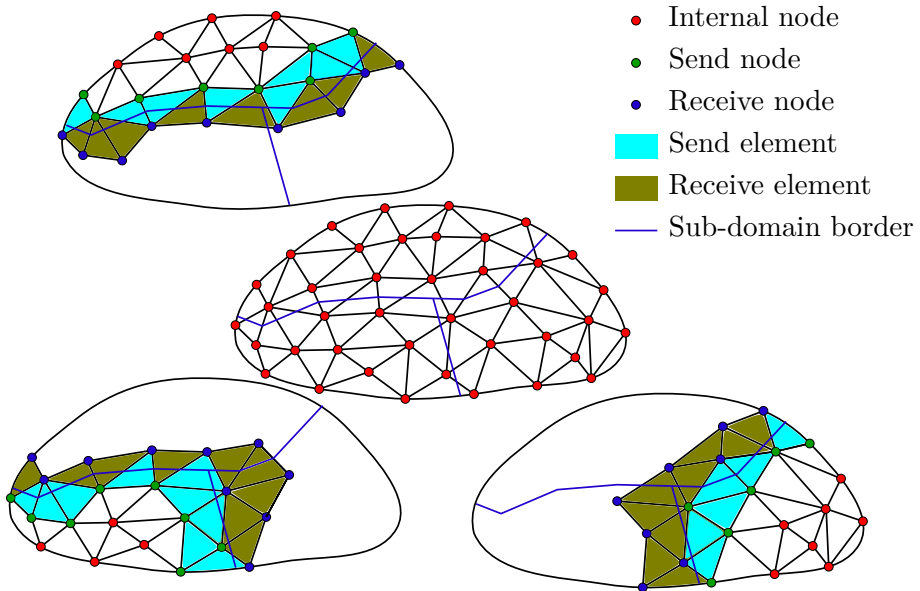


Figure 6.3: Domain decomposition applied at a general finite element mesh. The mesh is divided into three sub-domains indicated by the blue line. The colours illustrate whether the nodes are internal quantities or are part of the overlapping region between the sub-domains. Note that a send quantity can have multiple receive counterparts on other sub-domains.

6.1.3 Domain decomposition

The domain decomposition approach can be used to parallelize iterative solvers. The idea behind this approach is to divide a global problem in many sub-problems that can be solved almost independently on different processors. Some data exchange between the sub-problems is needed since the solution within one sub-domain is not completely independent of other sub-domains. The finite element mesh is first partitioned into n_s non-overlapping groups of elements that we name blocks. The blocks are slightly extended by adding elements from neighbour blocks. Strictly speaking this overlap is not necessary in the domain decomposition approach but it improves the convergence rate of the iterative solver. Also the parallel X-FEM implementation becomes more simple because element-related data, including information about crack growth, is more easily exchanged between processes. The elements and nodes that are only part of a sub-domain are referred to as internal elements and internal nodes respectively (see Figure 6.3). The elements and nodes that are shared are named overlap elements and overlap nodes. Each overlapping node and element is always an internal

quantity in one sub-process. These unique elements and nodes are referred to as send elements and send nodes. The corresponding overlap nodes in the other sub-process are named receive elements and receive nodes. Note that, as seen in Figure 6.3, one send quantity may have more than one receive quantity.

To obtain the best achievable speed-up, the entire finite element model is divided among the sub-processes defined by the domain decomposition. This means that besides solving Equation (6.6) also the assembly of matrix \mathbf{K} is performed in parallel. In a regular finite element model this requires pre-processing the mesh but further modifications are not required since the solver and the preconditioner can handle all communication between the sub-domains.

6.1.4 Tracking the fracture location

An important aspect in applying domain decomposition to an extended finite element model is the manner in which the fracture surface is tracked. In this work we use the level set method, which is a common technique to track moving interfaces (Sethian, 1999). The interface is represented by the zero level set of a function $\phi(\mathbf{x}, t)$, that is one dimension higher than the interface. The movement of the interface can be described by a velocity vector resulting in a hyperbolic propagation equation.

The level set method is compatible with the X-FEM since the values of the level set may be stored as a nodal quantity. Sukumar et al. (2001) used one level set to describe a planar crack. Propagation of the crack was governed by solving the level set equation with the fast marching method. Moës et al. introduced a second level set to solve non planar crack growth (Moës et al., 2002; Gravouil et al., 2002). The surface and front of the crack are represented by a separate level set. They solved the movement of the level set on an unstructured triangular finite element mesh based on a method introduced by Barth and Sethian (1998). We chose not to adopt this approach because i) the crack propagation goes from element edge to element edge and is therefore not smooth which is in conflict with the level set evolution equation and ii) using the method introduces overhead in computation time that increases with large meshes or when multiple fracture are considered. Instead we use the idea to represent the fracture location by two level sets but update the values based on the propagation direction of the crack. Representing a fracture with two level sets is also an ideal method in parallel computing, as will be discussed next, because it is stored as a nodal quantity.

6.1.5 Numerical implementation of DD with X-FEM

Additional modifications have to be made to our extended finite element model due to applying the domain decomposition also to the element assembly. As the fracture grows, additional degrees of freedom are added to the system, thus changing the dimension of the stiffness matrix and force vectors. This requires updating the preconditioners when these degrees of freedom are added. However, the main modifications are related to the part of the model involved with the fracture propagation. The general flow chart of our X-FEM model is shown in Figure 6.4. The part of the code that performs the X-FEM routines is subdivided in three subroutines on the right. Each subroutine needs, depending on the fracture location, data exchange between sub-domains. This additional communication is only necessary when a fracture is propagating towards the boundaries of a sub-domain. It would therefore be possible to define the sub-domains in such a way that a fracture never leaves a sub-domain. This approach was e.g. adopted by Berger-Vergiat et al. (2012). However, this leads to elongated sub-domains and/or sub-domains that differ significantly in size. This, in turn, results in more data to be exchanged between processes and/or imbalances in the work load per process. We therefore want to apply the DD irrespectively of when and where a fracture propagates.

The decision whether a fracture tip propagates is always made on one sub-domain. Also any other consequences of a propagating fracture, relevant to other sub-domains, are signalled by this sub-domain. We define the signalling sub-domain based on the location of the tip. The tip element is the element which will be cut next by the fracture. This element is always uniquely defined and therefore a perfect marker for the signalling sub-domain. A tip is said to lie in sub-domain i if the tip element is either an internal element or a send element of that sub-domain (see also Figure 6.6). A fracture can only cross one element per propagation step. The newton iteration is restarted until no fracture propagation occurs (see also Section 3.2). Implementation wise we therefore only consider situations where one element is cut per propagating fracture tip within one converged Newton iteration.

In the following we explain what additional requirements are needed per subroutine, as shown in Figure 6.4, to apply domain decomposition on the extended finite element method. Note that the initial placed fractures do not need additional data exchange because their location is known in all of the sub-domains. Within the numerical implementation the open source Jem/Jive parallel FEM libraries were used (Lingen, 2016).

The initial mesh is divided in n_s partitions using the Jem/Jive partition-

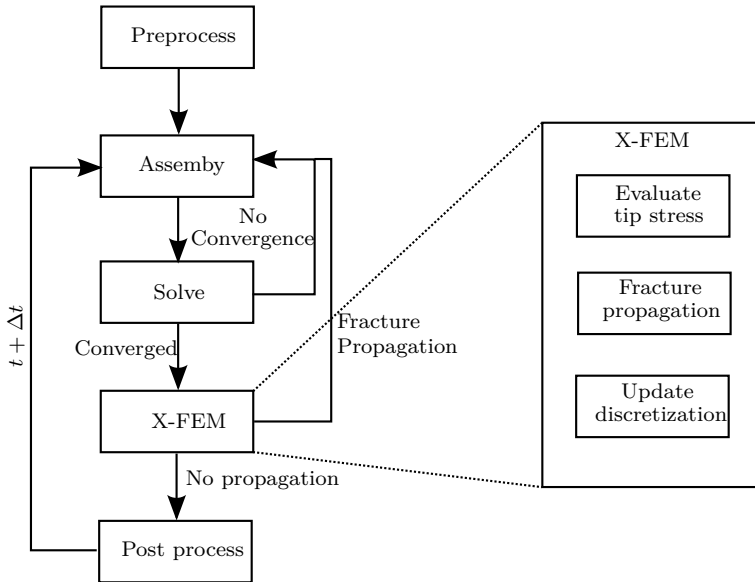


Figure 6.4: General flowchart of an X-FEM code. Applying domain decomposition requires modification in the X-FEM routines shown on the right.

ing procedures. These apply multi-level graph partitioning algorithms, similar to those implemented in Metis (Karypis and Kumar, 1998). Nodes and elements are numbered locally but communication between them is based on unique global IDs assigned during the partitioning process. After the partitioning, further calculations are performed on one computational core per sub-domain. Post-processing is also fully parallel. Each sub-process writes output files for the sub-domain only. These can be coupled together for the entire domain by using Paraview.

Messaging is only possible between neighbouring sub-domains. The message is a vector with a certain length that contains a data type such as integers or floats. The procedure for sending a message around is as follows: each sub-process first sends out a request to all neighbouring domains. The purpose of this request is to determine if other sub-processes want to send information and if so what the length of the message (vector) is. The request is thus followed by also sending a message to all neighbouring domains that is either empty if no information is going to be communicated or contains the length of the message that it is going to receive. All the sub-processes are put on wait until all messages are exchanged. This procedure is repeated a second time but now the actual message is exchanged to neighbouring domains and messages with a known length are received. A pseudo-code of this procedure is shown in algorithm 1.

Algorithm 1 A vector *SendMessage* is send to all other sub-processes and a vector *ReceiveMessage* is received.

```

for  $i \leftarrow 1, n_s$  do ▷  $n_s$  neighbouring sub-processes
     $R_i = \text{RequestMessage}(i)$ 
     $L_i = \text{SendMessage.size}()$ 
     $\text{SendMessage}(i, L_i)$ 
end for
waitAll()
for  $i \leftarrow 1, n_s$  do
     $\text{ReceiveMessage.resize}(R_i)$ 
     $\text{ReceiveMessage} = \text{RequestMessage}(i)$ 
     $\text{SendMessage}(i, \text{SendMessage})$ 
end for
waitAll()

```

The start of the X-FEM subroutines is the determination whether a fracture is propagating. The propagation criterion used in this chapter is based on an averages stress calculated with a Gaussian weighting function depending on length scale parameter l_a (Section 2.3). As a fracture tip propagates towards the sub-domain boundaries the length scale may span also other sub-domains (see Figure 6.5). It is therefore necessary that the neighbouring sub-domains know the tip location and can be called to exchange the average stress. This exchange is performed in the first X-FEM subroutine before the propagation criterion is evaluated. The stresses are exchanged with the correct sub-process by linking the latter to the local tip ID. Algorithm 2 shows the pseudo-code for the communication of tip stresses. Note that contributions to the average stress are only accounted for in internal elements since receive elements can be defined on multiple sub-domains.

An important aspect of any X-FEM model is the bookkeeping of the location of a propagating fracture. This bookkeeping is performed in the second X-FEM subroutine (Figure 6.4). We use two level sets, interpolated at finite element nodes, to describe a fracture surface. Communication between sub-domains within the iterative solver is based on the nodes. The advantage of storing the fracture as a nodal quantity is thus that these communication libraries can also be used to communicate the fracture location between sub-domains. This exchange is facilitated by a database structure in which the finite element nodes are stored. A synchronizing command can be executed on this database which exchanges all nodal quantities of a send node to to all corresponding receive nodes. However, there are scenarios in

Algorithm 2 Subroutine 1) evaluate tip stresses.

```

Collect tip stresses to send
Exchange the stresses using Algorithm 1
for  $iTip \leftarrow 1, nTip$  do
  if  $exchangeTip(iTip) = True$  then
    Add received stresses to the local stress
  end if
  if  $violation(iTip) = True$  then
    Propagate the tip
  end if
end for

```

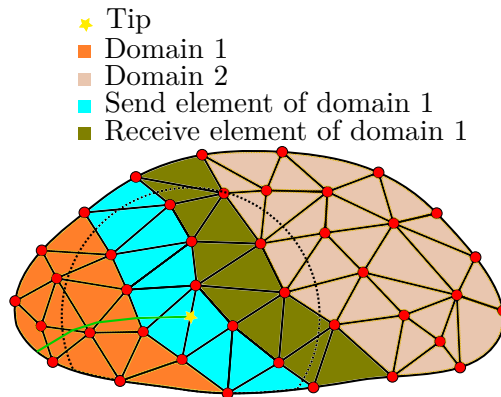


Figure 6.5: Data exchange due to the average stress propagation criterion. Elements lying within the dashed circle have contribution to the average stress.

which the level set values in a receive node are modified due to crack propagation. The database exchange will overwrite these values by the values of the send node residing on a different sub-domain. Thus, before performing the exchange we first modify the value of this send node by using the communication Algorithm 1. Once all level set values are changed within the sub-domains of the tip elements, the database is exchanged synchronizing the fracture as a unique quantity to all sub-domains. We realize that communicating all level sets over all the sub-domains is excessive since the modification takes only place in certain sub-domains. However, the communication routines must be started in all sub-processes since it is unknown which sub-domains are effected by fracture propagation. Exchanging the actual values is therefore not giving much overhead. The process of updating the level set is shown in Algorithm 3.

Once the level set values are updated in all sub-domains it is possible

Algorithm 3 Subroutine 2) propagate the fracture.

```

for  $iTip \leftarrow 1, nTip$  do
  if violation( $iTip$ ) = True then
    Propagate the level set within the sub-domain
    Store modified nodes in  $modNodes$ 
  end if
end for
Exchange values of  $modNodes$  with Algorithm 1
Synchronize the database with level set values

```

to enrich nodes and update integration schemes in elements effected by a propagating fracture. The updated integration schemes are necessary in elements crossed by the fracture but also the neighbouring elements require a modified integration due to the nodal enrichment (Wells and Sluys, 2001). Since the enrichment is based on the geometrical location of the fracture it is not possible to exchange the data as nodal interpolations as is often done in domain decomposition methods, see e.g. Lingen and Tijssens (2001). Additional data exchange procedures based on Algorithm 1 were therefore used. We distinguish between three different situations of fracture propagation that require additional data exchange which are also shown in Figure 6.6

- The most simple and straight forward situation occurs when the fracture is crossing a send element. In this case it is sufficient to transfer only the element ID that got crossed to all sub-domains where this element exist. Based on the level set values further enrichment and modifications to the integration scheme can be performed (Figure 6.6b and 6.6c).
- Another situation occurs when a fracture propagates neighbouring to send elements. The send element, belonging also to other sub-domains, receives a nodal enrichment. These additional DOFS need to be added in each sub-domain. A consequence of the enrichment is that the element contributes to the enriched part of the system of equations and therefore needs additional numerical integration in the element assembly (Figure 6.6a).
- The additional displacement field in nodes that form the edge at which the tip is located must be constrained to prevent the opening of the fracture tip. Similar to the previous situation this implies that a fracture propagating along send elements also need to signal

neighbouring sub-domains to release the correct degree of freedom (Figure 6.6a).

A Newton iteration is started until no fracture propagation occurs. Implementation wise we therefore did not consider situations where updates were necessary in an iterative way due to cutting multiple elements.

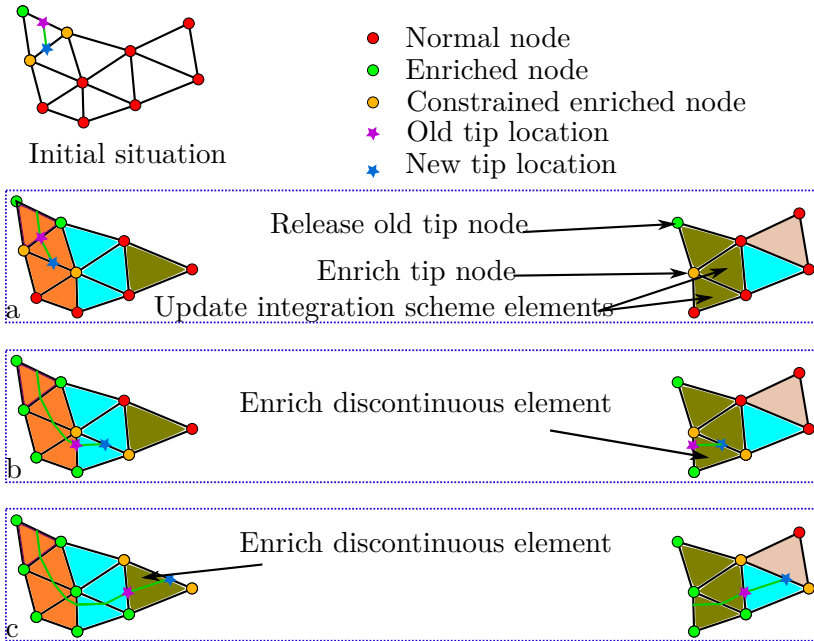


Figure 6.6: Schematic representation of three possible propagation steps that require data exchange between two sub-domains. The initial situation without domain decomposition is shown at the top. We refer to the two domains as domain 1 and domain 2 being the right and the left sub-domain, respectively. The three different situations, going from top to bottom, are a) when a fracture propagates neighbouring to a send element b) fracture propagation in a send element of domain 1 and c) fracture propagation in domain 2. Note that the fracture behaviour is controlled by domain 2 in the last step compared to the first two steps where domain 1 controlled the propagation.

6.2 Results

In this section we consider three examples to demonstrate the parallel X-FEM implementation and to address the performance. The performance is given as speed-up which is defined as the ratio between the computation time of one core compared to the time on multiple cores. The computations

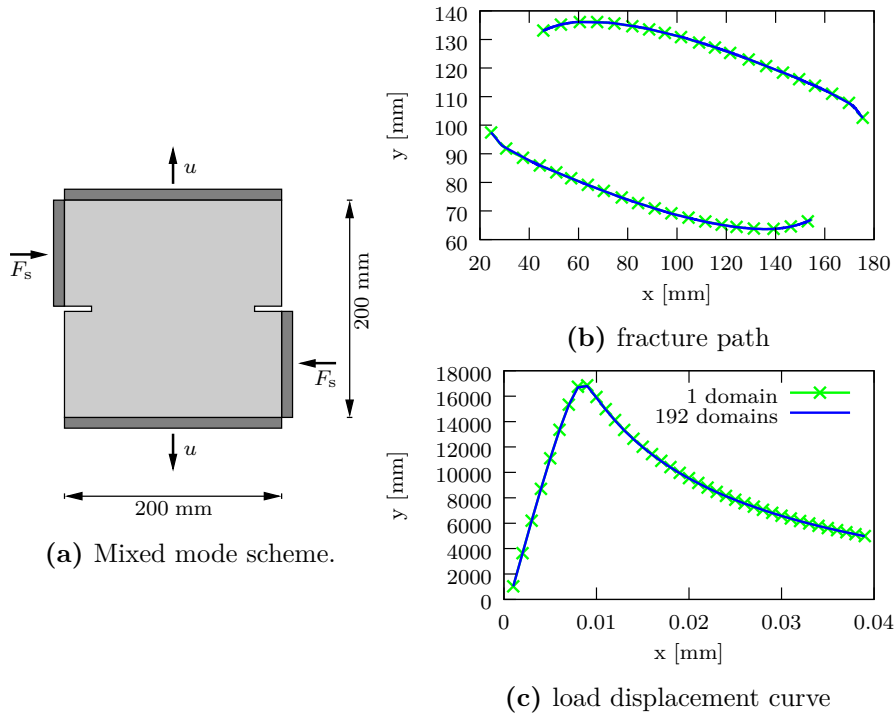


Figure 6.7: Scheme of the mixed mode and two simulation results.

were run on the Dutch HPC Cartesius system owned by the SURF Cooperative. This system is equipped with Haswell E5-2690 v3 Intel processors having 24 cores and 64 GB memory per compute node. In the first example we have used the regular X-FEM model without the additional p_d degree of freedom. The last two examples are performed with the ELP model and thus are about hydraulic fracturing. All the FE meshes consist of linear triangular elements.

6.2.1 Mixed mode fracture propagation

In this first example a squared double notched experiment in mortar is considered. The experiment was performed by Nooru-Mohamed (1992) and was used as a benchmark example for X-FEM models by Dumstorff and Meschke (2007). The geometry and the loading conditions of the specimen are shown in Figure 6.7a. The shear load $F_s = 10$ kN is applied instantaneous. The top and bottom surface are being pulled by a prescribed displacement of $1 \mu\text{m/s}$. A small initial fracture with a length of 2 mm is created at both notches. The specimen has a Young's modulus

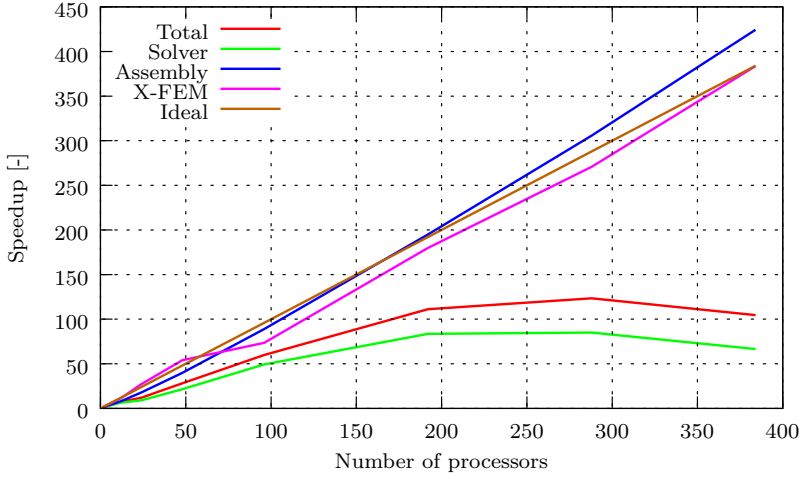


Figure 6.8: Speed-up graph for the mixed mode X-FEM simulation. The total speed-up of the simulation is shown in red. A separate speed-up is also shown for the element assembly phase, the X-FEM part of the code where the fracture propagation is being determined, and for the iterative GMRES solver.

of $E = 30$ MPa and a Poisson's ratio of $\nu = 0.20$. The ultimate strength is $\tau_{\text{ult}} = 3$ MPa with a fracture toughness of $\mathcal{G}_c = 0.11$ N/mm. The finite element mesh is made of 5.6 million elements with 2.8 million nodes, i.e. 5.6 million degrees of freedom. The crack path and the force displacement curve for a reference solution obtained without domain decomposition is compared with the result of using 192 cores in Figure 6.7. The path and force displacement curve are not influenced by the DD which illustrates the correct implementation of parallel X-FEM. The results are also in the range reported by the numerical study of Dumstorff and Meschke (2007).

To assess the speed-up the simulation is performed for six loading increments. This is sufficient to address the speed-up since the fracture can propagate through multiple elements within a load increment. A total of 1466 degrees of freedom are added to the system. The fracture grows over sub-domain boundaries depending on the number of cores used per simulation. As shown in Figure 6.4 the loading is only increased after the fracture propagation criterion is no longer violated.

Within the six loading increments the GMRES solver was called 766 times, performing 35944 iterations on a single core. The total simulation took 74 hours. The speed-up is divided for the three main parts of the X-FEM model, i.e. the matrix assembly, the GMRES solver and preconditioner, and the X-FEM routines. In Figure 6.8 we show these three

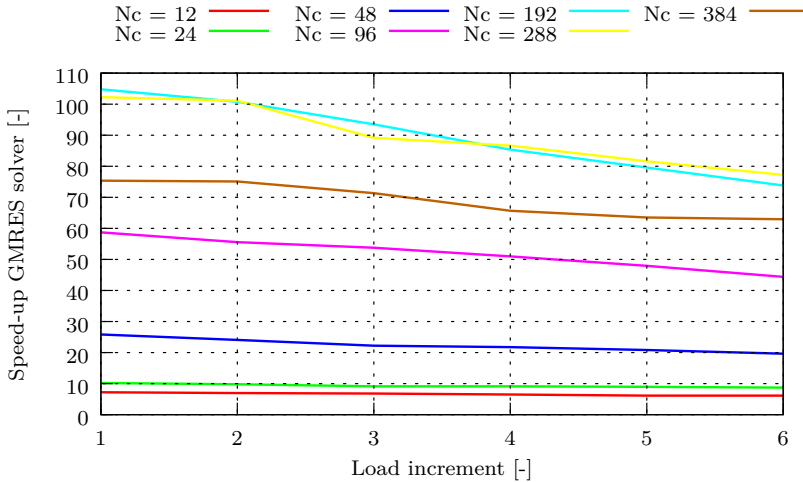


Figure 6.9: Speed-up graph for the GMRES solver shown against the loading increment. The speed-up decreases with increasing loading increments. This effect is more pronounced in simulations where the number of cores (N_c) is larger.

components and the total speed-up. The speed-up of the element assembly scales most optimal compared to the X-FEM part and the GMRES solver. The element assembly speed-up exceeds ideal behaviour which is caused by unequal Newton iterations. This also reflects on other speed-up results. The speed-up of the GMRES solver is the delaying factor in this simulation. This is caused by a combination of overhead due to data communication but also due to a decrease in efficiency of the preconditioners as the amount of sub-domains increase. The propagating fracture also has an effect on the speed-up of the GMRES solver as shown in Figure 6.9. With increasing amount of sub-domains the fracture crosses more domain boundaries and is therefore influencing the convergence rate of the GMRES solver. This leads to a stronger decrease in speed-up in simulations with a larger number of sub-domains. The largest total speed-up of 123.3 is achieved on 288 cores leading to a final simulation time of 37 minutes and 57 seconds.

6.2.2 KGD Hydraulic fracture problem

This mesh is having initially 3.4 million degrees of freedom which is less than the previous example. We apply the ELP model to simulate the plane strain KGD problem (see Figure 6.10a). The mesh is refined around the injection point within a circle of 0.5 m. The rock has a Young's modulus of $E = 17$ MPa and a Poisson's ratio of $\nu = 0.20$. The ultimate strength is $\tau_{\text{ult}} = 15$ MPa with a fracture toughness of $\mathcal{G}_c = 0.12$ N/mm. Fluid

is injected with a rate of $Q_{\text{in}} = 0.5 \text{ mm}^2/\text{s}$, the fluid viscosity is $\mu = 1.0\text{e}^{-5} \text{ Pa} \cdot \text{s}$, and an implicit time step of 1 second is used.

The implementation of the DD in combination with the ELP model is compared with the available analytical solution for the KGD problem (Geertsma and De Klerk, 1969). In Figure 6.10b the fracture length in a simulation with 192 cores is shown together with the analytical solution. There is some discrepancy between the analytical solution and the numerical solution. We expect this to be attributed to the fact that the analytical solution is based on different assumptions such as, linear elastic fracture mechanics. However, the trend of the results is consistent enough to conclude that the parallel implementation of the ELP model was successful. The speed-up of this simulation is shown in Figure 6.11. The speed-up of the GMRES solver is again the least efficient. Scalability is also lower compared to the first example which can partly be attributed to the lower amount of DOFS in this example. However, the addition of the p_d DOF also results in higher number of iterations of the GMRES solver. This effect deteriorates as the amount of sub-domains increases. The simulation is performed for two time steps and the duration is 12 hours and 11 minutes on one core.

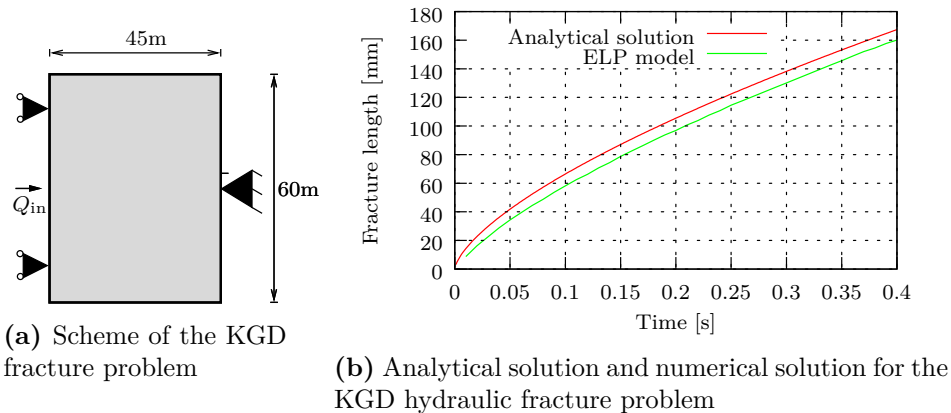


Figure 6.10: The schematic representation of the KGD hydraulic fracture problem is shown on the left. The result of the fracture length versus the time for this problem using 192 cores is shown on the right.

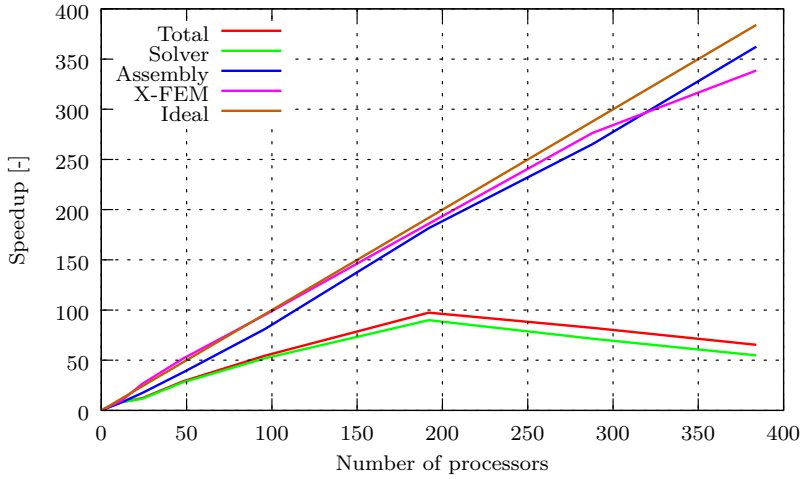


Figure 6.11: Speed-up for the KGD hydraulic fracture problem simulated using the ELP model. The total speed-up of the simulation is shown in red. A separate speed-up is also shown for the element assembly phase, the X-FEM part of the code where the fracture propagation is being determined, and for the iterative GMRES solver.

6.2.3 Two parallel hydraulic fractures

The last example consists of two hydraulic fractures in a 4 by 4 m block having a Young's modulus of $E = 30$ MPa and a Poisson's ratio of $\nu = 0.20$. Both fractures have a fluid injection point in the middle and are subjected to a constant fluid inflow of $20 \text{ mm}^2/\text{s}$ with a dynamic viscosity of $\mu = 1.0e^{-3} \text{ Pa} \cdot \text{s}$. The ultimate strength is $\tau_{\text{ult}} = 5$ MPa with a fracture toughness of $\mathcal{G}_c = 2.0 \text{ N/mm}$. The initial system has 7.4 million degrees of freedom and calculations are performed on 288 cores. The initial length of both fractures is 0.6 meter and they are spaced 1 meter apart. Due to the ratio between the length of the hydraulic fractures and the spacing between the fractures influence each other propagation direction. The hydraulic fractures curve away from the initial fractures. This is referred to as the stress shadowing effect (Bunger and Peirce, 2014; Lee et al., 2016).

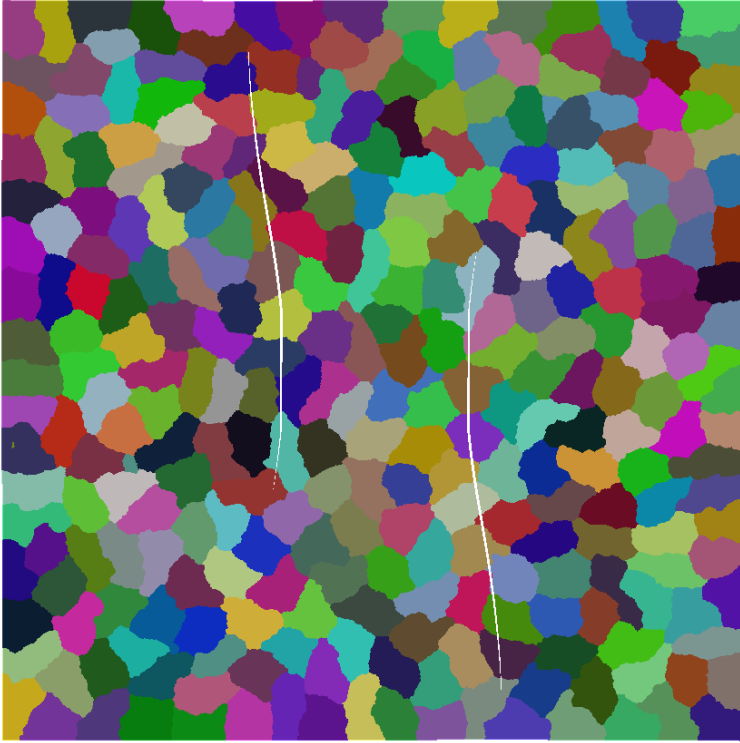


Figure 6.12: Visualization of the mesh with two propagating hydraulic fractures. The 288 domains are coloured differently illustrating that the fracture crosses multiple domains. The deformed configuration is magnified 25 times.

The curving away of the hydraulic fractures is also observed in our results as shown in Figure 6.12. It can be seen that the left fracture propagates more upwards while the right fracture grows farther in downward direction. In an ideal symmetrical situation this growth would be exactly the same. However, the used propagation criterion in this chapter is stress based and therefore subject to some mesh dependency. There is a moment in the simulation that the top left tip and bottom right tip are slightly more loaded than the other two tips. They therefore grow, increasing their loading surface, escaping from the stress shadow effect of the neighbouring fracture and therefore keep propagating while the other two tips are prevented from growing. In Figure 6.12 the 288 different sub-domains are also all given a different colour. The fractures are free to propagate through domain boundaries and are not influenced by the shape of domains. This approach leads to almost optimal load balance during assembly of the stiffness matrix and solving the system in the iterative solver. A small discrepancy

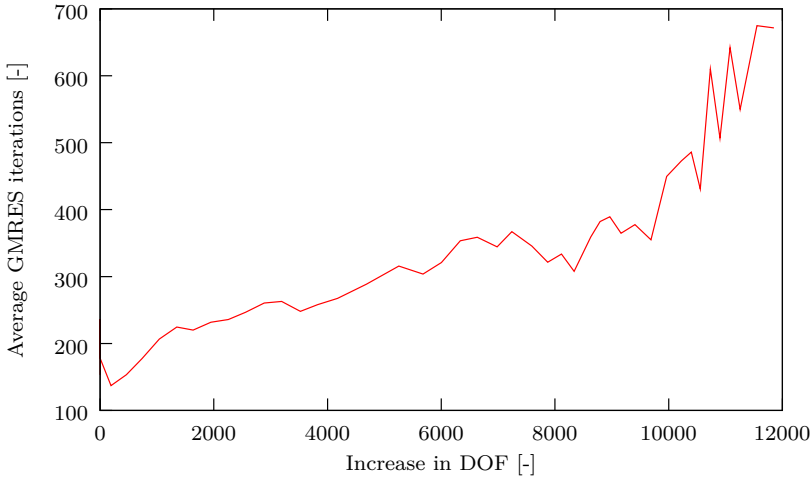


Figure 6.13: Average iteration count of the GMRES solver in the simulation with two parallel hydraulic fractures. The iteration count is shown against the increase in degrees of freedom due to fracture propagation.

of load balancing occurs due to the degrees of freedom that are added when the fracture propagates. However, the 11850 DOFS that are added are still a low amount compared to the initial 7.4 million DOFS. The main reason for non ideal speed-up is the increasing amount of iterations needed in the GMRES solver. The average amount of the GMRES iterations within one time step are shown in Figure 6.13. The increase of iterations as the fracture propagates can be attributed to worsening of the condition number of the stiffness matrix but also to the fracture crossing through multiple sub-domains. The former is also observed in other X-FEM works that applied the domain decomposition approach (Berger-Vergiat et al., 2012). The coarse grid preconditioner, responsible for keeping the number of iterations stable as the number of sub-domains increase, does not take the additional displacement DOFS into account nor is the p_d DOF considered in it. This has a large impact on the convergence rates of the GMRES solver as more domains are crossed.

6.3 Conclusions

In this chapter we have presented a parallel implementation of a our ELP model, which is based on the extended finite element method, using the domain decomposition approach. Both matrix assembly and solving the system of equations with a GMRES solver are performed in parallel. We

have illustrated the key implementation aspects that should be considered when applying domain decomposition in an X-FEM model. In three examples we have shown the successful DD implementation. The model is consistent irrespective of the chosen sub-domains and is compared with other numerical data and an analytical solution. The results show that it is possible to apply the domain decomposition method at any X-FEM model to benefit from parallel computing power. Enrichment functions are not restricted to discontinuous elements but can be extended across sub-domains by using additional data exchange within the X-FEM routines. We have shown that the scalability of these routines should not be the limiting factor in parallel X-FEM computations. The total speed-up achieved is not ideal. This can mainly be attributed to the not optimal conditioning of the system of equations resulting from the X-FEM model. Despite this we can still achieve a speed-up above 100 using a moderate amount of cores decreasing, computational times significantly. This is a necessary improvement in order to use the ELP model for large scale 2D hydraulic fracture simulations.

In the following chapter the model is extended to simulate fracture propagation in 3D. This extension is necessary to simulate tortuous fracture geometries that may occur near deviated wells. The 3D model may eventually benefit greatly from the parallel implementation due to having more computational demands than a 2D model.

7

A 3D partition of unity based hydraulic fracture model

Abstract

A 3D model for the simulation of hydraulic fracturing is presented in this chapter. A fracture is included in the finite element mesh by exploiting the partition of unity property of finite element shape function. Based on the concept of the extended finite element method an additional displacement field is included to nodes surrounding the fracture. The additional field is multiplied by a Heaviside step function defined across the fracture, leading to a discontinuity in the displacement field. By representing the fracture surface with two level sets a framework for tracking the fracture surface in 3D is introduced. The framework is based on the fact that a fracture grows from element face to element face. Energy dissipation is controlled by a cohesive zone formulation. The enhanced local pressure model, which is based on the extended finite element, includes an additional degree of freedom to model a fluid pressure within the fracture. The framework derived for the extended finite element model is used to simulate the 3D hydraulic fracturing based on the enhanced local pressure model. The performance of the 3D model is demonstrated with three examples.

The simulations shown in the previous chapters were performed in a 2D situation under plane strain assumptions. This is sufficient to obtain insight in general trends such as length of a single fracture or fracture interaction behaviour. Hydraulic fracture propagation from a deviated well leads to the growth of complex fracture patterns. A tortuous fracture surface can grow due to the initial deviated fracture plane being not orthogonal to the least horizontal stress. Tortuous fractures hinder fluid flow resulting a smaller fracture network and thus lower production rates. Modelling such behaviour is only possible with a 3D model (Hossain and Rahman, 2008). In this chapter the framework for extending the fracture model used in the previous chapters to 3D is presented.

The eXtended Finite Element Method (X-FEM) is an elegant tool to incorporate a discontinuity in the displacement field irrespectively of the underlying mesh. Based on the partition of unity (Melenk and Babuška, 1996) property of finite element shape function a discontinuity is included to the displacement field by adding an additional displacement field to nodes surrounding the discontinuity (Belytschko and Black, 1999; Moës et al., 1999). The extension of the extended finite element method to 3D is primarily a computational challenge. The kinematic relations and the balance equations hold both in 2D and in 3D. What changes is the representation of a fracture as a line and the fracture tip as a point in 2D into being a plane and a line in 3D, respectively. Keeping track of the fracture location as a plane is more challenging than a line. The propagation of the fracture in 3D can no longer be controlled by a single point but should be possible along the entire fracture front. Both tracking the surface as well as determining where and when the fracture front propagates lead to additional requirements in a 3D model.

Sukumar et al. (2000) were the first to apply the extended finite element method in 3D solids and demonstrated a good accuracy of numerical stress intensity factors with exact solutions. Planar crack propagation was included in a later work by using a fast marching algorithm to track the fracture surface (Sukumar et al., 2003). Non-planar crack growth was considered by Gravouil et al. (2002) using the model introduced by Moës et al. (2002). The location of the fracture surface was controlled by two level sets, one for the fracture surface and one for the fracture front, respectively. Fracture propagation was described by evolving the level set equation by solving several Hamilton-Jacobi equations. The elegance of their approach is that these solutions were obtained using the same mesh as was used for the extended finite element method simulations. This led to a direct coupling between the crack discretization and the level set.

However, difficulties in updating the level set equations arise in decoupling the update between a fixed part (the already existing fracture surface) and a propagating part. Ventura et al. (2003) used a tuple representation of the level set and updated the values using geometric formulas. This method has in common with the work of Moës et al. (2002) that an effort is made to maintain the level set as a smooth surface. Our numerical framework allows for element edge to element edge propagation. Thus it is not a necessity to maintain the smooth property of the level set. In this chapter we introduce a level set update based purely on geometrical formulas. This approach has many similarities with the 3D partition of unity based approach by Gasser and Holzapfel (2005, 2006). They define a local tracking algorithm based on also propagating element by element. The orientation of the new fracture plane within an element is defined by a normal and a point on the plane. A smoothing algorithm is included to predict a closed fracture surface. Information of elements cut by a fracture are stored on element basis. Becker et al. (2010) adopted the same approach in 3D to model fracture propagation in concrete which was modelled as a porous material. Hygro-mechanical interactions in the concrete due to moisture transport were included.

In the context of hydraulic fracturing a 3D boundary element was developed by Hossain and Rahman (2008). Li et al. (2012) used a finite element model with a smeared damage approach to simulate 3D fracturing. Gupta and Duarte (2014) developed an extended finite element method based model for 3D non planar hydraulic fracture propagation. This model did not include fluid flow within the fracture but assumed a constant pressure in the fracture. The fracture surface was calculated in explicit manner i.e. the actual surface within the finite element mesh is not identical to the geometrical representation. This approach was necessary since kinks in the fracture surface can be present within an element. Such a representation caused limitations on the continuity of the mesh giving problems to fluid flow integration, hence the constant pressure. A mesh approximation was performed in Gupta and Duarte (2015) to include fluid injection. Fracture propagation was not yet considered in this work.

The Enhanced Local Pressure (ELP) model is developed for hydraulic fracturing in low permeable rocks (Chapter 4). Based on the extended finite element method a fracture is included as a discontinuity in the displacement field. The model is improved to consider fracture interaction in Chapter 5. In this chapter we extend the X-FEM model and the ELP model to 3D. Pore pressure is not included in the formulation. The balance equations and constitutive equations given in 2D are also applicable in 3D. The main

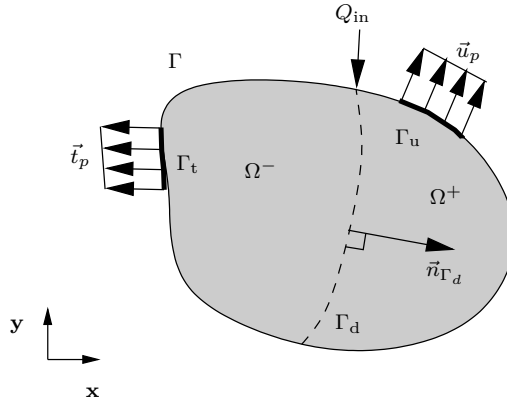


Figure 7.1: A body Ω crossed by a discontinuity.

challenge lies in representing and propagating the fracture surface. Instead of storing the crack as a geometrical entity as was proposed by Gasser and Holzapfel (2006) we store the surface and front location with two level sets as was proposed by Moës et al. (2002). The updating is similar as proposed in the work of Gasser and Holzapfel (2006). The advantage of this approach is that continuity of the fracture surface is preserved along element boundaries by the level set. We first apply the 3D update of the level sets to the extended finite element method without considering the enhanced local pressure model. The propagation of the fractures is validated with this formulation. The enhanced local pressure model is extended additionally to show the performance of hydraulic fracture propagation in a 3D solid material without leak-off.

7.1 Model background

The kinematic relations described in 2D (see Sections 4.1) can be generalized to 3D. Consider a body Ω with a discontinuity (see Figure 7.1 for the 2D representation). A discontinuity divides the body into two part Ω^+ and Ω^- . The displacement field becomes discontinuous and can be described by separating the total field in a continuous field and a discontinuous field as

$$\mathbf{u}(\mathbf{x}, t) = \hat{\mathbf{u}}(\mathbf{x}, t) + \mathcal{H}_\Gamma(\mathbf{x})\tilde{\mathbf{u}}(\mathbf{x}, t), \quad (7.1)$$

where \mathbf{x} is the position of a material point and \mathcal{H}_Γ is the Heaviside step function defined across the discontinuity as

$$\mathcal{H}_\Gamma = \begin{cases} 1 & \text{if } \mathbf{x} \in \Omega \\ 0 & \text{if } \mathbf{x} \in \Omega \end{cases} \quad (7.2)$$

At the discontinuity Γ_d , the strain field is undefined and the kinematic quantity is defined by a jump in the displacement field

$$[\mathbf{u}(\mathbf{x}, t)] = \tilde{\mathbf{u}}(\mathbf{x}, t), \quad \mathbf{x} \in \Gamma_d. \quad (7.3)$$

The linear quasi-static momentum balance without body forces is

$$\nabla \cdot \boldsymbol{\sigma} = \mathbf{0}, \quad (7.4)$$

where $\boldsymbol{\sigma}$ is the Cauchy stress tensor. The body is subject to the following boundary conditions

$$\begin{aligned} \boldsymbol{\sigma} \cdot \mathbf{n}_\Gamma &= \mathbf{t}_p(\mathbf{x}, t) & \mathbf{x} \in \Gamma_t, \\ \mathbf{u}(\mathbf{x}, t) &= \mathbf{u}_p(\mathbf{x}, t) & \mathbf{x} \in \Gamma_u, \end{aligned} \quad (7.5)$$

with $\Gamma_t \cup \Gamma_u = \Gamma, \Gamma_t \cap \Gamma_u = \emptyset$ and Γ is the entire surface of the body. Multiplying the momentum balance with the test function $\boldsymbol{\eta}$ which has the same form as the displacement field

$$\boldsymbol{\eta} = \hat{\boldsymbol{\eta}} + \mathcal{H}_{\Gamma_d} \tilde{\boldsymbol{\eta}}, \quad (7.6)$$

and using Gauss's theorem with the incorporation of the boundary conditions gives the momentum balance equation in the weak form as

$$\begin{aligned} \int_\Omega \nabla(\hat{\boldsymbol{\eta}} + \mathcal{H}_{\Gamma_d} \tilde{\boldsymbol{\eta}}) : \boldsymbol{\sigma} d\Omega &= \int_{\Gamma_t} \nabla(\hat{\boldsymbol{\eta}} + \mathcal{H}_{\Gamma_d} \tilde{\boldsymbol{\eta}}) \mathbf{t}_p d\Gamma_t \\ &- \int_{\Gamma_d^+} \nabla(\hat{\boldsymbol{\eta}} + \mathcal{H}_{\Gamma_d} \tilde{\boldsymbol{\eta}}) \cdot (\boldsymbol{\sigma} \cdot \mathbf{n}_d) d\Gamma_d^+ + \int_{\Gamma_d^-} \nabla(\hat{\boldsymbol{\eta}} + \mathcal{H}_{\Gamma_d} \tilde{\boldsymbol{\eta}}) \cdot (\boldsymbol{\sigma} \cdot \mathbf{n}_d) d\Gamma_d^-. \end{aligned} \quad (7.7)$$

For information about constitutive relations we refer to Section 4.3. Further derivation of the weak form and the discretization is given in Sections 4.4 and 4.5 in 2D. The procedures followed there are identical to the those required in 3D.

7.2 Numerical implementation

In this section we describe the computational aspects that were implemented to extend the X-FEM model to 3D situations. As will be discussed

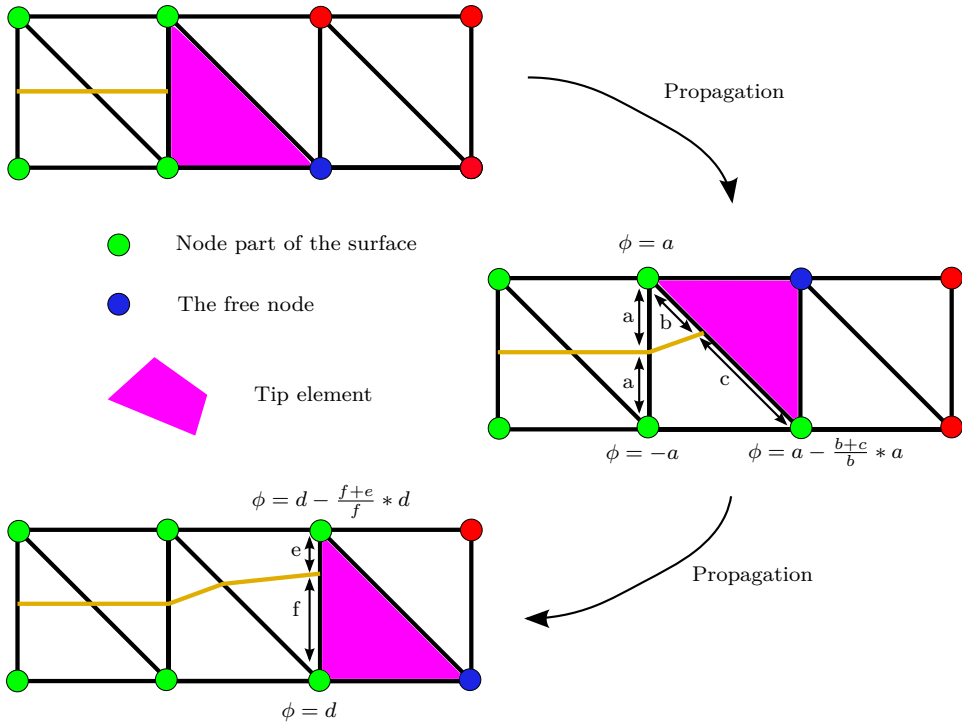


Figure 7.2: Scheme of a propagating fracture in a structured triangular mesh. The fracture is shown in yellow and the tip element in purple. The spatial location of the new tip is calculated using geometrical formulas. By using this location the level set value at the free node is calculated. Green nodes are part of the fracture surface characterized by $\psi < 0$. The blue and red nodes are not part of the surface and are characterized by $\psi > 0$

in the section the implementation is designed specifically for tetrahedral elements. It is possible to also consider cubic elements by subdividing them into tetrahedral elements within the part of the model that tracks the fracture location. Considering this implementation is however not the scope of this chapter.

7.2.1 Tracking the discontinuity surface

The level set method is a common technique to track evolving discontinuities (Sethian, 1999). A discontinuity is described as a continuous function in space and time, being one dimension higher than the shape it is representing. The zero value of this functions describes the location of the discontinuity. To track a fracture surface two orthogonal level sets are required, one describing the surface and one describing the fracture front (Sukumar et al., 2001; Moës et al., 2002). Evolving the discontinuity is governed by a velocity field resulting in a partial differential equation that is often solved by a finite difference scheme or by a fast marching algorithm (Sethian, 1999). Solving this equation can be expensive and may cause overhead in simulation time. Additional calculations are necessary to maintain the signed distance property of the level sets and kinks in the discontinuity need to be smoothed (Gupta and Duarte, 2014). In this chapter, we adopt the idea of storing the location of the discontinuity as nodal quantity based on the level set method. However, the level set equation is not solved to determine the location of a propagated discontinuity.

In our 2D model a discontinuity is assumed to be a straight line within an element and ends at an element edge (see Section 2.3). The tip of the discontinuity is therefore always located on the edge of an element. It is intuitive to use this approach in combination with the cohesive zone description since the latter lumps the fracture process along a line. We discuss the implementation aspects first in 2D and show that cutting the entire element is also advantageous in the 3D implementation.



Figure 7.3: A tetrahedron cut by a discontinuity either forms a triangular surface (a) or a rectangular surface (b).

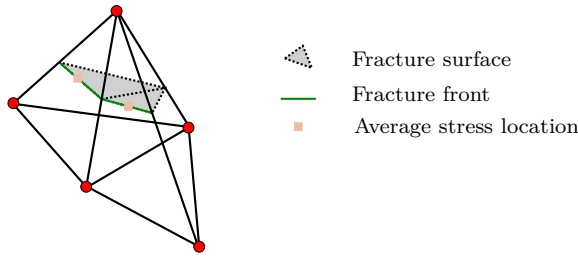


Figure 7.4: Two tetrahedral elements cut by a discontinuity in grey. The fracture front, shown in green, contains within each element one point located in the middle of the front to calculate an average stress used in the fracture propagation criterion.

7.2.2 2D level set propagation

Consider two level set functions , $\phi(\mathbf{x}, t)$ and $\psi(\mathbf{x}, t)$ that describe the surface of the discontinuity and the front of the discontinuity, respectively. Elements containing a spatial location \mathbf{x} that satisfies $\phi(\mathbf{x}, t) = 0$ are part of the discontinuity if $\psi(\mathbf{x}, t) < 0$ in the entire element. The location of the crosspoint between the discontinuity and an element edge is determined by the zero value of level set ϕ interpolated from the two nodes that form the edge.

We define a tip element as satisfying the relation $\phi(\mathbf{x}, t) = 0$ and having two nodes with a negative ψ value and one node with a positive value (the free node) when restricting ourself to only triangular elements. The tip location after propagation is always located on an edge that has the free node as a vertex and can be calculated using geometrical formulas (Ericson, 2004). The concept of this approach on a structured triangular mesh is shown in Figure 7.2. The fracture is extended through the tip element by modifying the ϕ level set value of the free node (shown in blue). The free node becomes part of the surface by setting ψ to a negative value. Kinks in the surface of the discontinuity occur due the element edge to element edge propagation as shown in the figure. These kinks would have to be sufficiently small or smoothed out if the level set equation would have been solved directly.

7.2.3 3D level set propagation

In 3D a similar approach is followed with tetrahedral elements. The restriction of using this type of element is advantageous since a discontinuity can only cut the element in two different ways (see Figure 7.3). Either a triangular or a rectangular surface is formed which simplifies the numerical implementation. The volume of the tetrahedral element is divided in

either a new tetrahedron and a wedge (in the case of a triangular fracture surface) or in two wedges (with a rectangular fracture surface). The zero value of the level set ϕ defines the crosspoint of the discontinuity with an element edge. Similar as in 2D the front is located in elements having only one node with a positive ψ value and satisfying the relation $\phi(\mathbf{x}, t) = 0$. The front is a line located in the triangular face of the tetrahedron spanned by the three negative ψ nodes. Upon propagation of the discontinuity the edges enclosed by the positive node are included to the surface. This results in a unique solution for triangular surfaces (Figure 7.3a). In the case of a rectangular surface (Figure 7.3b) the solution is non-unique. There are two new cross-points created by the fracture surface while there is only one level set value in the free node that can be modified. To obtain a unique location for both cross-points a third level set value is added. Both cross-points are stored correctly by linking the third level set value to the ID of the edge. This is a unique item within in the mesh. Thus it can be used in neighbouring elements to distinguish to which crosspoint the third level sets belongs.

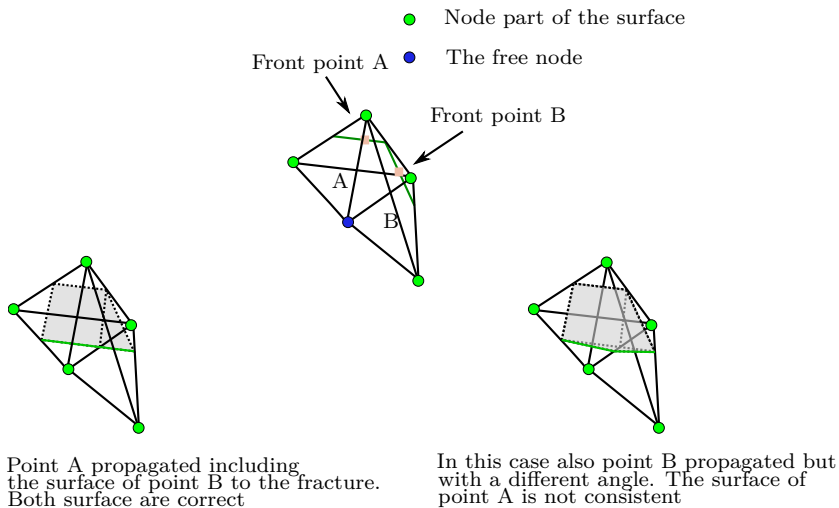


Figure 7.5: Representation of a fracture front (shown in green) that crosses two neighbouring elements. The top image represents the situation before fracture propagation. Propagation is checked in the front point based on an average stress criterion. It is therefore possible that the criterion is only violated in one of the front points. This situation for propagation of point A only is shown in the left image. By including the free node in the fracture surface the tip element belonging to front point B is also included in the surface. A second situation shown in the right image occurs when both front points propagate within the same time increment.

Propagation of the fracture is based on an average stress criterion (Section 2.3). Instead of a fracture tip, located in one element, there now is a fracture front that can span multiple elements. In each element that is part of the fracture front a point is added to calculate the average stress. The point is placed in the middle of the line that forms the fracture front within that element (see Figure 7.4). If the maximum principal stress exceeds the ultimate tensile strength the fracture is propagated toward the next element face. The normal of the surface within the element is equal to the normal of the maximum principal stress and it is assumed that the plane crosses the front point. In the case of a rectangular fracture surface this results in an inconsistent fracture plane since it is unlikely that the two existing cross-points are also on the plane.

The propagation moment and direction may differ amongst neighbouring elements. Two scenarios that can occur due to this are illustrated in Figure 7.5 by considering two neighbouring front elements, element A and B respectively. Element B can become part of the fracture surface by fracture propagation in element A (left image). Propagation in both elements results in two different cross-points at the edge shared by the two elements. The cross-points are only identical in the rare cases when the propagation normals are equal and the front spans the same directional vector in both elements. We decide to take the average of both points as the cross-point. Despite that averaging is a logical solution it has as a consequence that the cross-point is not exactly located on the plane and thus results again in an inconsistent rectangular surface.

Algorithm 4 Fetch all propagating front points

```

for  $iTip \leftarrow 1, nTip$  do
  if  $violation(iTip) = True$  then
     $\mathbf{n}_p =$  propagation normal
     $elemID =$  the element ID
    store  $\mathbf{n}_p$  and  $elemID =$  in  $propElems$ 
  end if
end for

```

Updating the level set with our proposed method has as a consequence that the four cross-points forming a rectangular surface are not on the same plane. This results in an error in the numerical integration of the fracture plane. We assume however that the cross-points are never far off the actual plane. The numerical inaccuracy is thus sufficiently small such that the proposed update scheme can be validated. A solution to this problem would be to subdivide every rectangular surface in two triangular surfaces.

This is however not the scope of this chapter.

To summarize, the proposed update scheme of the level is governed by first checking if the propagation criterion is violated in all front points. Each violated front point is stored together with the tip element ID and the propagation normal (see Algorithm 4). The level set can be updated based on this stored information. By using geometrical formulas the new cross-points can be calculated and level set values can be updated accordingly (see Algorithm 5). New front points are calculated after updating all the level set values. Elements that were not part of the fracture front become enclosed in the fracture by the update illustrating the major advantage of the fracture representation as a level set.

Algorithm 5 Propagate level set

```

oldLvl = curruntLvl      ▷ Copy the level sets since the front is lost when some elements
propagate
for iElm in propElems do
  elemID = propElems → elemID
  np = propElems → np
  xPoints = calcXpoints (oldLvl, np, elemID)      ▷ use old level sets
  updateLvlSet(curruntLvl, xPoints, elemID)      ▷ update current level sets
end for

```

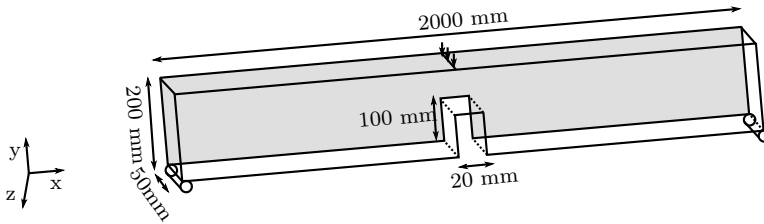


Figure 7.6: Scheme of the three point bending test.

7.3 Examples 3D X-FEM

In this first example a three point bending test (Figure 7.6) is analysed and compared to the experimental investigation performed by Petersson (1981). This benchmark problem was also considered in other numerical works (Rots et al., 1985; Armero and Kim, 2012; Linder and Zhang, 2013). The concrete specimen has a Young's modulus of 30 GPa and a Poisson's ratio of 0.2. A small initial fracture with a length of 5 mm is created and the growth of the fracture is restricted to the initial plane. A mode I exponential cohesive traction separation law (see Section 5.1.5) is used with an ultimate strength $\tau_{\text{ult}} = 3.3$ MPa and a fracture toughness of $\mathcal{G}_c = 0.124$ N/mm. The beam is subjected to a displacement of 0.01 mm per load increment.

The force reaction curve for the simulation is shown together with the experimental envelope of Petersson (1981) in Figure 7.7. The numerical result lies within the failure envelope. The combination of the principal stress propagation criterion and the cohesive zone description are adequate enough to describing the experimental result. The discrete fracture surface is shown in Figure 7.8. The elements have irregular shapes due to the arbitrary location of the fracture surface compared to the tetrahedral elements. The normal opening displacement of the surface is shown in the contour. As expected the opening decreases from the left (at the notch) to the right where the front of the cohesive zone is located. Note also that the front is not perfect line but is also having a irregular shape depending on the shape of the tetrahedral tip elements. This is not a concern as long as there are multiple elements within the cohesive zone. The damaging process is captured and energy dissipation is controlled by the traction separation law.

In the second example we consider the L-shape fracture test similar as was performed for a 2D porous material in Section 2.5.3. The initial planar fracture has a length of 35 mm and is inclined 45 degrees with the x-axis (Figure 7.9). The material has a Young's modulus of 28.85 GPa and a Poisson's ratio of 0.18. The mode I cohesive zone description is used with an ultimate strength $\tau_{\text{ult}} = 3.3$ MPa and a fracture toughness of $\mathcal{G}_c = 0.124$ N/mm. The displacement in all directions at the bottom surface of the L-shaped specimen are constrained and a load of F_1 of 750 N per load increment is added at the left boundary. Fracture growth is now not restricted within a plane. In Figure 7.10 the propagated fracture is visualized after 72 load increments. The surface of the fracture viewed from the top and from the side of the L-shape are shown in Figure 7.11. The surface is ir-

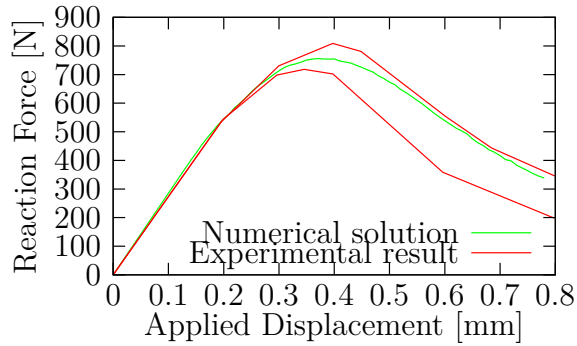


Figure 7.7: The force displacement curve of the 3 point bending test. The experimental envelope is given by Petersson (1981).

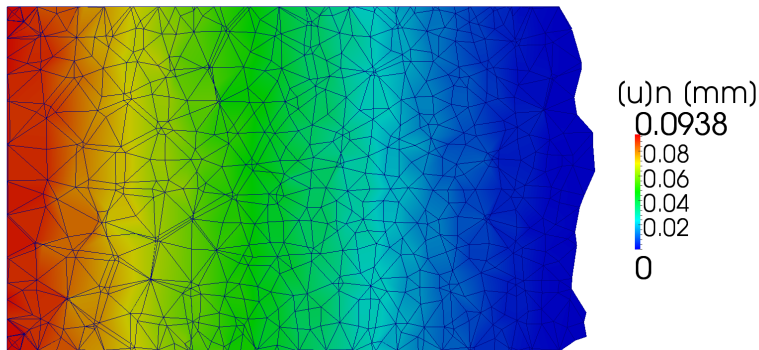


Figure 7.8: Visualization of the fracture surface in the three point bending test after 68 load increments. The normal opening displacement is shown as a contour. The irregular structure of the surface mesh is a result of the arbitrary cutting of the tetrahedral elements.

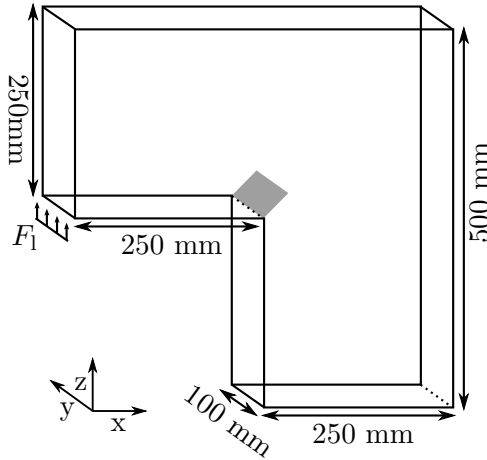


Figure 7.9: Schematic representation of the 3D L-shaped fracture problem. The initial fracture surface, shown in grey, has a length of 35 mm and is inclined under an angle of 45 degrees with the x-axis.

regular and non-planar. With this example we have demonstrated that the method is not confined to only planar fractures. The fracture path should have been located higher in z-direction based on experimental results by Winkler (2001). This may be related to inaccurate stress calculations near the fracture front due to insufficient mesh refinement.

7.4 The 3D ELP model

The additional mass balance equation in the fracture introduced by the ELP degree of freedom is solved by applying it in a local reference frame. Assuming incompressible constituents the volume integral over crack volume Ω_d can be written as

$$\int_{\Omega_d} \nabla \cdot \mathbf{v}_s + \nabla \cdot \mathbf{q}_d d\Omega_d = 0 \quad (7.8)$$

Assuming that the elongation of the fracture surface in tangential direction is negligible in a mode I hydraulic fracture the first term can be rewritten as a function of the opening of the fracture. Neglecting also the pressure difference in the normal direction the complete mass balance can be written as a domain integral

$$\int_{\Omega'_d} [\dot{\mathbf{u}} \cdot \mathbf{n}_d + [\mathbf{u}] \cdot \mathbf{n}_d \nabla_d \cdot \mathbf{q}_d + (\mathbf{q}_{\Gamma_d}^+ - \mathbf{q}_{\Gamma_d}^-) \cdot \mathbf{n}_d] d\Omega'_d = 0 \quad (7.9)$$

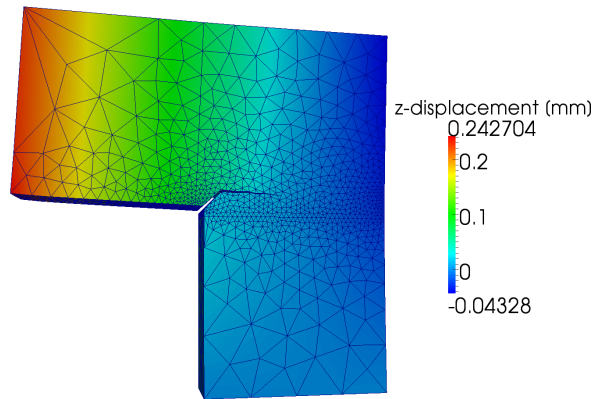


Figure 7.10: The L-shape specimen after 72 load increments. The deformed configuration is magnified 100 times. The stress in z-direction is shown in the contour.

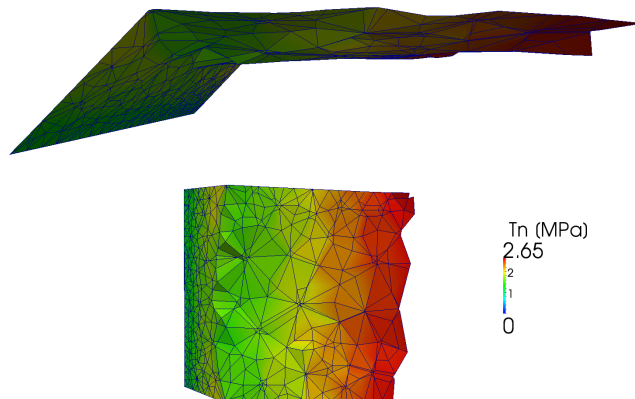


Figure 7.11: The fracture surface visualized from the side (top image) and from the top (bottom image). The traction in normal direction is shown in the contour.

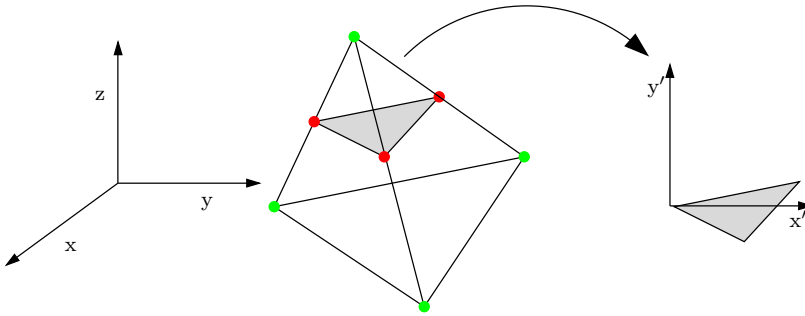


Figure 7.12: The fracture surface is rotated from the global reference plane in 3D to a local reference plane.

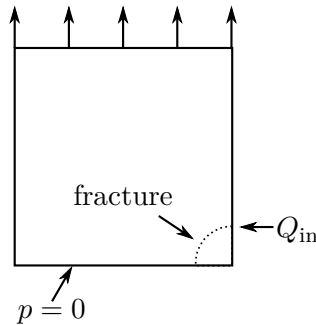


Figure 7.13: 2D representation of the 3D validation of the flow model. The initial fracture surface has the shape of one fourth of a cylinder. A displacement is prescribed at the top surface to open the fracture. Fluid is injected at a constant rate and the tip of the fracture is in contact with the bottom surface where a zero pressure is prescribed.

where Ω'_d is the local reference frame of the fracture within an element and ∇_d is the gradient operator within this reference frame (Figure 7.12). The reference frame is spanned by the normal vector of the 3D plane and therefore contains the fracture plane as a 2D entity. $\mathbf{q}_{\Gamma_d}^+$ and $\mathbf{q}_{\Gamma_d}^-$ represent the leakage terms of the positive and negative side of the surface, respectively. In the remainder of this chapter we consider hydraulic fracturing in an elastic material thus the leakage terms are not present.

The ELP degree of freedom is located at the cross-points of the discontinuity with element edges (see Section 4.5 for the 2D scheme). Similar as in 2D, where a line equation had to be solved, we now need to solve a planar equation in a 3D space. Numerical integration in the surface is based on the standard Gaussian quadrature. To demonstrate this implementation we consider a cubic mesh with a initial fracture surface of one

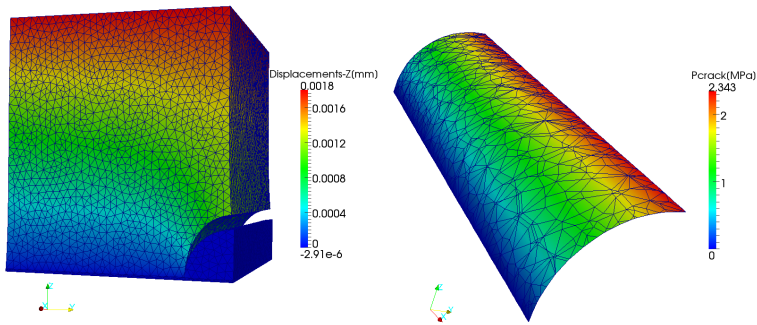


Figure 7.14: Validation of the flow model. An injection pressure of 2.36 is expected based on Darcy's law. Note the very irregular element size on the fracture surface caused by the random element cutting locations.

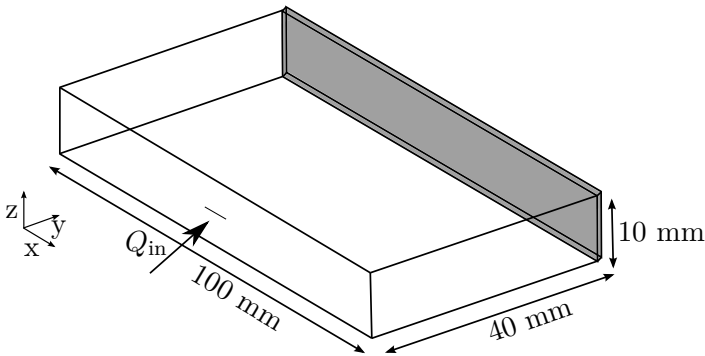


Figure 7.15: Scheme of the penny shaped hydraulic fracture simulation. The displacement at the the solid side of the specimen is constrained in displacement.

fourth of a cylinder (Figure 7.13). The mesh is refined at bottom such that a very thin slice is not part of the fracture surface. A zero pressure is prescribed artificially at the fracture front and fluid is injected with a rate of $Q_{in} = 75.0$ mm/s. Instead of using the cubic law for the fluid we implement a Darcy type of flow according to $\mathbf{q} = -k\nabla p$. Taking k large enough with a value of 100 mm⁴/s results in a linear pressure gradient ranging from zero at the bottom towards the injection boundary. The cylinder has a radius r of 2 mm gives an injection pressure of $p_{inj} = -\frac{\pi r Q_{in}}{2k} = 2.36$ Mpa. The found value of 2.343 MPa is consistent with the exact value (see Figure 7.14). It can also be seen in the figure that the location of the fracture is independent of the underlying mesh. The fracture surface consists of unstructured triangular and rectangular elements depending on where the fracture cuts the tetrahedral elements.

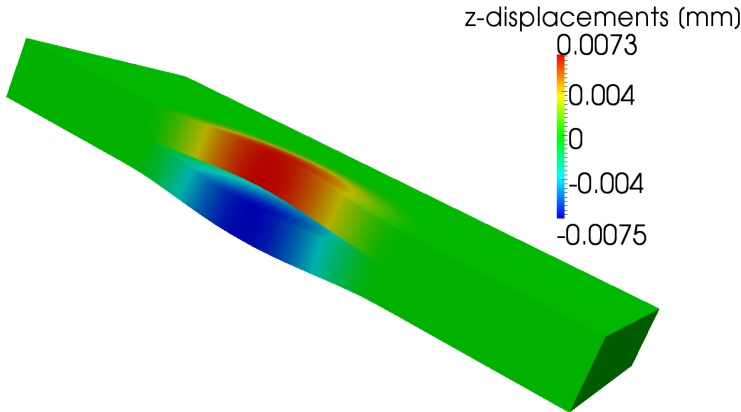


Figure 7.16: Result of the 3D hydraulic fracture propagation. In the contour the z-displacement is shown. The deformed configuration is magnified 200 times.

7.4.1 Example 3D hydraulic fracturing

In this last example a planar propagating hydraulic fracture is considered (Figure 7.15). Fracture growth is again constrained within the initial fracture plane leading to a penny type of hydraulic fracture. Fluid is injected as a line boundary condition on the left boundary with an injection rate of $Q_{\text{in}} = 0.50 \cdot 10^{-4} \text{ mm}^2/\text{s}$ along the fracture. This leads to an increased injection rate as the fracture propagates further along the boundary. An implicit time step with a magnitude of 50 seconds is used. An exponential mode I traction separation law with $\tau_{\text{ult}} = 3.33 \text{ MPa}$ and a fracture toughness of $\mathcal{G}_c = 0.124 \text{ N/mm}$ is applied. There is no fluid leakage. The displacement of the specimen is completely constrained on the back.

The opening of the hydraulic fracture in the specimen is shown in Figure 7.16. The fracture grows radially and the opening displacement is highest in z-direction. The fracture surface for three different time instances is shown in Figure 7.17. The mesh is made such that element topology is mirrored in the y-axis at the centre of the initial fracture to validate the fracture growth. In the figure it is shown that the fracture is propagating mirrored in the y-axis demonstrating no abnormal behaviour in the propagation algorithm. The front locations are also shown in the figure as red spheres. As the fracture grows the front expands and the number of front points increases. The fracture front is not a perfect circle due to the element face to element face propagation. This is not a restriction with the cohesive zone implementation. A circular normal opening profile of the fracture can be seen in Figure 7.17c.

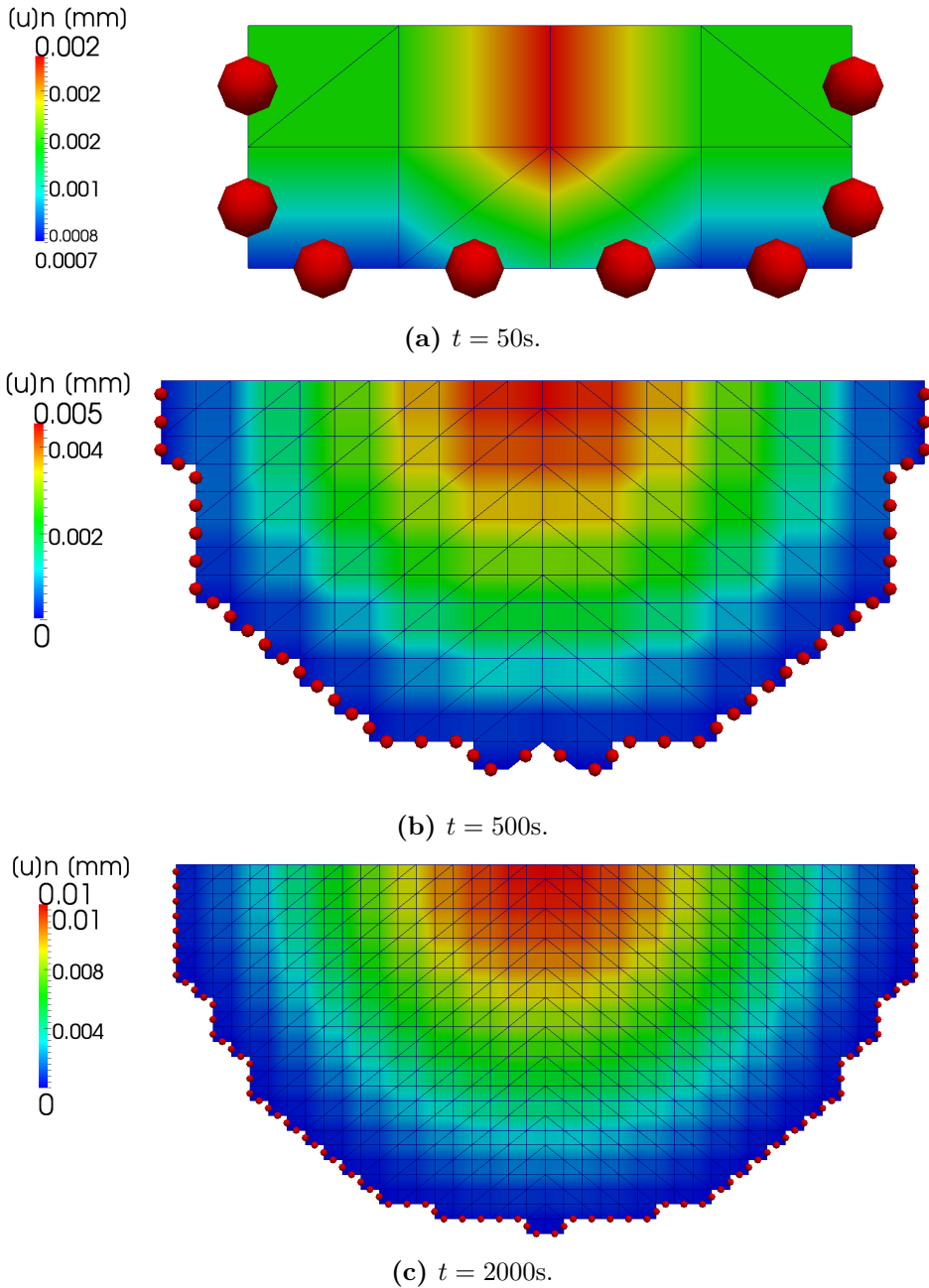


Figure 7.17: The fracture surface in the penny shaped hydraulic fracture for three different time instances. The normal opening displacement is shown in the contour. The front points are indicated with the red circles.

7.5 Conclusions and future work

In this chapter the implementation of a 3D fracture model using the extended finite element method is described. A fracture propagates from element face to element face with the propagation plane being given by a normal vector and a point on the existing fracture front. With the restriction of only using tetrahedral elements the fracture surface is spanned by a triangular or by a rectangular surface within an element. When the latter occurs the fracture surface is not a correct plane since the four cross-points do not form a plane. This numerical artefact is accepted for now since the main goal of this chapter is to illustrate the extension of the model to 3D. The strength of using a level set implementation for the fracture surface is that the fracture plane is uniquely defined in the mesh. This makes it possible to integrate the fluid flow along the fracture surface. In a future work the rectangular surfaces can be subdivided into two triangles giving a consistent fracture plane.

A three point bending test is used to benchmark the 3D model with an experimental result. The force displacement curve is consistent with experimental data. In this simulation fracture propagation is based on a principal stress criterion with the propagation direction defined. With a L-shaped fracture test non-planar fracture growth in 3D is demonstrated.

The ELP model is also extended to 3D. Fluid flow along a non-planar fracture surface is demonstrated. A planar penny shaped hydraulic fracture is also studied. These first results indicate the possibility to apply the ELP model in 3D situations. Hydraulic fracture patterns that are impossible to model in 2D could be investigated with this model. Combining the implementation with the parallel computing method introduced in Chapter 6 opens the possibility to use larger meshes. This most-likely improves convergence rates and gives the possibility to further investigate out of plane fracture propagation.

8

Conclusions and outlook

8.1 Conclusions

The main objective of this thesis is to develop numerical techniques that can be used to simulate realistic hydraulic fracturing treatments. The model is based on the extended finite element method and was introduced by Kraaijeveld (2009) and by Irzal et al. (2013) without considering complex fracture patterns and fluid-driven propagation. The fracture process is described by a cohesive traction separation law. Fracture propagation is considered in both linear elastic materials and in poro-elastic materials by using Biot's theory. The fluid flow within the porous material is described by Darcy's law.

In Chapter 2 a poro-elastic eXtended Finite Element Method (X-FEM) model is introduced. Fracture propagation and nucleation in a porous material induced by mechanical loading are investigated. Both propagation and nucleation are evaluated based on an average stress criterion. An orthotropic material description is used and the propagation criterion was modified accordingly. The model is validated using the analytical Mandel-Cryer solution for isotropic and transverse isotropic materials. The fracture path and propagation velocity are found to depend on the intrinsic permeability of the material.

In Chapter 3 the model is applied to shear failure. The limitation of fracture growth through only one element within one time increment is removed. Crack propagation using different levels of mesh refinement is investigated. Fluid flow across the fracture is found to depend on the propagation step of the fracture. In coarse meshes the fluid flow shows a large variation due to alternating phases of crack propagation and relaxation. In a refined mesh this effect is smaller and even vanishes when the fracture

propagates continuously. Lowering the time step in the refined mesh again led to step-wise fracture growth. The fluid behaviour found in the coarse mesh is retrieved again with the refined mesh using smaller time steps. These results indicate that the model is not completely free of influence of the element size and of the time step magnitude. Nevertheless the fracture path is identical for all simulations.

Hydraulic fracturing is considered in Chapter 4. Specifically for hydraulic fracturing situations in low permeable rocks a discontinuous pressure description over the fracture was adopted with an additional pressure within the fracture (the enhanced local pressure model). Hence, the pressure exhibits a jump from the formation to the fracture on the adjacent sides of the fracture surface. Physically the pressure profile over the fracture is of course continuous but in low permeable rocks the gradient near the fracture is so steep that a discontinuous approximation is justified. By doing so it is not necessary to resolve the steep pressure gradient near the fracture surface. This leads to a more robust simulation and a better approximation of the fluid pressure in the fracture. The formulation also ensures that all injected fluid goes exclusively into the fracture. The model is compared successfully with the analytical KGD hydraulic fracture problem. Simulated fracture propagation is parallel to the highest confining stress, which is consistent with experimental data (Weijers et al., 1994). Fracture nucleation is also studied. A situation where it is energetically favourable to nucleate a new fracture instead of propagating an existing hydraulic fracture is reproduced.

The enhanced local pressure model is improved in Chapter 5 to consider fracture interaction. An additional enrichment field is included per discontinuity to approximate the correct displacement jump when two or more discontinuities are in the vicinity of each other. Two criteria are introduced to determine whether or not a hydraulic fracture crosses a natural fracture and to determine if fluid will divert into the natural fracture. Fracture crossing is based on the nucleation of a new fracture at the opposite side of the natural fracture where the hydraulic fracture has stopped. Fluid is assumed to divert into the natural fracture only when there is fracture opening giving the fluid a pathway to flow through. These two criteria are checked simultaneously and the competition between them determines the interaction behaviour. Simulated fracture interaction is compared with experimental data from literature. Good agreement is found.

To consider larger meshes with more degrees of freedom, a parallel implementation of the extended finite element model as well as the enhanced pressure model is introduced in Chapter 6. The mesh is divided

in sub-domains whereby the problem defined on each subdomain is solved on one computational core. Implementation aspects are described in detail. New degrees of freedom are identified when fractures propagate across sub-domain boundaries. Therefore, an efficient bookkeeping scheme including communication between the sub-domains is needed. The system of equations is poorly conditioned due to the X-FEM degrees of freedom. Nevertheless a 100-fold speed-up is achieved on 192 computational cores. This 50 % efficiency is mainly caused by overhead in solving the system of equations. From a practical point of view the reduction of computational time is advantageous. Also the memory available for the simulation increases when more computational cores are used.

The model is extended to 3D in Chapter 7. The possibility to propagate from element to element is exploited to track the fracture surface. Examples of planar and non-planar fracture propagation are shown in an elastic material. A planar propagating hydraulic fracture is also considered and the implementation of fluid flow along a curved surface is validated. Fully curved 3D hydraulic fractures are not yet considered.

We conclude that several model improvements are made towards more realistic hydraulic fracturing simulations. Additional insight in the continuous pressure formulation is obtained. Allowing for the possibility to propagate the fracture through multiple elements within one time step gave more flexibility within the simulations. The enhanced local pressure model proves to be an efficient tool for the simulation of hydraulic fracturing. Interaction modelling allows fracture interaction with natural fracture networks. Extending this investigation to the influence of layered rocks on the propagation path is obvious. There are no longer restrictions to the size of the model by the use of parallel computing power. 3D simulations are carried out as well.

8.2 Outlook

The enhanced local pressure model is specifically designed for low permeable rocks. The fluid leakage from the fracture into the formation is approximated with an analytical solution. By applying this approximation the leaked volume is not coupled to the mass balance in the formation. Based on a separation of scales this assumption is valid as long as the consolidation time of elements near the fracture surface is long compared to the simulation time. In low permeable rocks such as shales this assumption holds true longer than in more permeable rocks. When the assumption is violated the leaked volume is not coupled to the formation but is still

present in the mass balance of the fracture. The enhanced local pressure model was found to be more accurate than an extended finite element model with a continuous pressure description across the fracture (Chapter 4). The model is also more robust since it is no longer necessary to resolve the pressure gradients near the fracture. As discussed, Meschke and Leonhart (2015) pioneered a related approach by applying the analytical approximation of fluid leakage as an enrichment function for the pressure across the fracture. This approach is somewhat more elaborate, but holds also for more permeable rocks. At small consolidation times the difference between the two methods is small. In the enhanced local pressure model fluid can be injected exclusively in the fracture due the separate degree of freedom whereas in Meschke and Leonhart (2015) model it cannot. No additional numerical integration is needed in the enhanced local pressure model to resolve the steep pressure gradient.

A careful comparison between the two methods is not performed. Doing a thorough comparison would benefit greatly from experimental benchmarks. As was observed by Coa et al. (2016, in press) different numerical models with similar constitutive relations can result in a different fracture history (propagation velocity) for the same problem. Quantitatively comparing different numerical methods such as the phase field approach (Lee et al., 2016), phantom node models (Sobhaniragh et al., 2016), boundary element methods (Dong and de Pater, 2001), the finite element method with remeshing (Schrefler et al., 2006), and other partition of unity approaches (Mohammadnejad and Andrade, 2016; Meschke and Leonhart, 2015; Gupta and Duarte, 2015) based on an experiment would give much insight in numerical accuracy and model possibilities. Finally a comparison with currently used tools in industry would be of great value.

A common approach in many numerical models is the assumption of the cubic law to describe the fluid flow along the fracture. Since the permeability almost completely goes to zero near the tip of the fracture it is difficult to correctly represent the pressure gradient towards the tip. The cubic law has been applied in many different numerical methods, see e.g. the finite element based works (Boone and Ingraffea, 1990; Carrier and Granet, 2012; Chen, 2012), the phase field method (Lee et al., 2016), and other partition of unity based models (Irzal et al., 2013). A correction factor is included to the law in some works to represent tortuosity of the fracture surface (Meschke and Leonhart, 2015; Mohammadnejad and Andrade, 2016). In a process zone this is still too simplified due to the damaged part of the material where the micro-separations grow. The permeability in the cohesive zone is larger than in the porous material due to an enhanced flow path

through the micro-separations, but much lower than in the fully developed crack. A different constitutive equation for the fluid flow within the cohesive zone is possible. Based on the damage parameter that is also used in the traction separation law, the constitutive relation could be defined as a Darcy type of flow near the tip of the cohesive zone which gradually transforms into the cubic law toward the completely damaged part of the fracture. Further improving the formulation of the permeability within the cohesive zone would be possible by using the cohesive band formulation as proposed by Remmers et al. (2013). In the cohesive band formulation the cohesive zone also has a thickness. In 2D this means that the process zone is approximated as an area over which fluid flow can be integrated. Volumetric changes within the process zone are better approximated compared to lumping the flow along a line with the traditional cohesive zone.

In Chapter 3 it is illustrated that even on very fine meshes there is a correlation between the time depended fluid flow and the step size through an element. The element to element propagation is advantageous from implementation point of view (see Chapter 7) as tip enrichments are superfluous. Having the possibility to stop the discontinuity within an element would require tip enrichments and would give the possibility to completely cancel out mesh dependency. However, the tip enrichments are based on analytical solutions that approximate the displacement field near the tip (Moës et al., 1999). In hydraulic fracturing this field depends on the propagation regime of the fracture determined by material properties and boundary conditions (Adachi and Detournay, 2008). Instead of using tip enrichment within the enhanced local pressure model it would be possible to triangulate tip elements into smaller elements. No assumptions on the propagation regime are needed, the proposed level set propagation scheme can than still be used and the computational cost for this procedure are not that severe. The triangulation is performed locally in an element and there are no boundaries that need to match the triangulation. Simply performing one or more Delaunay triangulations within the tip elements would be sufficient. A positive side effect would be that both opening as well as the pressure along the fracture are discretized on a finer mesh which could lead to a more accurate integration of the cubic law.

Crack propagation based on an average stress is easily implemented but in some scenarios not accurate. Sharp angles in crack growth can occur when the stress state is near biaxial. Also negative values in stress due to the confining pressures can influence the average stress in an undesired way. An advantage of using an average stress is that also fracture nucleation can be considered. A very elegant method to determine the crack propagation

direction is by an energy minimisation approach. Meschke and Dumstorff (2007) introduced such a method within the extended finite element framework based on a minimisation of total energy. The problem was formulated such that the crack propagation angle and the increase in crack surface are additional unknowns of the system. This method unfortunately requires severe implementation aspects when extending it to 3D. Moës et al. (2011) introduced a non-local damage approach, the thick level set method. This approach has similarities with the phase-field approach since a damage parameter is included regularizing the damage over a larger surface base on energy restrictions. The difference with the phase field models is that the damage parameter is only present in a small zone near the fracture surface. The characteristics of the level set are exploited to both propagate the surface and to define the zone with a damage parameter. The method is combined with the concept of the extended finite element method to make the displacement field discontinuous as damage is completed. Despite the use of the X-FEM to make the displacement field discontinuous there still exists a necessity to use a sufficiently fine mesh near the fracture to resolve the damage parameter (Cazes and Moës, 2015). The major advantage of extended finite elements, namely to allow for coarse meshes, is mostly lost. An ideal fracture model would combine the strength of the extended finite element method, i.e. representing a fracture on a coarse mesh, with the prediction of the fracture path that follows naturally from energy based methods such as the phase field approach or the thick level set method.

The main advantages of the enhanced local pressure model, i.e. no necessity to capture the steep pressure gradient near the surface and exclusively injection fluid in the fracture, would be maintained. The numerical improvement of considering fracture interaction (Chapter 5) is necessary to represent complex fracture geometries resulting from the energy based model. Together with the parallelization possibilities (Chapter 6) the combination of the two methods may lead to an optimal fracture model both in accuracy but also in computational times which is important for industrial purposes.

Bibliography

- Y. Abousleiman, A.H.D. Cheng, L. Cui, E. Detournay, and J.C. Roegiers. Mandel's problem revisited. *Geotechnique*, 46(2):187–195 (1996).
- J.I. Adachi and E. Detournay. Plane strain propagation of a hydraulic fracture in a permeable rock. *Engineering Fracture Mechanics*, 75(16):4666–4694 (2008).
- J.I. Adachi, E. Siebrits, A. Peirce, and J. Desroches. Computer simulation of hydraulic fractures. *International Journal of Rock Mechanics and Mining Sciences*, 44(5):739–757 (2007).
- T.L. Anderson. *Fracture mechanics: fundamentals and applications*. CRC press (2005).
- F. Armero and J. Kim. Three-dimensional finite elements with embedded strong discontinuities to model material failure in the infinitesimal range. *International Journal for Numerical Methods in Engineering*, 91(12):1291–1330 (2012).
- K. Asanovic, R. Bodik, J. Demmel, T. Keaveny, K. Keutzer, J. Kubiatiowicz, N. Morgan, D. Patterson, K. Sen, J. Wawrzynek, D. Wessel, and Yelick K. A view of the parallel computing landscape. *Communications of the ACM*, 52(10):56–67 (2009).
- G.I. Barenblatt. The mathematical theory of equilibrium cracks in brittle fracture. *Advances in applied mechanics*, 7(55-129):104 (1962).
- T.J. Barth and J.A. Sethian. Numerical schemes for the hamilton–jacobi and level set equations on triangulated domains. *Journal of Computational Physics*, 145(1):1–40 (1998).
- C. Becker, S. Jox, and G. Meschke. 3d higher-order x-fem model for the simulation of cohesive cracks in cementitious materials considering hygro-mechanical couplings. *Computer Modeling in Engineering and Sciences (CMES)*, 57(3):245 (2010).
- T. Belytschko and T. Black. Elastic crack growth in finite elements with minimal remeshing. *International journal for numerical methods in en-*

- gineering*, 45(5):601–620 (1999).
- T. Belytschko, R. Gracie, and G. Ventura. A review of extended/generalized finite element methods for material modeling. *Modelling and Simulation in Materials Science and Engineering*, 17(4):043001 (2009).
- L. Berger-Vergiat, H. Waisman, B. Hiriyyur, R. Tuminaro, and D. Keyes. Inexact schwarz-algebraic multigrid preconditioners for crack problems modeled by extended finite element methods. *International Journal for Numerical Methods in Engineering*, 90(3):311–328 (2012).
- G.C. Beroza and S. Ide. Deep tremors and slow quakes. *Science*, 324(5930):1025–1026 (2009).
- MA Biot. Le problème de la consolidation des matières argileuses sous une charge. *Ann. Soc. Sci. Bruxelles B*, 55:110–113 (1935).
- M.A. Biot. General theory of three-dimensional consolidation. *Journal of applied physics*, 12(2):155–164 (1941).
- T.L. Blanton. An experimental study of interaction between hydraulically induced and pre-existing fractures. In *SPE unconventional gas recovery symposium*. Society of Petroleum Engineers (1982).
- T.J. Boone and A.R. Ingraffea. A numerical procedure for simulation of hydraulically-driven fracture propagation in poroelastic media. *International Journal for Numerical and Analytical Methods in Geomechanics*, 14(1):27–47 (1990). ISSN 1096-9853.
- R. de Borst, J.J.C. Remmers, A. Needleman, and M.A. Abellan. Discrete vs smeared crack models for concrete fracture: bridging the gap. *International Journal for Numerical and Analytical Methods in Geomechanics*, 28(7-8):583–607 (2004).
- R. de Borst, J. Réthoré, and M.A. Abellan. A numerical approach for arbitrary cracks in a fluid-saturated medium. *Archive of Applied Mechanics*, 75(10):595–606 (2006).
- B. Bourdin, G.A. Francfort, and J. Marigo. The variational approach to fracture. *Journal of elasticity*, 91(1-3):5–148 (2008).
- F. Brezzi. On the existence, uniqueness and approximation of saddle-point problems arising from lagrangian multipliers. *ESAIM: Mathematical Modelling and Numerical Analysis-Modélisation Mathématique et Analyse Numérique*, 8(R2):129–151 (1974).
- A.P. Bungler, E. Detournay, and D.I. Garagash. Toughness-dominated hydraulic fracture with leak-off. *International journal of fracture*, 134(2):175–190 (2005).
- A.P. Bungler and A.P. Peirce. Numerical simulation of simultaneous growth of multiple interacting hydraulic fractures from horizontal wells. *Shale Energy Engineering*, pages 201–210 (2014).

- G.T. Camacho and M. Ortiz. Computational modelling of impact damage in brittle materials. *International Journal of solids and structures*, 33(20):2899–2938 (1996).
- B. Carrier and S. Granet. Numerical modeling of hydraulic fracture problem in permeable medium using cohesive zone model. *Engineering Fracture Mechanics*, 79:312–328 (2012).
- H.S. Carslaw and J.C. Jaeger. *Heat in solids*, volume 19591. Clarendon Press, Oxford (1959).
- F. Cazes and N. Moës. Comparison of a phase-field model and of a thick level set model for brittle and quasi-brittle fracture. *International Journal for Numerical Methods in Engineering*, 103(2):114–143 (2015).
- Z. Chen. Finite element modelling of viscosity-dominated hydraulic fractures. *Journal of Petroleum Science and Engineering*, 88:136–144 (2012).
- Z. Chen, A.P. Bungler, Xi. Zhang, and R.G. Jeffrey. Cohesive zone finite element-based modeling of hydraulic fractures. *Acta Mechanica Solida Sinica*, 22(5):443–452 (2009).
- T.D Coa, E. Milanese, E.W. Remij, P. Rizzato, J.J.C. Remmers, L. Simoni, J.M. Huyghe, F. Hussain, and B.A. Schrefler. Interaction between crack tip advancement and fluid flow in fracturing saturated porous media. *Mechanics Research Communications* (2016,in press).
- A. Correljé, C. van der Linde, and T. Westerwoudt. *Natural Gas in the Netherlands:from Cooperation to Competition?* Oranje-Nassau Groep, P.O. Box 22885,1100 DJ Amsterdam-Zuidoost, the Netherlands (2003).
- C.W. Cryer. A comparison of the three-dimensional consolidation theories of biot and terzaghi. *The Quarterly Journal of Mechanics and Applied Mathematics*, 16(4):401–412 (1963).
- A. Dahi-Taleghani and J.E. Olson. Numerical modeling of multistranded-hydraulic-fracture propagation: Accounting for the interaction between induced and natural fractures. *SPE journal*, 16(3):575–581 (2011).
- C. Daux, N. Moës, J. Dolbow, N. Sukumar, and T. Belytschko. Arbitrary branched and intersecting cracks with the extended finite element method. *International Journal for Numerical Methods in Engineering*, 48(12):1741–1760 (2000).
- E. Detournay and A.H.D. Cheng. *Fundamentals of poroelasticity*1 (1993).
- J. Dolbow, N. Moës, and T. Belytschko. Discontinuous enrichment in finite elements with a partition of unity method. *Finite elements in analysis and design*, 36(3):235–260 (2000).
- C.Y. Dong and C.J. de Pater. Numerical implementation of displacement discontinuity method and its application in hydraulic fracturing. *Computer methods in applied mechanics and engineering*, 191(8):745–760

- (2001).
- D.S. Dugdale. Yielding of steel sheets containing slits. *Journal of the Mechanics and Physics of Solids*, 8(2):100–104 (1960).
- P. Dumstorff and G. Meschke. Crack propagation criteria in the framework of x-fem-based structural analyses. *International journal for numerical and analytical methods in geomechanics*, 31(2):239–259 (2007).
- M.J. Economides and G. Nolte. *Reservoir stimulation*, volume 18. Wiley Chichester (2000).
- C. Ericson. *Real-time collision detection*. CRC Press (2004).
- D.R. Faulkner, T.M. Mitchell, D. Healy, and M.J. Heap. Slip on ‘weak’ faults by the rotation of regional stress in the fracture damage zone. *Nature*, 444(7121):922–925 (2006).
- L.B. Freund. *Dynamic fracture mechanics*. Cambridge university press (1998).
- T.P. Fries. A corrected xfem approximation without problems in blending elements. *International Journal for Numerical Methods in Engineering*, 75(5):503–532 (2008).
- T.P. Fries and T. Belytschko. The extended/generalized finite element method: an overview of the method and its applications. *International Journal for Numerical Methods in Engineering*, 84(3):253–304 (2010).
- J.F.W. Gale, R.M. Reed, and J. Holder. Natural fractures in the barnett shale and their importance for hydraulic fracture treatments. *AAPG bulletin*, 91(4):603–622 (2007).
- T.C. Gasser and G.A. Holzapfel. Modeling 3d crack propagation in unreinforced concrete using pufem. *Computer Methods in Applied Mechanics and Engineering*, 194(25):2859–2896 (2005).
- T.C. Gasser and G.A. Holzapfel. 3d crack propagation in unreinforced concrete.: A two-step algorithm for tracking 3d crack paths. *Computer Methods in Applied Mechanics and Engineering*, 195(37):5198–5219 (2006).
- J. Geertsma and F. De Klerk. A rapid method of predicting width and extent of hydraulically induced fractures. *Journal of Petroleum Technology*, 21(12):1571–1581 (1969).
- A Gerstenberger and R. Tuminaro. An algebraic multigrid approach to solve xfem based fracture problems. *Int J Numer Methods Eng*, 94(3):248–272 (2012).
- S.L. Graham, M. Snir, and C.A. Patterson. *Getting up to speed: The future of supercomputing*. National Academies Press (2005).
- P. Grassl, C. Fahy, D. Gallipoli, and S.J. Wheeler. On a 2D hydro-mechanical lattice approach for modelling hydraulic fracture. *Journal of the Mechanics and Physics of Solids*, 75:104–118 (2015).

- A. Gravouil, N. Moës, and T. Belytschko. Non-planar 3d crack growth by the extended finite element and level sets—part ii: Level set update. *International Journal for Numerical Methods in Engineering*, 53(11):2569–2586 (2002).
- A.A. Griffith. The phenomena of rupture and flow in solids. *Philosophical transactions of the royal society of london. Series A, containing papers of a mathematical or physical character*, 221:163–198 (1921).
- H. Gu, X. Weng, J.B. Lund, M.G. Mack, U. Ganguly, and R. Suarez-Rivera. Hydraulic fracture crossing natural fracture at nonorthogonal angles: a criterion and its validation. *SPE Production & Operations*, 27(01):20–26 (2012).
- P. Gupta and C.A. Duarte. Simulation of non-planar three-dimensional hydraulic fracture propagation. *International Journal for Numerical and Analytical Methods in Geomechanics*, 38(13):1397–1430 (2014).
- P. Gupta and C.A. Duarte. Coupled formulation and algorithms for the simulation of non-planar three-dimensional hydraulic fractures using the generalized finite element method. *International Journal for Numerical and Analytical Methods in Geomechanics* (2015).
- T. Heister, M.F. Wheeler, and T. Wick. A primal-dual active set method and predictor-corrector mesh adaptivity for computing fracture propagation using a phase-field approach. *Computer Methods in Applied Mechanics and Engineering*, 290:466–495 (2015).
- M.A. Heroux, P. Raghavan, and H.D. Simon. *Parallel processing for scientific computing*, volume 20. SIAM (2006).
- M. Hossain and M.K. Rahman. Numerical simulation of complex fracture growth during tight reservoir stimulation by hydraulic fracturing. *Journal of Petroleum Science and Engineering*, 60(2):86–104 (2008).
- M.E. Houben, A. Barnhoorn, J. Lie-A-Fat, T. Ravestein, C.J. Peach, and M.R. Drury. Microstructural characteristics of the whitby mudstone formation (uk). *Marine and Petroleum Geology*, 70:185–200 (2016).
- G.C. Howard and C.R. Fast. Optimum fluid characteristics for fracture extension. *Drilling and Production Practice* (1957).
- R.W. Howarth, A. Ingraffea, and T. Engelder. Natural gas: Should fracking stop? *Nature*, 477(7364):271–275 (2011).
- F. Irzal, J.J.C. Remmers, J.M. Huyghe, and R. de Borst. A large deformation formulation for fluid flow in a progressively fracturing porous material. *Computer Methods in Applied Mechanics and Engineering*, 256:29–37 (2013).
- M. Jirásek. Embedded crack models for concrete fracture. In *Computational Modelling of Concrete Structures, EURO C-98*, volume 1, pages 291–300

- (1998).
- G. Karypis and V. Kumar. A software package for partitioning unstructured graphs, partitioning meshes, and computing fill-reducing orderings of sparse matrices. *University of Minnesota, Department of Computer Science and Engineering, Army HPC Research Center, Minneapolis, MN* (1998).
- A.R. Khoei, O.R. Barani, and M. Mofid. Modeling of dynamic cohesive fracture propagation in porous saturated media. *International Journal for Numerical and Analytical Methods in Geomechanics*, 35(10):1160–1184 (2010).
- A.R. Khoei, M. Vahab, and M. Hirmand. Modeling the interaction between fluid-driven fracture and natural fault using an enriched-fem technique. *International Journal of Fracture*, 197(1):1–24 (2016).
- S.A. Khristianovic and Y.P. Zheltov. Formation of vertical fractures by means of highly viscous liquid. *Proceedings of the fourth world petroleum congress, Rome*, pages 579–586 (1955).
- G.E. King. Thirty years of gas shale fracturing: What have we learned? In *SPE Annual Technical Conference and Exhibition*. Society of Petroleum Engineers (2010).
- G. Kirsch. Die Theorie der Elastizität und die Bedürfnisse der Festigkeitslehre. *Zeitschrift des Vereines deutscher Ingenieure*, 42:797–807 (1898).
- F. Kraaijeveld. *Propagating discontinuities in ionized porous media*. Ph.D. thesis, Technische universiteit Eindhoven (2009).
- F. Kraaijeveld and J.M. Huyghe. Propagating cracks in saturated ionized porous media. *Multiscale Methods in Computational Mechanics*, pages 425–442 (2011).
- F. Kraaijeveld, J.M. Huyghe, J.J.C. Remmers, and R. de Borst. 2D mode I crack propagation in saturated ionized porous media using partition of unity finite elements. *Journal of Applied Mechanics*, 80(2):020907 (2013).
- O. Kresse, X. Weng, H. Gu, and R. Wu. Numerical modeling of hydraulic fractures interaction in complex naturally fractured formations. *Rock mechanics and rock engineering*, 46(3):555–568 (2013).
- B. Lecampion. An extended finite element method for hydraulic fracture problems. *Communications in Numerical Methods in Engineering*, 25(2):121–133 (2009).
- H.P. Lee, J.E. Olson, J. Holder, J.F.W. Gale, and R.D. Myers. The interaction of propagating opening mode fractures with preexisting discontinuities in shale. *Journal of Geophysical Research: Solid Earth*, 120(1):169–181 (2015).

- S. Lee, M.F. Wheeler, and T. Wick. Pressure and fluid-driven fracture propagation in porous media using an adaptive finite element phase field model. *Computer Methods in Applied Mechanics and Engineering*, 305:111–132 (2016).
- G. Legrain, N. Moës, and E. Verron. Stress analysis around crack tips in finite strain problems using the extended finite element method. *International Journal for Numerical Methods in Engineering*, 63(2):290–314 (2005).
- R.W. Lewis and B.A. Schrefler. *The finite element method in the deformation and consolidation of porous media*. John Wiley and Sons Inc., New York, NY (1987).
- L.C. Li, C.A. Tang, G. Li, S.Y. Wang, Z.Z. Liang, and Y.B. Zhang. Numerical simulation of 3d hydraulic fracturing based on an improved flow-stress-damage model and a parallel fem technique. *Rock Mechanics and rock engineering*, 45(5):801–818 (2012).
- C. Linder and X. Zhang. A marching cubes based failure surface propagation concept for three-dimensional finite elements with non-planar embedded strong discontinuities of higher-order kinematics. *International Journal for Numerical Methods in Engineering*, 96(6):339–372 (2013).
- F.J. Lingen. Jem-jive, a research-oriented C++ programming toolkit. <http://jem-jive.com> (2016).
- F.J. Lingen, P.G. Bonnier, R.B.J. Brinkgreve, M.B. van Gijzen, and C. Vuik. A parallel linear solver exploiting the physical properties of the underlying mechanical problem. *Computational Geosciences*, 18(6):913–926 (2014).
- F.J. Lingen and M.G.A. Tijssens. An efficient parallel procedure for the simulation of crack growth using the cohesive surface methodology. *International Journal for Numerical Methods in Engineering*, 52(8):867–888 (2001).
- S. Loehnert. A stabilization technique for the regularization of nearly singular extended finite elements. *Computational Mechanics*, 54(2):523–533 (2014).
- J. Mandel. Consolidation des sols (étude mathématique). *Geotechnique*, 3(7):287–299 (1953).
- S.C. Maxwell, T.I. Urbancic, N. Steinsberger, and R. Zinno. Microseismic imaging of hydraulic fracture complexity in the barnett shale. In *SPE Annual Technical Conference and Exhibition*. Society of Petroleum Engineers (2002).
- J.M. Melenk and I. Babuška. The partition of unity finite element method: basic theory and applications. *Computer methods in applied mechanics*

- and engineering*, 139(1):289–314 (1996).
- G. Meschke and P. Dumstorff. Energy-based modeling of cohesive and cohesionless cracks via x-fem. *Computer Methods in Applied Mechanics and Engineering*, 196(21):2338–2357 (2007).
- G. Meschke and D. Leonhart. A generalized finite element method for hydro-mechanically coupled analysis of hydraulic fracturing problems using space-time variant enrichment functions. *Computer Methods in Applied Mechanics and Engineering*, 290:438–465 (2015).
- C. Miehe, M. Hofacker, and F. Welschinger. A phase field model for rate-independent crack propagation: Robust algorithmic implementation based on operator splits. *Computer Methods in Applied Mechanics and Engineering*, 199(45):2765–2778 (2010).
- C. Miehe, S. Mauthe, and S. Teichtmeister. Minimization principles for the coupled problem of darcy-biot-type fluid transport in porous media linked to phase field modeling of fracture. *Journal of the Mechanics and Physics of Solids*, 82:186–217 (2015).
- A. Mikelić, M.F. Wheeler, and T. Wick. Phase-field modeling of a fluid-driven fracture in a poroelastic medium. *Computational Geosciences*, 19(6):1171–1195 (2015).
- E. Milanese, O. Yilmaz, J. Molinari, and B.A. Schrefler. Avalanches in dry and saturated disordered media at fracture in shear and mixed mode scenarios. *Mechanics Research Communications* (2016).
- N. Moës, J. Dolbow, and T. Belytschko. A finite element method for crack growth without remeshing. *International journal for numerical methods in engineering*, 46(1):131–150 (1999).
- N. Moës, A. Gravouil, and T. Belytschko. Non-planar 3d crack growth by the extended finite element and level sets—part i: Mechanical model. *International Journal for Numerical Methods in Engineering*, 53(11):2549–2568 (2002).
- N. Moës, C. Stolz, P.E. Bernard, and N. Chevaugeon. A level set based model for damage growth: the thick level set approach. *International Journal for Numerical Methods in Engineering*, 86(3):358–380 (2011).
- T. Mohammadnejad and J.E. Andrade. Numerical modeling of hydraulic fracture propagation, closure and reopening using xfem with application to in-situ stress estimation. *International Journal for Numerical and Analytical Methods in Geomechanics*, 40 (2016).
- T. Mohammadnejad and A.R. Khoei. Hydro-mechanical modeling of cohesive crack propagation in multiphase porous media using the extended finite element method. *International Journal for Numerical and Analytical Methods in Geomechanics*, 37(10):1247–1279 (2012).

- T. Mohammadnejad and A.R. Khoei. An extended finite element method for hydraulic fracture propagation in deformable porous media with the cohesive crack model. *Finite Elements in Analysis and Design*, 73:77–95 (2013).
- N.B. Nagel, M.A. Sanchez-Nagel, F. Zhang, X. Garcia, and B. Lee. Coupled numerical evaluations of the geomechanical interactions between a hydraulic fracture stimulation and a natural fracture system in shale formations. *Rock mechanics and rock engineering*, 46(3):581–609 (2013).
- M.B. Nooru-Mohamed. *Mixed-mode fracture of concrete: an experimental approach*. TU Delft, Delft University of Technology (1992).
- R.P. Nordgren. Propagation of a vertical hydraulic fracture. *Old SPE Journal*, 12(4):306–314 (1972).
- K. Obara, H. Hirose, F. Yamamizu, and K. Kasahara. Episodic slow slip events accompanied by non-volcanic tremors in southwest japan subduction zone. *Geophysical Research Letters*, 31(23) (2004).
- C.J. de Pater. Hydraulic fracture containment: New insights into mapped geometry. In *SPE Hydraulic Fracturing Technology Conference*. Society of Petroleum Engineers (2015).
- T.K. Perkins and L.R. Kern. Widths of hydraulic fractures. *Journal of Petroleum Technology*, 13(9):937–949 (1961).
- P.E. Petersson. *Crack growth and development of fracture zones in plain concrete and similar materials*. Division, Inst. (1981).
- F. Pizzocolo, J.M. Huyghe, and K. Ito. Mode I crack propagation in hydrogels is step wise. *Engineering Fracture Mechanics*, 97:72–79 (2013).
- K. Pruess. Enhanced geothermal systems (egs) using CO₂ as working fluid a novel approach for generating renewable energy with simultaneous sequestration of carbon. *Geothermics*, 35(4):351–367 (2006).
- M.M. Rahman, M.M. Hossain, D.G. Crosby, M.K. Rahman, and S.S. Rahman. Analytical, numerical and experimental investigations of transverse fracture propagation from horizontal wells. *Journal of Petroleum Science and Engineering*, 35(3):127–150 (2002).
- J. Rannou, A. Gravouil, and A. Combescure. A multi-grid extended finite element method for elastic crack growth simulation. *European Journal of Computational Mechanics/Revue Européenne de Mécanique Numérique*, 16(2):161–182 (2007).
- J.J.C. Remmers. *Discontinuities in materials and structures*. Ph.D. thesis, Delft University of Technology (2006).
- J.J.C. Remmers, E. de Borst, C.V. Verhoosel, and A. Needleman. The cohesive band model: a cohesive surface formulation with stress triaxiality. *International Journal of Fracture*, 181(2):177–188 (2013).

- J.J.C. Remmers, R. de Borst, and A. Needleman. A cohesive segments method for the simulation of crack growth. *Computational Mechanics*, 31(1-2):69–77 (2003).
- J.J.C. Remmers, R. de Borst, and A. Needleman. The simulation of dynamic crack propagation using the cohesive segments method. *Journal of the Mechanics and Physics of Solids*, 56(1):70–92 (2008).
- C.E. Renshaw and D.D. Pollard. An experimentally verified criterion for propagation across unbounded frictional interfaces in brittle, linear elastic materials. In *International journal of rock mechanics and mining sciences & geomechanics abstracts*, volume 32, pages 237–249. Elsevier (1995).
- J. Réthoré, R. de Borst, and M.A. Abellan. A two-scale approach for fluid flow in fractured porous media. *International Journal for Numerical Methods in Engineering*, 71(7):780–800 (2007).
- G. Rogers and H. Dragert. Episodic tremor and slip on the cascadia subduction zone: The chatter of silent slip. *Science*, 300(5627):1942–1943 (2003).
- J.G. Rots, P. Nauta, G.M.A. Kuster, and J. Blaauwendraad. Smearred crack approach and fracture localization in concrete. *HERON*, 30 (1), 1985 (1985).
- Y. Saad. *Iterative methods for sparse linear systems*. Siam (2003).
- E. Sarris and P. Papanastasiou. The influence of the cohesive process zone in hydraulic fracturing modelling. *International Journal of Fracture*, 167(1):33–45 (2011).
- E. Schlangen and J.G.M. van Mier. Experimental and numerical analysis of micromechanisms of fracture of cement-based composites. *Cement and concrete composites*, 14(2):105–118 (1992).
- B.A. Schrefler, S. Secchi, and L. Simoni. On adaptive refinement techniques in multi-field problems including cohesive fracture. *Computer methods in applied mechanics and engineering*, 195(4):444–461 (2006).
- S. Secchi and B.A. Schrefler. A method for 3D hydraulic fracturing simulation. *International Journal of Fracture*, pages 1–14 (2012). ISSN 0376-9429.
- S. Secchi, L. Simoni, and B.A. Schrefler. Mesh adaptation and transfer schemes for discrete fracture propagation in porous materials. *International Journal for Numerical and Analytical Methods in Geomechanics*, 31(2):331–345 (2007). ISSN 1096-9853.
- J.M. Segura and I. Carol. On zero-thickness interface elements for diffusion problems. *International journal for numerical and analytical methods in geomechanics*, 28(9):947–962 (2004).

- J.M. Segura and I. Carol. Coupled hm analysis using zero-thickness interface elements with double nodes. part i: Theoretical model. *International journal for numerical and analytical methods in geomechanics*, 32(18):2083–2101 (2008).
- J.A. Sethian. *Level set methods and fast marching methods: evolving interfaces in computational geometry, fluid mechanics, computer vision, and materials science*, volume 3. Cambridge university press (1999).
- C. Shet and N. Chandra. Analysis of energy balance when using cohesive zone models to simulate fracture processes. *Transaction of the ASME*, 124(4):440–450 (2002).
- B. Smith, P. Bjorstad, and W. Gropp. *Domain decomposition: parallel multilevel methods for elliptic partial differential equations*. Cambridge university press (2004).
- M.B. Smith and C. Montgomery. *Hydraulic Fracturing*. Crc Press (2015).
- B. Sobhaniragh, W.J. Mansur, and F.C. Peters. Three-dimensional investigation of multiple stage hydraulic fracturing in unconventional reservoirs. *Journal of Petroleum Science and Engineering* (2016).
- M. Stolarska, D.L. Chopp, N. Moës, and T. Belytschko. Modelling crack growth by level sets in the extended finite element method. *International journal for numerical methods in Engineering*, 51(8):943–960 (2001).
- N. Sukumar, D.L. Chopp, N. Moës, and T. Belytschko. Modeling holes and inclusions by level sets in the extended finite-element method. *Computer methods in applied mechanics and engineering*, 190(46):6183–6200 (2001).
- N. Sukumar, D.L. Chopp, and B. Moran. Extended finite element method and fast marching method for three-dimensional fatigue crack propagation. *Engineering Fracture Mechanics*, 70(1):29–48 (2003).
- N. Sukumar, N. Moës, B. Moran, and T. Belytschko. Extended finite element method for three-dimensional crack modelling. *International Journal for Numerical Methods in Engineering*, 48(11):1549–1570 (2000).
- K. Terzaghi. Die berechnung der durchlassigkeitsziffer des tones aus dem verlauf der hydrodynamischen spannungserscheinungen. *Sitzungsberichte der Akademie der Wissenschaften in Wien, Mathematisch-Naturwissenschaftliche Klasse, Abteilung IIa*, 132:125–138 (1923).
- K. Terzaghi. *Theoretical soil mechanics*. J. Wiley, New York (1943).
- J.F. Unger, S. Eckardt, and C. Könke. Modelling of cohesive crack growth in concrete structures with the extended finite element method. *Computer methods in applied mechanics and engineering*, 196(41):4087–4100 (2007).
- P. Valko and M.J. Economides. *Hydraulic fracture mechanics*. Wiley, New

- York (1995).
- G. Ventura, E. Budyn, and T. Belytschko. Vector level sets for description of propagating cracks in finite elements. *International Journal for Numerical Methods in Engineering*, 58(10):1571–1592 (2003).
- P.A. Vermeer and A. Verruijt. An accuracy condition for consolidation by finite elements. *International Journal for Numerical and Analytical Methods in Geomechanics*, 5(1):1–14 (1981).
- A. Verruijt. Elastic storage of aquifers. In *Flow Through Porous Media*, pages 331–376. Academic Press, New York (1969).
- G. Viguera, F. Sket, C. Samaniego, L. Wu, L. Noels, D. Tjahjanto, E. Casoni, G. Houzeaux, A. Makradi, J.M. Molina-Aldareguia, M. Vázquez, and A. Jérusalem. An xfem/czm implementation for massively parallel simulations of composites fracture. *Composite Structures*, 125:542–557 (2015).
- H. Waisman and L. Berger-Vergiat. An adaptive domain decomposition preconditioner for crack propagation problems modeled by xfem. *International Journal for Multiscale Computational Engineering*, 11(6) (2013).
- L. Weijers, C.J. de Pater, K.A Owens, and H.H Kogsbøll. Geometry of hydraulic fractures induced from horizontal wellbores. *SPE Production & Facilities*, 9(02):87–92 (1994).
- J.A. Weiss, B.N. Maker, and S. Govindjee. Finite element implementation of incompressible, transversely isotropic hyperelasticity. *Computer methods in applied mechanics and engineering*, 135(1):107–128 (1996).
- G.N. Wells and L.J. Sluys. A new method for modelling cohesive cracks using finite elements. *International Journal for Numerical Methods in Engineering*, 50(12):2667–2682 (2001).
- M.F. Wheeler, T. Wick, and W. Wollner. An augmented-lagrangian method for the phase-field approach for pressurized fractures. *Computer Methods in Applied Mechanics and Engineering*, 271:69–85 (2014).
- B.J. Winkler. *Traglastuntersuchungen von unbewehrten und bewehrten Betonstrukturen auf der Grundlage eines objektiven Werkstoffgesetzes für Beton*. Ph.D. thesis, Innsbruck University (2001).
- P.A. Witherspoon, J.S.Y. Wang, K. Iwai, and J.E. Gale. Validity of cubic law for fluid flow in a deformable rock fracture. *Water Resources Research*, 16(6):1016–1024 (1980).
- X.P. Xu and A. Needleman. Numerical simulations of fast crack growth in brittle solids. *Journal of the Mechanics and Physics of Solids*, 42(9):1397–1434 (1994).
- Y. Yao, L. Liu, and L.M. Keer. Pore pressure cohesive zone modeling of hydraulic fracture in quasi-brittle rocks. *Mechanics of Materials*, 83:17–

- 29 (2015).
- K. Yoshioka and B. Bourdin. A variational hydraulic fracturing model coupled to a reservoir simulator. *International Journal of Rock Mechanics and Mining Sciences*, 88:137–150 (2016).
- C. Yu, A. Pandolfi, M. Ortiz, D. Coker, and AJ Rosakis. Three-dimensional modeling of intersonic shear-crack growth in asymmetrically loaded unidirectional composite plates. *International journal of solids and structures*, 39(25):6135–6157 (2002).
- J. Zhou, M. Chen, Y. Jin, and G. Zhang. Analysis of fracture propagation behavior and fracture geometry using a tri-axial fracturing system in naturally fractured reservoirs. *International Journal of Rock Mechanics and Mining Sciences*, 45(7):1143–1152 (2008).

A

Leakage equation

In this appendix Terzaghi's one dimensional consolidation equation (Terzaghi, 1943) is solved for two different boundary conditions. First, we look at the consolidation of a soil layer under load. Secondly, we look at a soil column under the injection of a constant fluid flow. This is comparable to the early stages of hydraulic fracturing. The one dimensional consolidation equation is given by

$$\frac{\partial p}{\partial t} = c_v \frac{\partial^2 p}{\partial x^2}. \quad (\text{A.1})$$

Where c_v is the diffusion coefficient and is given by

$$c_v = kM \frac{K + \frac{4}{3}\mu}{K_u + \frac{4}{3}\mu}. \quad (\text{A.2})$$

Here K and μ are the bulk modulus and the shear modulus, respectively. The undrained bulk modulus is defined as

$$K_u = K + \alpha^2 M. \quad (\text{A.3})$$

Using separation of variables we can derive the well known 1D consolidation equation:

$$p(z, t) = \frac{2p_0}{h} \sum_{i=1}^{\infty} \frac{1}{\mu_i} e^{-\lambda_i c_v t} \sin(\mu_i z). \quad (\text{A.4})$$

Here is p_0 the applied load, h is the height of the soil layer, z is the coordinate system along the height of the consolidation column, and λ_i and μ_i are summation constants defined by

$$\lambda_i = \mu_i^2 = \left(\frac{(2i-1)\pi}{2h} \right)^2 \quad (\text{A.5})$$

Changing the bottom boundary condition to a constant fluid flow Q_{in} results in the following equation for the pressure

$$p(z, t) = -\frac{Q_{\text{in}}}{k}z + \frac{Q_{\text{in}}}{k}h - \frac{2Q_{\text{in}}}{hk} \sum_{i=1}^{\infty} \frac{1}{\mu_i^2} e^{-\lambda_i c_v t} \cos(\mu_i z). \quad (\text{A.6})$$

Since the latter solution is depended on the height of the soil layer we also give the solution for an semi-infinite soil layer

$$\frac{2Q_{\text{in}}}{k} \left(\sqrt{\frac{c_v t}{\pi}} \exp \frac{-\eta^2}{4c_v t} - \frac{\eta}{2} \operatorname{erfc} \left(\frac{\eta}{2\sqrt{c_v t}} \right) \right). \quad (\text{A.7})$$

Here η is the distance form the discontinuity to a point the formation. This equation was derived for the flux of heat trough a semi-infinite solid by Carslaw and Jaeger (1959).

B

System of equations in the ELP model

The matrices, defined in Eq. (4.54), are subdivided in four categories and are given below.

The stiffness matrices:

$$\begin{aligned}
 \mathbf{K}_{\hat{u}\hat{u}} &= \int_{\Omega_e} \mathbf{B}^T \mathbf{D} \mathbf{B} d\Omega_e & \mathbf{K}_{\hat{u}\hat{u}} &= \int_{\Omega_e} \mathcal{H}_{\Gamma_d} \mathbf{B}^T \mathbf{D} \mathbf{B} d\Omega_e \\
 \mathbf{K}_{\hat{u}\hat{u}} &= \int_{\Omega_e} \mathcal{H}_{\Gamma_d}^2 \mathbf{B}^T \mathbf{D} \mathbf{B} d\Omega_e + \int_{\Gamma_d^+} h^2 \mathbf{N}^T \mathbf{T} \mathbf{N} d\Gamma & \mathbf{K}_{\hat{p}\hat{p}} &= - \int_{\Omega_e} k \mathcal{H}_{\Gamma_d}^s \nabla \mathbf{H}^T \nabla \mathbf{H} d\Omega_e \\
 \mathbf{K}_{\hat{p}\hat{p}} &= - \int_{\Omega_e} k \nabla \mathbf{H}^T \nabla \mathbf{H} d\Omega_e & \mathbf{K}_{\hat{p}\hat{p}} &= - \int_{\Omega_e} k (\mathcal{H}_{\Gamma_d}^s)^2 \nabla \mathbf{H}^T \nabla \mathbf{H} d\Omega_e \\
 \mathbf{K}_{\hat{p}\hat{p}} &= - \int_{\Omega_e} k \mathcal{H}_{\Gamma_d}^s \nabla \mathbf{H}^T \nabla \mathbf{H} d\Omega_e & &
 \end{aligned}$$

the mass matrices:

$$\begin{aligned}
 \mathbf{M}_{\hat{p}\hat{p}} &= - \int_{\Omega_e} \frac{1}{M} \mathbf{H}^T \mathbf{H} d\Omega_e & \mathbf{M}_{\hat{p}\hat{p}} &= - \int_{\Omega_e} \frac{1}{M} \mathcal{H}_{\Gamma_d}^s \mathbf{H}^T \mathbf{H} d\Omega_e \\
 \mathbf{M}_{\hat{p}\hat{p}} &= - \int_{\Omega_e} \frac{1}{M} \mathcal{H}_{\Gamma_d}^s \mathbf{H}^T \mathbf{H} d\Omega_e & \mathbf{M}_{\hat{p}\hat{p}} &= - \int_{\Omega_e} \frac{1}{M} (\mathcal{H}_{\Gamma_d}^s)^2 \mathbf{H}^T \mathbf{H} d\Omega_e
 \end{aligned}$$

the coupling matrices:

$$\begin{aligned}
\mathbf{C}_{\tilde{u}\tilde{p}} &= -\alpha \int_{\Omega_e} \mathbf{B}^T (\mathbf{m}\mathbf{H}) d\Omega_e & \mathbf{C}_{\tilde{u}\tilde{p}} &= -\alpha \int_{\Omega_e} \mathcal{H}_{\Gamma_d}^s \mathbf{B}^T (\mathbf{m}\mathbf{H}) d\Omega_e \\
\mathbf{C}_{\tilde{u}\tilde{p}} &= -\alpha \int_{\Omega_e} \mathcal{H}_{\Gamma_d} \mathbf{B}^T (\mathbf{m}\mathbf{H}) d\Omega_e & \mathbf{C}_{\tilde{u}\tilde{p}} &= -\alpha \int_{\Omega_e} \mathcal{H}_{\Gamma_d} \mathcal{H}_{\Gamma_d}^s \mathbf{B}^T (\mathbf{m}\mathbf{H}) d\Omega_e \\
\mathbf{C}_{\tilde{p}\tilde{u}} &= -\alpha \int_{\Omega_e} \mathbf{H}^T \mathbf{m}^T \mathbf{B} d\Omega_e & \mathbf{C}_{\tilde{p}\tilde{u}} &= -\alpha \int_{\Omega_e} \mathcal{H}_{\Gamma_d} \mathbf{H}^T \mathbf{m}^T \mathbf{B} d\Omega_e \\
\mathbf{C}_{\tilde{p}\tilde{u}} &= -\alpha \int_{\Omega_e} \mathcal{H}_{\Gamma_d}^s \mathbf{H}^T \mathbf{m}^T \mathbf{B} d\Omega_e & \mathbf{C}_{\tilde{p}\tilde{u}} &= -\alpha \int_{\Omega_e} \mathcal{H}_{\Gamma_d} \mathcal{H}_{\Gamma_d}^s \mathbf{H}^T \mathbf{m}^T \mathbf{B} d\Omega_e
\end{aligned}$$

and the crack flow terms:

$$\begin{aligned}
\mathbf{Q}_{\tilde{u}p_d} &= -\int_{\Gamma_d^+} h \mathbf{N}^T \mathbf{n}_d \mathbf{V} d\Gamma & \mathbf{Q}_{p_d\tilde{u}}^{(2)} &= \int_{\Gamma_d} \frac{3}{12\mu} \frac{\partial \mathbf{V}^T}{\partial s} \frac{\partial \mathbf{V}}{\partial s} p_d u_n^2 h \mathbf{n}_d^T \mathbf{N} d\Gamma \\
\mathbf{Q}_{p_d p_d} &= \int_{\Gamma_d} \frac{1}{12\mu} \frac{\partial \mathbf{V}^T}{\partial s} u_n^3 \frac{\partial \mathbf{V}}{\partial s} d\Gamma & \mathbf{Q}_{p_d\tilde{p}} &= -2C_a \int_{\Gamma_d} \mathbf{V}^T \mathbf{H} d\Gamma \\
\mathbf{Q}_{p_d\tilde{u}} &= \int_{\Gamma_d} u_n \mathbf{V}^T \mathbf{t}^T \frac{\partial \mathbf{N}}{\partial s} d\Gamma & \mathbf{Q}_{p_d\tilde{u}}^{(3)} &= \int_{\Gamma_d} \frac{1}{2} u_n \mathbf{V}^T \mathbf{t}^T \frac{\partial \mathbf{N}}{\partial s} d\Gamma \\
\mathbf{Q}_{p_d p_d}^{(2)} &= \int_{\Gamma_d} \frac{u_n}{K_f} \mathbf{V}^T \mathbf{V} d\Gamma & \mathbf{Q}_{p_d\tilde{u}}^{(1)} &= \int_{\Gamma_d} h \mathbf{V}^T \mathbf{n}_d \mathbf{N} d\Gamma \\
\mathbf{Q}_{p_d p_d}^{(3)} &= 2C_a \int_{\Gamma_d} \mathbf{V} \mathbf{V}^T d\Gamma & \mathbf{Q}_{p_d\tilde{p}} &= -C_a \int_{\Gamma_d} \mathbf{V}^T \mathbf{H} d\Gamma
\end{aligned}$$

The additional terms in the stiffness matrix are defined by

$$\begin{aligned}
\mathbf{D}_{\tilde{p}\tilde{p}} &= \bar{\theta} \Delta t \mathbf{K}_{\tilde{p}\tilde{p}} + \mathbf{M}_{\tilde{p}\tilde{p}} & \mathbf{D}_{\tilde{p}\tilde{p}} &= \bar{\theta} \Delta t \mathbf{K}_{\tilde{p}\tilde{p}} + \mathbf{M}_{\tilde{p}\tilde{p}} \\
\mathbf{D}_{\tilde{p}\tilde{p}} &= \bar{\theta} \Delta t \mathbf{K}_{\tilde{p}\tilde{p}} + \mathbf{M}_{\tilde{p}\tilde{p}} & \mathbf{D}_{\tilde{p}\tilde{p}} &= \bar{\theta} \Delta t \mathbf{K}_{\tilde{p}\tilde{p}} \\
\mathbf{F}_{p_d\tilde{u}} &= \mathbf{Q}_{p_d\tilde{u}}^{(1)} + \bar{\theta} \Delta t \mathbf{Q}_{p_d\tilde{u}}^{(2)} + \mathbf{Q}_{p_d\tilde{u}}^{(3)} & \mathbf{F}_{p_d p_d} &= \bar{\theta} \Delta t (\mathbf{Q}_{p_d p_d} + \mathbf{Q}_{p_d p_d}^{(3)}) + \mathbf{Q}_{p_d p_d}^{(2)}
\end{aligned}$$

The derivative of \mathbf{N} in the tangential direction of the fracture is calculated as follows:

$$\mathbf{t}^T \frac{\partial \mathbf{N}^T}{\partial s} = \mathbf{t}^T \nabla \mathbf{N}^T \mathbf{W} \mathbf{M}, \quad (\text{B.1})$$

with \mathbf{W} being the following support matrix in the case of four nodal elements

$$\mathbf{W} = \begin{pmatrix} 1 & 1 & 0 & 0 & 0 & 0 & 0 & 0 \\ 1 & 1 & 0 & 0 & 0 & 0 & 0 & 0 \\ 0 & 0 & 1 & 1 & 0 & 0 & 0 & 0 \\ 0 & 0 & 1 & 1 & 0 & 0 & 0 & 0 \\ 0 & 0 & 0 & 0 & 1 & 1 & 0 & 0 \\ 0 & 0 & 0 & 0 & 1 & 1 & 0 & 0 \\ 0 & 0 & 0 & 0 & 0 & 0 & 1 & 1 \\ 0 & 0 & 0 & 0 & 0 & 0 & 1 & 1 \end{pmatrix}, \quad (\text{B.2})$$

and \mathbf{M} being a support matrix containing the contributions of the tangent vector on its diagonal

$$M = \text{diag}[\mathbf{t}_x, \mathbf{t}_y, \mathbf{t}_x, \mathbf{t}_y, \mathbf{t}_x, \mathbf{t}_y, \mathbf{t}_x, \mathbf{t}_y]. \quad (\text{B.3})$$

C

System of equations in the ELP model with multiple fractures

The discretized balance equations for the enhanced local pressure model with multiple fractures are given in Equations (5.18)-(5.22). The discretized forms of the displacement field and the discretized pressure field, and the constitutive relations are not included in the balance equations. In this appendix these are added and the complete system of equations is derived. Including the discretized displacement and pressure fields (Eq. 5.16), the constitutive relations defined by Terzaghi effective stress (4.18), and by Darcy's law (4.20) into Equations (5.18)-(5.22) gives the continuous momentum balance

$$\int_{\Omega} \mathbf{B}^T \mathbf{D} \mathbf{B} \left(\dot{\mathbf{u}} + \sum_{i=1}^m \mathcal{H}_{\Gamma_{d_i}} \dot{\mathbf{u}}_i \right) d\Omega - \int_{\Omega} \alpha \mathbf{B}^T \mathbf{m} \mathbf{H} \left(\dot{\mathbf{p}} + \sum_{i=1}^m \mathcal{H}_{\Gamma_{d_i}} \dot{\mathbf{p}}_i \right) d\Omega = \int_{\Gamma_t} \mathbf{N}^T \mathbf{t}_p d\Gamma, \quad (\text{C.1})$$

the continuous mass balance

$$\begin{aligned} & - \int_{\Omega} \alpha \mathbf{H}^T \mathbf{m}^T \mathbf{B} \left(\dot{\mathbf{u}} + \sum_{i=1}^m \mathcal{H}_{\Gamma_{d_i}} \dot{\mathbf{u}}_i \right) d\Omega \\ & - \int_{\Omega} k \nabla \mathbf{H}^T \nabla \mathbf{H} \left(\dot{\mathbf{p}} + \sum_{i=1}^m \mathcal{H}_{\Gamma_{d_i}} \dot{\mathbf{p}}_i \right) d\Omega - \int_{\Omega} \frac{1}{M} \mathbf{H}^T \mathbf{H} \left(\dot{\mathbf{p}} + \sum_{i=1}^m \mathcal{H}_{\Gamma_{d_i}} \dot{\mathbf{p}}_i \right) d\Omega = \\ & \int_{\Gamma_f} \mathbf{H}^T f_f d\Gamma, \end{aligned} \quad (\text{C.2})$$

$k = 1 \dots m$ discontinuous momentum balance equations

$$\begin{aligned} & \int_{\Omega} \mathcal{H}_{\Gamma_{d_k}} \mathbf{B}^T \mathbf{D} \mathbf{B} \left(\dot{\mathbf{u}} + \sum_{i=1}^m \mathcal{H}_{\Gamma_{d_i}} \dot{\mathbf{u}}_i \right) d\Omega - \int_{\Omega} \alpha \mathcal{H}_{\Gamma_{d_k}} \mathbf{B}^T \mathbf{m} \mathbf{H} \left(\dot{\mathbf{p}} + \sum_{i=1}^m \mathcal{H}_{\Gamma_{d_i}} \dot{\mathbf{p}}_i \right) d\Omega = \\ & \int_{\Gamma_t} \mathcal{H}_{\Gamma_{d_k}} \mathbf{N}^T \mathbf{t}_p d\Gamma_t - \int_{\Gamma_{d_k}} \mathbf{N}^T \mathbf{t}_k d\Gamma_{d_k} \\ & - \mathbf{N}^T \left(\sum_{j=1, j \neq k}^m \int_{\Gamma_{d_j}} \left[\mathcal{H}_{\Gamma_{d_k}(\Gamma_{d_j}^+)} - \mathcal{H}_{\Gamma_{d_k}(\Gamma_{d_j}^-)} \right] \mathbf{t}_j d\Gamma_{d_j} \right), \end{aligned} \quad (\text{C.3})$$

$k = 1 \dots m$ discontinuous mass balance equations

$$\begin{aligned} & - \int_{\Omega} \alpha \mathcal{H}_{\Gamma_{d_k}} \mathbf{H}^T \mathbf{m}^T \mathbf{B} \left(\dot{\mathbf{u}} + \sum_{i=1}^m \mathcal{H}_{\Gamma_{d_i}} \dot{\mathbf{u}}_i \right) d\Omega \\ & - \int_{\Omega} k \mathcal{H}_{\Gamma_{d_k}} \nabla \mathbf{H}^T (\nabla \mathbf{H}) \left(\dot{\mathbf{p}} + \sum_{i=1}^m \mathcal{H}_{\Gamma_{d_i}} \dot{\mathbf{p}}_i \right) d\Omega - \int_{\Omega} \frac{1}{M} \mathcal{H}_{\Gamma_{d_k}} \mathbf{H}^T \mathbf{H} \left(\dot{\mathbf{p}} + \sum_{i=1}^m \mathcal{H}_{\Gamma_{d_i}} \dot{\mathbf{p}}_i \right) d\Omega = \\ & \int_{\Gamma_f} \mathcal{H}_{\Gamma_{d_k}} \mathbf{H}^T f_f d\Gamma, \end{aligned} \quad (\text{C.4})$$

and the mass balance of fluid in the fracture

$$\begin{aligned} & \sum_{j=1}^m \int_{\Gamma_{d_j}} \mathbf{v}^T (\mathbf{q}_{\Gamma_d}^+ + \mathbf{q}_{\Gamma_d}^-) \cdot \mathbf{n}_j^d d\Gamma_{d_j} \\ & + \sum_{j=1}^m \int_{\Gamma_{d_j}} \frac{1}{K_f} \mathbf{v}^T \mathbf{n}_j^d \mathbf{N} \left(\dot{\mathbf{u}}_j + \sum_{l=1, l \neq j}^m \left[\mathcal{H}_{\Gamma_{d_l}(\Gamma_{d_j}^+)} - \mathcal{H}_{\Gamma_{d_l}(\Gamma_{d_j}^-)} \right] \dot{\mathbf{u}}_l \right) \mathbf{v} \dot{\mathbf{p}}_d d\Gamma_{d_j} \\ & + \sum_{j=1}^m \int_{\Gamma_{d_j}} \mathbf{v}^T \mathbf{n}_j^d \mathbf{N} \left(\dot{\mathbf{u}}_j + \sum_{l=1, l \neq j}^m \left[\mathcal{H}_{\Gamma_{d_l}(\Gamma_{d_j}^+)} - \mathcal{H}_{\Gamma_{d_l}(\Gamma_{d_j}^-)} \right] \dot{\mathbf{u}}_l \right) d\Gamma_{d_j} \\ & + \sum_{j=1}^m \int_{\Gamma_{d_j}} \frac{1}{12\mu} \left(\mathbf{n}_j^d \mathbf{N} \left(\dot{\mathbf{u}}_j + \sum_{l=1, l \neq j}^m \left[\mathcal{H}_{\Gamma_{d_l}(\Gamma_{d_j}^+)} - \mathcal{H}_{\Gamma_{d_l}(\Gamma_{d_j}^-)} \right] \dot{\mathbf{u}}_l \right) \right)^3 \frac{\partial \mathbf{v}^T}{\partial s} \cdot \frac{\partial \mathbf{v}}{\partial s} \dot{\mathbf{p}}_d d\Gamma_{d_j} = \\ & \sum_{j=1}^m \psi Q_{\text{in}}^j |S_d|. \end{aligned} \quad (\text{C.5})$$

Before linearizing these equations the dependency of the displacement jump in Equation (5.6) on the cohesive traction in the discontinuous momentum balance must be taken into account. Using the following notation for the Heaviside jump:

$$\left(\mathcal{H}_{\Gamma_{d_a}}(\Gamma_{d_b}^+) - \mathcal{H}_{\Gamma_{d_a}}(\Gamma_{d_b}^-) \right) = \Delta \mathcal{H}_{\Gamma_{d_a}}(\Gamma_{d_b}), \quad (\text{C.6})$$

which represents the value of the Heaviside step function of discontinuity a at a point on discontinuity b . The $k = 1 \dots m$ discontinuous momentum balance equation are then rewritten as

$$\begin{aligned} & \int_{\Omega} \mathcal{H}_{\Gamma_{d_k}} \mathbf{B}^T \mathbf{D} \mathbf{B} \left(\underline{\mathbf{u}} + \sum_{i=1}^m \mathcal{H}_{\Gamma_{d_i}} \underline{\mathbf{u}}_i \right) d\Omega - \int_{\Omega} \alpha \mathcal{H}_{\Gamma_{d_k}} \mathbf{B}^T \mathbf{m} \mathbf{H} \left(\underline{\mathbf{p}} + \sum_{i=1}^m \mathcal{H}_{\Gamma_{d_i}} \underline{\mathbf{p}}_i \right) d\Omega = \\ & \int_{\Gamma_t} \mathcal{H}_{\Gamma_{d_k}} \mathbf{N}^T \mathbf{t}_p d\Gamma_t - \int_{\Gamma_{d_k}} \mathbf{N}^T \mathbf{Q}^T \mathbf{T}_d \mathbf{Q} \mathbf{N} \underline{\mathbf{u}}_k d\Gamma_{d_k} \\ & - \int_{\Gamma_{d_k}} \mathbf{N}^T \mathbf{Q}^T \mathbf{T}_d \mathbf{Q} \sum_{j=1, j \neq k}^m \left(\Delta \mathcal{H}_{\Gamma_{d_j}}(\Gamma_{d_k}) \mathbf{N} \underline{\mathbf{u}}_j \right) d\Gamma_{d_k} \\ & - \left(\sum_{j=1, j \neq k}^m \int_{\Gamma_{d_j}} \mathbf{N}^T \mathbf{Q}^T \mathbf{T}_d \mathbf{Q} \Delta \mathcal{H}_{\Gamma_{d_k}}(\Gamma_{d_j}) \mathbf{N} \underline{\mathbf{u}}_j d\Gamma_{d_j} \right) \\ & - \left(\sum_{j=1, j \neq k}^m \int_{\Gamma_{d_j}} \mathbf{N}^T \mathbf{Q}^T \mathbf{T}_d \mathbf{Q} \Delta \mathcal{H}_{\Gamma_{d_k}}(\Gamma_{d_j}) \sum_{l=1, l \neq j}^m \Delta \mathcal{H}_{\Gamma_{d_l}}(\Gamma_{d_j}) \mathbf{N} \underline{\mathbf{u}}_l d\Gamma_{d_j} \right) \end{aligned} \quad (\text{C.7})$$

By also filling in the analytical leakage law, given in Equation (4.29), leads to the final mass balance equation in the fracture.

$$\begin{aligned} & \sum_{j=1}^m \int_{\Gamma_{d_j}} 2C_a \mathbf{V}^T \mathbf{V} \underline{\mathbf{p}}_d d\Gamma_{d_j} \\ & - \sum_{j=1}^m \int_{\Gamma_{d_j}} C_a \mathbf{V}^T \mathbf{H} \left(2\underline{\mathbf{p}} + \underline{\mathbf{p}}_j + \sum_{l=1, l \neq j}^m \Delta \mathcal{H}_{\Gamma_{d_l}}(\Gamma_{d_j}) \underline{\mathbf{p}}_l \right) d\Gamma_{d_j} \\ & + \sum_{j=1}^m \int_{\Gamma_{d_j}} \frac{1}{K_f} \mathbf{V}^T \mathbf{n}_j^d \mathbf{N} \left(\underline{\mathbf{u}}_j + \sum_{l=1, l \neq j}^m \Delta \mathcal{H}_{\Gamma_{d_l}}(\Gamma_{d_j}) \underline{\mathbf{u}}_l \right) \mathbf{V} \underline{\mathbf{p}}_d d\Gamma_{d_j} \\ & + \sum_{j=1}^m \int_{\Gamma_{d_j}} \mathbf{V}^T \mathbf{n}_j^d \mathbf{N} \left(\underline{\mathbf{u}}_j + \sum_{l=1, l \neq j}^m \Delta \mathcal{H}_{\Gamma_{d_l}}(\Gamma_{d_j}) \underline{\mathbf{u}}_l \right) d\Gamma_{d_j} \\ & + \sum_{j=1}^m \int_{\Gamma_{d_j}} \frac{1}{12\mu} \left(\mathbf{n}_j^d \mathbf{N} \left(\underline{\mathbf{u}}_j + \sum_{l=1, l \neq j}^m \Delta \mathcal{H}_{\Gamma_{d_l}}(\Gamma_{d_j}) \underline{\mathbf{u}}_l \right) \right)^3 \frac{\partial \mathbf{V}^T}{\partial s} \cdot \frac{\partial \mathbf{V}}{\partial s} \underline{\mathbf{p}}_d d\Gamma_{d_j} = \\ & \sum_{j=1}^m \psi Q_{in}^j |_{S_d}. \end{aligned} \quad (\text{C.8})$$

The final system of equations is given on the next page:

$$\begin{bmatrix} \mathbf{K}_{\hat{u}\hat{u}} \\ \mathbf{K}_{\hat{u}_1\hat{u}} \\ \vdots \\ \mathbf{K}_{\hat{u}_m\hat{u}} \\ \mathbf{C}_{\hat{p}\hat{u}} \\ \mathbf{C}_{\hat{p}_1\hat{u}} \\ \vdots \\ \mathbf{C}_{\hat{p}_m\hat{u}} \\ \mathbf{Q}_{p_d\hat{u}} \end{bmatrix} \begin{bmatrix} \mathbf{K}_{\hat{u}\hat{u}_1} \\ \mathbf{K}_{\hat{u}_1\hat{u}_1} \\ \vdots \\ \mathbf{K}_{\hat{u}_m\hat{u}_1} \\ \mathbf{C}_{\hat{p}\hat{u}_1} \\ \mathbf{C}_{\hat{p}_1\hat{u}_1} \\ \vdots \\ \mathbf{C}_{\hat{p}_m\hat{u}_1} \\ \mathbf{Q}_{p_d\hat{u}_1} \end{bmatrix} \begin{bmatrix} \mathbf{C}_{\hat{u}\hat{p}} \\ \mathbf{C}_{\hat{u}_1\hat{p}} \\ \vdots \\ \mathbf{C}_{\hat{u}_m\hat{p}} \\ \mathbf{D}_{\hat{p}\hat{p}} \\ \mathbf{D}_{\hat{p}_1\hat{p}} \\ \vdots \\ \mathbf{D}_{\hat{p}_m\hat{p}} \\ \theta \Delta t \mathbf{Q}_{p_d\hat{p}} \end{bmatrix} \begin{bmatrix} \mathbf{C}_{\hat{u}\hat{p}_m} \\ \mathbf{C}_{\hat{u}_1\hat{p}_m} \\ \vdots \\ \mathbf{C}_{\hat{u}_m\hat{p}_m} \\ \mathbf{D}_{\hat{p}\hat{p}_m} \\ \mathbf{D}_{\hat{p}_1\hat{p}_m} \\ \vdots \\ \mathbf{D}_{\hat{p}_m\hat{p}_m} \\ \theta \Delta t \mathbf{Q}_{p_d\hat{p}_m} \end{bmatrix} \begin{bmatrix} \mathbf{0} \\ \mathbf{Q}_{\hat{u}_1 p_d} \\ \vdots \\ \mathbf{Q}_{\hat{u}_m p_d} \\ \mathbf{0} \\ \mathbf{0} \\ \vdots \\ \mathbf{0} \\ \mathbf{F}_{p_d p_d} \end{bmatrix} = \begin{bmatrix} \partial \hat{\mathbf{u}} \\ \partial \hat{\mathbf{u}}_1 \\ \vdots \\ \partial \hat{\mathbf{u}}_m \\ \partial \hat{\mathbf{p}} \\ \partial \hat{\mathbf{p}}_1 \\ \vdots \\ \partial \hat{\mathbf{p}}_m \\ \partial \hat{\mathbf{p}}_d \end{bmatrix} = \begin{bmatrix} \mathbf{f}_{\hat{u}}^{\text{ext}} \\ \mathbf{f}_{\hat{u}_1}^{\text{ext}} \\ \vdots \\ \mathbf{f}_{\hat{u}_m}^{\text{ext}} \\ \Delta t \mathbf{f}_{\hat{p}}^{\text{ext}} \\ \Delta t \mathbf{f}_{\hat{p}_1}^{\text{ext}} \\ \vdots \\ \Delta t \mathbf{f}_{\hat{p}_m}^{\text{ext}} \\ \Delta t \mathbf{f}_{p_d}^{\text{ext}} \end{bmatrix} - \begin{bmatrix} \mathbf{f}_{\hat{u}}^{\text{int}} \\ \mathbf{f}_{\hat{u}_1}^{\text{int}} \\ \vdots \\ \mathbf{f}_{\hat{u}_m}^{\text{int}} \\ \mathbf{f}_{\hat{p}}^{\text{int}} \\ \mathbf{f}_{\hat{p}_1}^{\text{int}} \\ \vdots \\ \mathbf{f}_{\hat{p}_m}^{\text{int}} \\ \mathbf{f}_{p_d}^{\text{int}} \end{bmatrix} \quad (\text{C.9})$$

for m discontinuities. The parts of the stiffness matrix are

$$\begin{aligned}
\mathbf{D}_{\hat{p}\hat{p}} &= \bar{\theta} \Delta t \mathbf{K}_{\hat{p}\hat{p}} + \mathbf{M}_{\hat{p}\hat{p}} & \mathbf{D}_{\hat{p}\hat{p}_k} &= \bar{\theta} \Delta t \mathbf{K}_{\hat{p}\hat{p}_k} + \mathbf{M}_{\hat{p}\hat{p}_k} \\
\mathbf{D}_{\hat{p}_k\hat{p}} &= \bar{\theta} \Delta t \mathbf{K}_{\hat{p}_k\hat{p}} + \mathbf{M}_{\hat{p}_k\hat{p}} & \mathbf{D}_{\hat{p}_k\hat{p}_j} &= \bar{\theta} \Delta t \mathbf{K}_{\hat{p}_k\hat{p}_j} \\
\mathbf{F}_{p_d p_d} &= \bar{\theta} \Delta t (\mathbf{Q}_{p_d p_d} + \mathbf{Q}_{p_d p_d}^{(3)}) + \mathbf{Q}_{p_d p_d}^{(2)}
\end{aligned}$$

with all terms defined as

$$\begin{aligned}
\mathbf{K}_{\hat{u}\hat{u}} &= \int_{\Omega_e} \mathbf{B}^T \mathbf{D} \mathbf{B} \, d\Omega_e & \mathbf{K}_{\hat{u}\hat{u}_k} &= \int_{\Omega_e} \mathcal{H}_{\Gamma_k} \mathbf{B}^T \mathbf{D} \mathbf{B} \, d\Omega_e \\
\mathbf{K}_{\hat{u}_k \hat{u}} &= \int_{\Omega_e} \mathcal{H}_{\Gamma_k} \mathbf{B}^T \mathbf{D} \mathbf{B} \, d\Omega_e \\
\mathbf{K}_{\hat{u}_k \hat{u}_k} &= \int_{\Omega_e} \mathcal{H}_{\Gamma_k}^2 \mathbf{B}^T \mathbf{D} \mathbf{B} \, d\Omega_e + \int_{\Gamma_k} \mathbf{N}^T \mathbf{Q}^T \mathbf{T}_d \mathbf{Q} \mathbf{N} \hat{\mathbf{u}}_k \, d\Gamma_k \\
&+ \sum_{j=1, j \neq k}^m \int_{\Gamma_j} \mathbf{N}^T \mathbf{Q}^T \mathbf{T}_d \mathbf{Q} \Delta \mathcal{H}_{\Gamma_k}(\Gamma_j) \Delta \mathcal{H}_{\Gamma_k}(\Gamma_j) \\
\mathbf{K}_{\hat{u}_k \hat{u}_j \neq k} &= \int_{\Omega_e} \mathcal{H}_{\Gamma_k} \mathcal{H}_{\Gamma_j} \mathbf{B}^T \mathbf{D} \mathbf{B} \, d\Omega_e \\
&+ \int_{\Gamma_k} \mathbf{N}^T \mathbf{Q}^T \mathbf{T}_d \mathbf{Q} \Delta \mathcal{H}_{\Gamma_j}(\Gamma_k) \mathbf{N} \, d\Gamma_k \\
&+ \int_{\Gamma_j} \mathbf{N}^T \mathbf{Q}^T \mathbf{T}_d \mathbf{Q} \Delta \mathcal{H}_{\Gamma_k}(\Gamma_j) \mathbf{N} \, d\Gamma_j \\
&+ \sum_{l=1, l \neq k \& j}^m \int_{\Gamma_j} \mathbf{N}^T \mathbf{Q}^T \mathbf{T}_d \mathbf{Q} \Delta \mathcal{H}_{\Gamma_k}(\Gamma_j) \Delta \mathcal{H}_{\Gamma_l}(\Gamma_j) \mathbf{N} \, d\Gamma_j \\
\mathbf{K}_{\hat{p}\hat{p}} &= - \int_{\Omega_e} k \nabla \mathbf{H}^T \nabla \mathbf{H} \, d\Omega_e & \mathbf{K}_{\hat{p}\hat{p}_k} &= - \int_{\Omega_e} k \mathcal{H}_{\Gamma_k} \nabla \mathbf{H}^T \nabla \mathbf{H} \, d\Omega_e \\
\mathbf{K}_{\hat{p}_k \hat{p}} &= - \int_{\Omega_e} k \mathcal{H}_{\Gamma_k} \nabla \mathbf{H}^T \nabla \mathbf{H} \, d\Omega_e & \mathbf{K}_{\hat{p}_k \hat{p}_j} &= - \int_{\Omega_e} k \mathcal{H}_{\Gamma_k} \mathcal{H}_{\Gamma_j} \nabla \mathbf{H}^T \nabla \mathbf{H} \, d\Omega_e
\end{aligned}$$

$$\begin{aligned}
\mathbf{M}_{\hat{p}\hat{p}} &= - \int_{\Omega_e} \frac{1}{M} \mathbf{H}^T \mathbf{H} d\Omega_e \\
\mathbf{M}_{\hat{p}k\hat{p}} &= - \int_{\Omega_e} \frac{1}{M} \mathcal{H}_{\Gamma_k} \mathbf{H}^T \mathbf{H} d\Omega_e \\
\mathbf{C}_{\hat{u}\hat{p}} &= -\alpha \int_{\Omega_e} \mathbf{B}^T (\mathbf{m}\mathbf{H}) d\Omega_e \\
\mathbf{C}_{\hat{u}_k\hat{p}} &= -\alpha \int_{\Omega_e} \mathcal{H}_{\Gamma_k} \mathbf{B}^T (\mathbf{m}\mathbf{H}) d\Omega_e \\
\mathbf{C}_{\hat{p}\hat{u}} &= -\alpha \int_{\Omega_e} \mathbf{H}^T \mathbf{m}^T \mathbf{B} d\Omega_e \\
\mathbf{C}_{\hat{p}k\hat{u}} &= -\alpha \int_{\Omega_e} \mathcal{H}_{\Gamma_k} \mathbf{H}^T \mathbf{m}^T \mathbf{B} d\Omega_e \\
\mathbf{Q}_{\hat{u}_k\hat{p}d} &= - \int_{\Gamma_k} \mathbf{N}^T \mathbf{n}_j^d \mathbf{V} d\Gamma_k - \sum_{j=1, j \neq k}^m \int_{\Gamma_j} \Delta \mathcal{H}_{\Gamma_k}(\Gamma_j) \mathbf{N}^T \mathbf{n}_j^d \mathbf{V} d\Gamma_j \\
\mathbf{Q}_{\hat{p}d\hat{u}_k} &= \int_{\Gamma_k} \mathbf{V}^T \mathbf{n}_j^d \mathbf{N} d\Gamma_k + \sum_{j=1, j \neq k}^m \int_{\Gamma_j} \Delta \mathcal{H}_{\Gamma_k}(\Gamma_j) \mathbf{V}^T \mathbf{n}_j^d \mathbf{N} d\Gamma_j \\
\mathbf{Q}_{\hat{p}d\hat{p}}^{(3)} &= \sum_{j=1}^m \int_{\Gamma_j} 2C_a \mathbf{V}^T \mathbf{V} d\Gamma_j \\
\mathbf{Q}_{\hat{p}d\hat{p}k} &= - \int_{\Gamma_k} C_a \mathbf{V}^T \mathbf{H} d\Gamma_k - \sum_{j=1, j \neq k}^m \int_{\Gamma_j} \Delta \mathcal{H}_{\Gamma_k}(\Gamma_j) C_a \mathbf{V}^T \mathbf{H} d\Gamma_j \\
\mathbf{Q}_{\hat{p}d\hat{p}d}^{(2)} &= \sum_{j=1}^m \int_{\Gamma_j} ([\mathbf{u}]_j \cdot \mathbf{n}_j^d) \frac{\mathbf{V}^T}{K_f} \mathbf{V} d\Gamma_j \\
\mathbf{M}_{\hat{p}\hat{p}k} &= - \int_{\Omega_e} \frac{1}{M} \mathcal{H}_{\Gamma_k} \mathbf{H}^T \mathbf{H} d\Omega_e \\
\mathbf{M}_{\hat{p}_k\hat{p}_j} &= - \int_{\Omega_e} \frac{1}{M} \mathcal{H}_{\Gamma_k} \mathcal{H}_{\Gamma_j} \mathbf{H}^T \mathbf{H} d\Omega_e \\
\mathbf{C}_{\hat{u}\hat{p}k} &= -\alpha \int_{\Omega_e} \mathcal{H}_{\Gamma_k} \mathbf{B}^T (\mathbf{m}\mathbf{H}) d\Omega_e \\
\mathbf{C}_{\hat{u}_k\hat{p}_j} &= -\alpha \int_{\Omega_e} \mathcal{H}_{\Gamma_k} \mathcal{H}_{\Gamma_j} \mathbf{B}^T (\mathbf{m}\mathbf{H}) d\Omega_e \\
\mathbf{C}_{\hat{p}\hat{u}_k} &= -\alpha \int_{\Omega_e} \mathcal{H}_{\Gamma_k} \mathbf{H}^T \mathbf{m}^T \mathbf{B} d\Omega_e \\
\mathbf{C}_{\hat{p}k\hat{u}_j} &= -\alpha \int_{\Omega_e} \mathcal{H}_{\Gamma_k} \mathcal{H}_{\Gamma_j} \mathbf{H}^T \mathbf{m}^T \mathbf{B} d\Omega_e \\
\mathbf{Q}_{\hat{p}d\hat{p}} &= - \sum_{j=1}^m \int_{\Gamma_j} 2C_a \mathbf{V}^T \mathbf{H} d\Gamma_j \\
\mathbf{Q}_{\hat{p}d\hat{p}d} &= \frac{1}{12\mu} \sum_{j=1}^m \int_{\Gamma_j} ([\mathbf{u}]_j \cdot \mathbf{n}_j^d)^3 \frac{\partial \mathbf{V}^T}{\partial s} \cdot \frac{\partial \mathbf{V}}{\partial s} d\Gamma_j
\end{aligned}$$

Note that the compressibility and tangential fluid flow in the fracture are only linearized to the pressure in the fracture and not to the displacement. It was noticed during this work that convergence rates increased when adopting this approach. The system is solved using a Newton-Raphson iterative method with a weighted time integration scheme (see Section 4.5). To simplify the notation of the terms from the iteration and time integration scheme we adopt the following notation.

$$A_{k_{r-1}}^{t+\Delta t} - A^t = \Delta A_k \quad (\text{C.10})$$

$$\bar{\theta} A_{k_{r-1}}^{t+\Delta t} - (1 - \bar{\theta}) A^t = \Delta A_k^{\bar{\theta}} \quad (\text{C.11})$$

where A can be either an additional displacement field or an additional pressure field belong to discontinuity k and r is the Newton-Raphson iteration. The force vectors then are defined as

$$\begin{aligned} \mathbf{f}_u^{\text{ext}} &= \int_{\Gamma_t} \mathbf{N}^T \mathbf{t}_p^{t+\Delta t} d\Gamma \\ \mathbf{f}_u^{\text{int}} &= \int_{\Omega_e} \mathbf{B}^T \boldsymbol{\sigma}_{r-1} d\Omega_e \\ \mathbf{f}_{u_k}^{\text{ext}} &= \int_{\Gamma_t} \mathcal{H}_{\Gamma_{d_k}} \mathbf{N}^T \mathbf{t}_p^{t+\Delta t} d\Gamma \\ \mathbf{f}_{u_k}^{\text{int}} &= \int_{\Omega_e} \mathcal{H}_{\Gamma_{d_k}} \mathbf{B}^T \boldsymbol{\sigma}_{r-1} d\Omega_e + \int_{\Gamma_{d_k}} \mathbf{N}^T \mathbf{t}_{k_{r-1}} d\Gamma_{d_k} + \sum_{j=1, j \neq k}^m \int_{\Gamma_{d_j}} \Delta \mathcal{H}_{\Gamma_k}(\Gamma_j) \mathbf{N}^T \mathbf{t}_{j_{r-1}} d\Gamma_{d_j} \\ \mathbf{f}_p^{\text{ext}} &= \int_{\Gamma_f} \Delta t \mathbf{H}^T (\bar{\theta} f_f^{t+\Delta t} + (1 - \bar{\theta}) f_f^t) d\Gamma \\ \mathbf{f}_p^{\text{int}} &= \mathbf{C}_{\hat{p}\hat{u}} \cdot (\hat{\mathbf{u}}_{k-1}^{t+\Delta t} - \hat{\mathbf{u}}^t) + \sum_{j=1}^m \mathbf{C}_{\hat{p}\hat{u}_j} \Delta \hat{\mathbf{u}}_j + \Delta t \mathbf{K}_{\hat{p}\hat{p}} \cdot (\bar{\theta} \hat{\mathbf{p}}_{k-1}^{t+\Delta t} + (1 - \bar{\theta}) \hat{\mathbf{p}}^t) \\ &\quad + \Delta t \sum_{j=1}^m \mathbf{K}_{\hat{p}\hat{p}_j} \Delta \hat{\mathbf{p}}_j^{\bar{\theta}} + \mathbf{M}_{\hat{p}\hat{p}} \cdot (\hat{\mathbf{p}}_{r-1}^{t+\Delta t} - \hat{\mathbf{p}}^t) + \sum_{j=1}^m \mathbf{M}_{\hat{p}\hat{p}_j} \Delta \hat{\mathbf{p}}_j \end{aligned}$$

$$\begin{aligned}
\mathbf{f}_{\bar{p}_k}^{\text{ext}} &= \int_{\Gamma_f} \Delta t \mathcal{H}_{\Gamma_{dk}} \mathbf{H}^T (\bar{\theta} f_f^{t+\Delta t} + (1-\bar{\theta}) f_f^t) d\Gamma \\
\mathbf{f}_{\bar{p}_k}^{\text{int}} &= \mathbf{C}_{\bar{p}_k \hat{u}} \cdot (\hat{\mathbf{u}}_{r-1}^{t+\Delta t} - \hat{\mathbf{u}}^t) + \sum_{j=1}^m \mathbf{C}_{\bar{p}_k \hat{u}_j} \Delta \hat{\mathbf{u}}_j + \Delta t \mathbf{K}_{\bar{p}_k \hat{p}} \cdot (\bar{\theta} \hat{\mathbf{p}}_{r-1}^{t+\Delta t} + (1-\bar{\theta}) \hat{\mathbf{p}}^t) \\
&+ \Delta t \sum_{j=1}^m (\mathbf{K}_{\bar{p}_k \bar{p}_j} + \mathbf{Q}_{\bar{p}_k \bar{p}_j}) \Delta \hat{\mathbf{p}}_j^{\bar{\theta}} + \mathbf{M}_{\bar{p}_k \hat{p}} \cdot (\hat{\mathbf{p}}_{r-1}^{t+\Delta t} - \hat{\mathbf{p}}^t) + \sum_{j=1}^m \mathbf{M}_{\bar{p}_k \bar{p}_j} \Delta \hat{\mathbf{p}}_j \\
\mathbf{f}_{p_d}^{\text{ext}} &= \mathbf{H} \mathbf{Q}_{\text{in}} |_{S_d} \\
\mathbf{f}_{p_d}^{\text{int}} &= \mathbf{Q}_{p_d \hat{u}} \cdot (\hat{\mathbf{u}}_{r-1}^{t+\Delta t} - \hat{\mathbf{u}}^t) + \sum_{j=1}^m \mathbf{Q}_{p_d \hat{u}_j} \Delta \hat{\mathbf{u}}_j + \Delta t \mathbf{Q}_{p_d \hat{p}} \cdot (\bar{\theta} \hat{\mathbf{p}}_{r-1}^{t+\Delta t} + (1-\bar{\theta}) \hat{\mathbf{p}}^t) \\
&+ \sum_{j=1}^m \Delta t \mathbf{Q}_{p_d \bar{p}_j} \Delta \hat{\mathbf{p}}_j^{\bar{\theta}} + \mathbf{Q}_{p_d p_d}^{(2)} \cdot (\mathbf{p}_{d,r-1}^{t+\Delta t} - \mathbf{p}_d^t) + \Delta t \mathbf{Q}_{p_d p_d}^{(3)} \cdot (\bar{\theta} \mathbf{p}_{d,j-1}^{t+\Delta t} + (1-\bar{\theta}) \mathbf{p}_d^t) \\
&+ \Delta t \bar{\theta} \frac{\delta \mathbf{V}^T}{\delta s} q_{t,r-1}^{t+\Delta t} + \Delta t (1-\bar{\theta}) \frac{\delta \mathbf{V}^T}{\delta s} q_t^t
\end{aligned}$$

with q_t being the tangential fluid flow:

$$q_t = \frac{1}{12\mu} [u]_n^3 \frac{\partial \mathbf{V}}{\partial s} \mathbf{p}_d. \quad (\text{C.12})$$

Dankwoord

In vier jaar tijd heb ik met veel plezier het proefschrift dat voor u ligt afgerond. Er zijn natuurlijk een aantal personen die ik wil bedanken voor het tot stand komen van dit boekje. Laat me beginnen met de belangrijkste drie, in volgorde van ontmoeting gedurende mijn studie.

Jacques, je was al mijn begeleider tijdens mijn afstudeeropdracht bij Biomedische Technologie. Hier gaf je al blijk van wellicht de prettigste eigenschap die iedere student zich maar kan wensen, je was zeer betrokken bij mijn onderzoek maar gaf me ook de vrijheid om mezelf te ontplooiën tot daar waar mijn interesses lagen. Zo werd een experimenteel pad snel vaarwel gezegd en heb ik me vol overgave op ons numerieke model gestort. Hierdoor kom ik uit bij Joris, de architect van onze numerieke code Dawn. Gaandeweg mijn afstuderen raakte je steeds meer betrokken bij mijn project omdat ik aanpassingen wilde doen in allerlei modules. Je hebt me hiermee vanaf het eerste moment geholpen en ik waardeer het enorm hoe snel je me vertrouwde om mijn eigen gang te gaan in Dawn. De vele vergaderingen die we hebben gehad waren altijd een mix van even gezellig bijpraten om vervolgens kritisch mijn resultaten te bespreken. Je daagde me altijd uit door de lat hoog te leggen, wat zeker heeft bijgedragen tot dit mooie proefschrift. David, bedankt dat je me de gelegenheid hebt gegeven om mijn proefschrift te schrijven in jouw groep. Ik ben je dankbaar voor het gestelde vertrouwen in mij. Je liet me erg vrij in mijn onderzoek en gaf me de gelegenheid vele interessante steden en conferenties te bezoeken. Merci voor alles mannen, ik ben ervan overtuigd dat wij met z'n vieren een perfect team vormden.

Het werk gepresenteerd in dit proefschrift is uitgevoerd als deel van het 2F2S consortium dat gesponsord werd door Baker Hughes, EBN, ENGIE, the Dutch TKI Gas Foundation, en Wintershall. Naast deze financiële steun ben ik de industriële partners dankbaar voor de nuttige feedback die ik heb mogen ontvangen tijdens de 2F2S meetings. Het 2F2S consortium bestaat hiernaast ook nog uit vier andere projecten uitgevoerd op de Universiteiten van Utrecht en Delft. Allen in het 2F2S consortium bedankt voor de pret-

tige samenwerking. Speciaal woord van dank aan mijn collega's van het eerste uur Auke, Jeroen, Maartje en Nico. Ik waardeer alle hulp die jullie me hebben gegeven en ik denk met veel plezier terug aan mijn eerste en waarschijnlijk enige field trip samen met jullie naar de Whitby outcrops.

Naast alle collega's van de Energy Technology groep wil ik speciaal onze secretaresse Linda bedanken voor alle hulp die ze me heeft gegeven aangaande de organisatorische rompslomp rondom dit proefschrift. Ik ben altijd met veel plezier naar mijn kantoor gegaan mede dankzij mijn kantorgenoten Bouko, Kees en Raluca.

Erik Jan wil ik bedanken voor zijn hulp met de parallelle rekensommen en zijn advies omtrent de ELP implementatie. Bovendien zou dit werk niet mogelijk zijn geweest als we geen toegang hadden gehad tot zijn zeer goede JEM/JIVE libraries.

During this PhD I collaborated with the University of Padova. I would like to thank the exchange students Giulio and Paolo for the work they did in Eindhoven. My special thanks go to Francesco Pesavento and Bernhard Schrefler for giving me the opportunity to immerse myself, outside of the scope of this thesis, into isogeometric analysis at the University of Padova. I really enjoyed the stay, and of course the food, in Padova.

Het afronden van dit proefschrift was niet mogelijk geweest zonder de nodige ontspanning. Ondanks dat mijn "Nokkie Nokkie" vrienden altijd behoorlijk sarcastisch zijn als ik het over "werk" heb, denk ik met veel plezier terug aan de vele gezellige weekenden die we samen hadden en die we hopelijk in de toekomst blijven hebben. Daarnaast heb ik het geluk dat zowel de familie Remij als de familie Verheijen een erg leuke en gezellige groep is. Speciaal is de jaarlijkse skivakantie met de familie Verheijen in La Tzoumaz met veel gezelligheid, bordspellen en natuurlijk de oneindige skimogelijkheden. Dankzij dit promotietraject heb ik Eleanor leren kennen. Ik vind het erg leuk dat je aanwezig bent bij mijn verdediging en ik ben blij met al je gegeven hulp bij het afronden van dit boekje. Ik ben mijn broer Frank dankbaar voor zijn gevraagde en ongevraagde adviezen op het gebied van voetbal, kleding en mijn toekomstige salaris. Cecile bedankt voor de belangstelling die je altijd voor me hebt. Dat stel ik op prijs. Pap en Mam, dit proefschrift is aan jullie opgedragen want ik had geen betere ouders kunnen wensen. Als laatste wil ik mijn Opa en Oma, die ook jarenlang deel hebben uitgemaakt van mijn leven op de Kruiszijweg, bedanken voor alles wat ze voor me hebben gedaan. Ik zou willen dat we het afronden van dit proefschrift nog samen hadden kunnen vieren, vae zulle d'r waal nog eine op drinke names uch.

Ernst Remij

Eindhoven, januari 2017

Publications

Journal publications

- E.W. Remij, F.J. Lingen, J.M. Huyghe, D.M.J. Smeulders and J.J.C. Remmers. An efficient parallel X-FEM computing method. *Finite Elements in Analysis and Design*, submitted, 2017.
- E.W. Remij, J.J.C. Remmers, J.M. Huyghe and D.M.J. Smeulders. On the numerical simulation of crack interaction in hydraulic fracturing. *Computational Geosciences*, submitted, 2017.
- E.W. Remij, F. Pesavento, Y. Bazilevs, D.M.J. Smeulders, B.A. Schrefler and J.M. Huyghe. Isogeometric analysis of a multiphase porous media model for concrete at early age. *Journal of Engineering Mechanics*, submitted, 2016.
- D.C. Toan, E. Milanese, E.W. Remij, P. Rizzato, J.J.C. Remmers, L. Simoni, J.M. Huyghe, F. Hussain and B.A. Schrefler. Interaction between crack tip advancement and fluid flow in fracturing saturated porous media. *Mechanics Research Communications*, in press, 2016.
- E.W. Remij, J.J.C. Remmers, J.M. Huyghe and D.M.J. Smeulders. An investigation of the step-wise propagation of a mode-II fracture in a poroelastic medium. *Mechanics Research Communications*, in press, 2016.
- E.W. Remij, J.J.C. Remmers, J.M. Huyghe and D.M.J. Smeulders. The enhanced local pressure model for the accurate analysis of fluid pressure driven fracture in porous materials. *Computer Methods in Applied Mechanics and Engineering*, 286:296-312, 2015.

- E.W. Remij, J.J.C. Remmers, D.M.J. Smeulders and J.M. Huyghe. A partition of unity-based model for crack nucleation and propagation in porous media, including orthotropic materials. *Transport in Porous Media*, 106(3):505-522, 2015.

Conference proceedings

- E.W. Remij, J.J.C. Remmers, J.M. Huyghe and D.M.J. Smeulders. Numerical modelling of hydraulic fracturing. In F. Oka, A. Murakami, R. Uzuoka and S. Kimoto (Eds.), *Conference Paper : Proceedings of the 14th international conference of international association for computer methods and recent advances in geomechanics*, Kyoto, Japan, 22-25 September 2014, CRC Press.
- E.W. Remij, J.J.C. Remmers, J.M. Huyghe and D.M.J. Smeulders. A partition of unity based model for hydraulic fracturing. *Conference Paper : 76th EAGE Conference and Exhibition 2014*, Amsterdam RAI, The Netherlands, 16-19 June 2014, AEGE.
- E.W. Remij, Pizzocolo, F., J.J.C. Remmers, D.M.J. Smeulders and J.M. Huyghe. Nucleation and mixed mode crack propagation in a porous material. In C. Hellmich, B. Pichler and P. Adam (Eds.), *Conference Paper : Poromechanics V: Proceedings of the Fifth Biot Conference on Poromechanics*, July 10-12, 2013, Vienna, Austria, (pp. 2260-2269). Reston: American Society of Civil Engineers

Curriculum Vitae

Ernst Remij was born on the 17th of February 1987 in Nederweert-Eind, the Netherlands. After finishing the VWO at the Philips van Horne Scholengemeenschap in Weert he started studying Applied Physics at Eindhoven University of Technology in 2005. After one year Ernst switched to the study of Biomedical Engineering within the same university. He obtained his Bachelor of Science in 2009. Ernst chose to continue his studying in the Master program of Biomedical Engineering at the same university, in the Orthopaedic Biomechanics group of prof.dr. K. Ito. In 2011 Ernst performed an internship at the École Polytechnique Fédérale de Lausanne, Switzerland, under the supervision of Dr. A. Terrier. During this four month project he performed a numerical investigation of the effects of damage in knee cartilage. Ernst obtained his MSc in 2013 with his thesis entitled: "Arbitrary crack propagation and nucleation in porous materials". In the same year he started his PhD project in the Energy Technology group in the Department of Mechanical Engineering at Eindhoven University of Technology. His PhD project, entitled "Fluid driven and mechanically induced fracture propagation: theory and numerical simulation", was supervised by prof.dr.ir. D.M.J. Smeulders, prof.dr.ir. J.M.R.J. Huyghe and dr.ir. J.J.C. Remmers. During his PhD project Ernst stayed for a short period at the University of Padova, Italy. In Padova he collaborated with dr. F. Pesavento and prof.dr. B.A Schrefler on an isogeometric implementation of a multiphase porous media model for concrete at early age.